Conducting Metal Oxide Materials for Printed Electronics

Jack R. McGhee

A Doctoral Thesis

Submitted in partial fulfilment of the requirements for the award for

Doctor of Philosophy of Loughborough University

September 2019

“I know not all that may be coming, but be it what it will, I'll go to it laughing.” — Herman Melville, Moby-Dick, or, the Whale

“Even a fool learns something once it hits him.” — Homer, Iliad

Abstract

Printed electronics as a manufacturing process has many advantages, mainly, it allows for the high throughput rapid fabrication of thin, flexible electronic components with minimal waste. There are many printing processes that can be utilised for printing electronics and although each process can differ vastly, the materials currently used in these processes are generally the same, silver and carbon. However, to develop printing as a more mainstream manufacturing method for electronics, a wider variety of materials are required which can provide better stability and longevity of components, new functionality for printed applications and allow for in-situ processing and tuning of components. Conducting metal oxides are a good candidate for integrating into printed electronics processes, these materials are typically semiconductors, they have bandgaps, and properties can be altered via altering the band gap. They are also oxides, so they cannot oxidise further and therefore atmospheric damage is reduced compared to pure metals. They can also be fabricated into a wide range of particle morphologies, all with advantages in different fields and electronic applications. Therefore, the ability to print these materials is valuable to the field.

In this thesis, the integration of conducting metal oxide electro-ceramic materials into the field of printed electronics has been explored. This was performed through the completion of five research objectives including, the selection of appropriate materials for the research, the formulation of conductive inks with the materials, the investigation of post-processing techniques for printed films and further research into passive component fabrication and sensor applications. Firstly, following an extensive literature review, four materials were selected including three doped zinc oxide materials synthesised via different methods. The fourth material is commercially sourced indium tin oxide (ITO). A nitrocellulose vehicle was determined to be the most compatible with the oxides and selected for ink formulation. Inks were then formulated with all four materials, with optical and electrical properties analysed. Gallium doped Zinc Oxide (GZO) and ITO were selected for further investigation based on the excellent conductivity of the indium tin oxide (57.77$\Omega\square^{-1}$) and the highly transparent optical properties of the gallium doped zinc oxide (>84% transmittance).

Laser processing was selected as a post processing method. It was found that the laser processing dramatically increased conductivity. The GZO improving from a non-conductive

film to 10.21% of bulk conductivity. The ITO improved from 3.46% to 40.47% of the bulk conductivity. It was also found that the laser processing invoked a carbothermal reduction process allowing for a rapid manufacturing process for converting spherical particles into useful nanoparticle morphologies (nanorods, nanowires etc). Following this, resistive and capacitive applications involving laser processing and conventionally heat-treated conductive oxide inks were developed. Combining the new materials and manufacturing processes, tuneable printed resistors with a tuning range of 50Ω to 20MΩ could be fabricated. All metal oxide, ITO based capacitors were also fabricated and characterised. These were then developed into humidity sensors which provided excellent humidity sensing properties, showing linearity between 5 and 95% relative humidity (RH) and sensitivities of up to 7.76pF/RH%, demonstrating higher performance than commercial equivalents (0.2 – 0.5pF/RH%). In conclusion, this work provides a breakthrough for conductive metal oxide materials research and its place in Printed Electronics research by providing insight into the processes required to make these materials conduct and by developing useful manufacturing methods, post processing techniques and applications.

Acknowledgements

I would like to take the opportunity to thank all the people who have helped and supported me during my PhD. Firstly, I would like to thank my supervisor Dr Darren Southee for providing support with his extensive knowledge of all things printing and electronics and for providing me with the opportunities to develop my skills throughout the years, I couldn't have asked for a better supervisor. In addition, thanks to Dr Peter Evans for training me in the art of ink formulation and mentoring me in a way which prepared me for the ~~primal hallucinatory nightmare~~ academic experience, something he believes I am "cursed" to endure 'til the end of my days.

This research has taken me on an odyssey through the different departments of Loughborough University, meeting many different people who have all helped me immensely. Firstly, in the Design School, thanks to Dr Matt Sinclair who introduced me to the wonderful world of additive manufacturing and to Dr Andrew Johnson who unfortunately had to read and scrutinise copious amounts of text every August in the form of yearly reviews. In the Department of Chemistry, I would like to thank Al Daley whose health and safety advice helped me to stay safe and enabled me to not write my thesis from a hospital bed. Thanks to Pauline King for training me up on equipment and providing guidance throughout the years. I would also like to thank Dr Jagdeep Sagu, he has been extremely helpful and knowledgeable throughout the PhD and he deserves some sort of award for SEM beauty shots. In the Wolfson School, thanks to Dr David Hutt who has always provided immensely helpful guidance and support, I learn a great deal during every conversation. Thanks to Dr Jing Wang and Dr Sherry Ghanizadeh for all the support they have provided. Finally, thanks to Dr Athanasios Goulas who has been a good friend, even during 10-hour long experiments during summer heat…

During this journey, I have been kept sane by many friends old and new. Firstly, from the best county (Lancashire), I am always kept in high spirits by childhood friends Ben (this is the first time I have not called him by his nickname in 15 years), Dale and John. Secondly, all my friends from undergraduate university, who keep my liver in check a few times each year. Finally, the friends I have made throughout my PhD, Jamie, Ryan and Paulo. One important mention is for Diana Mehta, we met on the first day of our undergraduate course, since then for 8 years we have worked together at both undergraduate and PhD level and even lived together and I

have been grateful to have a friend who is experiencing the same strange life choices simultaneously.

I would like to thank my family for also supporting me through this process, they do a good job of making me not think of work when I am home, and it has been important having that downtime. Finally, a massive thank you to my partner Sora, who has had to put up with me during this long and arduous process, especially during the final stages. She has plans to enter academia (I warned her already) and hopefully I can be a fraction of how patient she has been when her time comes. Thanks for all the support.

Publications

Published

J. R. McGhee, D. J. Southee, P. S. A. Evans, R. B. Middlemiss, K.G.U. Wijayantha, "Flexible, All Metal-Oxide Capacitors for Printed Electronics", in Thirteenth International Conference on Nanotechnology Materials and Devices, Portland, Oregon, United States of America, 2018.

J. R. McGhee, J. S. Sagu, D. J. Southee, K.G.U. Wijayantha, "Humidity Sensing Properties of Transparent Sputter Coated Indium Tin Oxide and Printed Polymer Structures", IEEE Sensors, vol. 18, no. 18, pp 7358-7364, 2018 (*Nominated for IEEE Sensors Best Paper Award 2018*)

J. R. McGhee, M. Sinclair, D. J. Southee, K.G.U. Wijayantha, "Strain Sensing Characteristics of 3D-Printed Conductive Plastics", Electronics Letters, vol. 54, no. 9, pp 570-571, 2018 (*Featured Article for the issue*)

Featured Articles

J. R. McGhee, M. Sinclair, D. J. Southee, K.G.U. Wijayantha, "Printing Conductive Plastics", Electronics Letters, vol. 54, no. 9, pp 541, 2018

Poster Presentations

J. R. McGhee, M. Sinclair, D. J. Southee, K.G.U. Wijayantha, "3D Printed Piezoresistive Sensors, viability and applications", IDTechEX Europe, Berlin, Germany, 2017.

Invited Talks

"New Materials and Methods for Printed Electronics", 45th Annual Symposium, Institute of Circuit Technology, June 4th, 2019.

Contents

List of Figures, Tables, and Equations

List of Figures

List of Tables

List of Equations

Acronyms

AD	Anno Domini
AZO	Aluminium doped Zinc Oxide
AGZO	Aluminium/Gallium doped Zinc Oxide
AgNW	Silver (Ag) Nanowires
BC	Before Christ
CHFS	Continuous Hydrothermal Flow Synthesis
CNT	Carbon Nanotubes
GRA	Graphene Flakes
GZO	Gallium doped Zinc Oxide
ITO	Indium Tin Oxide
FTO	Fluorine doped Tin Oxide
MW	Microwaved
XRD	X-ray Diffraction
SEM	Scanning Electron Microscopy
TEM	Transmission Electron Microscopy
UV	Ultra-violet
VIS	Visible

Chapter 1

Introduction

1.1 Background

Conductive metal oxides are extremely useful materials, typically made up of semiconductors. Depending on the dopant and the bandgap, they can show metallic conductivity or n-type and p-type semiconducting properties. Alongside this, they are more resistant to environmental changes than commonly used printed electronics materials like silver or carbon, they can only oxidise further through the filling of oxygen vacancies in the material structure, a reversible process typically allowing the material to function for over 25 years. Of these materials, an extremely useful subset is transparent conducting oxides, which are used in displays, smart phones and solar cells with research into flexible, transparent devices growing. There are a wide variety of materials which can be used for these applications. However, transparent conducting oxides (TCOs) are the most popular. A definition of transparent conducting oxides is that they are metal oxide-based materials (e.g. iron oxide, zinc oxide) which in thin layers ($3\mu m$ or below) are transparent and conduct electricity across the film.

There are two main challenges currently facing the transparent conducting oxide industry . The first is the sustainability of the highest performing materials. Indium tin oxide (ITO) is the most popular material for transparent electronics, taking a 97% market share [1]. Indium is becoming increasingly difficult to mine efficiently due to it being a secondary product in other ores and if used at the current rate, has a predicted 20 years left [2]. Tin is also used in large amounts, over 40000 metric tonnes of tin is consumed a year [3] and is currently estimated at having only enough stable, easily mined supply for the next 16 years [4]. Recycling is also not a viable option, although there are techniques to recycle they require high energy, halogenated processes and the thin film nature of most TCO applications creates cross contamination issues. This suggests the transparent device market is currently unsustainable and research must be conducted in order to address this issue by developing sustainable alternative materials and materials processing methods.

The second challenge is a manufacturing issue, currently the only viable manufacturing techniques for TCO based electronics are for large area coatings through high temperature,

environmentally damaging halogenated (Chlorine, Fluorine) chemical processes [5]. These large area coatings are then subjected to chemical etching processes to fabricate more complex electrical devices again using harmful chemicals. This challenge can be addressed by developing these materials for high resolution, additive manufacturing processes – eliminating the need for chemical etching. Reviewing the current challenges of the TCO industry any new manufacturing method is required to:

- Be able to deposit controlled layers of material with minimal waste
- Pattern the material with minimal waste
- Be able to have an efficient post processing treatment performed for optimal electronic properties

One potential new manufacturing method which addresses the issues discussed and meets the criteria set out above is printing. Originally used for the visual communication of ideas and graphics. Inks were solely made for visually conveying graphical information or text. Since 1972, researchers developed the idea of using printing for the fabrication of devices rather than printing for communication [6]. Inks were developed that had electrical properties rather than visual properties and disrupted the electronics and printing industry. The field of printed electronics involves the fabrication of two-dimensional, high resolution, electrical devices onto various substrates (glass, plastic film etc.) via printed processes.

Printed electronics appears to be a viable manufacturing method for transparent conducting oxides, there are multiple printing processes which give control over layer thickness affecting transparency and conductivity [7]. The process is additive making it a more sustainable manufacturing method and complex patterns can be printed making it ideal for printing conductive areas and patterns [8]. Since 2009, various attempts have been made to integrate transparent conducting oxides into the inkjet printing process [9]. However, inkjet printing has yet to solve two major issues. The first is the sustainability of the technique compared to traditional deposition techniques. Although it is a less environmentally harmful process which does not require chemical etching or halogenated gas use, the printing nozzles on industrial inkjet printers suffer from regular blockage [10]. This requires the printhead to purge ink into a vessel for disposal after every layer, leading to relatively large quantities of waste material for disposal [11]. Secondly, one feature of transparent conducting oxides is that they belong

to a family of materials called Ceramics. These are highly stable polycrystalline materials with high melting points and glass transition temperatures, requiring high temperature processing (>600^{O}C) to reach their optimal transparency and conductivity [12].

Inkjet inks generally have a water-like low viscosity and the mechanics of how well they work are governed by contact angles, surface tension and colloidal dispersions. There has been one attempt at integrating these materials with the gravure printing process [13]. However, how these materials function in other printing processes such as screen, offset lithography and 3D material extrusion after being formulated into steric hindrance based highly viscous inks has yet to be explored. The characteristics of TCOs in traditional printing manufacturing processes are currently unknown and therefore electronic components utilising these processes have not been developed. Considering the applications of TCOs discussed earlier in this section (thin films and capacitive meshes requiring thin tracks), it is important that any printed metal oxide has good conductivity in both films and tracks. For the majority of applications, a sheet resistance of sub 500Ω$\square^{-1}$.

The research contained in this thesis develops and optimises inks for integration with sustainable additive manufacturing printing processes such as screen printing and micro-dispensing based material extrusion. Post-processing techniques are investigated to determine whether the electrical and optical performance of the inks are improved. Conductive tracking and passive electronic components are then printed using the developed inks and post-processing techniques to determine their viability for printed electronics. These developments then allow for more advanced uses of the passive components such as sensor devices and signal processing circuits.

If these processes are developed further, it could lead to a more sustainable manufacturing process for most of the world's consumer electronics. There is also scope for research into post-processing techniques for high temperature materials on low temperature substrates (flexible polymer sheets etc.) such a photonic flash sintering, laser processing and selective microwave treatment.

1.2 Research Aim

To develop a method of depositing conducting oxides in complex patterns with an industrially viable post-processing method, towards the manufacture of conducting oxide based electronic devices with the long-term aim of improving sustainability via reduction of waste and harmful halogenated chemical processing.

1.3 Research Objectives

Research objectives have been developed to meet the research aim outlined in section 1.2. There are six overall research objectives:

(RO1) Identify and determine the characteristics of ITO and ITO Alternatives

To replace indium tin oxide (ITO) a viable alternative is required, this research is not one of fundamental material discovery but one of identifying a comparable material for the replacement of ITO. An alternative, sustainable transparent conducting oxide will be selected. This alternative material will be researched alongside ITO to identify differences in material quality and to determine whether ITO currently has a viable indium free alternative.

(RO2) To formulate and optimise conductive oxide-based inks and characterise the properties of printed films

Firstly, the fluid part of the ink, also known is the vehicle must be selected. A vehicle will typically contain additives to help the ink adhere to a substrate, solvents to aid in printability and additives to aid in drying and shelf life. A variety of these “vehicles” for ink formulation will be tested to determine the most suitable for these materials. For the purposes of this research, a suitable vehicle will be one that enables high quality printing, high conductivity and one which provides the best film densification, a crucial factor in improving conductivity. Once a suitable vehicle has been selected, conductive oxide inks will be formulated and optimised through optical, electrical and rheological data to determine their characteristics as printed electronic films. Two formulations will be selected, one giving the most conductive prints and the other giving the most transparent prints. Composite material inks will then be developed with other

transparent conductors to see if an improvement in electrical or optical properties occurs.

(RO3) To investigate an industrially viable post-processing technique for optimisation

Conducting oxides are ceramic class materials and typically require high temperature sintering to achieve their best optical and electrical performance. An industrially viable post-processing technique which allows for high temperature processing on low temperature flexible substrates will be investigated to see if an improvement of performance occurs.

(RO4) Develop and Characterise Printed tracks and passive devices

Printed conductive tracking will be electrically characterised to determine the performance of thin tracks of conductive oxide material. This is important due to one of the main uses of oxides, resistive meshes as heating elements. The second most popular industrial use for conducting oxides is components based on capacitance, for example touch screens. Capacitors will be developed using printed conductive oxide materials allowing for characterisation and comparison.

(RO5) Fabricate Printed 2-D Applications Utilizing the Printed Passive Components

Fully printed signal processing and sensor applications will be fabricated using the printed capacitors. Investigating the performance of the conducting oxide materials in this way allows for determining the viability of the printing process to allow for useful applications.

Upon the completion of these research objectives, the research will provide a building block for others developing electro-ceramic based viscous printing inks for electronic applications. This will help to build upon with the long-term aim of reaching sustainable, viable manufacturing methods for transparent conducting materials with comparable performance to traditional coating methods.

1.4 Research Methodology and Thesis Structure

The design research methodology formulated for this thesis was informed by Blessing and Chakrabarti [14]. In their 2009 book, “DRM, a Design Research Methodology”, they describe the need for more scientific rigour in Design research and how a well-designed research methodology can “guide the selection and application of a suitable approach and appropriate methods”. Most of the research contained in this thesis uses the traditional scientific method described by Edgar Wilson in his 1952 book “An Introduction of Scientific Research” as shown in Figure 1 [15].

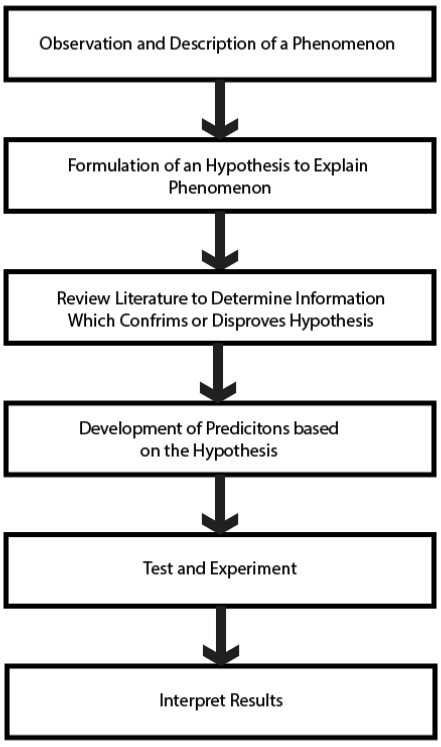

Figure 1 The Scientific Method [15]

However, research is not as straight forward as adhering to this model and there are some aspects of this thesis however which focus on the design of applications. The methodological framework formulated by Blessing and Chakrabarti can be seen in Figure 2 [14]. This framework is similar in many ways to the scientific method, research clarification is essentially the third step of the traditional method shown in Figure 1. The framework describe in Figure 2 allows for a more iterative process which suits process optimisation and applications design more.

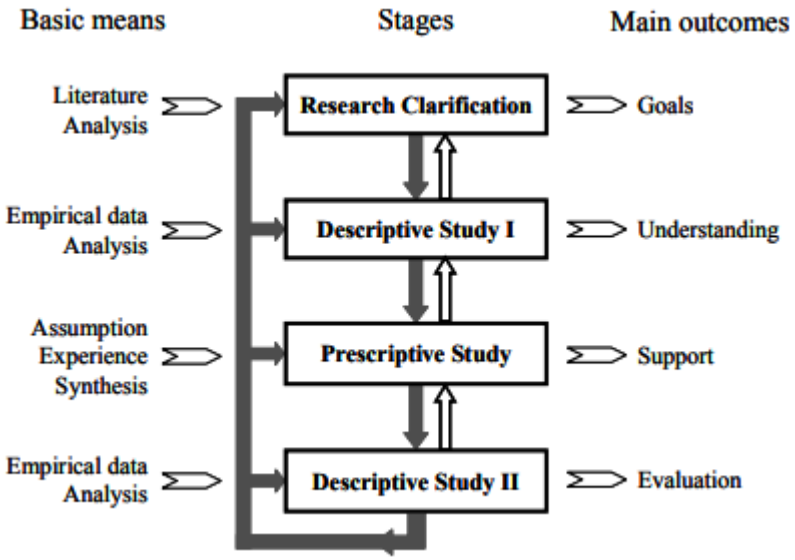

Figure 2 DRM Framework as Described in Blessing and Chakrabarti [14]

This framework has been adapted and shown in Figure 3. The research clarification in this thesis is a review of the literature which confirms, or denies, the plausibility of the research aim in Section 1.2. The first descriptive study tackles ink formulation with conductive oxides (RO2) which is a comprehensive study.

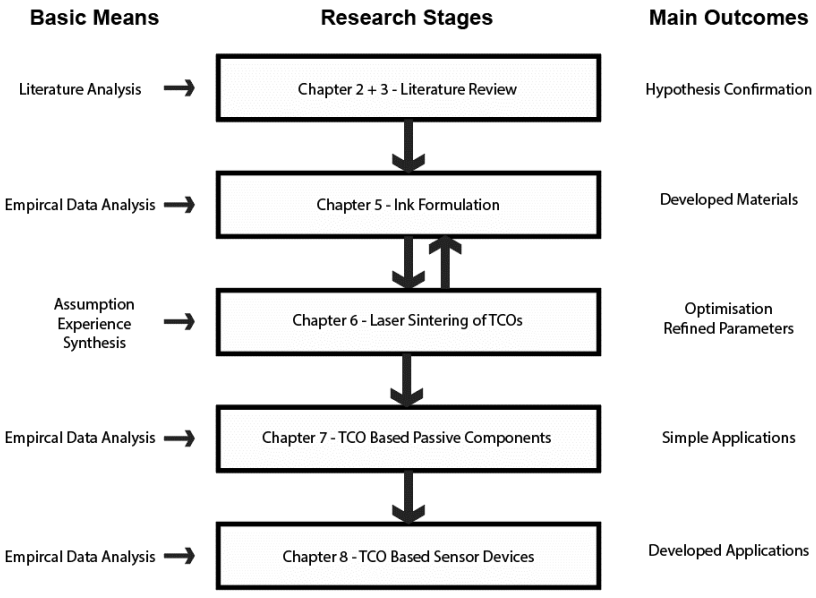

Figure 3 Adapted DRM Framework for Research

The prescriptive study is contained only in Chapter 6, this will be the chapter that optimises the ink performance using both experience from Chapter 5 and uses a synthesis of data to

refine the parameters needed for the second descriptive study. Chapter 6 also forms a comprehensive set of work where a design of experiments is set up to optimise the post processing parameters to develop inks with the best performance. Chapters 7, and 8 form the final descriptive study where chapters form a mix of comprehensive and initial studies. Chapters 7 and 8 are assigned as comprehensive studies where the fabrication of passive electronic components and sensors are fully explored. Chapter 9 will then conclude the research discussing how the research objectives were achieved, the limitations of the research and will provide some suggestions of future work. A full plan of the research to be conducted with regards to chapters and research objectives can be seen in Figure 4.

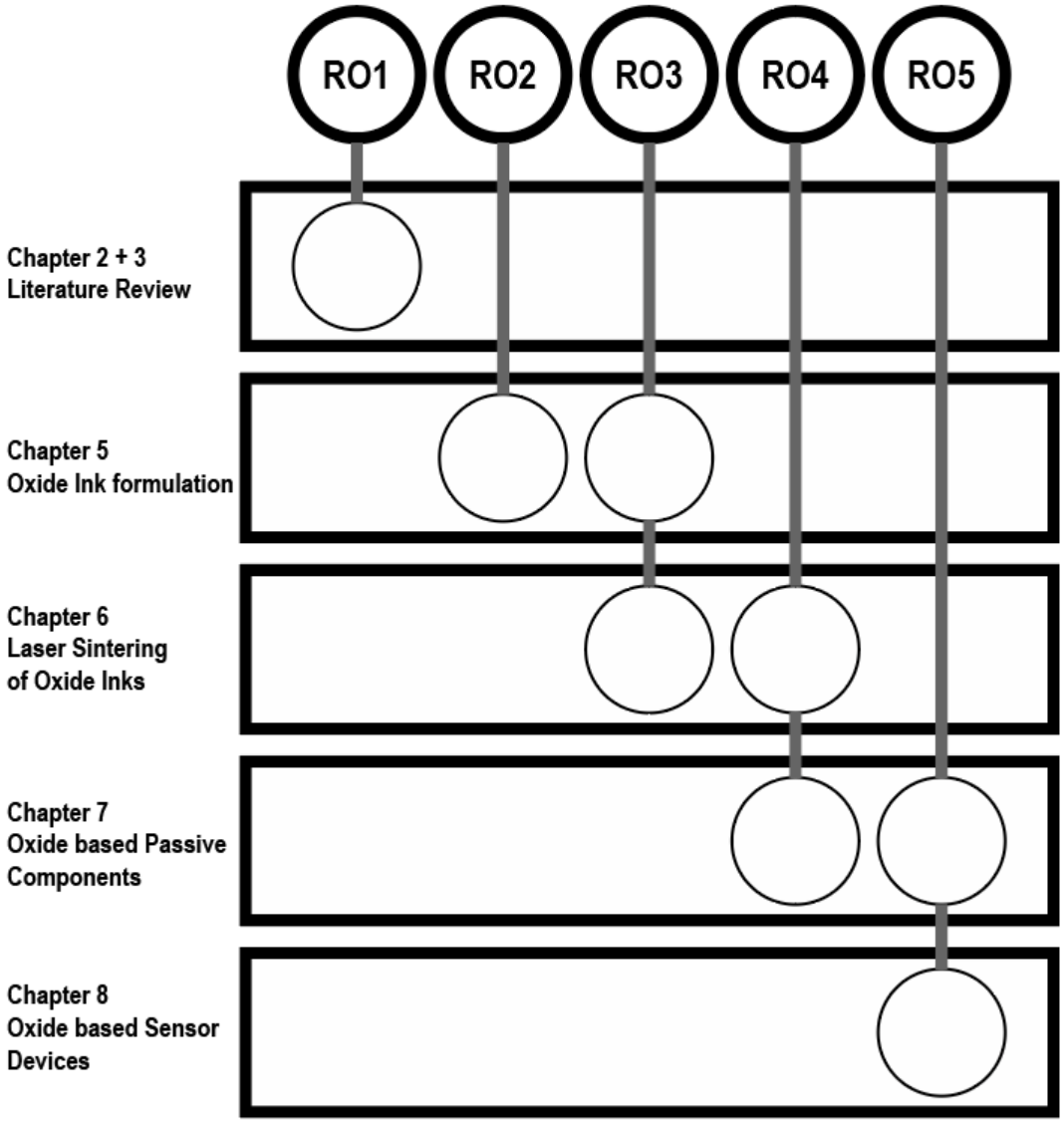

Figure 4 Research Plan and Structure of the thesis

Chapter 1 provides a brief introduction to the topics surrounding this research. It supplies the relevant background information required for understanding the work conducted in fulfilment of this Ph.D. It also outlines the overarching aims of the research and its overall research methodology.

Chapters 2 and 3 feature literature reviews in the fields of printing processes, printed electronics, ink formulation and applications. It also provides a review of conducting oxides, transparent conducting oxides, transparent electronic components, transparent electrically conductive materials and manufacturing processes for these materials. These chapters form a descriptive study to clarify gaps in the research and guide the direction of the work.

Chapter 4 outlines the theory and experimental methods for the research conducted in this thesis. It provides a literature-based background on equipment, measurement techniques and processes used in the experimental research.

Chapter 5 is the first study conducted. This research was conducted into ink formulation using TCO powders. It provides electrical and optical characterisation of printed TCO films and an investigation into both conventional and microwave sintering techniques.

Chapter 6 is the second study conducted. This study investigates the use of lasers as a method for sintering TCO materials at high temperatures onto substrates to enhance electrical and optical properties. It contains a full design of experiments optimisation process designed to optimise the laser sintering process for 8 inks.

Chapter 7 pertains to the third set of experimental work conducted, the development of applications for the conducting oxides using the newly developed post processing technique and the screen-printing technique. Conducting oxides are used in conjunction with screen printing to develop resistive and capacitive applications. The capacitors are characterised and are used to RC circuits in order to assess their performance.

Chapter 8 presents the experimental work conducted into the development of TCO based sensors. Both sputtered and printed conductive oxide materials are characterised as humidity sensors.

Chapter 9 concludes this thesis, analysing the research as a whole, whether the research objectives have been met and presenting the contributions to knowledge provided by the research. Recommendations for future work, based on the findings of this thesis will also be discussed.

1.5 Research Acknowledgements

This Ph.D. research is part of an overarching collaboration between Loughborough University Design School, Department of Chemistry, the Wolfson School of Mechanical Engineering, and the University of Central London with industry to develop sustainable alternatives to indium tin oxide and to develop and discover sustainable manufacturing methods.

The work in this thesis has been solely conducted by the author unless otherwise stated. This Ph.D. was funded by Loughborough University with the experimental work being funded by the UK EPSRC 'Sustainable Manufacturing of Transparent Conducting Oxide (TCO) inks and Thin Films' project.

In Chapter 5, Dr Peter Evans, an expert in ink formulation and printed electronics performed training in ink formulation techniques and in the use of vital equipment. He gave advice for the types of materials required to form a good screen-printing ink. Ink formulation is an art with few papers detailing the full process and therefore it is difficult to learn from reading literature.

Throughout Chapters 5, 6 and 7, printed electrodes were mainly deposited onto Melinex ST504 polyethylene terephthalate (PET) plastic film. Thanks to one of our industry partners, Dr Bill MacDonald from Dupont Teijin Films for supplying a 90m roll in support of this research. Thanks to our industry partner Dr Rick Spencer and Diamond Coatings LTD for supplying this research with ITO sputter-coated plastic films used in Chapter 8. Thanks to Dr Thanos Goulas and Dr Daniel Engstrøm for support with micro-dispensing and laser processing and providing valuable insight with regards to Chapter 6. Also, in Chapter 6, thanks to Dr Zhaoxia Zhou for taking the time to help analyse samples through transmission electron microscopy. Also, a big thank you to Jamie Lowe who helped immensely in collecting Hall Effect measurements in Chapter 6.

Chapter 2

Printing Processes and Ink Formulation

2.1 A Brief History of Printing

Printing has been a staple of how humans communicate with each other since ca. 35000 BC, when Palaeolithic cave art was painted with hand stencils in Europe [16]. Advances in the area were not made until the third century BC in China, were bronze casts were imprinted with designs to print ink onto pottery [17]. Woodblock printing as shown in Figure 5, also known as xylography was then developed in China and Japan ca. 200 AD to bring about the first method of printing designs onto paper and textiles [18]. This was the first iteration of the printing press and helped scholars in the Far East mass produce literature for the first time. Printed Chinese literature can be dated back to ca. 650 AD [19]. However, although it became cheaper and faster to reproduce books in China, most printed materials were still handwritten up until the 15th century. This was due to it still being less expensive and more profitable to hire a copywriter than to use woodblock printing presses [20].

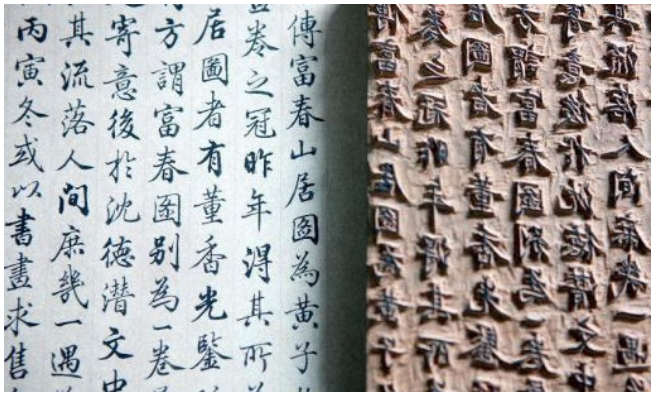

Figure 5 Woodblock printing board with printed text [21]

In China, the moveable type printing press was also developed. This type of printing press utilised movable components to form complete pages and was not invented until 1041AD [18]. This later catalysed the invention of the first paper based printed money, as reported by Marco Polo in 1298 [18] [22].

However, the success of the woodblock printing press in China led to stagnation in printing advances, enabling Europe to develop printing processes into what we recognise today [23].

Paper was not introduced to Europe until the Moorish invasion of Spain in 711AD and access to printed literature was rare [18]. Due to the Silk Road, printing technology spread to Europe in the early 14th century [24]. As shown in Figure 6, Johannes Gutenberg, a German blacksmith reinvented this technology in 1439 to develop the traditional printing press and European books.

Figure 6 (a) Gutenberg Printing Press, (b) First mass produced book – 180 copies of the Bible printed by Gutenberg, 1455 [25]

This brought about the European golden age of printing, with Gutenberg's printing press facilitating the large-scale mass production of books using oil-based inks [26]. The printing press enabled societal change due to the mass production and dissemination of information. This led historian Marshal McLuhan to develop a four-step evolution to mankind's civilisation [27]:

- The Era of Oral Communication - also known as "tribe culture"
- The Culture of the Manuscript - memory and information transferred through art
- The Gutenberg Galaxy - widely available local literature enabling societal and cognitive evolution
- The Electronic Age – also known as "the global village", enabling instant mass communication across the globe

The invention of Gutenberg's printing press facilitated the renaissance in the west. It increased access to education, revolutionary ideas and concepts about the organisation of society [26]. Literacy rates changed drastically from 30% of adults in 1440 to 83% of adults in 2008 being literate [28][29]. The invention of the printing press has also been associated with population

growth. In the renaissance era, cities with access to printing presses grew 60% faster than cities without [30].

The next major advance in printing technology was in 1875 when Robert Barclay developed the Offset Lithograph printing press [31]. The initial Offset Lithography press was created for mass printing on metal and smooth surfaces and in 1904, Ira Washington modified the process to print directly onto paper [31]. The offset lithography process, as seen in Figure 7, transfers an inked image from a metal plate to a rubber-based roller which then uses the hydrophobic repulsion between ink and water. This hydrophobic repulsion keeps areas on the paper ink free to print detailed, high resolution images – this is explained in greater depth in Chapter 2.

Figure 7 Modern Offset Lithography Printing Press [32]

Offset lithography is a roll to roll process enabling higher printing quality with greater throughput. Due to this, it became the method of choice for printing newspapers [31].

Printing methods such as flexography and gravure built upon offset lithography with limited success. Flexography was developed to work in a similar way to offset lithography with the main change being a flexible image relief plate, allowing for printing onto flexible substrates with ease. Gravure is also similar with the major difference being that instead of having a relief plate, the image is engraved directly onto the rollers and utilises water-based inks. Both techniques went on to later find their own uses in printing on flexible plastic (i.e. labels, tapes etc.).

In 1907, Samuel Simon invented screen printing (as shown in Figure 8), updating the stencil printing method. The artwork was woven into a mesh stencil. The ink is then forced through the stencil using a blade. Production output was not as large as offset lithography. However,

it was easier to print multicoloured graphics and was mainly used for replication art or printing for multicoloured posters or signs [33]. The method became popular during the 1960's with famous artists (e.g. Andy Warhol) using it to design popular works.

Figure 8 Modern Industrial Screen-Printing Setup [34]

Dot matrix printing was invented in 1968 by Epson in Japan. They used metal pins coated in ink to physically strike paper, enabling multiple fonts to be used [35]. These were the first printers which could be realistically owned by household consumers, creating another evolution of mass communication [27]. Inkjet printers followed in the late 1970s using piezoelectric crystals or heat to control the flow of the ink and providing a high-quality image.

Inkjet printing is an entirely wet process and its use in commercial environments was limited due to the cost of the ink and the relatively slow time to print a single page. Due to this, a new printing technique was developed in 1957 based on electrostatics, the printing technology commonly found in Laser Printers and Photocopiers [36]. Electrostatic printing is a dry process and uses static electricity to selectively deposit material onto a substrate. A high voltage wire statically charges a metal cylinder (also known as a drum) and provides it with a uniformly positive charge. A laser then essentially draws the image to be printed onto the drum, creating an image in negative charge. This material can either be a wet ink, or more commonly in the modern era, a powdered material which is typically known as toner is then coated onto the charged drum, sticking to the negatively charged imaged. A substrate is then passed through and is coated in the material, ejecting from the printer as a fully printed document. This enables printing to be performed at a much higher speed than inkjet, gaining popularity within

businesses due to it' high speed, high throughput capability and relatively low cost per printed page [37].

The next "printing revolution" took hold in the early 2000s with the original patents for Additive Manufacturing (AM) based Material Extrusion (ME) expiring in 2006 [36]. As can be seen in Figure 9, Material Extrusion typically extrudes molten material layer by layer building a 3D object giving it the colloquial name of "3D Printing".

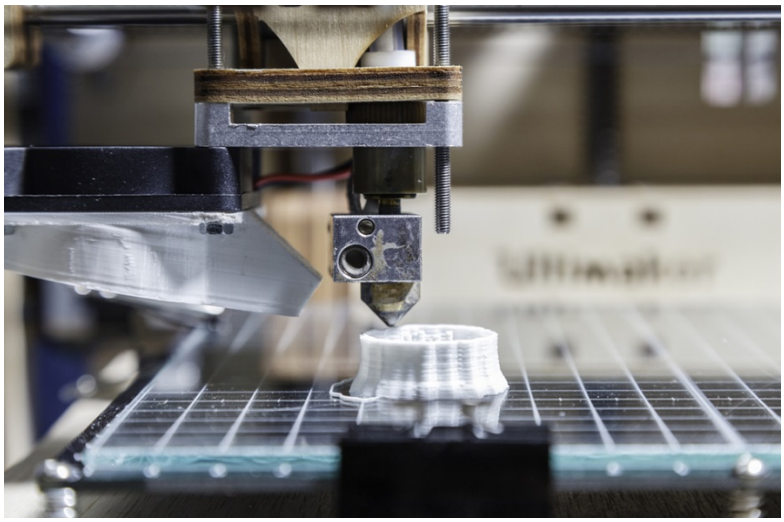

Figure 9 Material extrusion - 3D printing [37]

Using printing to democratise the manufacturing process itself 3D-printing is used for manufacturing prototypes, and functional devices. It has been predicted by researchers in economics that individuals and communities having the control to manufacture at the press of a button will have geopolitical ramifications equating to the invention of the printing press [38].

Since the invention of the inkjet printer, research has focused not on how printers can be improved to convey visual information but has instead focused on how these techniques can be used to create disruption in other markets. This thesis will focus on printing as a disruptive manufacturing method for functional electronic components.

2.2 Printing Processes for Electronics

In 1972 research into functionalising inks for printing processes began which enabled academics and industry to develop printed electrical devices from electrically conducting inks. A key paper at the time was Scarisbrick's "Electrically Conducting Mixtures" which laid out the key physics of conducting inks providing a base for researchers to formulate their own inks from [39].

A major benefit for printing electrical devices is that low cost, high throughput fabrication can be achieved using traditional printing press equipment. This has enabled technologies such as RFID tagging to become widespread in markets. Other common applications of printed electronics are smart labels, sensors, flexible displays and power sources, with new applications being developed for paper-based sensors and printed platforms for microfluidics [40] [41].

The first reported printed conductive material used a conductive silver/palladium ink with a dispensing extrusion system for the ink to print fine lines [42]. Since the 1970s, research has been performed to integrate conductive inks into commonly used printing processes. The most common printing process for electronics is screen printing (the process which will be discussed in this research). However, inkjet is also popular and flexography, offset lithography and gravure are also used as presented in Section 2.1. These printing processes were initially designed for printed graphics, the human eye can only resolve features to approximately 20 microns and due to this, printers cannot generally go below 20-micron resolution [43].

Both the resolution and registration of the printing process is important as it determines the level of complexity and functionality printed electrical devices can have [44]. Typically, the printed process should be chosen for the application required. Applications such as transistors require a much higher level of resolution are typically printed using gravure [45]. For sheet-based applications such as basic electrodes or sensors, inkjet and screen printing are common for high precision low volume prints [46] [47]. High volume low precision devices typically use Offset Lithography and Flexography [48] [49].

Printed electronics are generally used for large area printing on flexible substrates for simple devices. They can be manufactured at an extremely low cost and are commonly used to

produce smart labels, sensors, and power sources. Consumer technology companies are researching how flexible displays, batteries and transistors can utilise printing technology [50]. This section reviews the processes involved in printing conductive materials, how they are developed into a printable medium and what ink features are desirable for an experimentally manufactured ink. Literature states there are five main printing techniques used by the electronics printing industry [51]. A brief literature overview of printing states:

- Inkjet Printing
    - Digital direct write printing method
    - >100nm layers with 50μm resolution
- Viscosities between 1 – 20mPasScreen Printing
    - Inks are printed through a screen mesh stencil
    - >1μm layer thickness with 100μm resolution, 13μm layers are typical
    - Viscosity can range from 50 – 100000mPas
- Offset Lithographic Printing
    - Printed layers are typically between 0.5 to 5 microns depending on press setup
    - Printing resolutions of 20 – 50 microns are difficult but achievable with most presses set up for >100μm resolution
    - Shear thinning inks are required with viscosities in the range of 40000 – 100000mPas
- Flexographic Printing
    - A flexible surface relief is used for printing
    - Prints of 1μm layer thickness with 20μm resolution
    - Viscosities between 50 – 500mPas
- Gravure Printing
    - A rigid surface relief of the printing image is used to print in gravure presses
    - Film thicknesses between 1 – 8μm is typical with less than 20μm resolution
    - Ink viscosities range between 50 – 200mPas
- Gravure Printing
    - A rigid surface relief of the printing image is used to print in gravure presses
    - Film thicknesses between 1 – 8μm is typical with less than 20μm resolution
    - Ink viscosities range between 50 – 200mPas

There are five traditional printing processes used in printed electronics, each requiring different parameters to successfully manufacture specific types of devices. Each process, their mode of printing and which electronics they are most well suited to printing are discussed.

2.2.1 Inkjet Printing

Inks can be printed through both industrial and cheap commercially available inkjet printers, with the only set up required being filling a cartridge up with ink. Printing with inkjet is a direct write process and it enables quick prototyping of printed electronic circuits in research labs. Most commercial and industrial printers work with thermal or piezoelectric effects. For Piezoelectric based inkjet nozzles, electrodes coat channels in a nozzle, these are placed near a piezoelectric ceramic which then can use electric charge to provide a drop on demand system for ink deposition [51]. The ceramic deflects as the charge is passed through, this pushes the ink through the nozzle with the electrodes at an ambient pressure. The charge can be pulsed digitally giving highly controlled, reproducible results. A diagram of the inkjet printing process is shown in Figure 10 Continuous inkjet printer nozzle mechanism.

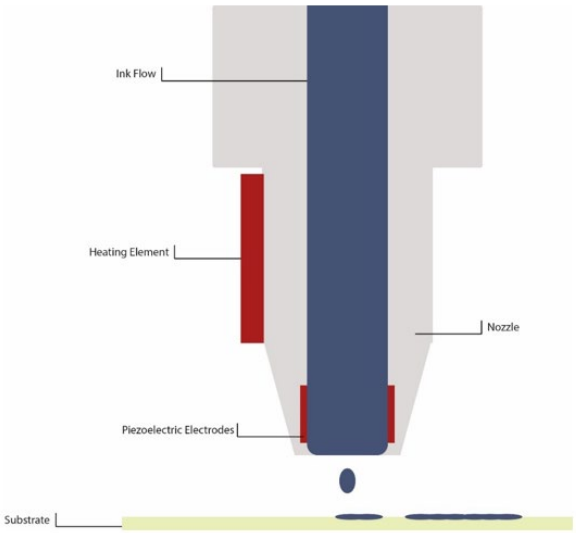

Figure 10 Continuous inkjet printer nozzle mechanism

With regards to thermal drop on demand inkjet printing, droplets of ink are expelled from the nozzle through thermal excitation. This is performed by a rapid heating of the ink which then vaporises it and forms a bubble, this pressure change then ejects a droplet of ink onto the

substrate. Inks for inkjet printers need to balance adhesion of the particles with the rapid evaporation of the solvent. As the particle deposition can be controlled it is a highly adaptable process. For printed electronics, a dense printed film or track is crucial to conductivity and with the inkjet process, multiple layers can be printed to ensure there are no gaps in printed films, increasing the conductivity. It is also a more sustainable process compared to other common electronics printing processes due to it being drop on demand. However, industrial inkjet printers are high cost and they are yet to take over screen printing (2.2.2 Screen Printing) or flexography (Section 2.2.4) in terms of industrial popularity.

Figure 11 A common industrial inkjet printer [52]

In printed electronics, inkjet has the advantage of being digital, each other traditional printing process requires image plates or screens to be designed and developed before manufacturing can commence. To print with inkjet, computer aided designs can be printed instantly, only requiring the relevant software [51]. It offers the most control over any printing process with extremely high resolutions and can build sections of the design layer by layer and allow for the printing of varying film thickness.

Due to the high resolution achieved via inkjet printing, researchers have been successful in printing a variety of electrical components. Both Light Emitting Diodes (LEDs) and Organic Light Emitting Diodes (OLEDs) have been fabricated using inkjet [53]. Thin film transistors (TFTs) have been printed using inkjet, however, compared to non-printed manufacturing methods performance is poor and more suited to simple applications [54]. Inkjet is also capable of printing simple passive components such as resistors [55], photovoltaic cells [56], diodes [57] and sensors [58]. However, even for these relatively simple components start-up costs are high as shown in the list in Section 2.2 and industry uptake has been slow [59].

2.2.2 Screen Printing

Screen printing is commonly used in industry. It can be automated to create highly reproducible prints through a stencil mesh. The layer thickness of the print can be controlled by the thread number of the stencil and ink is printed from a fill blade pressing the ink over the stencil. In electronics screen printing is mainly used for solar cells and sensors [60]. Inks must be thixotropic, meaning their viscosity decreases after agitation. However, almost any form of ink that shows non-newtonian motion (viscosity decreases with shear stress) can be used with a screen printer. Its versatility means it is useful for research as an ink can be tested instantly in a reproducible way.

Most materials which have applications using thin/thick films have had a screen-printing ink made from them (see Section 2 2.5). It is unique in its ability to print heavy, thick films in one go. For comparison, a standard screen printer can print films between 1um and 50um in layer thickness, whereas an inkjet printer utilising low weight loading inks with low viscosities need multiple passes to print thick films [52]. Films are normally oven or belt dried after printing due to its thickness and a low curing time would be around 30 minutes in an oven heated at 90^{o}C or faster if a UV curing process is performed. A schematic of the printing process can be seen in Figure 12 Screen Printing Method.

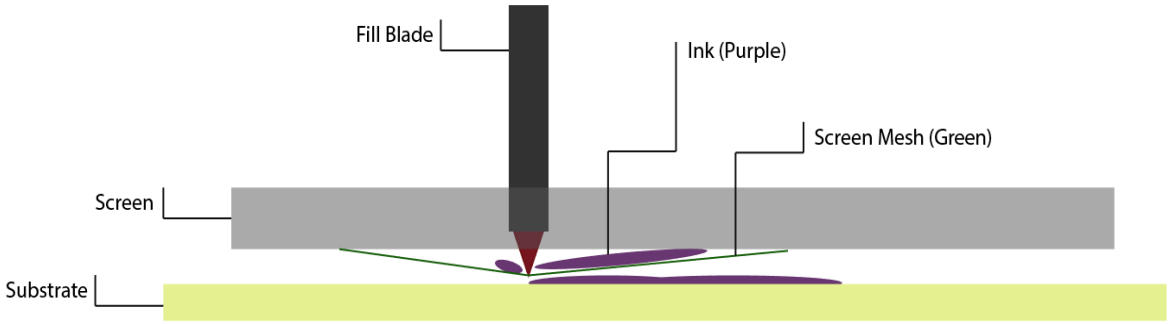

Figure 12 Screen Printing Method

Screen printing as presented in Section 2.2 has the most forgiving rheological demands out of any printing process allowing inks with viscosity ranges of water-like to clay-like [60]. However, how this rheology acts with regards to shear is critical for high resolution printing. The process is easier to set up than inkjet, however only simple electronics can be fabricated through this

method as it does not have as much control over layer thickness and it has a lower resolution [51]. One advantage screen printing has over inkjet printing is it can be integrated into high throughput roll to roll machinery as seen in Figure 13.

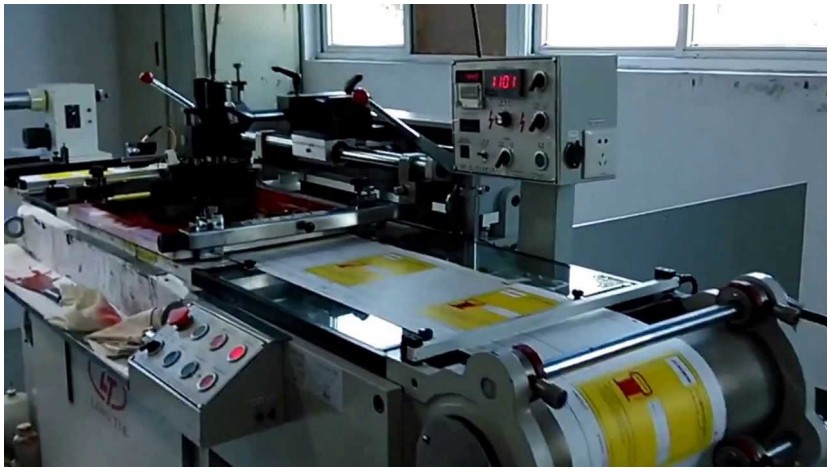

Figure 13 Automated Screen-Printing Equipment [61]

Screen printing is the most popular method of printing electronics and it is the only mainstream printed electronics process to be widely adopted by industry [62]. Although it has disadvantages by being an analogue process with little flexibility, screen printers can print both thick and thin films for simple passive electronic components [62]. Screen printing is a relatively wasteful printing process, however, the ink waste is reduced with the amount of prints as the ink stays on the screen for multiple printing passes. Industry has adopted screen printing due to its ability to print well controlled, simple conductive layers for simple passive electronic components at a low cost. Inks do not require as much control or development as other process and are easier to make and therefore less expensive. As screen printing is not a digital process, costs are also lowered by less complex machinery requiring less maintenance and more uptime on production runs [62].

In printed electronics, the sensor industry typically uses screen printing as the low cost can provide customers is well performing, disposable sensors. Disposable electrochemical sensors are common which at a low cost can be used once and thrown away [63]. Biosensors are a large part of the screen-printing industry and find widespread uses in the medical profession for detecting chemicals in biological samples [64]. Printed photovoltaics are possible with screen printing [65] as well as capacitors, resistors, RFID and inductive coils [66]. More

complex applications such as TFTs or LEDs are currently difficult but have been achieved using high resolution, semi-digital screen printers [67].

2.2.3 Offset Lithography

Offset Lithography is the trade name for the traditional printing press, used since 1796 for mass production of printed materials. The basis of the method is that oil and water do not mix. Using oil or grease-based inks, when the ink hits the printing rolls, water repels the oil in the oil-based ink and the ink that is left is then printed onto a substrate [69]. Offset lithography is a newer version of the traditional Gutenberg printing press discussed in Section 2.1 and uses a metal relief plate and a series of rubber plates for fast roll to roll production. The offset lithographic printing process works via the hydrophobic interactions between oil and water to create high resolution images, a schematic of the roll to roll process can be seen in Figure 14 Offset Lithography Printing Process.

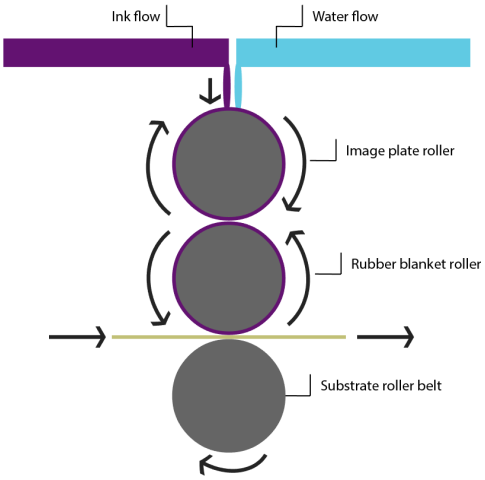

Figure 14 Offset Lithography Printing Process

Offset lithography is less wasteful than screen printing and can provide more layer thickness flexibility and control than other methods. Typical layer thickness is generally between 3 and 5 microns and it can print similar applications to screen printing. Voltaic power sources have been developed using offset processes [68] along with strain sensors [69] and electroluminescent displays [70]. Offset lithography has better resolution than screen printing, however, it is difficult to manufacture complex components due to the printing mechanism

and flexography, gravure and inkjet are all much more capable for sub 50-micron resolution [51].

2.2.4 Flexography

Flexographic printing is the main choice of printing for consumer packaging. It can print on to almost any substrate. The method is similar to traditional printing press methods such as offset lithography discussed in Section 2.2.3 as it utilises rollers to transfer the ink onto the substrate. It can only print one colour at a time and therefore multiple rolling stations are often used for multilayer or multicolour prints. The mechanism for the flexographic printing press can be seen in Figure 15.

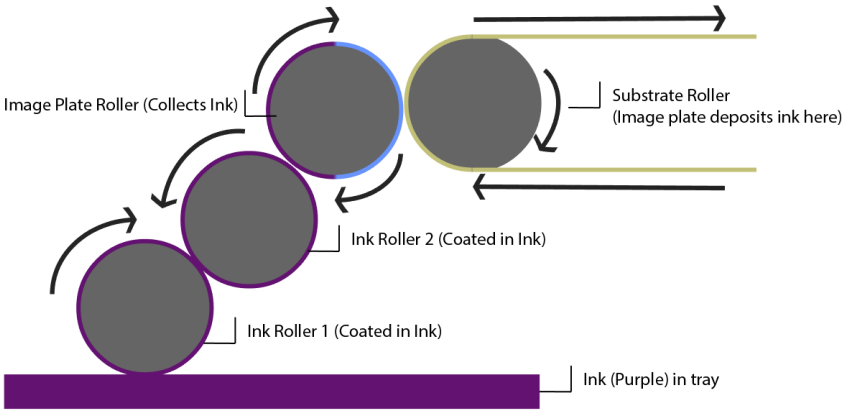

Figure 15 Flexography Printing Mechanism

It works by rolling ink through two rolls onto a plate, once the substrate passes over the relief plate. The image is printed on to the substrate. Inks for flexographic printing generally have low viscosity and are fast drying. Flexography requires vastly different inks compared to screen printing and offset lithography. Inks are generally water based and developed for thin plastic substrates as flexography is generally used for label art and printing on tapes. Flexography has recently managed to be able to print resolutions down to 1mm [71], opening it up for the potential printing of complex applications. Published literature has shown that flexography can be used to print supercapacitors [49] and wide area electrodes and interconnect [72]. However, flexography is mainly used for packaging and labelling, an area which is yet to introduce printed electronics widely. Little published research has been conducted for this printing process in terms of electronics as special ink requirements (water based) hold it back

and other, more popular processes are able to compete in terms of device manufacturing and performance.

2.2.5 Gravure

Gravure, also known as rotogravure, has similarities to both offset lithography and flexography printing processes in that is uses an image plate in conjuction with a rotary mechanism to pick up the ink and imprint it onto the substrate in a roll to roll fashion [73]. The image plate roller is suspended in the ink flow, the roller then rotates into the ink to coat the image plate. A blade then removes the excess ink from the image plate, and this is then coated directly onto the substrate. A second roller is used to push through the substrate and to keep it in contact with the image plate [73]. The printing process mechanism can be seen in Figure 16.

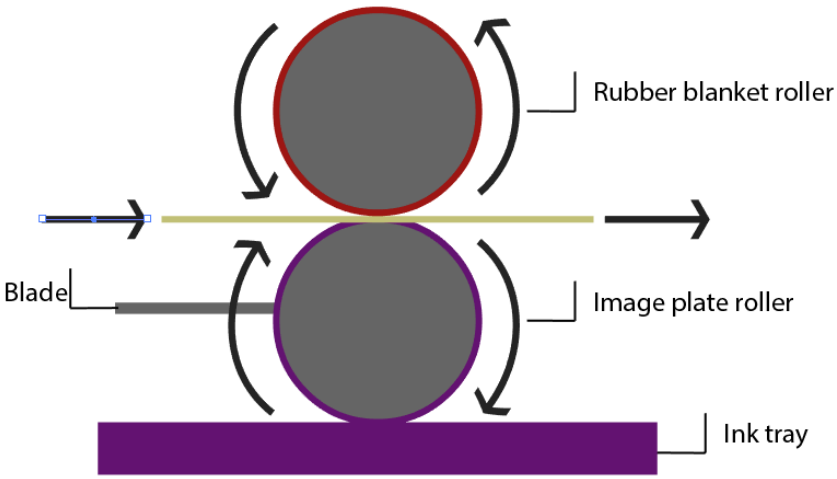

Figure 16 Gravure Printing Mechanism

Gravure has similar ink requirements to flexography, requiring a relatively low viscosity water-based ink to print. Before recent developments gravure had much higher resolution than flexography and has therefore had more published research into printed electronics using the process [71] [74]. Due to the higher resolution, applications can be more complex and include high performance transistors [45] [75], printed interconnects [76] and large area electrodes [77]. Gravure is also an analogue process with the requirement to design and manufacture an image plate before printing making it difficult for lab-based research. Layer thickness can be

controlled via the blade providing more layer resolution control than traditional flexography and offset lithography [73].

2.2.6 Additive Manufacturing

The term additive manufacturing (AM) refers to manufacturing processes which construct three dimensional (3D) objects through layer by layer material deposition. The popular name for additive manufacturing is 3D printing with material extrusion (ME) being the commonly known method with the public [78]. Traditional printing processes share similarities with AM processes as both are tool-less manufacturing methods for device production, AM being 3D part production and printing being 2D device production [79]. There are seven types of core AM technologies [78]:

- Material Extrusion
- Vat Photopolymerization
- Material Jetting
- Binder Jetting
- Powder Bed Fusion
- Directed Energy Deposition
- Sheet Lamination

In terms of printed electronics, material extrusion is the only pure method (others combine ink deposition with ME) type to have published literature investigating conductive materials and tracking [80] [81]. This experimentation of extruded materials started being published in 2012 to include conductive materials for developing functional electronic objects [82]. Rather than focusing on extruded molten material, start-up companies such as Voxel8 or Nano-Dimension focused on printing conductive inks in conjunction with ME techniques. These tend to use the extrusion of silver-based nanoparticle inks on to printed plastic or dielectric substrates for the printing of PCBs or embedded systems. A schematic from the literature of 3D printing material extrusion for pastes can be seen in Figure 17 [83].

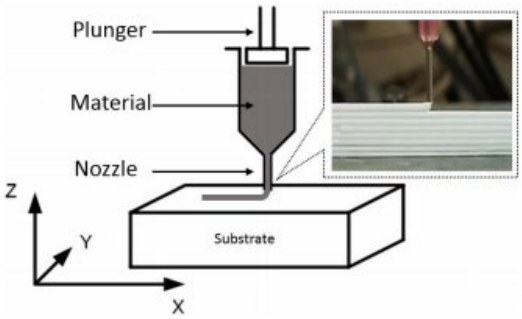

Figure 17 Material extrusion example [83]

However, such systems have significant start-up hardware costs and use silver-based inks, which are expensive and toxic to the environment, an example of which can be seen in Figure 18. Material extrusion uses plastics instead, most notably polylactic acid (PLA) and acrylonitrile butadiene styrene (ABS). The first conductive plastics for 3D printing emerged in 2012 with a focus being on conductive carbon filler being dispersed into PLA [81].

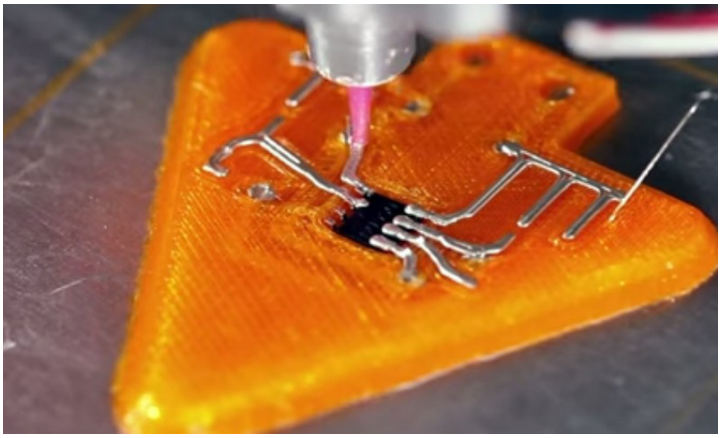

Figure 18 Voxel8, ink deposition combined with material extrusion [84]

The simplest plastics adapt common ink formulation techniques to polymers. Carbon Black is generally used as a filler and this is melted with a polymer until the percolation threshold – the point at which the electrical properties of the conducting material propagate throughout the structure, has been reached [85]. This is then melted and drawn into a filament, generally 1.75mm or 2.85mm in thickness to then be used for material extrusion [86].

More complex manufacturing techniques have been developed to enable plastics with higher conductivity. Surfactant based polymerisation has been used to create conductive graphene dispersed PLA with high conductivities [87]. However, most commercially available graphene

PLA manufacturers appear to just mix dispersed and reduced graphene oxide powder with melted PLA or ABS [88].

3D printed sensing devices have been used in the literature as a proof of concept for newly developed conductive filaments [81]. Non-conductive single material models have also been printed to aid the design for existing sensors into systems [89]. Others have also researched embedding conductive inks into 3D objects for sensing devices. However, there has been no research on commercially available conductive materials [90]. This is important as manufacturers for these materials give very little information regarding the electrical characteristics.

Material extrusion involving conductive ink deposition is currently a growing field with applications from simple sensing devices to metamaterials [91]. However, at this time there are no publications in the field of integrating TCO materials into material extrusion additive manufacturing.

For printed electronics, other techniques are currently unviable in their current technological state with little to no literature involving the printing of electrical components. Vat photopolymerization is an AM technique which uses light to selectively cross-link a photosensitive polymer, it can create 3D structures with high resolution at 10-micron layer heights finding uses in biotechnology and microfluidics [92]. The scanning speed and intensity of the light source have been found to affect the resolution of vat polymerisation [93]. There have been suggestions in the literature that electrically conducting structures could be printed via this method, however, challenges in formulating inks and resins capable of crosslinking into a 3D structure need to be overcome first [94]. A single paper utilising copper nanoparticles for metamaterial printing has been published however, the researchers concerned with thermal conductivity rather than electrical conductivity [95].

Powder bed fusion printing involves placing the powder of a desired material into a chamber and sintering the materials with an electron or laser beam [96]. This method has advantages in printing highly complex three-dimensional structures out of metallic and ceramic particles, however, there is currently no way of structuring electrical circuits into the print. Researchers in this field looking to integrate electronics into this system usually employ a stop and go process. For this, the printing process is stopped, the electronics placed into the printed object

and then the printing process is continued, essentially embedding the electronics within the object creating a “smart object” [97].

Directed energy deposition is similar to powder bed fusion in that an electron beam is used to fuse powder or wire into a three-dimensional structure and therefore is not a suitable candidate for printed electronics. However, the additive manufacturing method has proved useful for fabricating and repairing structures in metallurgy with improved performance reported in many alloys [98].

A selection of the printing method is made in 2.6.2 Selection of the Printing Process considering the literature review performed in this chapter. An overview of the AM techniques discussed can be seen in Table 1.

Table 1 Comparison of AM Techniques [99]

Ink Code	Materials	Suitable for Printed Electronics?
Material Extrusion	Plastics, Extrudable Pastes	Yes
Vat Polymerisation	Resins, Ceramic Precursors	No
Powder Bed Fusion	Metallic, Ceramic Powders	No
Directed Energy Deposition	Metallic Wire / Powder	No
Material Jetting	Inkjet inks (drop on demand), Polymers	Yes
Binder Jetting	Drop on Powders – metals, polymers, ceramics	No
Sheet Lamination	Sheets of metal, paper, plastic	No

2.3 Current Applications of Printed Electronics

2.3.1 An Introduction to Printed Electronic Devices

Printed electronics continue to be used in many growing industries [100]. Including:

- Sensors and simple monitoring devices
- Radio-frequency identification tags (RFID)
- Display technology
- Transistors and Printed Memory
- Printed power sources
- Photovoltaics

Areas which are a challenge to both industry and research institutes are printed displays, transistors and photovoltaics. Each one faces challenges in availability of materials to print versions comparable to devices made by current manufacturing methods. Mass production processes are also yet to come to fruition as this requires substantial investment by industry. Encapsulation of devices such as the sensors shown in Figure 19 has also become an issue. Many conductive and printed materials oxidise in the atmosphere and require encapsulating with a non-conducting layer to protect the devices from the environment.

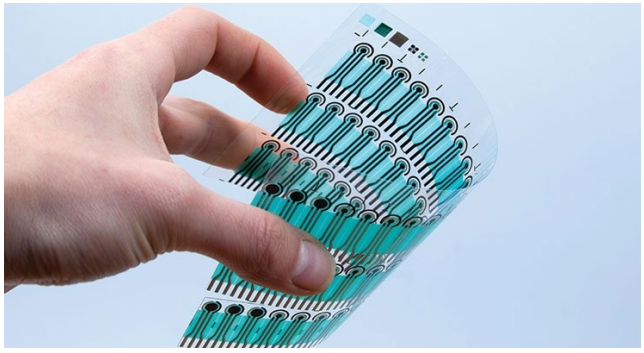

Figure 19 Silver / Carbon Screen Printed Force Sensors with encapsulation in green [101]

Another challenge the printed electronics industry currently has is a lack of standardisation between companies for the industry [100]. There are no agreed upon standards for the development of conductive and dielectric inks, how these should be developed and used in individual processes and there are also no set standards for the quality and performance of

printed devices. This lack of cohesion has meant this industry has struggled gaining ground in mainstream electronic devices.

Currently in Printed Electronics, printed sensors as seen in Figure 20 and RFID are the most advanced areas in terms of research and industrial development.

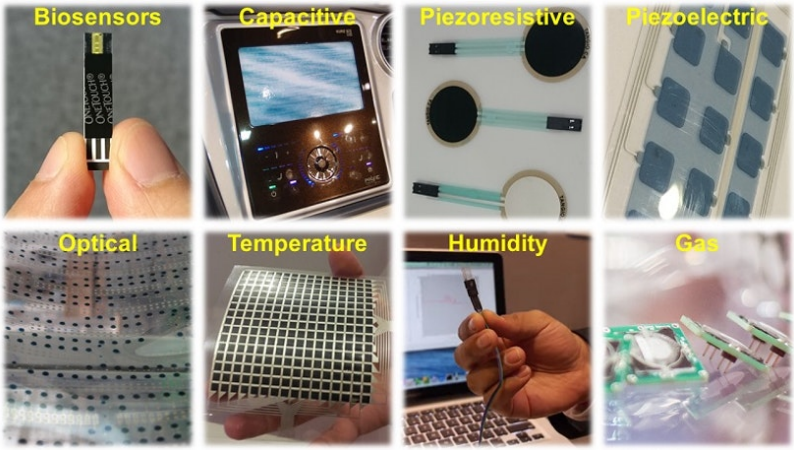

Figure 20 Examples of printed sensors and their industry [102]

Sensors can be printed which cover every area made by conventional manufacturing processes with the advantages of:

- Low cost production
- High volume mass throughput
- Low profile electronics

Printing in the sensor industry is not a new technique and this application usually uses screen printing for the method of manufacturing. Sensors are generally manufactured as a 'thick film' (3μm or above) which improves properties such as electrical conductivity and ink flexibility. The most commonly used printed sensor is the consumer market is blood glucose sensors for monitoring diabetes. Printed gas and temperature sensors have also moved into mass production and printed photodetectors are starting to be used in conjunction with thin film transistors (TFTs) in display technology [102].

In the current, early state of the printed electronics industry the replacement of complementary metal-oxide semiconductor (CMOS) silicon with printing processes seems impossible [103]. However, companies such as ARM in recent years have developed printed,

organic, conductive plastic-based microprocessor technologies which currently has the processing power level of an ARM Cortex M0 32-bit processor [104]. With this development, the ability to print fully functional complex electronic devices is becoming possible.

2.3.2 Printed Resistors

Resistors, capacitors and inductors are the three basic linear circuit components used in most electronic circuits with resistance, capacitance and inductance influencing most electronic measurements.

A resistor is defined as a passive component which opposes the flow of direct (DC) or alternating (AC) current [105]. They are the simplest electrical component to construct as every material (excluding superconductors) exhibit an inherent resistance and they are typically fabricated from a resistive but electrically conductive material being placed between two electrical contacts (terminals). They are found in almost all electronic circuits and are vital for any electronic device to work. There are many types of resistors and many types of fabrication methods including but not limited to:

- ***Thin Film Resistors*** – Manufacturing via Sputter Coating [106]
- ***Thick Film Resistors*** – Manufactured via Screen Printing [107]
- ***Carbon Composition Resistors*** – Made via Resistive Carbon Particles in Casing [108]
- ***Metal Film Resistors*** – Fabricated by winding metal wire around non-conducting core with the wire being cut to reach desired value, most common resistor today [109]

In printed electronics, all resistors are either thin film manufactured via inkjet printing or thick film resistors manufactured by other printing processes such as screen printing [110] [111]. However, these printed resistors suffer from poor resistive reproducibility (tolerances) and a poor ability to cope with power ratings required by most circuits. Resistors manufacturing for traditional components tend to be sputtered or screen printed onto thick ceramic substrates with high thermal conductivities essentially acting as a heatsink, allowing for higher currents to flow through [112]. These types of resistors also have multiple post-processing methods available to them to reach low tolerances of between 0.005 – 5%, such as material ablation via laser or high temperature thermal annealing [113] [114]. Resistors integrated into the printed electronics process are normally printed directly onto substrates with poor thermal conductivities (paper, polymer sheets) and to do not have high temperature annealing methods available to them. These issues with integrated printed resistors have not prevented

researchers and industry from finding a use for them. Due to their lack of suitable heat dissipation, printed resistors dissipate heat through the top of the printed film allowing for printed thermochromic layers to be used for dot matrix printed display technology [115]. Resistive sensing applications which utilise a change in resistance to detect phenomenon have also been widely studied including strain sensors [116], pressure sensors [117], humidity sensors [118] and even printed resistive memory cells which can store a on or off bit due to a resistance change after voltage application [119].

2.3.3 Printed Capacitors

Capacitors are passive electrical components which store electrical energy between two electrodes within an electric field. There are multiple ways of constructing capacitors, the simplest and most conventional method is the parallel plate capacitor. Parallel-plate capacitors are made up of two parallel electrode plates separated by a dielectric barrier and are non-polarised. Electrochemical capacitors are less common and utilize an electrolytic barrier between polarized electrodes using oxidation of the anode as a dielectric barrier. Double layer electrolytic capacitors are also commonly known as 'supercapacitors' and use polarized electrodes with an electrolyte to store electrostatic charge in a Helmholtz double-layer [120].

Capacitors are used as passive components in almost all modern electronic applications. Their uses include signal processing where the energy stored inside a capacitor can be used as memory storage [121]. Other uses include AC/DC signal coupling and decoupling [122] and signal filtering [123] making their use vital to modern computing.

Traditionally parallel plate capacitors are manufactured using two metallic foil conductive electrodes with a thin film dielectric separating them. However, in the last 20 years advances have been made in low cost, high throughput printed electronics and with capacitors being an integral part of most circuitry, research has been conducted into printed capacitors for flexible printed electronics. One of the earliest works in this field used offset lithography and other roll to roll printing methods with silver inks and polymer dielectric films to produce fully printed capacitors [124] [62] [125]. Research then expanded into looking at the properties of high dielectric constant ceramic inks for printed capacitors using both ink-jet and screen printing [126] [127] [128]. Currently, the biggest challenges to printing integrated capacitors

are pinholes [129]. Pinholes are small holes or voids in the dielectric layer which allows ink from one of the conductive plates in a capacitor to touch with the opposing plate, creating a short circuit [130]. It is generally thought that changes in printing parameters and ink rheology can eliminate the creation of these pinholes [130] [131].

Capacitors, much like resistors can also be used as sensor devices with printed electronics research being performed in humidity sensing [132] and capacitive touch sensors [133].

2.3.4 Printed Inductors

. Inductors store electrical energy in magnetic fields and were first invented by Nicholas Callan in 1836 [134]. There are two types of inductance, self-inductance where the flow of current alters the voltage of a circuit due to electromagnetic effects. The second type is mutual inductance where a current change in one of two circuits linked by the magnetic force alters the voltage in another circuit. The fabrication of an inductor typically involves creating a coil of electrically conducting material around a magnetic core.

The first published evidence of printed inductors was in a 1969 patent “Printed Circuit Inductor” by Edward Rich [135]. It details the initial designs most printed inductors are now based on, a spiral of highly conducting material on insulating flexible substrates. The width, length and thickness of the printed spiral causes the effect of self-inductance [136]. Although the first patent for this technology was filed in 1969, little research was performed into printed inductors until 1995 with research being conducted into printed nickel ferrite paste inductors printed on alumina substrates [137]. Following this, research into printed inductors became more widespread with advanced applications being developed in the years after. Screen printed thin film embedded inductors were fabricated soon after [138]. These evolved into more advanced applications of printed inductors as devices for microwave radiation interaction [139] and radio frequency electromagnetic radiation detection, allowing for the first printed RFID devices to be developed [140]. The ability of printed inductors to be used for radio frequency interaction influenced more research into the area with inkjet printed RFID tags utilizing gold based inks being developed [141] and paving the way for printed copper/silver RFID tags [ink-jetted silver/copper conductors for printed RFID applications [142]. These silver and copper RFID tags find their use today embedded in packaging mainly for anti-theft purposes on consumer products [143].

Recently, printed inductor developments include inductors being printed directly onto fabric [144], inkjet printed transformers [145] and even 3-D Printed toroidal coils formed via material extrusion [146].

2.3.5 Printed Logic

More advanced circuit components in printed electronics include diodes and transistors. Diodes are components which allow current to flow in only one direction, a double layer system is created with p and n type semiconductors (see Chapter 2) which only allows current to flow in one direction allowing for applications in signal rectification, logic gates or circuit protection. The transistor is essentially built upon a diode, adding another semiconductor layer (N-P-N or P-N-P) allowing for amplification of circuit currents and more advanced logic, these effects make transistors one of the most important electronic components with all modern computing being based off of the technology [147].

In printed electronics, diodes were difficult to achieve throughout the 20th century with advances only being made in the last decade with little literature being produced. This is due to the fact the ink used not only needs to conduct but also needs a high degree of amorphicity to ensure the semiconductor layers act as one semiconductor creating a well-defined barrier between particles. This requires amorphous layers created by high temperature annealing rather than the polycrystalline films printed electronics produces with polycrystalline silicon layers creating issues in the photovoltaic industry [148]. Due to the main advances in printed diodes have come from the field of organic based electronics. Organic conductors have the advantages of low temperature curing into highly amorphous layers however, they are high cost with generally lower performance [149]. These materials have led to breakthroughs in printed diodes with organic printed diodes being used for frequency modulation and as logic for display technologies [150] [151] [152].

There has only been one instance of a printed semiconductor diode from 2014 where researcher's inkjet printed silicon layers onto silver/carbon electrodes for rectification up to 1.6GHz [153]. These diodes have been shown to have uses in packaging technology, however, their performance is limited with the researchers reporting a maximum current of 19 microamps. With the challenges associated with printing diodes, the challenge of printed transistors is even greater. Most of the literature again focuses on organic based electronics

with transistors being inkjet printed into 2D [154] [155] and 3D structures [156]. Fully silicon-based transistors have been reported for screen printing however these devices only show stability over a 6-hour period [157].

2.3.6 Printed Display Technology

Research into printed display technology remains focused on five main methods of luminescence:

- Electro-chromics
- Thermochromics
- Organic LEDs
- Electroluminescence
- Quantum dots

Electro-chromism is where a material which change colour depending on the current passing through it. Printed electrochromic displays have been manufactured with a wide range of materials including the development of active matrix displays utilising organic conductors, however a disadvantage of active displays in printing is the requirement of printed transistors [158]. Simple electrochromic displays have also been fabricated using organic polymers on roll to roll printing presses with the advantages of large area displays manufactured via high throughput methods [159]. However, the cost of conducting polymers is generally too high for this scale of manufacturing in industry with the cost of PEDOT: PSS - the polymer used retailing at over £5000 per kilogram. The same authors built upon this technology later by demonstrating the displays ability to be powered by printed integrated organic based photovoltaic cells [160]. Other electrochromic materials have also been used in printed displays such as metal oxides [161], printed metalorganic complexes [162] and organic active displays based on carbon nanotube transistors [163].

Thermochromic displays are based on a thermochromic layer which changes colour with temperature being printed on top of a conducting layer which generates heat when current passes through. As discussed in earlier in Chapter 2, printed materials generally have higher resistances than their traditionally manufactured counterparts, as a result this higher resistance dissipates heat when a current is passing through. This effect has lent itself to the

development of thermochromic dot matrix displays, utilising an unwanted by product of printed carbon inks for new technology [115]. All organic thermochromic displays have also been developed via inkjet printing organic precursors leading to fully flexible printed displays [164]. Thermochromic displays have some disadvantages, the main being that it is difficult to manufacture high resolution displays due to heat dissipation. However, they are extremely useful for producing low cost, flexible and fully printed indicators.

Printed organic LEDs have been favoured in research due to their simpler working mechanism compared to normal LEDs. A normal LED requires a high degree of crystallinity in multilayer semiconductors which are also highly transparent, the difficulties of printing this have been discussed in Section 2.3.5 Printed Logic. However, organic light emitters only require a current to pass through for the emission of light, this means a printed LED can be manufactured as a printed one-layer pixel. These can therefore be used to fabricate much thinner displays compared to traditional multilayer LEDs. Organic printed LEDs are relatively common in research due to their ease of fabrication and LEDs have been fabricated using these organic electroluminescent materials in inkjet printing [165]. Recently advances have been made in fully printing semiconductor inorganic LEDs via microcontact printing [166]. Perovskite LEDs have also been stencil-printed, however, perovskite materials are generally made from lead with these LEDs being printed from lead tribromide making them unsuitable for use by consumers [167]. The use of additive manufacturing for quantum dot LEDs has also been recently demonstrated which has the advantage of directly embedding LEDs into 3D structures [168].

Electroluminescent displays have also been popular in printed display research, these displays utilise doped inorganic materials called phosphors which emit light while under the influence of an electric field. Little is known about the actual mechanism of how phosphors work with multiple researchers suggesting theories. The first theory suggested in 1953 electron transitions to hidden states currently unknown were behind the phenomenon [169]. Later theories suggested oxygen vacancies created by doping at the surface of the materials are responsible however there is no current agreement in the field 65 years later [170]. EL displays are typically fabricated by placing a phosphor in the electric field created by a capacitor with one of the capacitors conducting electrodes being transparent to let the light escape. However, fully printed electroluminescent displays typically utilise the printing of an interdigitated

capacitor followed by the phosphor layer being printed on top [171]. This is due to a lack of transparent conducting layers available for printing multilayer versions while this method of interdigitation also allows for lower voltages to be used creating greater efficiency [172].

2.4 Conductive inks

To be able to print electronic devices, a conductive ink must first be formulated. Inks are generally made up of two overarching components, the filler, which is the conductive material and usually a powder or flakes. The second component is the vehicle which is usually made up of multiple chemicals. In inkjet inks, the vehicle is generally a solvent mixed with a surfactant to keep the filler in suspension, curing additives are also added [173]. In offset lithography, the vehicle must be hydrophobic for the printer to work. The vehicle is usually a thixotropic polymeric resin which uses a solvent to control viscosity, the inks are high viscosity in the region of 10000 to 20000 mPas [174]. Flexographic and Gravure inks can be interchanged as both have similar requirements. Both processes primarily use water-based inks and polymeric resins (acrylic resin etc.) with viscous, paint like properties at lower viscosities between 1000 to 5000mPas [175].

The ink must be tailored to the printing process and device. Screens are essentially a stencil made from a thread mesh, changing the width and spacing of the mesh means each screen can be tailored to the rheological properties of the ink [176]. Inkjet inks are usually surfactant suspension-based inks with low viscosities (5 – 10mPas), these water-like properties enable it to be deposited through the inkjet nozzle.

When formulating inks, the process used depends on the ink. For inkjet printing, the filler is normally sonicated into the solvent. This solvent is then mixed with the surfactant to create a colloidal suspension. A Sonicator is used to create an even suspension which can reliably print. For other printing processes (screen printing, offset lithography, flexography, gravure) the filler can be pre-prepared mechanically typically via ball-mill to ensure an even particle size is achieved. The filler is then mixed with the full vehicle and mechanically dispersed either through a three-roll mill or a Sonicator. The ink will become glossy after the ink has become sufficiently dispersed. Due to the amount of shear stress inflicted upon the ink, the ink needs to be left for 24 hours before printing to obtain a stable viscosity. For conductive inks and printed electronics, the conductivity after printing is measured in ohms per square ($\Omega\square^{-1}$), this gives the average conductivity over the area of the print for the ink used as presented within Section 2.3.

2.4.1 Components of Conductive Inks

When formulating functional inks, multiple components are required to get a fully optimised, stable formulation for manufacturing. The pigment or filler is the most vital component and in a printed electronics context, the conductive powder material represents the pigment in traditional inks. The pigment is usually wetted with a binder. This process removes surrounding air from the particles and allows it to be dispersed easily, changing the interface of the particle to solid – liquid. The binder also aids adhesion to the substrate and to particles themselves. After this, mechanical energy is supplied to the system to disperse the agglomerates into a smaller, more even particle size.

A dispersing agent is then added which either uses electrostatic forces, or steric hindrance to prevent the particles from joining together in solution. Solvents which can be polar or non-polar are used as a vehicle for these additives and thickeners can also be used, which alter the viscosity without changing function. Additives for adhesion are also common. However, the binder can also be used to aid substrate adhesion [177].

Ink formulations are normally either patented intellectual property or secretly held by individual researchers and it is rare for research groups to publish data on the exact composition. This section aims to break down which individual components are needed when developing a conductive ink. Formulations can then be designed in experimental work and optimised for a chosen manufacturing process. The review has been conducted with the perspective of how transparent conducting oxides can be introduced for research.

2.4.2 Filler in Conductive Inks

In traditional inks and paints, the pigment is the base particle which provides the colour. For these inks, the conducting materials take the role of the pigments during formulation as the base material that should be worked around. Conductive inks are almost identical in design to inks for graphical uses. The only difference is that filler (which provides conducting properties) is used instead of a pigment [177].

Generally, the weight percentage of filler needed depends on the formulation and the method of printing used. A higher weight percentage can provide more conductivity but can have adverse effects on how it prints [85].

Low filler content inks tend to be less viscous and therefore and more well suited to inkjet printing applications. High content inks tend to be used for screen printing, offset lithography, or flexography. With conductive inks, each individual aspect of the ink must be tailored around the filler and what its intended purpose is. To achieve conductivity, wet and dry properties must be considered. Previous reviews of this area define the wet properties as being an inks viscosity and printability. Dry properties which must be considered are surface structure and adhesion, substrate, and intended surface properties [178].

2.4.3 Vehicles for Conductive Inks

The vehicle is the fluid component of the ink, typically made up of three main components. These components are the binder, the solvent and the third component is typically a mixture of additives which aid in curing, mechanical strength, ink stability and shelf life. In manufacturing via printed ink, the binder is any material which allows the base material to fixate onto the substrate (i.e. PET Film, Mylar, Paper) and are traditionally resin (a highly viscous or solid polymer) based. When formulating inks, the binder must be carefully selected. In the case of printed conducting materials, too much binder and the resistance will increase, too little and the material will fail to conduct or print with shape. Highly viscous binders can also be used to help stabilise an ink and increase shelf life. A large molecule can remove the air surrounding the filler particles by adsorbing onto the surface. A solid-liquid interface is then created which enables the particles to be separated in a controlled manner by interacting with ink stability additives (also known as dispersants). This slows down the process of the vehicle and filler from separating, improving the length of time before ink expiry.

Once printed, the binder facilitates contact between the substrate and the particles. Therefore, it must be chosen with both the dispersant and substrate in mind. Binders can also be used to coat a substrate which will then allow an ink to adhere more effectively. A majority of binders are polymeric materials and also aid in viscosity control. Some common examples include polyacrylic acid, polyethylene glycol and ethyl cellulose. For conductive inks, the binder also performs a crucial task in allowing and enhancing conductivity. In a printed ink, the conductivity comes from physical contact between individual conductive particles. A good binder for conductive inks, will “cross-link”, a phenomenon were individual molecules of the binder chemically join together (polymerisation) and in this process shrink. This shrinking

through crosslinking pulls the individual particles into a dense film creating what is known as “film densification”. In this dense film, conductive particles have enhanced physical contact and therefore conductivity is greatly improved.

Solvents are required to lower the viscosity of the binders and to enhance printability. Care must be taken to ensure compatibility between the solvent and the binder and the and printing method to be used. For example, Offset lithography and screen printing often have heavy mineral oil solvents where a mineral oil is a form of petroleum distillates which contains higher alkanes whereas inkjet inks use less viscous water and alcohol-based solvents. Heavy oil-based solvents are generally combined with alkyd polymer resin binders. For screen printing water and alcohol-based inks can also be used, these normally contain acrylic resin binders and it is possible to form an emulsion (a mixture of oil and water) to aid printing. The emulsion is a dispersion of micelles or droplets throughout an organic system which uses the immiscibility of oil and water to separate and dry.

2.4.4 Current Examples of Conductive Inks

Both carbon and silver conductive inks currently dominate the printed electronics market. They can be applied and tailored to all printing processes and examples from flexography, offset lithography, inkjet printing and screen printing are common [179]. Carbon based inks have been around for centuries and exhibit conductive properties. They are cheap and due to years of widespread use are optimised enough to give high quality, consistent printing. There is a trade-off between performance (electrical conductivity) and price where a printed carbon tile may only cost a few pence but give a 600Ωcm reading. Although they are normally used as a resistive ink, it is possible to combine carbon with silver particulates to achieve higher conductivities. With the rise of carbon nanotubes and graphene powders, conductive inks can be made which have a resistance of 0.1Ωcm [180]. Applications tend to be printed sensing devices, switches and resistors. However, recent progress has been made in the field of printed supercapacitors where carbon provides a porous conducting surface for electron transfer.

Despite their large cost, silver-based inks hold a 99% market share of the metal based conductive ink market [181]. These formulations can give conductivity readings between 10^{-5} and 10^{-3} Ωcm levels. To achieve these levels of low resistance, content of silver is generally between 40 and 60 weight percent in solution [182]. Silver is preferred to other metals such as copper, this is because it oxidises extremely slowly meaning performance loss over time is minimal (2 mins oxidation time for copper, silver is months) [183]. It has been applied to every printing method available and is currently the ink of choice for experimental, additive manufacturing machinery.

For transparent electronics, conductive inks do exist for transparent conducting oxides, mostly built around indium tin oxide. ITO printed with inkjet can give approximately 95% optical transmission while achieving a resistivity of 0.01Ωcm. Screen printed ITO is also common in the manufacturing of nitrous oxide gas sensors [184]. Although they can achieve low amounts of transparency, resistance is normally in the range of kilo-ohm.cm (kΩcm). Inks can be used with flexography, giving high transparency and conductivity. Offset lithography has never been performed in published work with a TCO ink which merits investigation. This is most likely due to a large surface area for the TCO (requires higher weight percentage to cross

percolation threshold) and haze leading to low light transmission. Screen printing also merits more research to see if it is possible to match traditional TCO manufacturing methods in terms of performance as this has never been presented in published research.

2.5 Methods of Curing Printed Inks

2.5.1 Conventional Heat Treatments

Typically, most conductive inks for printed electronics are cured using conventional heat, either via passing a production line through a drying oven for belt curing or by placing the electronics in an oven for a specified time. Generally commercial inks have curing temperature ranges between 100 to 150^{o}C with a 5 to 10-minute curing time. For a lot of conductive inks, large flake like conducting fillers are used which enables a high degree of particle overlap increasing conductivity. This generally means low temperature curing techniques are suitable for most conducting inks and popular vehicles are generally chosen for their ability to crosslink to a high degree.

2.5.2 UV Curing

Many organic polymers are susceptible to crosslinking via excitation through ultraviolet light (UV). In this process, rather than heat causing crosslinking, the UV light causes a reaction in the resin causing a crosslinking polymerisation to occur. As there is little heat involved in this process, inks can be solvent-less and just dispersed in a liquid polymer allowing for no evaporation when curing [185]. The ability for inks to cure via UV has many advantages, high powered lamps can be used on production lines which instantly cure samples without releasing harmful solvents into the atmosphere [186].

Most commonly used resins such as acrylic can also be adapted to cure via UV light by the addition of photo-initiators - additives which generate highly reactive agents under UV light which cause crosslinking to occur in the resin [187]. One simultaneous advantage and disadvantage for UV curing is that is has been found to cause ozone generation when performed in a natural atmosphere with mercury based high intensity lamps [188]. Ozone is a reactive gas which can cause safety issues for staff in factories performing large amounts of UV curing. However, on a lab scale with experimental materials it has shown to perform surface smoothing for experimental fillers which have improved properties of materials [189]. UV LEDs while much lower power, have been shown to reduce ozone generation, removing this often unwanted by product from the curing process [190]. Although UV crosslinking resins are solvent-less and avoid the evaporation of solvents, some of the most popular ones which

exhibit the highest degree of crosslinking are usually harmful and toxic organics. UV inks are generally for dielectric materials which do not require conductivity as the weight loadings of polymer are so high they generally add large resistances to printed films.

2.5.3 Photonic Flash Curing

In research, some materials require higher temperatures to cure than the substrate allows for. Polyethylene terephthalate polymer sheets are a typical substrate for printed electronics, however, the heat stabilised version of this material provides the highest temperature it can handle as 250^{o}C [191]. Materials such as ceramics need 600^{o}C plus to approach their recrystallisation temperature where grain growth and particle fusion occurs [192]. Photonic flash sintering is becoming a more popular technique in research, it works via providing high power (>1000W) pulsed flashes of light to printed films with all the energy being directed towards the film [193]. This fast burst of energy is generally absorbed by the printed material with heat dissipating so quickly the substrate is left undamaged. Equipment for flash lamp sintering is high cost with bench top models costing more than £20000, requiring high start-up costs for integration into roll to roll printing lines.

2.5.4 Laser Processing

Lasers can be used for processing printed electronics, much like photonic flash sintering, a laser can direct a high amount of power into a small area which allows for the curing of ceramics. However, laser sintering has gained popularity in all areas of printed electronics due to its ability to raster over the surface of any ink to form high resolution patterns – referred to as selective laser sintering [194]. As laser processing can direct 100's of millijoules of energy into small areas, many papers report much lower sheet resistivities for laser processed materials such as silver and tin oxide [195] and gold, copper and nickel [196]. Laser processing does have its disadvantages, materials have to absorb the energy at the given wavelength which means not all materials can be processed by all lasers. There are also a lot of parameters involved in laser processing such as power, energy density and processing speed which means a lengthy optimisation process is usually required to get good performance from electronic inks.

2.5.5 Chemical Sintering

A recent discovery for sintering printed inks has been chemical sintering. So far, this method has only been proved to work with silver particles and its method of action can only be used with metallic particles due to the chemistry involved [197]. The process requires stabilising and coating metallic nanoparticle ions in an ion of opposite charge. Once the film has been printed, a dilute solution of polymer electrolyte is then used to wash the printed film which harvests the particle coating resulting in a cold welding of the metallic nanoparticles [198]. This process is potentially a disruptive technology for the printed electronics industry as it eliminates the need for any high temperature metallic sintering processes while enabling high conductivities and print resolutions [199]. The main issue with this process however is that it cannot be used for materials which require high temperature sintering techniques such as ceramics. Silver can be processed below 150^{o}C with high conductivities, whereas ceramics requiring high temperature processing are very stable, non-reacting, non-dissolving materials which cannot perform the same chemical processes as metallic silver.

A selection of the sintering methods for research is made in Section 2.6.3 considering the literature review performed in this chapter.

2.6 Conclusions

2.6.1 Summary

A review of the current literature has been performed into the history of printing, traditional and modern printing processes, electronics manufactured from these processes and methods of material preparation and curing for printed electronics. This section discusses the literature in terms of the research objectives to determine which printing processes should be researched. An ink formulation method is selected to match the printing process and some electronic applications are chosen to properly test the formulated inks.

2.6.2 Selection of the Printing Process

To select a printing process, key requirements must be met. A requirement is that for research, the system must allow a wide variety of inks and due to this, work with a wide variety of viscosities. As the inks formulated will need to be printed from an early, unoptimized stage, the printing system also needs to reliable and to not be damaged by highly experiment formulations. Another requirement is that the process must be able to print a wide variety of layers from thin to thick films.

For research into conducting inks, screen printing appears to be the most suitable. It has the least strict rheological requirements with inks between 50 – 100000mPas being useable with screens. Until an ink is formulated there is no way to know what the rheology is, meaning a printing method which allows for trial and error across a large viscosity range is ideal. Screen printers are also highly reliable and robust machines. The mechanics behind screen printing is simple, with a squeegee moving over a screen. With experimental materials, processes such as inkjet will have a high risk of nozzle blockage, a costly and time-consuming issue. Screen printing avoids these issues. Also, the ability to change layer thickness versus thread count allows for studies into transparency and conductivity of materials against layer thickness. Resolution is also sufficient, since metallic particles are not being used, any details below 100-micron resolution in the x and y planes will be too resistive.

There is also scope for research into material extrusion processes such as micro-dispensing. TCO materials have never been used as conductive coatings in additive manufacturing methods before and research into this area represents a novel manufacturing method. With

regards to post processing methods, material extrusion systems are direct write processes which allows for modifications to include a post processing system. Screen-printing inks will require little alteration to be dispensed from a material extrusion system due to the thixotropic nature.

2.6.3 Ink Formulation Method Selection

For this research the inks formulation method is dispersion via three roll mill into polymeric crosslinking resins. Again, this is a new formulation design for TCOs which has never been reported in the literature. The three-roll mill provides high amounts of shear making it the most appropriate equipment for particle dispersal, the high shear enables steric hindrance of the vehicle to keep the particles dispersed rather than surfactants. Conventional curing and laser curing are the selected sintering methods, this enables a comparison between the effect of crosslinking and high energy sintering on the conductivity and transparency of the prints.

2.6.4 Printed Electronic Applications for Investigation

The selected application for this research is a printed capacitor. Building capacitors from printed materials enables many applications from force sensors and capacitive meshes to humidity sensors. TCO materials as discussed in Section 1.1 are typically used in consumer devices as capacitive touch sensors. Printing capacitors from these materials allows for a direct comparison to non-printed manufacturing methods.

Chapter 3

Transparent Conducting Oxides

3.1 The History of Transparent Conducting Oxides

Transparent conducting oxides (TCOs) are thin layers of metal oxide materials which are transparent in the visible wavelength spectrum. The most commonly used of these materials are indium tin oxide (ITO) and fluorine tin oxide (FTO). Their current, main applications are in optoelectronics where an electrode is needed without the impedance of light (e.g. touchscreens, monitors, solar cells). Transparent conducting oxides were first discovered by Karl Bädeker in 1907 [200]. He developed the first thin film transparent conducting materials by sputtering compounds onto glass and leaving them to oxidise in air [201]. This sparked the advent of thin film semiconductor physics with cuprous iodide (CuI) and cadmium oxide (CdO) being successful materials that warranted further research. Bädeker and his Ph.D. student Steinberg [202] struggled to explain the low specific resistivities of CdO ($1.28 \times 10^{-3}\Omega$cm) and CuI ($4.56 \times 10^{-2}\Omega$cm) [201] from their Hall Effect measurements [202]. In 1912 a paper was released detailing a methodical change in the amount of Iodine in CuI to see the impact on the Hall Effect [203]. This is the first reference in literature to doping semiconductors which is now seen as a staple method in semiconductor material discovery.

Useful applications for these materials arrived in the early 1970s [204] with the field focusing on four materials, zinc oxide (ZnO), tin oxide (SnO_2), indium oxide (In_2O_3) and indium tin oxide (ITO). For 20 years there were no new TCOs discovered [204]. During this period, Tadatsugi Minami was established as the most prominent researcher in the field by using TCOs to develop diodes and performing research into electroluminescence [205]. During this period, the majority of TCO research is focused around solar cells. Over this period, research groups mainly looked at optimisation for higher energy harvesting efficiency with ITO. Little research was conducted into other sustainable alternatives.

At the turn of the century research into new TCO materials [206] started as the modern computing age required higher performance transparent electrodes. In the late 1990s, research groups thought about what is needed from the materials with two key points being made [204].

- Discover new and improved materials
- Find better manufacturing methods of making conventional TCO materials

Since then progress has been made on the latter point. Large amounts of focus have been on TCO nanoparticles, enabling researchers to developed coatings with enhanced conductivities and tailored structures to improve transparency and conductivity [207]. New transparent conducting oxides have also been developed, none have beaten indium tin oxide in terms of optical or electrical properties but doped zinc oxides, including indium zinc oxide are becoming comparable.

3.2 General Properties of Transparent Conducting Oxides

Transparent conducting oxides (TCOs) are highly transparent, electrically conductive materials. The conductive properties of TCOs can range from conducting to semiconducting and can consist of both n-type and p-type conductors [208]. For the TCO material to become transparent, structure requirements need to be achieved and for it to be conducting, particle to particle interactions need to be considered. This section will provide an insight into the overarching properties of TCOs materials in order to gain an understanding of how they can be printed and achieve the same performance as traditionally manufactured TCOs discussed further in

3.2.1 Material Structure and Electrical Properties

The electrical properties of TCOs stem from a chemical makeup of A_yB_z:D, where A is a metal or metal alloy, B is oxygen and D is an optional dopant. The dopant can be made up of metals, non-metals, or combinations such as metalloids or metal alloys. For polycrystalline thin films such as TCOs one of the defining features of conductivity is charge carrier mobility [209]. The mobility of the charge carrier gives a measure of the resistance in the system. TCOs follow the bixbyite mineral structure (Figure 21) which provides structure defects which allow electrons to pass through. In Figure 21, the crystal structure for ITO is shown with tin (Sn) in orange, indium (In) in yellow and oxygen (O) in blue.

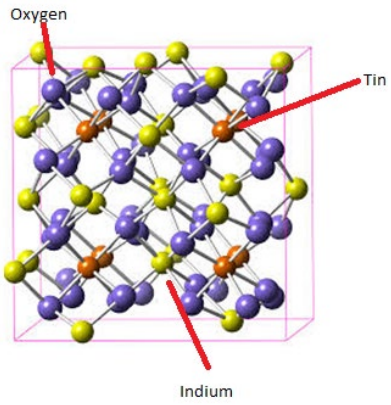

Figure 21 ITO Crystal Structure [210]

For the electrical properties of transparent conducting oxides to be explained, knowledge about the structure of the material is needed. The crystal structure of any material determines how the material can be altered, also known as doped and how the system can be optimised for maximum conductivity and optical transparency [211]. In the next section, key definitions relating to solid state materials chemistry will be given with detail about their effect on TCOs.

3.2.2 Dopants and their Effect on Electrical Properties

In semiconductors, doping is when an impurity is introduced into the crystal structure in order to change the physical properties of the system. The secondary material introduced can either create an electron source or electron deficiency, leading to n-type and p-type semiconductors respectively. Common n-type dopants are pentavalent, meaning five electrons occupy their

outer shell. This allows for four single electrons to be shared with neighbouring bulk atoms with one in excess to move freely through the system. In p-type dopants, trivalent atoms are used which contain three electrons in their outer shell. With this system, three electrons can be shared with three other atoms leaving a final fourth atom without a pair. This creates an electron hole where electrically introduced electrons can pass, creating enhanced conductivity which is displayed in Figure 22.

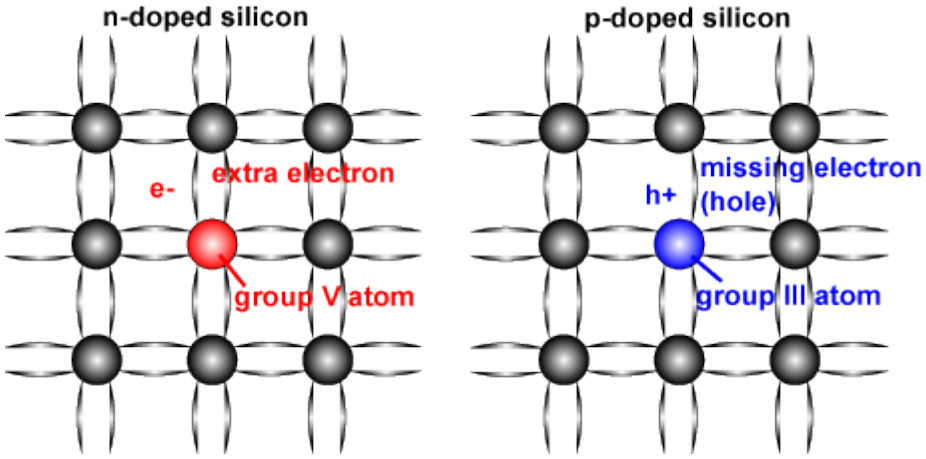

Figure 22 Crystal structure change after doping with different elements [212]

A semiconductor which has not been doped is known as an intrinsic semiconductor. Extrinsic semiconductors are ones that are not pure metal semiconductors but an amalgamation of multiple elements. An n-type semiconductor is one which has an excess of electrons giving pathways (or 'electron holes' – absence of electron) for the electrons to pass through. This creates a system where the electrons are the major charge carrier of the material [213]. In a p-type semiconductor, the structure of atoms creates an excess of electron holes (absences in electrons) to allow an increase in conductivity. The holes let free electrons move without hindrance. Common dopants used to create p-type semiconductors are gallium and aluminium. An important characteristic of conducting materials is the carrier concentration and the mobility of these carriers. Both intrinsic and extrinsic semiconductors have this property and one reason for doping the material is to alter carrier density and mobility.

The carrier concentration can be described as the concentration or density of electron holes or electrons in a conductor which participate in conduction. The carrier mobility is a measure of the velocity at which holes or electrons move throughout the system. Both can be measured using the hall effect shown in Equation 1, which is the voltage difference created when the

semiconductor is exposed to a magnetic field [214]. The result of this provides the Hall coefficient (R_H) which contains the information:

$$R_H = \frac{p\mu_h^2 - n\mu_e^2}{e(p\mu_h - n\mu_e)^2}$$

Equation 1 The Hall Effect [215]

Where the carrier electron hole concentration (p) and the carrier hole mobility (μ_h) are related to the to the charge (e), the carrier electron concentration (n) and the carrier electron mobility (μ_e) [216]. This hall effect measures each aspect of conductivity in the TCO and enables the person synthesising the base material to choose dopants to tailor conductivities to their specific needs.

3.2.3 Band Structures and Electrical Conductivity

The band structure of a material is a way of describing the allowed and forbidden energies for electrons within a lattice of atoms, ions, or molecules [214]. From this, each material can be assigned a band gap (a measurable characteristic) which is a range of energies between an electron's valence band the conduction band. For example, a semiconductor with a bandgap of 1.5eV (electron volts) would require that much energy to enhance conductivity. This creates a common characteristic of semiconductor materials, which is to conduct more with increasing temperatures or increases in atomic vibrations [217]. There are two types of systems which characterise bandgaps, indirect and direct variations which are determined by 'crystal momentum'. A schematic showing band structures can be seen in Figure 23.

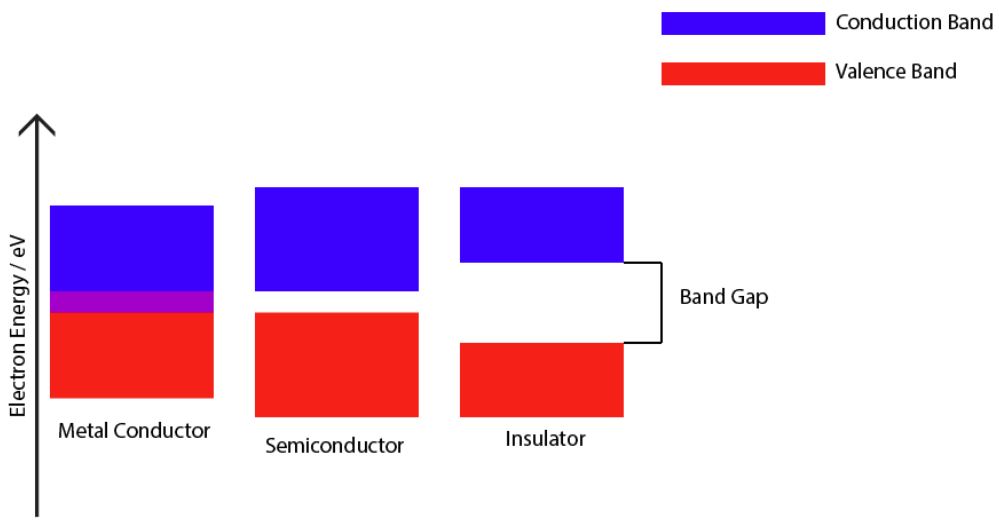

Figure 23 Band gap for conductors, semiconductors, and insulators

Crystal momentum is a vector quantity which describes the way in which an electron moves through the crystal lattice. If the momentum between the electrons and the areas in which there are an absence of electrons is the same, this is a direct bandgap and a photon can be released creating electroluminescence. If the momentum between the electrons and electron holes are opposite, a photon cannot escape the crystal lattice and is instead absorbed [218].

Direct bandgap systems emit light and therefore direct bandgap TCOs can be used as light emitting diodes and in electroluminescent applications. Indirect bandgap TCOs aid in the absorption of light and have gained popularity in solar energy harvesting. Therefore, when developing a transparent conducting oxide for applications, the band structure is an important factor in determining which application can be created.

3.2.4 Work Functions

One important application of transparent conducting oxides is electrodes. The purpose of an electrode is to establish a connection for the collection or emission of electrons as a specific location. The work function of the semiconductor describes the amount of energy required for the electrode to emit electrons from the electrode surface into free space [219]. This is an important factor to consider when developing TCOs as electrodes. The work function is constant for each material and will only change when the material is changed (i.e. through

doping). The frequency of electron vibration increases with energy until a threshold frequency is reached where the electron will emit – shown in Figure 24.

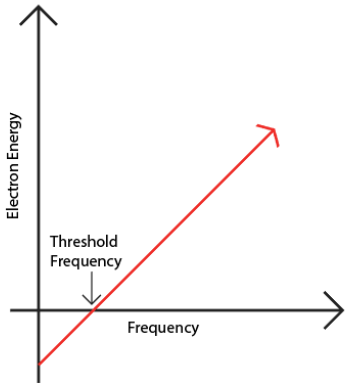

Figure 24 Work Function

Two methods are used when determining the work function for a material. One of these methods is to excite the material with photons and look for electron emission. The second method is to use a Kelvin probe, which measures contact potential through a piezoelectric tip [220]. The difference in contact potential provides a surface map of the work function.

3.2.5 Optical Properties of Transparent Conducting Oxides

One of the main properties of transparent conducting oxides is their ability to allow light to pass through without being scattered. The optical properties of TCOs are dictated by multiple film characteristics, including porosity, crystallinity, and density.

The measured value of optical transmission for materials is the optical transmittance and is shown in Equation 2. The percentage of optical transmittance is defined as:

$$\%T = 100(\frac{P}{P_0})$$

Equation 2 Percentage of Optical Transmission [221]

Where %T is the percentage of light to pass through the material with 100% being all light passed through and 0% being no light has passed through. This equals the ratio of incident power of light over the resulting power of light. For reference, clear uncoated glass averages

90% optical transmittance. This provides a reference value that can be used to compare to different materials to each other. Embedded in the value is reflection, absorption, and haze.

Haze can be used as a description of the percentage of light scattering through the material. If the material has a percentage of haze above zero, it provides evidence of material defects or porosity. For high optical transmission, haze should be kept to a minimum. However, it cannot be completely avoided, and some manufacturing methods provide more than others (e.g. screen printing creates more than sputter coating) [222]. When creating a film, a value of below 10 - 15% should be aimed for. Screen printed ITO creates up to 12% at 4.5µm [222].

3.3 Common Transparent Conducting Oxides

3.3.1 Indium Tin Oxide

The properties of indium tin oxide (ITO) vary depending on the manufacturing method. However, ITO is generally accepted as having a resistance between $5x10^{-3}\Omega cm$ and $5x10^{-4}\Omega cm$ (depending on film thickness) and a sheet resistance of approximately 15 $\Omega\square^{-1}$ [223]. It has an extremely high optical transparency which has been reported as high as 96% transmittance and still has relatively high levels of conductivity [224]. Published research has shown, the band gap also varies between 3.0eV up to 4.3eV with tin acting as a dopant to achieve a versatile n-type semiconductor [225]. Indium tin oxide is a doped tin material. Typically, the tin dopant content varies from between 6% to 10% atomic weight which is due to different preparation techniques [226]. Tin is relatively rare at an approximate 2 parts per million in the earth's crust and the last comprehensive major report on tin resources in 1969 predicted reserves would be depleted in 2056 [227]. Indium is more earth abundant in the core, however it is a factor of ten lower in abundance in the earth's crust. It can also only be mined from the ores of other metals meaning extraction is difficult and production is wasteful [228].

Currently, indium tin oxide accounts for approximately 97% of the transparent conducting films industry and $2 billion worth of market share [229]. ITO is the only transparent conducting oxide that provides the electrical and optical properties needed by the consumer electronics industry but also can be utilised in a wide variety of well tested manufacturing methods. Due to this, indium production has expanded year on year since the start of the millennium. Between 2002 and 2006 consumption increased by 147% and the price rose from $97 per kg to $855 per kg reaching a peak in 2014 at approximately $900 per kg [228]. Recently in 2018, indium prices have settled back to earlier levels at $230 per kg due to an increase in discoveries of crude indium reserves.

Most ITO is sputter coated for the consumer electronics industry into wide area electrodes. In terms of printed electronics, ITO can also be coated via screen printing and inkjet printing. In screen printing the process has a large effect on the characteristics of the material [230]. Screen printing ITO is a common method for creating gas sensors [231]. It has also been demonstrated as a way of creating layered light emitting diodes [222]. Published literature shows that for a 1µm thick film of screen-printed ITO at room temperature, impedance (in AC)

was approximately 200Ω with a resistance (in DC) of $8.5x10^3\Omega$ [230]. Optical transparency measurements were not taken in the gas sensing papers and very little data on the curing process or inks were given [136]. When used in LEDs, the haze value was 1 – 4% at film thicknesses of 0.16µm to 1.7µm due to porosity [232]. This provided an optical transmittance of "*97% and 96% respectively"* and when annealed at 480°c the 1.7µm film gave a resistivity of 30mΩcm [222].

Inkjet printing of ITO gives the closest performance in relation to sputter coating with sheet resistances reported as low as 500 $\Omega\square^{-1}$ [233]. However, due to these conductivities research groups have started printing ITO electrodes on silver nanowire meshes to achieve conductivities as low as 3.4 $\Omega\square^{-1}$ [233]. This however substantially increases the cost of manufacturing ITO electrodes via inkjet printing and has not been taken up by industry.

Indium tin oxide does have some issues associated with it. It has been reported as a carcinogen in rats after inhalation, causing lung tumours [234]. It has also been suggested in solar cells, ITO diffuses into surrounding components which decreases efficiency over time [235]. Both of these make it difficult to recycle the materials from consumer technology contributing to increasing indium and tin prices, adding to unsustainability. There is currently no literature involving material extrusion with ITO.

3.3.2 Zinc Oxide and Doped Zinc Oxides

Zinc based transparent conducting oxides consist of a small few viable replacements for indium tin oxide. Pure zinc oxide has an average reported conductivity of $10^{-3}\Omega$cm which is comparable to ITO [238]. Doped versions and pure zinc oxide are worse than ITO in terms of transmission, usually averaging between 80% and 92% optical transmittance [239]. Zinc oxides are the only subset of transparent conducting oxides which exhibit piezoelectric behaviour. This means when mechanical stress is applied to the coating, an electric charge is generated. Pure zinc oxide has a wide band gap of 3.4ev which is controllable with doping [236]. It also has a high chemical binding energy allowing devices to be stable at higher temperatures [237].

Aluminium doped zinc oxide (AZO) performs much better in direct comparison to ITO. Resistivity has been recorded as low as $3.8x10^{-4}\Omega$cm at 300nm film thickness with 91% optical transmission [240].

In terms of sustainability, zinc usage has remained stable for the last five years with 37% of yearly zinc production coming from recycled sources. Dividing the total earth supply by yearly mining production gives a supply lifetime of 141 years assuming production remains stable. Price has also remained stable and is currently at $2.26 per kg [241]. Zinc oxide is non-toxic. However, zinc nanoparticles show mild toxicity in rats [242].

In printed electronics, a common form of post processing for screen printed inks is UV curing. This cures the ink via polymerisation using high intensity ultraviolet rays. The method rectifies some problems with printing for flexible applications. It provides substantially lower temperatures (100 – 200^{o}c) compared to some conventional annealing techniques (500 – 800^{o}c) can be used and a high production speed. However, zinc oxides are very effective at blocking UV rays and thus have become a staple in sunscreen formulations. Any formulations using zinc oxide-based filler must be optimised to give a quick curing time in air at room temperature. There is currently no reported literature for integrating doped zinc oxides into a material extrusion process.

Other doped zinc oxide materials which have gained interest in recent years is gallium doped zinc oxide (GZO) and the co-doped aluminium gallium doped zinc oxide (AGZO). As gallium is an immediate neighbour to aluminium in the periodic table, the size of the gallium ion allows it to incorporate into zinc oxide and co dope with aluminium to alter the bandgap. With regards to GZO, it has been reported in the literature to be able to achieve a slightly lower resistivity than AZO at 2.8x10^{-4}Ωcm, however, this is with an increased film thickness of 1100nm and a sheet resistance of 2.5 Ω□$^{-1}$ with transmittance values approaching 90% [245]. Gallium is more expensive than aluminium, however, the dopant concentrations are typically below 2%, bringing a kilogram of GZO into the $5 – 10 range which is still provides a great cost advantage over ITO.

Aluminium gallium co-doped zinc oxide shows similar properties to both AZO and GZO, with a reported resistivity of 4.8x10^{-4}Ωcm approaching a transmittance value of 90% [246]. Due to the presence of both aluminium and gallium and the interactions the two elements have with each other, the dopants are reported to have better surface diffusion meaning that in powdered form, the dopants should be more uniform throughout a particle. Both GZO and

AGZO have never been printed and according to their doping behaviour, powder variations of these materials should provide consistent electrical properties.

3.3.3 Other Transparent Conducting Oxides

Other TCO materials are used in applications such as solar cells or glass coatings. However, none truly satisfy the requirements for sustainability or performance. Fluorine tin oxide is commonly used as a substrate for the preparation of other thin films, FTO powder is approximately 15x more expensive than ITO due to the reactivity of fluorine, therefore it is normally sold as premade coated sheets. It has an average recorded resistance of $7.5x10^{-4}$ Ωcm which is good in terms of performance. As discussed earlier, tin and indium based TCOs are unsustainable and alternatives using more earth abundant materials must have greater research conducted into them [240]. Nb doped TiO_2 has also shown promise with reported resistivity's of $2x10^{-4}$Ωcm and an internal transmittance of 95% which is misleading. The TiO_2 after heat treatment exhibits a high reflectance making the actual optical transmission between 60-80%. Titanium is also double the price of zinc while offering less performance [243]. Other TCOs include Copper Oxides, however these are in early materials discovery stages and stable powders are yet to be developed due to the oxidation states of copper.

3.3.4 Conclusions

Indium tin oxide can give transparent and conductive films at a wide range of layer thicknesses. The material used for this research needs to meet these criteria while also meeting sustainability requirements. Reviewing the literature, aluminium zinc oxide appears to be a very good match for replacement. Comparable films give similar results to ITO while being a fraction of the cost, lest harmful for the environment, more stable in devices and have extra functionality. A comparison of widely available TCOs is shown in Table 1 with the best of each category in bold.

Table 2 Available TCOs vs Performance and Cost

TCO	Average Resistivity / Ωcm	Average Cost ($/kg)
Indium Tin Oxide	$5.0x10^{-4}$	855
Fluorine Tin Oxide	$7.5x10^{-4}$	13,130
Al:Ga Zinc Oxide	$4.8x10^{-4}$	≈ 3-4
Titanium Oxide	$9.5×10^{-4}$	13.60
Aluminium Zinc Oxide	$3.8x10^{-4}$	2.24
Gallium Zinc Oxide	$2.8x10^{-4}$	≈ 5 - 10

Recent published research has shown that Al doped zinc oxide has the potential to be a better performing and less expensive TCO than ITO. Literature shows that ITO is much more advanced in terms of printing as more research has been conducted. As this work is to replace ITO, zinc oxides are the most suitable replacements to develop printing methods. A plot detailing the resistivities versus cost versus transparency can be seen in **Figure 25**.

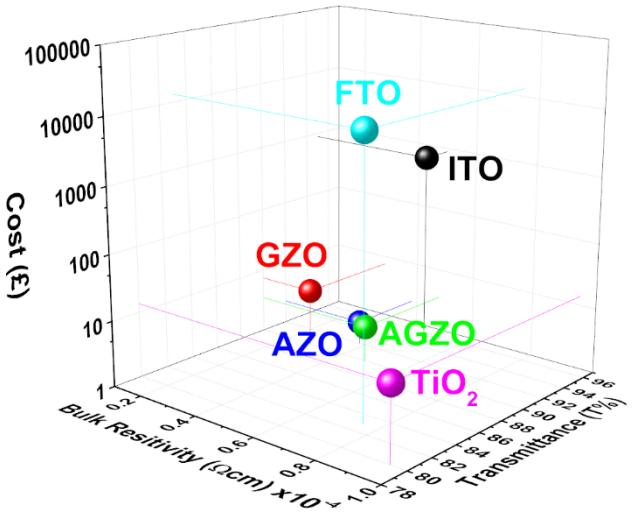

Figure 25 Comparison Between Doped Zinc Oxides and Common TCOs

3.4 Synthesis of Transparent Conducting Oxides

Traditionally TCO films have been manufactured using particle deposition techniques such as pyrolysis, vapour deposition or sputter coating with further explanation in later in this section. Since 2010, efforts have been made to develop ITO inks for inkjet printing as industrial inkjet printers have made large scale manufacturing more cost effective. In small research environments, spray pyrolysis [244] and sputter coating [245] were common methods used in 1965 and 1972 respectively. Magnetron sputter coating became the method of coating favoured by the coatings industry as it can be sufficiently scaled up to meet demand. This involves the TCO powder being pressed into a compact pellet as shown in Figure 26(b). The pellet is then bombarded with ions or atoms at an angle. The material the pellet is formed is then removed from the target by the ion beam, forming a physical vapour which deposits onto the substrate as demonstrated in Figure 26.

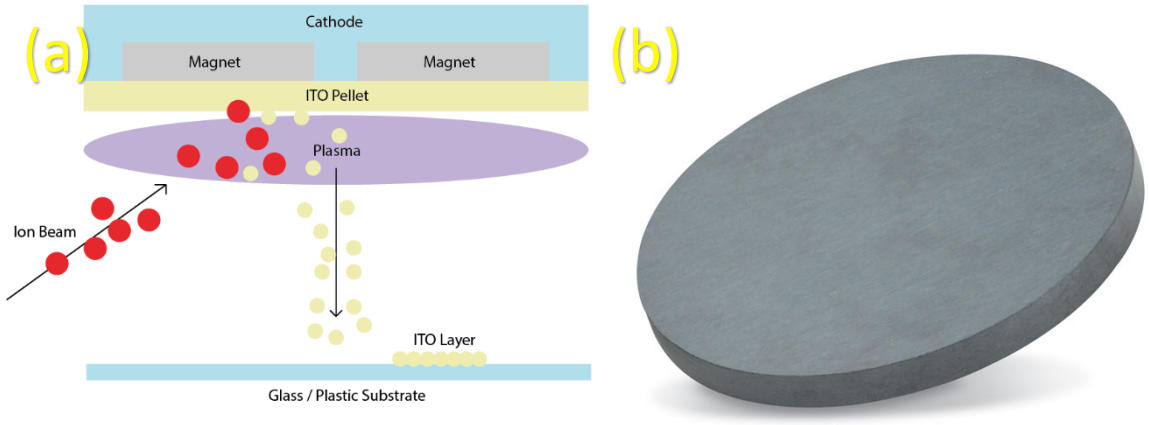

Figure 26 Sputter Coating, (a) Manufacturing Process, (b) ITO Sputter Coating Target [246]

Sputter coating is currently dominant in industry. Advantages are a uniform, thin, transparent film with relatively high conductivities. Disadvantages are high running costs, large amounts of energy (10000keV +) to sustain plasmas and maintenance. A vacuum must be sustained during the process and requires clean room like conditions to prepare a manufacturing run.

More environmentally sustainable methods of manufacturing are being researched, such as printing methods. Printers can run in non-clean conditions, require a fraction of the energy and give more control over the coating.

When synthesising transparent conducting oxides for use as conductive filler in conductive inks, multiple considerations must be made. The method used in the creation of the particles can have a significant outcome on the properties of the final sample. Good conductivity can be achieved with loosely controlled particle size. However, recent TCO synthesis in the literature focuses around nanoparticles due to their potential to control size and orientation for maximum conductivity. Synthesising nanoparticles has been shown to increase conductivity by up to three thousand times greater than its uncontrolled thermal decomposition counterpart [247].

The common traditional manufacturing methods for TCOs are [248]:

- Sputter coating using precursor materials
- Spray Pyrolysis
- Mechanical doping through two precursor powders
- Microwave synthesis
- Solution Gelation
- Aerosol assisted chemical vapour deposition (AACVD)
- Continuous Hydrothermal Flow Synthesis (CHFS)

For transparent conducting oxides, nanoparticles can either be made using a top-down approach or using bottom-up methods. Top-down nanoparticles are made by mechanically breaking up materials using milling techniques. Ball milling for fixed times can produce a particle size saturation point which is different for each material. Using barium titanite as an example, ball milling for 30 hours at 300rpm can produce an average particle size of 16nm with the size increasing after due to agglomeration [249]. Top-down techniques are generally used to create composite materials at nanoparticle scales and don't enable any fine tuning of particle shape. Impurities are also an issue with top-down techniques and for pure, well designed particles, bottom up techniques are used.

Bottom-up methods generally involve either the heat treatment of precursors in solution or the building of nanoparticles via polymerisation techniques.

The traditional method is *pyrolysis* which uses extreme temperatures on nebulised sprays to create nanoparticles. Weight percentage of the precursor, nebulising pressure and

temperature dictates the particle size. During the pyrolysis of zinc oxide, using 5wt% precursor can deliver an average size of 14.3nm at 1200^{o}C and a move to 20wt% at 1000 ^{o}C can achieve an average size of 10nm [250]. Pyrolysis cannot control particle shape but can still provide good conductivities, reported at 2.3x10^{-3}Ωcm with 80% optical transmission. This method produces a film directly onto the substrate rather than creating a powder which can then be used later, demonstrated in Figure 27.

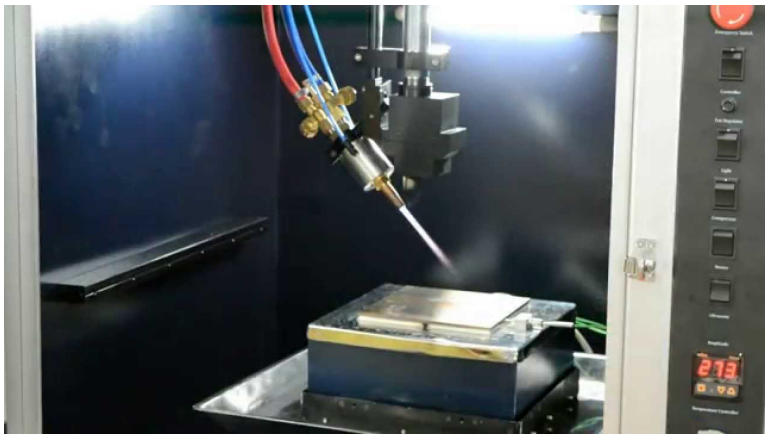

Figure 27 Spray pyrolysis setup [251]

Microwave synthesis has been developed into a suitable manufacturing method in recent years and due to this, more research groups select this method for TCO particle synthesis. This method uses applied heat like pyrolysis, however, the precursor solution is kept inside a containment vessel and the microwave energy creates the nanoparticles. The microwave provides more control than pyrolysis as all the solution is treated equally for a known time at a known energy. Particle shape can also be changed by altering the precursor. Using zinc acetate instead of zinc nitrate, zinc oxide nanorods can be created resulting in a different morphology once used [252]. As the microwave is a closed system, high purities can be achieved. Doped ZnO films created after using microwave synthesis can give conductivities of up to 4.02x10^{-4} at 85% transmission [253]. This method can provide a powder which can then be used by another medium to deposit onto a surface, giving it an advantage over other methods which either directly coat a substrate in TCO or require extra steps for extracting powders (leading to a loss of yield). Although microwave synthesis has gained popularity, its use in particle preparation for manufacturing is limited. It has been used once in inkjet printing for quantum dot manufacturing, however very little research has been conducted into other manufacturing methods [254].

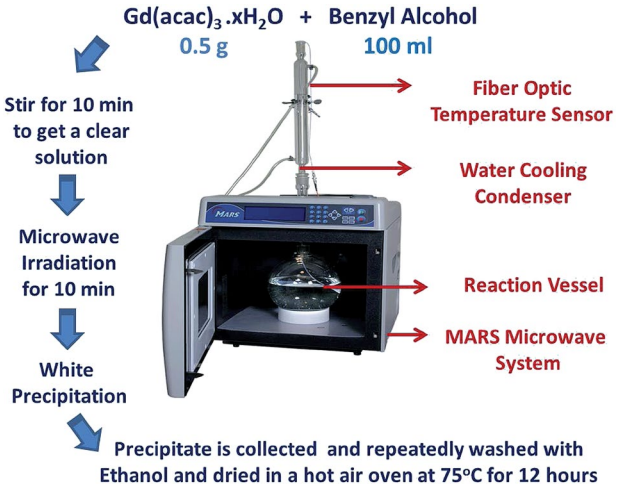

Figure 28 Example of microwave synthesis for Gd2O3 nanocrystals [255]

Sol-gel is a purely solution-based method of TCO nanoparticle synthesis and the method of synthesis can be seen in Figure 29. The method is very effective at giving good conductivity as each stage of the process can be optimised to fine tune the final material. A solution of precursors is polymerised, usually via hydrolysis to provide a polymer-based solution. These polymers can either then be directly used in spin-coating or dip-coating or condensed to form a gel. If the gel is chosen, heat treatment then provides a dense ceramic which can then be mechanically separated for use in another vehicle [256]. Sol-gel processing gives good control over the final product. This quality, however, is balanced out by the need to optimise each individual step for reliable results. The number of steps also makes it a poor choice for large scale use in industry.

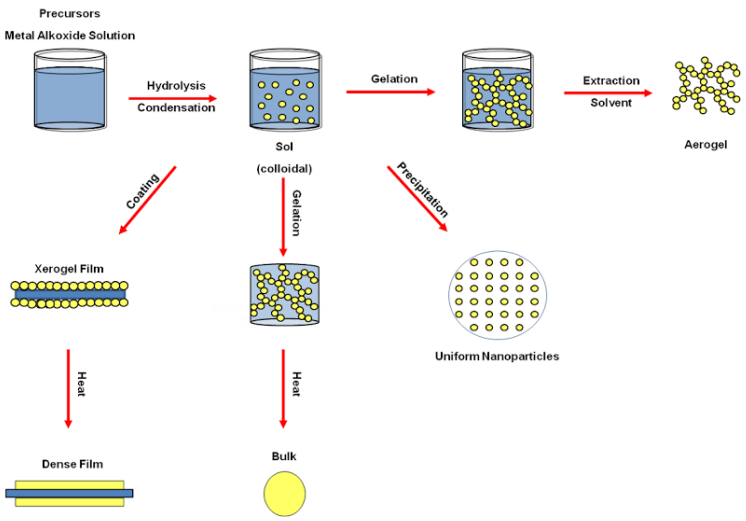

Figure 29 Example of sol-gel synthesis for nanoparticles [257]

Two more popular synthesis methods which deposit directly onto the surface are *aerosol assisted chemical vapour deposition* (AACVD) and *metal-organic chemical vapour deposition* (MOCVD). Like spray pyrolysis, these use nebulised precursor materials to build up layers of material on a substrate. MOCVD is a complex process compared to AACVD due to the use of toxic metal organics but can provide high control over film characteristics. AACVD gives less control but can be done in atmospheric pressure meaning large scale coatings of glass can be manufactured from a precursor solution [258]. The experimental setup can be seen in Figure 30.

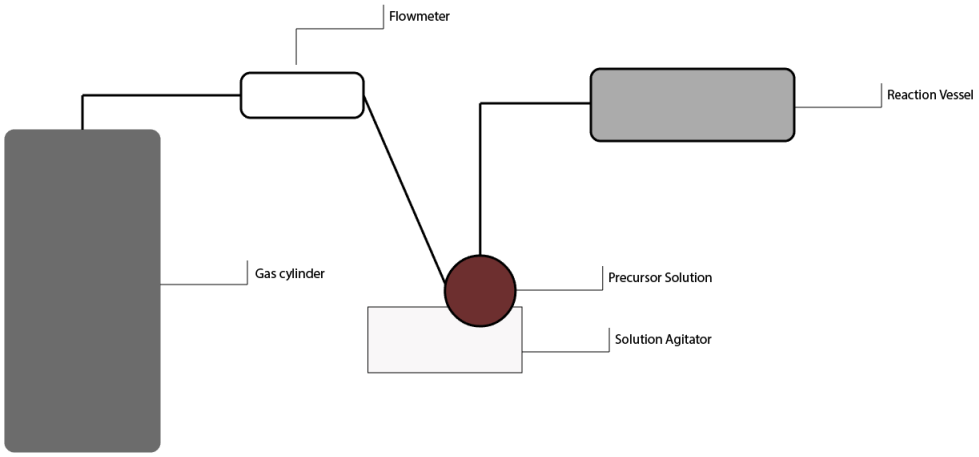

Figure 30 AACVD experimental set up

The final method to be discussed is also one of the most recently developed synthesis methods. As both sol-gel and microwave synthesising are both processes that are difficult to scale up for large scale manufacturing, continuous hydrothermal flow synthesis (CHFS) is a process designed for high throughput nanoparticle synthesis [265]. It was developed as an iteration upon a traditional manufacturing technique known as the Hydrothermal Method [266]. The Hydrothermal Method could manufacture large batches of powder by crystallising materials out of water-based solutions by mixing salts with supercritical water. The CHFS process adapts this into a continuous process which is highly scalable and allows theoretical lab scale production rates of 100's of grams per hour to large industrial manufacturing plants providing kilograms per hour [267]. In the continuous process, a water-based solution of a salt is

combined in a jet-mixer with super-critical water, using pressure to push crystallised nanoparticles out of the system where they can be collected in slurry form. By increasing the inlets to the jet-mixer, a secondary material can be introduced to allow for doping, making it an attractive option for obtaining high quantities of powder for ink formulation.

Out of these methods '*microwave synthesis*' provides the best balance between particle control and flexibility. The microwave processed solution can also be evaporated to provide nano-powder, these powders can then be used in printing. Work is currently being done with microwave synthesis to ensure larger amounts of material can be made [259]**.** Research has also been conducted into microwave annealing as a post treatment which is providing promising results. Samples of semiconductor can be annealed under an atmosphere using microwave energy to provide better material structure and properties compared to conventional heat treatments [260]**.** This is too hot for flexible substrates, however, with the right equipment the microwave energy can be directed to the print and anneal a print without melting the substrate. Continuous hydrothermal flow synthesis is also a good method for obtaining TCO nanoparticles. For ink formulation, large quantities of powder will be required, and this is currently the only method to obtain nano-powders in the 100's of grams. Synthesis methods which supply nano-powder are attractive as conductive inks can then be developed for consumer technology.

3.5 Applications of Transparent Conducting Oxides

Since the arrival of transparent conducting oxides, there has been widespread use for these materials in architecture, displays, photovoltaics and aerospace [261]. A common and widely used application is in flat panel displays and touchscreens. Each type of display needs unique film characteristics. In LCD / thin film transistor displays (TFTs) effort must be made to create a transparent film with a high aperture ratio. The TCO is sputtered on to a silicon nitride microcrystal and then patterned using acid etching techniques [262]. This application has accuracy issues and due to this, OLED applications are much higher quality.

TCOs are used in applications where optical transparency is essential with a conductive layer. For example, in a liquid crystal display, an ITO layer is placed over thin film transistors (TFTs) and the pixels (LEDs) with the liquid crystal solution between the two layers as shown in Figure 31. The ITO film then changes the orientation of each liquid crystal to polarise the light and filter what the viewer can see [263]. The structure of which can be seen in Figure 31.

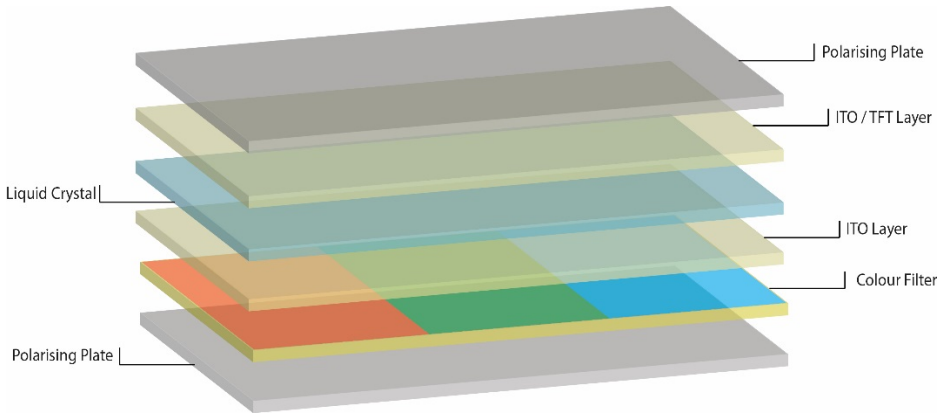

Figure 31 Common ITO Display Structure

Transparent conducting oxides are still used in organic LED technology. In organic light emitting diodes, the TCO is used as part of a LED, rather than a transistor coating like in LCDs. In OLEDs, the TCO acts as a transparent electrode between a glass substrate and the organic light emitting compounds and the transistors used for switching are used by materials other than the TCO. This is a much simpler application and provides higher quality results. To achieve this, a TCO will need a sheet resistance of 10-20$\Omega\square^{-1}$which should be achievable with non-ITO substances [264].

In touchscreens, the transparent conducting oxide works as a capacitive sensor. This is when an electrode can sense anything that has a dielectric different from the atmosphere or is conductive. The TCO is printed directly onto glass or a flexible substrate as an x-y grid, once touched a circuit is completed with another section of the grid, allowing the electrode to detect the area that was pressed [265]. Most consumer electronics applications of TCOs are used with capacitance being a factor. Once an alternative TCO has been developed a capacitive sensor should be attempted and both ITO and sustainable TCOs should be characterised for their capacitive behaviour. This will provide the best overall comparison for selecting a material for a product.

Another application to test with a new TCO is a humidity sensor, this will generate data on how the temperature and humidity in the environment affect electrical properties of the materials and printed films. This is important as an understanding of electrode stability is a feature that needs to be understood before complex applications are built. Humidity sensors have been created using ITO, prepared by thin film nano-structuring techniques such as sol-gel [266]. For these techniques, the main focus is on the resistance of a TCO film changing with the amount of water vapour absorbed onto the surface. However, traditionally manufactured TCOs are not very porous and therefore humidity absorption and therefore sensing quality is generally poor. This creates an opportunity for printed TCO humidity sensors to perform to a higher standard than their traditionally manufactured counterparts as printed powders will inherently be more porous due to vehicle evaporation creating voids, allowing for greater sensing performance. Literature has also focused on gas sensing using these materials, however, this provides no insight into the environmental stability performance of the printed TCO materials and will not be in the scope of this research [268].

ITO is generally deposited through sputter coating or large area aerosol deposition, however, with all TCOs, a powdered version can be synthesised for use in printing processes.

3.6 Conclusions

Doped and non-doped zinc oxides have been identified as the most viable candidates for the replacement of indium tin oxide. Recent research has shown its optical and electrical properties are becoming close to ITO. Zinc oxides have been shown to be more stable than ITO in devices after reports of ITO chemically diffusing into surrounding components [268]**.** Zinc oxides have also been found to be non-toxic making them suitable for consumer electronics. Zinc based nanoparticles have been found to be slightly toxic however meaning care should be taken during application design.

Most early applications found used spray coating as a deposition method. However, as devices become flexible, smaller and thinner, high temperature deposition methods like spray pyrolysis are unsuitable as they deposit layers of material rather than powder (which can then be made into an ink). Chemically deposited films are also not as robust making them unsuitable for portable devices. Printed electronics are gaining popularity in industry as printing is an inexpensive and versatile manufacturing method. During the comparison of certain transparent conducting oxides, various printed manufacturing methods were found for ITO. These were inkjet printing, screen printing and flexographic printing. Zinc oxide and AZO both had reports of screen printing. However, there was no mention in the literature of screen printed Ga doped or Ga/Al doped zinc oxides which is worth investigation. The only publication with screen printed AZO did not make traditional conductive ink, only dissolving the particles in ethanol. Zinc oxide also had no mention of flexographic printing, which has been successful in providing transparent conductive depositions for ITO [269]. There are also no publications at this time on the integration of TCO materials into an additive manufacturing process which warrants research.

The key findings of chapters 2 and 3 in relation to the literature are:

With regards to TCO Materials

The field of ITO alternative materials is relatively new compared to the decades of research that has been performed on ITO. However, there are already some promising alternative materials. Doped zinc oxides appear to have the closest properties with co-doped aluminium gallium doped zinc oxide and gallium doped zinc oxide warranting

further research. There is currently no literature investigating the integration of these materials into printed electronics processes. There are also multiple manufacturing methods available for synthesising bulk powders for the ink formulation process. Indium tin oxide should also be investigated as the literature shows there has not been a proper investigation into these materials for printed electronics.

With regards to Printing Processes

Although there are some papers on screen printing and gravure printing ITO, there are no papers in the literature for conductive ink formulation involving doped zinc oxides for any printing process. As discussed in 2.6.2 Selection of the Printing Process, screen printing and material extrusion are the methods of choice for this thesis. With these experimental materials the printing processes selected will allow for adaptability in terms of rheology, complexity of devices fabricated and material compatibility.

With regards to Post-Processing

For this body of work, conventional heat treatments and laser processing are the post processing methods of choice. This will enable a comparison between the efficiency of low temperature vehicle crosslinking to a non-destructive high temperature sintering method. The TCOs selected have glass transition temperatures above 600^{O}C suggesting conventional heat treatments will not provide enough energy at lower temperatures to provide conducting layers.

With regards to Electronic Devices

In Section 2.6.4, capacitors were selected as the electronic device as choice. TCOs are typically used as capacitive sensors in consumer electronics and fabricating these devices comparing sputter coated TCOs to printed TCOs will demonstrate the performance of the materials optically and electrically. The review of literature for transparent conducting oxides yields no publications in printed TCO based capacitors.

The following chapter presents the research methodology for this body of work and provides an outline for experimental methods into developing printed electronics and printed transparent conducting oxides.

Chapter 4

Experimental Methods

4.1 Introduction

The introduction of conductive metal oxide materials into the realm of printed electronics requires many methods of physical experimental and interdisciplinary analysis, combining analytical techniques for both electronics and materials characterisation. There are two ways of discussing research methodology, one method is to formulate and discuss the framework (or methodology) for creating hypotheses and collecting and evaluating data as discussed in Chapter 1. The second way involves the methodology (or experimental techniques) that will be used in to fabricate samples and collect data in a set of research which heavily involves the physical sciences. This chapter sets out a problem definition informed by the literature review, funding body and industrial collaborators. The following sections will then set out the experimental techniques that are to be used to achieve the research objectives set out in Chapter 1, informed by the literature reviews in Chapter 2 and 3.

4.2 Problem Definition

Part of the funding for this Ph.D. comes from the EPSRC funded project for the "sustainable manufacturing of transparent conducting oxides". The synopsis of the EPSRC research proposal is:

"This project seeks to develop processes and resources towards sustainable and inexpensive high quality transparent conducting oxide (TCO) films (and printed tracks) on float glass, plastics and steel. In particular, replacement materials for Indium Tin Oxide (ITO) and F-doped Tin Oxide (FTO). These materials are used in low-e window coatings (>£5B pa), computers, phones and PV devices. The current electronics market alone is worth in excess of £0.9 Trillion and every tablet PC uses ca 3g of tin. Indium is listed as a critical element- available in limited amounts often in unstable geopolitical areas."

"Tin metal has had the biggest rise in price of any metal consecutively in the last four years (valued at >£30K per ton) and indium is seen as one of the most difficult to source elements. In this project we will develop sustainable upscaled routes to TCO materials from precursors containing earth abundant elements (titanium, aluminium, zinc) with equivalent or better figures of merit to existing TCOs."

The research collaboration focuses on the larger issue of replacing indium tin oxide for thin film deposition processing. The main aim is to select materials, integrate them into scalable traditional manufacturing properties and then perform materials characterisation on the thin films to determine film quality. However, there is also scope for the integration of these materials into printing processes and as discussed in earlier chapters, there has been little research performed into printing the current best conductive oxide ITO and no research has been performed into printing sustainable alternatives such as GZO and AGZO for a majority of printing processes.

Therefore, the groundwork for introducing these materials into printing processes needs to be performed with ITO alongside the sustainable alternatives to give the best picture of how these materials will function in a printed electronics context. The process for doing this should be a materials characterisation study of the starting materials, in order to determine the quality. A suitable vehicle should then be selected which is compatible with the materials and then inks are to be formulated. The best material should then be selected in the terms of conductivity. Due to there being little research in developing these materials for printing processes, the sustainability of the materials should not be considered and simply the best material should be selected. Considering this research has not been performed with unsustainable materials, choosing the best material will give the best overall picture of whether these materials can be used successfully with printing processes.

Considering the high temperature requirements of these materials as discussed in the literature review, a suitable post processing method will then be researched. Following this, electronic application will be printed and characterised. Due to this framework, the experimental methodology needs to include ink formulation methods, materials characterisation techniques, ink characterisation techniques, methods of analysing the

electrical and optical properties and techniques for printing and post-processing. These will be selected and discussed in subsequent sections of this chapter.

4.3 Research Objectives in Relation to the Literature

The research objectives set out in section 1.3 are clarified below, relating the research objectives to the key findings in the literature review:

RO1) Identify and determine the characteristics of ITO and ITO Alternatives

Viable alternatives were found after a review of the literature, doped zinc oxide materials fabricated into powders will be investigated in comparison to ITO powders. This will determine the performance of both printed ITO and zinc oxide optically and electrically and will allow for a comparison between the materials.

(RO2) To formulate and optimise TCO based inks and characterise the properties of printed films

Thixotropic ink formulation processes were identified as a gap in the literature for TCO materials. Inks will be formulated into multiple commercial and experimental materials to determine the material compatibility and the results this has on performance. Initial characterisation will be performed with conventional heat treatments.

(RO3) To investigate an industrially viable post-processing technique for optimisation

The viable post processing technique selected is laser processing of the printed materials. This provides the best route to sintering printed ceramic materials onto flexible substrates without destroying the substrate.

(RO4) Develop and Characterise Printed Interconnect and Passive Devices

Printing tracks of TCO material is required to determine the electrical performance of the materials to perform at high resolutions of printing. The passive device selected for research is the capacitor, a gap in the literature was found and there are no publications relating to printed TCO based capacitors.

(RO5) Fabricate Printed 2-D Applications Utilizing the Printed Passive Components

Capacitors can be used for both signal processing and sensing applications. Humidity sensors are to be fabricated using sputtered and printed TCOs which helps to characterise the stability of the materials in the atmosphere. The capacitors can also be characterised by determining their performance in R-C signal filter circuits. These capacitors can then be characterised as humidity sensors providing environmental stability data for printed TCOs while also developing the first capacitive TCO based humidity sensors.

4.4 Material Characterisation Techniques

4.4.1 Scanning Electron Microscopy (SEM)

One of the best ways to determine what is happening to a material, is to simply see it. Due to this, microscopes have long been a staple of scientific research. The first microscope was invented by Zacharias Janssen in 1590 [270]. The most common type is the optical microscope which functions from illuminating a sample with light which is detailed further in Section 4.6.4. Optical microscopes have a maximum magnification of 1250x magnification due the wavelength. Most optical microscopes are nowhere near this resolute and are not useful when needed to distinguish particle size, surface morphology and coverage, crystal structure etc. The most direct method of measuring this is by using a Scanning Electron Microscope seen in Figure 32(a-b).

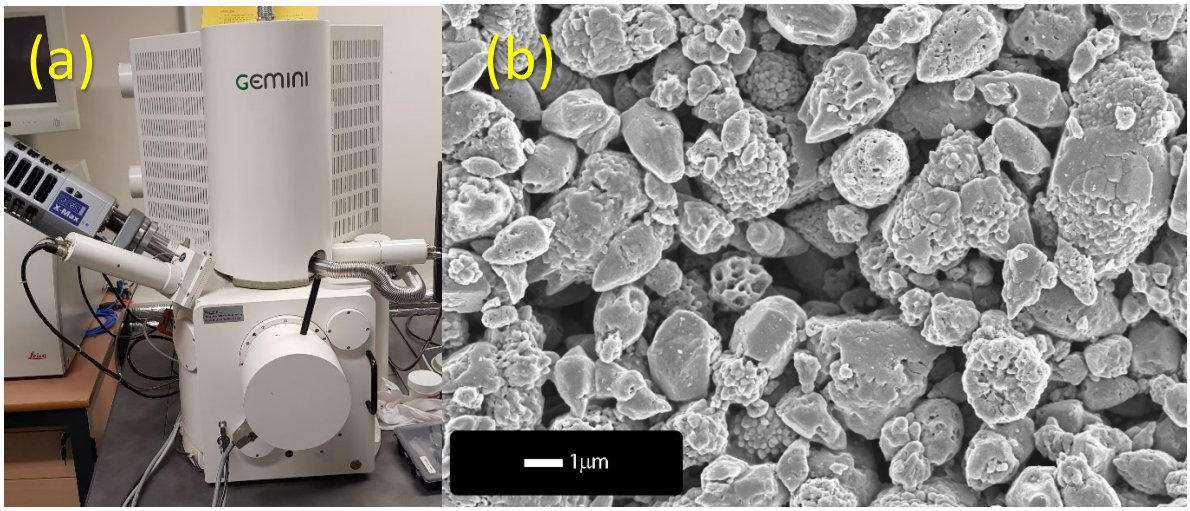

Figure 32 (a) Zeiss VP 1500 SEM and (b) SEM Image of Particles

The Scanning Electron Microscope (SEM) utilises electron beams instead of photon beams, these electron beams are much smaller than light and can be reflected off smaller particles and magnifications of up to 250000x can be achieved depending on beam energy [271]. In quantum mechanics, wave-particle duality is the phenomenon matter has the properties of both waves and solid particles [272]. Scanning electron microscopy uses this phenomenon to change the atomic density of the measured sample to a solid-like state which then scatters electrons back towards an electron detector which makes up the image. Therefore, SEM

techniques are suitable, and two microscopes were used for this research, a Zeiss VP 1500 Field Emission Gun SEM and a JEOL 7800F SEM.

4.4.2 Energy-Dispersive X-Ray Spectroscopy Analysis (EDX/EDS)

Considering information on chemical and doping stability of the materials is required for the printed films, some sort of elemental analysis technique is required. Energy dispersive X-ray spectroscopy (EDX or EDS) is a microanalysis feature of many scanning electron microscopes. It is a powerful tool which provides elemental composition data on the sample being imaged and can even map the distribution of individual elements in a sample [273]. The method works by firing a high energy electron beam at the sample, generally more than 20keV. This electron beam ejects electrons from the inner shells of the atoms, a higher energy electron then drops into the lower energy state held by the original electron. As the electron moves from the higher to the lower energy state, an x-ray is emitted from the atom as shown in Figure 33. These x-rays are then detected with the energy being characteristic of certain atoms providing a full elemental analysis of the sample [271].

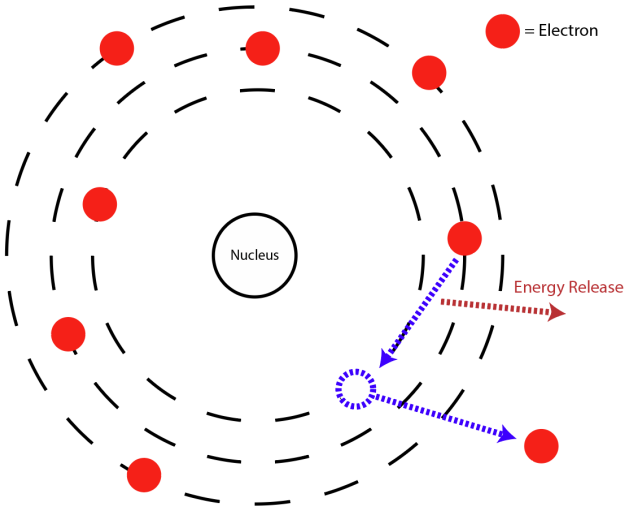

Figure 33 Electron excitation and x-ray generation via EDS/EDX

For this research, Oxford Instruments EDX silicon drift detectors (SDD) were utilised and data processing of the collected information with Oxford Instruments Aztec EDX Analysis software. Main methods of data collection were elemental mapping where a scan is made of an SEM image and point and ID analysis, where data is collected from a small area of a sample.

4.4.3 X-Ray Diffraction

X-ray diffraction is a staple materials characterisation technique for crystalline materials (including metal oxides) which provides information on the crystal structure and phase of the material. This technique uses an x-ray source, typically copper (K-α, wavelength = 1.5406 Å) fired at a sample over a range of angle of incidences and detects the diffracted x-rays as shown in Figure 34. The angle at which x-rays are diffracted are characteristic of both materials and the atomic arrangements of the atoms. This combined with a rotating sample means that all orientations of crystal can be detected with XRD. In a polycrystalline medium where crystals are at different, random angles, the sample is rotated to allow for particles in any angle to diffract into the detector.

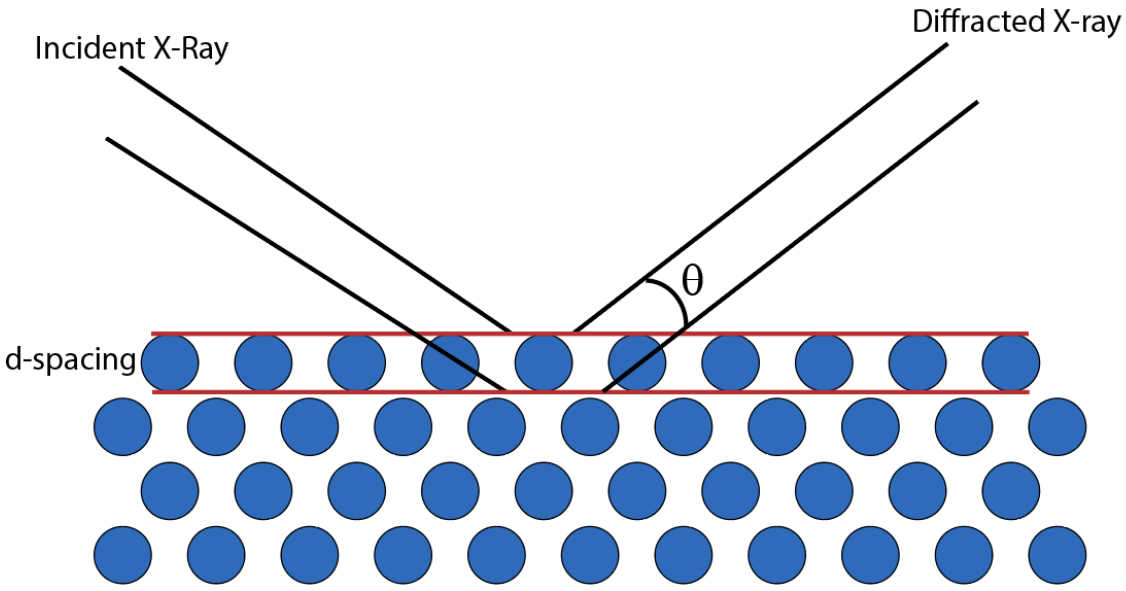

Figure 34 Schematic of X-ray Diffraction Process

The wavelength of the incident copper x-ray can be related to the angle of diffraction and the atomic d-spacing using Bragg's law, detailed in Equation 3:

$$n\lambda = 2dsin\theta$$

Equation 3 Bragg's Law

Where lambda (λ) is the wavelength in angstroms, n is the order of reflection, d is the atomic spacing of the reflection in angstroms and theta (θ) is the angle of diffraction. This can provide information on the level of doping, the crystal structure of the material pre and post

processing and even the grain size of the printed films. The X-ray diffractometer for this research is the Bruker D2 using a copper x-ray source (K-α, 1.5406 Å).

4.4.4 Particle Size Analysis

Particle size is represented as a distribution and due to this, when controlling the size, the aim is to keep particles within a certain range of each other. Sonication or milling techniques mechanically separate the particles and running the process for specific times will give an expected size distribution. These are rudimentary but tried and tested methods of controlling size. Recently, computational chemistry has gained traction in industry for predicting ink quality, using chemical data to predict the amount of nucleation and growth in the system [168]. In suspensions, particle size can be controlled through electrostatics or through steric hindrance [169]. Electrostatic control is where the particle either has an inherent charge or functionalised materials bound to it with a charge. This charge is then repelled by either the solution or other particles, stopping agglomeration.

Steric hindrance is more commonly used in polymer chemistry and will be the focus of the binders in this research. Steric hindrance is where the particle is coated in other large particles, normally long chain organics, and the size of these chains blocks other particles from getting close. Both methods provide stabilisation to the ink and increase its shelf life. As non-polar solvents will be used, inks will be formulated around increasing steric hindrance to stabilise the particle size.

To measure the particle size, two methods can be employed. The first method is measuring the Zeta potential. The zeta potential, also known as the electrokinetic potential (ζ – measured in mV) is defined as “the potential drop across the mobile part of the double layer” [170]. In a colloidal system such as an ink, the binder forms a double layer between the solvent and the particles acting as the pigment. The electrokinetic potential therefore shows the attraction or repulsion of the particle to the binder and the binder to solvent. Measuring the zeta potential can provide information on particle stability on a scale of 0 to >61 mV where 0 is no stability and >61 shows excellent stability. Zeta cannot be measured directed and is calculated via experimental data.

The second method that can be used is the fineness of grind test (FOG Test) [171]. Measuring fineness of grind is a method of measuring the particle size for dispersions which contain particles with a size distribution in micrometres rather than nanometres. Measured using a Hegman gauge, the ink is scraped across the gauge intro surface grooves. The length and depth of the grooves correlate to the particulate size, often from 100 to 0 micrometres [172]. Using this method will aid in optimising ink uniformity.

The method that is employed for this research is electrophoresis via Zetasizer (Malvern Instruments NanoZS), due to the use of nano-powders and micro-powders. Whereas fineness of grind can only give information in the micron region, the zetasizer allows for a full range of particle measurements with much less error.

4.4.5 UV-Vis Spectrophotometry

UV-Vis Spectrophotometry, also known as Ultra-Violet, Visible Light Spectrophotometry is a spectroscopic technique which involves shining a light on a sample, scanning across wavelengths typically with between 190nm to 1100nm and measuring the either the transmission, absorption or reflection of light. For solid state samples, the ones which will be used in this research, the sample is mounted into a solid sample holder and the light is fed into a monochromator which scans between a minimum and maximum wavelength of light. As shown in Figure 35, the light from the monochromator is then fed through an aperture which controls the beam width, typically between 0.5 to 4nm with a smaller beam width increasing resolution while also increasing noise. The beam is then directed towards the sample where the samples interaction with light is recorded through a detector.

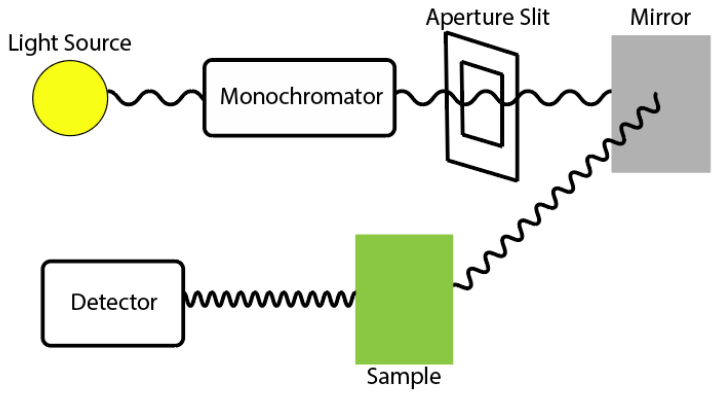

Figure 35 UV/Vis Spectroscopy Schematic

For this research, a Perkin Elmer 35 UV/VIS Spectrophotometer is used with a slit width of 1nm, data processing is performed on Perkin Elmer's Winlab software.

4.4.6 Transmission Electron Microscopy (TEM)

Most of the materials that will be used will be nanoparticles, sub micrometre in size meaning traditional SEM may not have high enough resolution for some samples. When absolutely required, the use of transmission electron microscopy will be used. This fires a high energy electron beam through an extremely thin sample and the particles then create a shadow over a detector. The sample is generally an extremely dilute suspension of particles within an alcohol, a copper mesh is then passed through the suspension and small amounts of particles attach themselves to the mesh. The shadow formed by these particles is then recorded and allows for imaging with magnifications up to 1 million times. In Figure 36(a), the TEM apparatus that will be used it is the FEI Tecnai F20 transmission electron microscope which also uses a silicon drift detector and Gatan ENFINA Electron Energy Loss Spectrometer to allow for EDX analysis and mapping. An example of an image captured via TEM can be seen in Figure 36(b).

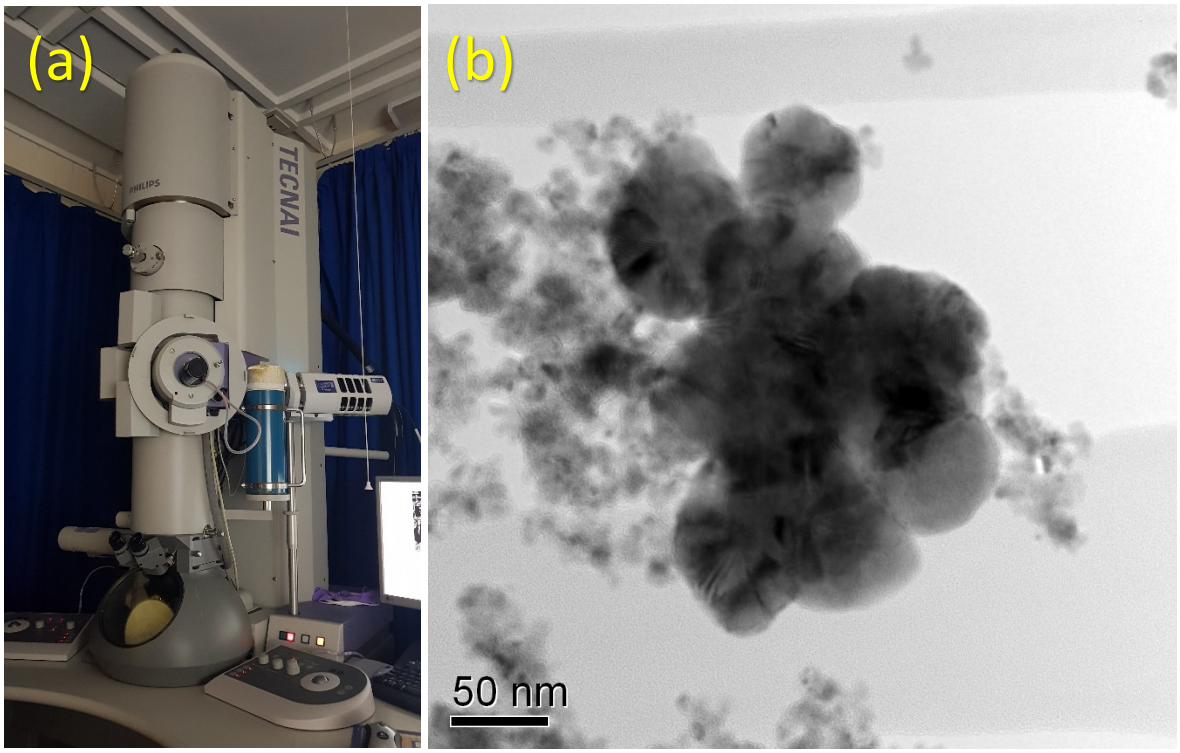

Figure 36 (a) Image of the TEM to be used and (b) an example TEM image of doped zinc oxide

4.4.7 Thermogravimetric Analysis / Differential Scanning Calorimetry (TGA/DSC)

Thermogravimetric analysis (TGA) is a technique where a small amount of material is placed in a highly sensitive balance with an inert reference (generally alumina) and it is then heated, the weight is then recorded with an increasing temperature at varying ramp rates. The weight decrease or increase (oxidation) versus temperature can then be measured and provides insights into curing times, melting points, sintering temperatures etc. Differential scanning calorimetry is a technique which is performed in conjunction with TGA and measures the amount of heat flow required in order to increase the temperature of the sample, this provides data on the exothermic and endothermic properties of the material and gives more information on melting and sintering points. The TGA/DSC apparatus used for this research is the TA instruments SDT Q600s, ramp rates were 1 degree per minute for polymers and 5 degrees per minute for ceramics.

4.4.8 X-ray Photoelectron Spectroscopy (XPS)

X-ray photoelectron spectroscopy (XPS) is a surface analysis technique which measures the top few nanometres of a sample for elemental composition. Although the technique is surface only, it is a powerful tool as it can provide insight into doping and elemental bonding which other materials characterisation methods cannot. As shown in Figure 37, XPS uses an electron beam, fired at a metal target (Al, Mg) to generate X-rays, these X-rays are then monochromated and fired at the sample. Photoelectrons are then generated at the surface of the sample with an energy dependant on the bond electron cloud type and atomic structure, allowing for elemental compositions with bond information to be analysed.

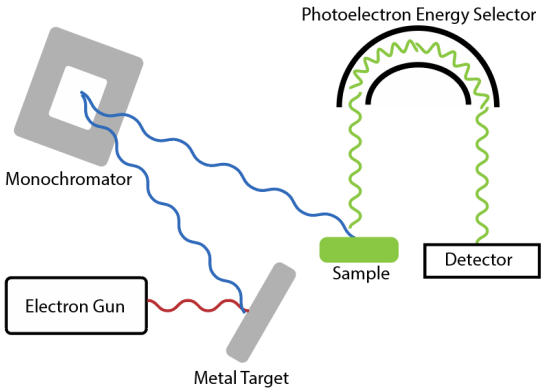

Figure 37 Schematic of the XPS Process

For this research, a thermo-scientific K-ALPHA Surface Analysis XPS system is used, utilising an Aluminium (Al) metal target.

4.5 Ink Characterisation and Formulation Techniques

4.5.1 Rheology

Viscosity is a measure of the internal resistance of a fluid to an external force and is essentially how sticky or susceptible to friction a fluid is. The rheology of a fluid is how this fluid reacts when either under flow or deformation [274]. For printing inks, the main form of ink deformation comes from the shear stress, this shear stress is a force applied per unit area to the material in a perpendicular axis [274]. The SI units of measurement for shear stress are newtons per square metre (N/m^2) which converts directly into a unit of measurement called the Pascal (Pa), when measuring shear stress, the Pascal is the unit of measurement used. Viscosity which is defined as newton seconds per square metre contains this shear stress information and is measured as pascal seconds (Pa.s) which directly converts into Poise (P) the typical unit of viscosity used in the printing industry [275].

Rheology only typically applies to Brownian (or Non-Newtonian) fluids which while under stress can either be shear thickening or shear thinning. For a shear thickening (also referred to as dilatant) material

When measuring viscosity, there are multiple methods that can be employed. A fast, rudimentary way of measurement is by determining how long the fluid takes to move from point A to point B. This is commonly done by dropping a sphere through a cylinder of the ink and the absolute viscosity, the viscosity of a material related to its density can be calculated by rearranging Stoke's law:

$$\mu = \frac{2}{9}\left(\frac{r^2 g\left(\rho_p - \rho_f\right)}{V_S}\right)$$

Equation 4 Stokes Law of Viscosity

μ, the dynamic viscosity measured in pascal seconds, can be calculated by considering the stokes radius of the particle (r), the settling velocity (Vs), the gravitational acceleration (g) and the density of the particles and fluids (pf and pp). Temperature must be controlled for accurate readings.

Another way viscosity will be measured is by using a commercial SV-10 Malvern Instruments viscometer. The machine works by vibrating a gold-plated fork in the fluid at specific frequencies. The current required by actuator to vibrate the forks at a certain frequency is then used to calculate the viscosity. The machine calculates this as:

$$x = F/c\omega$$

Equation 5 Vibrational Viscosity

Where x is the amplitude, F is the excitation force, C is the viscosity coefficient and ω is the vibrational frequency. The equipment for measuring absolute viscosity used is a Cambridge Viscolab Viscometer for measuring small sample viscosity vs temperature. For rheological data a Haake VT550 rotational cone and plate viscometer is used which provides data on viscosity and stress versus shear rates.

4.5.2 Profilometry

For the accurate calculation of a printed films dry thickness, profilometry is required. This is a technique which precisely measures the thickness of a material by either passing a light source or stylus over a sample and either recording a pressure change or change in the reflection of light. As most printing experiments are typically performed on transparent glass or polymer, a stylus based profilometer needs to be used to accurately determine the substrate layer height before a printed film. For this research, a Taylor Hobson Talysurf Stylus Profilometer will be used in conjunction with Taylor Hobson's Talymap profilometry data analysis software.

4.5.3 Ink Formulation via Three Roll Mill

All ink formulation was performed using an EXAKT three-roll mill with the milling mechanism displayed in Figure 38. This method was selected after being determined to provide the most shear stress to the ink in Chapter 2, enabling higher weight loadings and more uniform dispersions to be formulated.

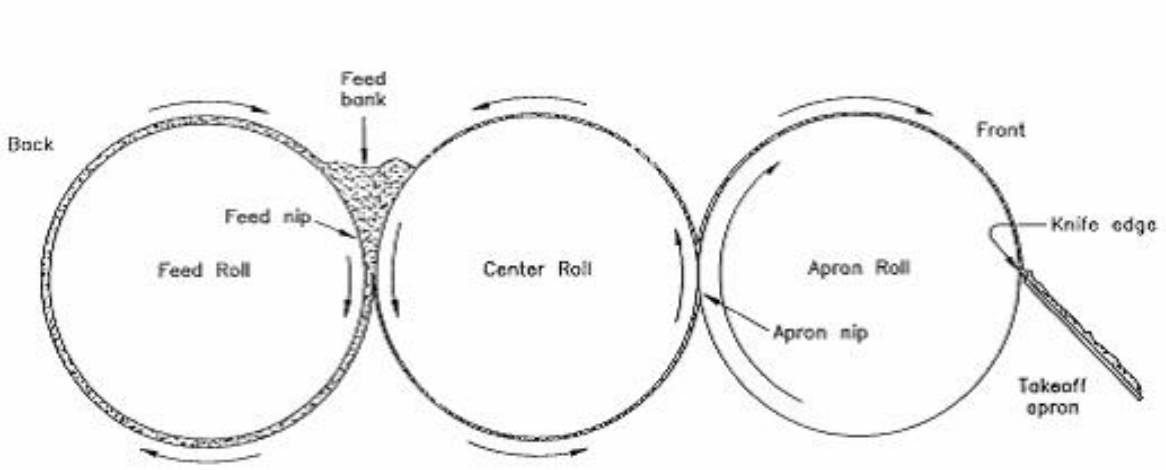

Figure 38 Three Roll Mill mechanism [167]

The three-roll mill uses two rollers (feed roll and centre roll – see fig 38 and 39) to disperse the particles into the ink vehicle. The third roll is then used to collect the dispersed ink with a blade. With this method well dispersed inks with high weight loadings and stable rheology's can be developed.

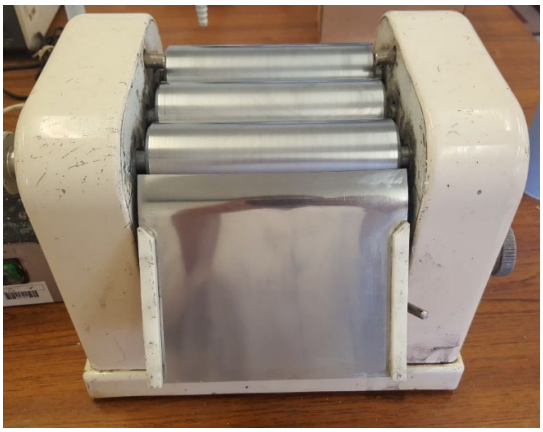

Figure 39 EXAKT Three Roll Mill to be used

4.5.4 Print Quality Assessment

Ink analysis can help optimise properties such as viscosity and conductivity. However, printability – the quality of the actual print and film requires qualitative assessment. For this, a scale was devised for judging the quality of a print. The quality involves coverage of the film, the ability of the ink to keep to the screens defined resolution. The scale is shown in Table 3. There is currently no dedicated qualitative system for determining screen printing print quality in the literature, due to this, the system in Table 3 has been adapted from the Bandey scale [278]. The Bandey scale is a qualitative analysis technique developed for the forensic analysis of fingerprints at crime scenes developed in 2012. Adapting it for screen printing enables the visual quality of prints to be quantised for further optimisation.

Table 3. Designed quality level system for inks

Quality Level	Comments
0	No ink coverage on substrate, ruins screen
1	Small amount of ink coverage, particulates in screen,
2	Medium amount of ink coverage, difficult to clean, messy print
3	Almost full ink coverage, ink not in defined artwork, relatively easy to clean
4	Perfect print, easy to clean good film coverage and no excess ink

4.6 Electrical Characterisation Techniques

4.6.1 Impedance Spectroscopy

Impedance spectroscopy measures of an electronic component responds to an AC signal rather than a DC signal. It is generally used by chemists to investigate solid – liquid surface electrochemical reactions. However, it can also be used for purely solid-state electronic components which include a solid dielectric layer. For measurements of this type, the AC wave excites an electrical dipole in the dielectric material and creates an electrical field. By measuring the real and imaginary impedance, a wealth of information can be extracted such as the capacitance and dielectric constant with respect to frequency, the ideality of a capacitor. When this method is used, it is often called “dielectric impedance spectroscopy”. Another way this technique can be useful for the following research is that with regards to sensors, measuring the impedance of the sensor with respect to the external sensing force being altered, it is possible to deduce the sensing mechanism. This is performed by creating an equivalent circuit model while not sensing and creating one with a maximum sensing load. By analysing the differences in the circuit model and what the components represent in the physical system, the method of sensing can be discovered. For this research, Metrohm Autolab Instruments multi-channel potentiostat / galvanostat (PGSTAT12) using Metrohm’s Frequency Response Analyzer software (v4.7.900) for data recording.

4.6.2 Sheet Resistance via Four-Point Probe

In conductive film research, the two measurements every paper contains are sheet resistance and optical transmission. Measuring sheet resistance ($\Omega\square^{-1}$) is a common way of determining the electrical characteristics of a conducting film over the area printed on. It measures the resistance of the surface which provides useful information when developing 2D electrodes. It is calculated via:

$$\rho = t(R_S)$$

Equation 6 Calculation of Sheet Resistance 1

Where R_S is the sheet resistance measured in $\Omega\square^{-1}$, t is the film thickness in cm and ρ is the bulk resistivity in Ωcm. A four-point probe takes the measurement (Fig. 40) [173]. The probe

works by having four terminals in parallel, the two outer terminals supply a current into the film and the two inner terminals then measure the voltage being supplied from the film. Then using:

$$V = IR_s$$

Equation 7 Calculation of Sheet Resistance 2

We can determine the sheet resistance (R_s) as the voltage (V) measured, divided by the current (I) which has been supplied. The four-point probe used (Jandell HM21), outputs the sheet resistance already calculated.

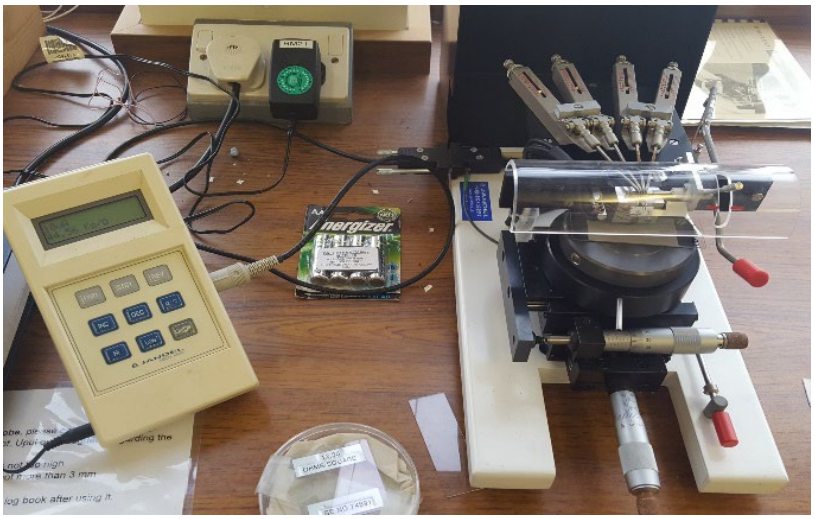

Figure 40 Four Point Probe measurement of sample

4.6.3 Inductance/Capacitance/Resistance Meters

Multi-meters are generally the equipment of choice for DC measurements, this research will use a Fluke 179 calibrated multi-meter for all two-point probe measurements. When AC measurements are required, for example for capacitive applications an LCR (Inductance, Capacitance, Resistance) meter is required. For AC measurements, a UNI-T 612 LCR meter is to be used which also includes software for real time measurement recording.

4.7 Chapter Summary

This chapter has outlined the experimental methods and equipment that will be used for the bulk of the experimental based research conducted in this thesis. As this research will be interdisciplinary, an overview of experimental techniques for ink formulation, materials characterisation and electronics characterisation have been discussed and chosen. In the next chapter, experimental research will begin with the characterisation of the chosen metal oxide materials using techniques discussed here. Ink formulation will then begin with the selection of a suitable vehicle and then the resulting inks will be characterised electronically and optically.

Chapter 5

Conductive Metal Oxide Ink Formulation

5.1 Introduction

In the previous chapters, printing processes and materials were selected in order to conduct research into printing TCO materials. In this chapter, these materials are formulated into inks and characterised as outlined in research objective 2. In these experiments, three ink formulation vehicles and four metal oxide filler materials are investigated with the intention of finding the most suitable vehicle and the best performing metal oxide materials. First, a materials characterisation study is performed on the four metal oxide filler powders to provide a baseline for further analysis and to determine the overall material characterisation. Preliminary metal oxide inks are made with each of the three vehicles to determine the best vehicle, selected by assessing film densification. Once the most suitable vehicle has been selected, a preliminary study details the conductivity versus weight fraction of the filler material to determine the most conductive metal oxides. As metal oxides can also display transparent and optoelectronic properties, the optical properties are analysed. To fully develop a usable ink, both the most conductive and most transparent materials are selected for further investigation. These printing inks are characterised via analysing the rheological, optical and electric properties and in this chapter all curing is performed with oven based conventional heat treatments.

Using the conductivity as the primary parameter to base ink development on, a Taguchi L8 design of experiments is performed on the selected metal oxide material to determine the effects of:

- Binder concentration
- Solvent concentration
- Curing additives
- Surfactants for ink stabilisation
- Printed film thickness
- Curing temperatures

Analysis of the design of experiments is used to provide information about the effects of each component on the final conductive, optical and rheological performance of the ink. The Taguchi L12 is chosen over a mixture experiment as mixture experiments typically provide statistically confounded results, providing little information on the component effects on performance. The final conductive metal oxide ink to be used for the remaining thesis chapters is chosen. A final study is performed on composite metal oxide / nanoparticle conductor inks in an effort to investigate the effect of a secondary conductor on the final conductive, optical and rheological properties of the films.

5.2 Conductive Filler Materials

In order to determine the performance of a formulated ink, the characteristics of the starting filler (the dry, powdered component of the ink) material must be determined. In this section, each of the four chosen TCOs are characterised in powder form to determine the quality of the material and the expected characteristics in terms of electrical and optical performance.

5.2.1 Indium Tin Oxide (ITO)

Indium Tin Oxide is a common conducting oxide material, it is a degenerate n-type semiconductor meaning that the doping provides the ceramic with near-metallic electrical properties. However, it is still a ceramic and it is also a highly environmentally stable material. Typically, the material is sputter coated leading to a highly crystalline, conductive and transparent layer. For the comparison of sputter coated indium tin oxide to printed ink indium tin oxide, radio frequency magnetron sputtering of ITO onto flexible polyethylene terephthalate sheets (PET, Dupont Teijin Melinex O) was performed at Diamond Coatings LTD. Sheets were coated at different layer thickness to give different conductivities. The high polycrystallinity of the sputter coated ITO films can be seen in Figure 41.

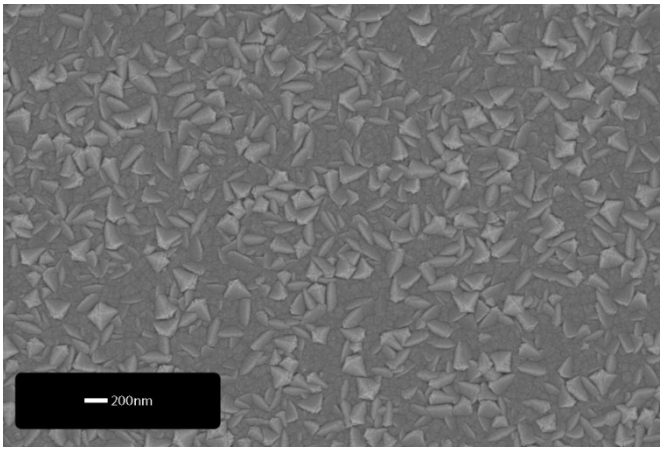

Figure 41 SEM of 10Ω□$^{-1}$ Sputtered Indium Tin Oxide Layers

Ink formulation requires a powdered conductive filler, for this series of experiments a commercial ITO powder (Alfa Aesar, 99.99% Metals Basis) was used which has a doping ratio of 10% tin oxide (SnO_2) to 90% indium oxide (In_2O_3). The crystal structure of the ITO is typically in a cubic lattice configuration with electron holes in the unit cells contributing to a high electrical conductivity [276].

This cubic lattice can be seen by performing scanning electron microscopy (SEM). An SEM of milled ITO powder can be seen with a cubic crystal highlighted in red in Figure 42. Given optimal conditions for crystal growth (i.e. reaching glass transition temperature, recrystallization temperature), films of this material should match that of the sputtered material seen in Figure 41. The initial particle size of the starting powder has a value of 325 mesh which converted to a maximum particle size of 44μm. The three-roll mill has a spacing of 5μm, meaning inks should have a maximum particle size of 5μm.

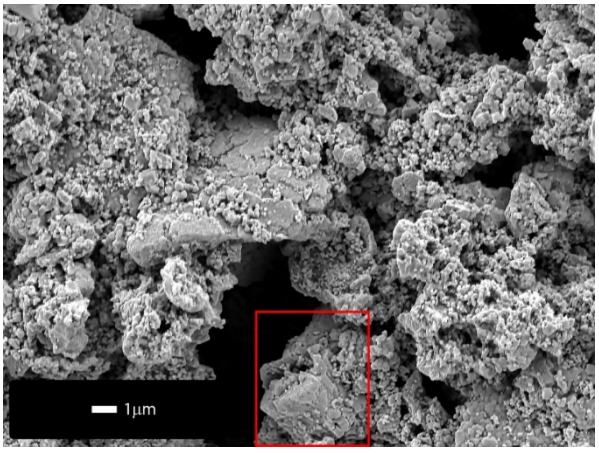

Figure 42 SEM Image of Indium Tin Oxide Powder

Powder X-Ray Diffraction was performed on the ITO powder for a 12h 30 run on a D8 Advance X-Ray Diffractometer. From the XRD, shown in Figure 43, we can see that the material correctly matches literature values for crystal orientations and peaks [277]. The data shows indium oxide in its correct state as the bulk material, with peaks shifted to the left compared to pure indium oxide which shows that the material has been doped. The tin oxide phase of the material matches the cassiterite tin oxide ore crystal structure which is common in indium tin oxide. Elemental analysis of the indium tin oxide powder was performed using energy-dispersive X-ray spectroscopy (EDX/EDS). Combining this technique with scanning electron microscopy, dopant concentrations, dopant location on the material and impurities can be determined. EDX was performed on the indium tin oxide powder to give a 9.7wt% tin dopant concentration. Typically, indium tin oxide is doped 10% tin oxide to 90wt% indium tin oxide, this shows that the material is doped to the correct concentration and is of good quality.

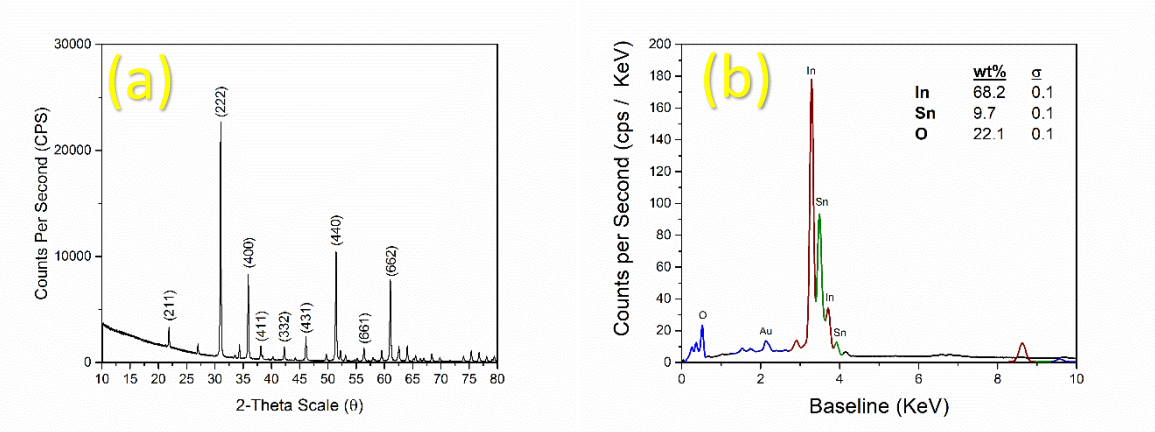

Figure 43 ITO Starting Materials Characterisation showing (a) x-ray diffraction pattern of ITO powder and (b) energy dispersive x-ray analysis of ITO

5.2.2 Gallium doped Zinc Oxide (GZO) Via Continuous Hydrothermal Flow Synthesis

Gallium doped Zinc Oxide powders synthesised via the continuous hydrothermal flow synthesis method described in Chapter 3 were also used as conductive fillers. As discussed in Chapter 3, GZO is a promising replacement material for ITO due to similar resistivity and transparency values while also being less expensive. The continuous hydrothermal flow synthesis process allows for high throughput synthesis of nano-powders which would otherwise be difficult to produce on large scales. Limitations of this method however are a

reduced ability to manipulate particle size and shape. Particles of GZO manufactured via CHFS can be seen in Figure 44(a). With X-ray diffraction data shown in Figure 44(b).

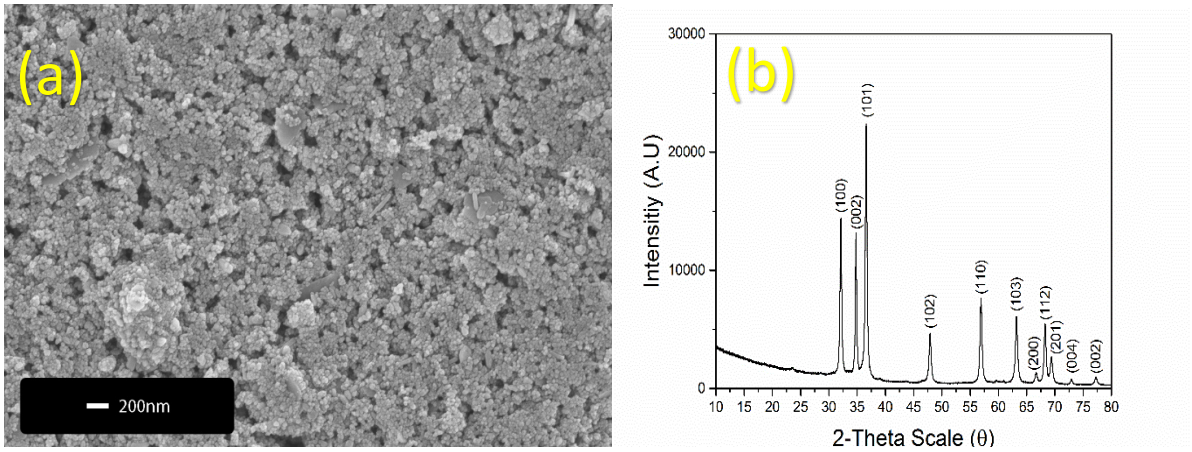

Figure 44 Analysis of GZO Powder via (a) FEG-SEM Image of GZO and (b) X-ray diffraction pattern of GZO powder

Previous research into the GZO has suggested a 2% Gallium Oxide (Ga_2O_3) doping into 98% Zinc Oxide (ZnO) is optimal for the highest conductivities [278]. Gallium doped zinc oxide typically has a cubic hexagonal crystal structure and as a degenerate n-type semiconductor relies on oxygen vacancies acting as electron holes for conductivity. This crystal structure creates stability issues in oxygenated atmospheres as further oxidation of the material can reduce electrical conductivity. The powder x-ray diffraction spectrum for CHFS process GZO shown in Figure 44(b). From the XRD data, the unit cell volume can be calculated. The unit cell volume calculated from the diffraction pattern was determined to be 58.61Å3, which is larger than the undoped zinc oxide unit cell volume of 54.93Å3. This difference can be accounted for with the replacement of a zinc ion, in the unit cell with a gallium ion and suggested the material is indeed doped.

Elemental analysis of the gallium doped zinc oxide powder was performed using energy-dispersive X-ray spectroscopy (EDX/EDS). Combining this technique with scanning electron microscopy, dopant concentrations, dopant location on the material and impurities can be determined. For the EDX analysis, GZO powder was dispersed at 50w/w% into a nitrocellulose-based vehicle and a thin film was coated onto soda lime glass. The sample was then sputter coated with a gold/platinum alloy to create a conductive film which would allow for scanning electron microscopy. The sample was then loaded into a Field Emission Gun Scanning Electron

Microscope (Leo 1530 VP) and three 100x100μm sample area images were taken as shown in Figure 45(a-b).

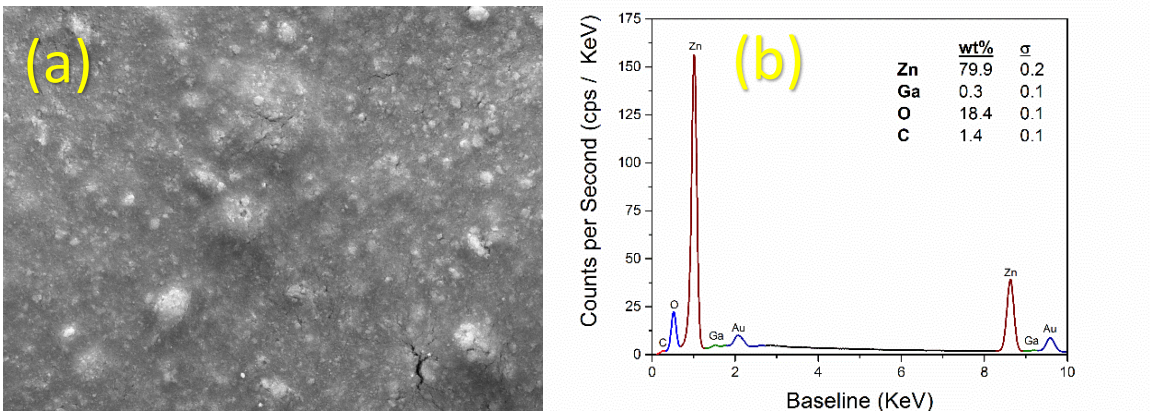

Figure 45 (a) EDX Image of CHFS GZO Powder and (b) EDX Spectrum

Energy-dispersive X-Ray analysis was then performed on the three imaged areas to determine the Gallium, Zinc, Oxygen and Carbon concentrations and to detect impurities. It is important to note that although EDX is a powerful elemental analysis technique. Gallium and Zinc are neighbours in the periodic table meaning the large percentage of Zinc Oxide in the powder may overlap with the gallium peaks, giving the appearance of a lower concentration of gallium in the powder. The elemental weight percentages of each element for each spectrum are shown in Table 4. Removing carbon impurities gives a total Gallium dopant percentage of 0.355wt% which is far from the literature optimal value 2% indicating that the bulk conductivity of the material may not be as high as theoretically possible. The powders are still doped however this data suggests that although the CHFS process is high throughput, the methods ability to dope is lacking.

Table 4 Elemental Analysis Data for CHFS GZO Powder

Element	Spectrum 1 / wt%	Spectrum 2 / wt%	Spectrum 3 / wt%	Average / wt%
Zinc	79.90	73.90	75.41	76.40
Oxygen	18.40	19.63	18.61	18.88
Gallium	0.30	0.43	0.30	0.34
Carbon	1.40	6.04	6.13	4.52

With carbon impurities removed, the total makeup of the sample is 79.90% zinc, 19.75% oxygen and 0.35% gallium. Particle size analysis was performed on the GZO nano-powders using a Malvern Instruments Zetasizer. Small amounts of powders were dispersed into methanol via ultrasonication. The dispersion is then placed into a cuvette and into the zetasizer measurement system. The distribution is very narrow suggesting the bulk powder has a uniform particle size. However, the particle size is larger than the typical 25 – 100nm the CHFS process usually creates. The particle size analysis gives a mean particle size of 114nm which can be compared to the SEM image in Figure 44(a). The microscope images suggest particle sizes are between 30 - 70nm. Showing a discrepancy between the two techniques. Research has shown that when a particle is smaller than the wavelength of light used to analyse it, an artefact called “double diffraction” can occur [279]. This double diffraction is detected by the measurement equipment as a doubling in size of the particles. When this is considered, the true particle size is 57nm, which matches the analysis of the SEM image.

5.2.3 Gallium doped Zinc Oxide (GZO) Via Microwave Synthesis

Gallium doped zinc oxide powders were fabricated using the methods described in the literature [280]. Gallium oxide and zinc oxide precursors are mixed into polyethylene glycol (PEG), the polyethylene glycol is a good microwave absorber leading to good microwave radiation absorption for the mixture [281]. This mixture is then placed into a reaction vessel and purged with argon to remove any oxygen. The yield of powders increases with molar concentration of precursors. However, this increase in concentration also increases the particle size of the material as the probability of nanoparticles interacting to fuse together increases. To get a meaningful yield of powders (approximately 15g for 1 week of manufacturing) a particle size of 500 - 1000nm was fabricated. The mixture was reacted in the microwave (Anton Paar Microwave System) at 500W for 2 hours and was kept at a pressure of 23bar. The mixture was then decanted into centrifuge tubes to separate out the TCO powder and the powder was washed and centrifuged with methanol 3 times. The powder was then collected through a vacuum-assisted Buchner funnel and placed into sample tubes. Scanning electron microscope images were taken of the resulting powder and these can be seen in Figure 46.

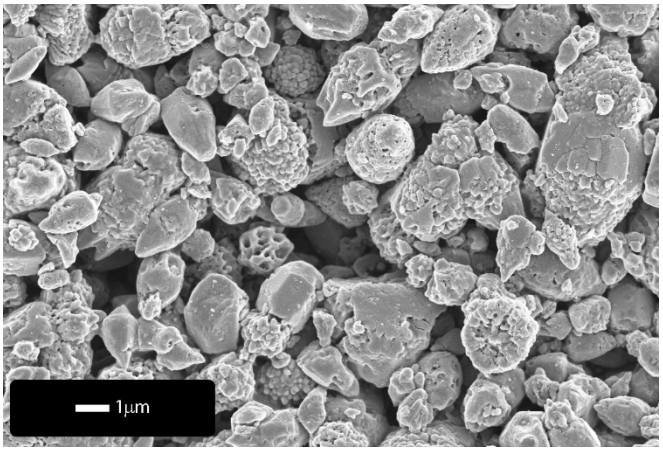

Figure 46 SEM of MW GZO Powder

As can be seen in the SEM image of the microwaved GZO powder, there is a large mix of particle sizes formed by the process. Most crystals also appear to have the cubic hexagonal structure zinc oxide materials typically have. This material was fabricated to have a 2% gallium oxide to 98% zinc oxide doping level.

Powder X-Ray Diffraction was performed on the MW GZO powder providing a similar pattern to the CHFS GZO, showing the material fabricated is indeed a zinc oxide.

EDX analysis was performed on vehicle dispersed microwave synthesised gallium doped zinc oxide films with 100x100μm SEM analysed areas shown in Figure 47(a). The sample was prepared via the method described in F 4.

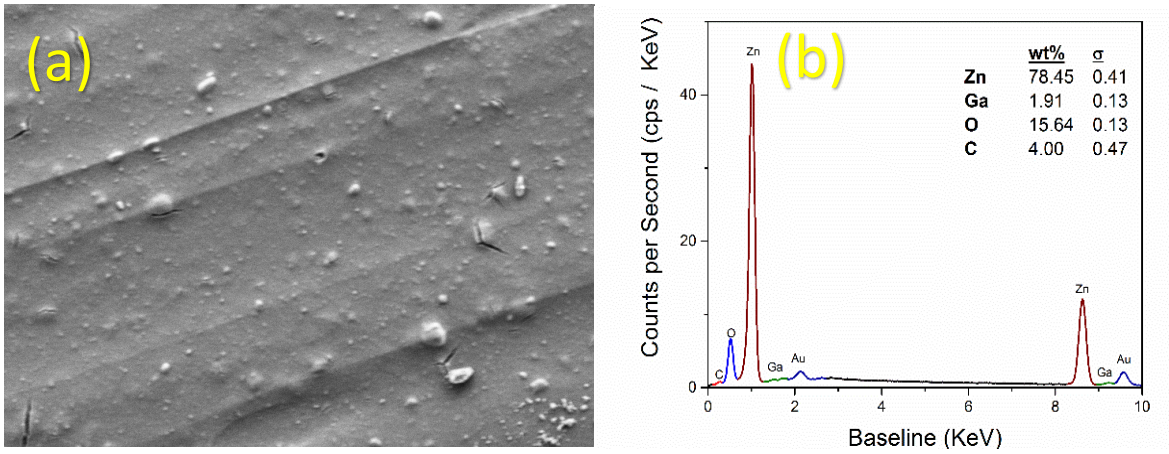

Figure 47 (a) EDX Image of MW GZO Powder and (b) Elemental Analysis for MW GZO Powder

EDX spectra can be seen in Figure 47(b). The data shows that the doping quality of the microwaved powders is improved over GZO synthesised via the CHFS process. The target doping level was 2% and an average of 1.74% has been obtained.

With carbon impurities removed, the total makeup of the sample is 82% zinc, 16.18% oxygen and 1.82% gallium. This data shows that the microwaved synthesised GZO powder has the correct level of doping for optimal conductivity and it should perform well electronically. Carbon impurities makeup an average of 3.9% of the film, this corresponds with the impurity levels found in other powders.

Particle size analysis was performed on the GZO nano-powders. The analysis gave an average particle size of 573nm. The large distribution between 300 – 900nm corresponds with the SEM images of the powders. However, in the SEM images a small number of larger particles are seen in the 1 – 5-micron region. These larger particles are most likely the result of particle fusion because of heat treatment in the SEM films. The particles in this case are large enough to be free of error created by double diffraction of light.

5.2.4 Aluminium/Gallium doped Zinc Oxide (GZO) Via Microwave Synthesis

Aluminium/Gallium doped Zinc Oxide materials were synthesised using the process described in Section 5.2.3. An aluminium based precursor is added to the mixing solution and concentrations were calculated to produce a 1% gallium, 1% aluminium doped zinc oxide powder at a 1-micron particle size. An SEM image of the material can be seen in Figure 48 with a similar particle size distribution to the MW GZO.

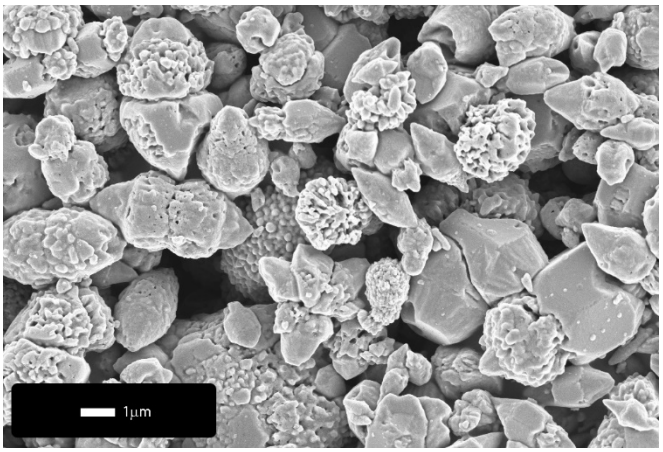

Figure 48 SEM of MW AGZO Powder

The XRD data shown in Figure 49(a) again shows synthesis was successful with zinc oxide being made. As can be seen in Figure 49(b), the EDX spectra shows lower than expected dopant concentrations. However, EDX cannot penetrate far into large particles so it is possible the missing material is a sign the doping is not only surface level.

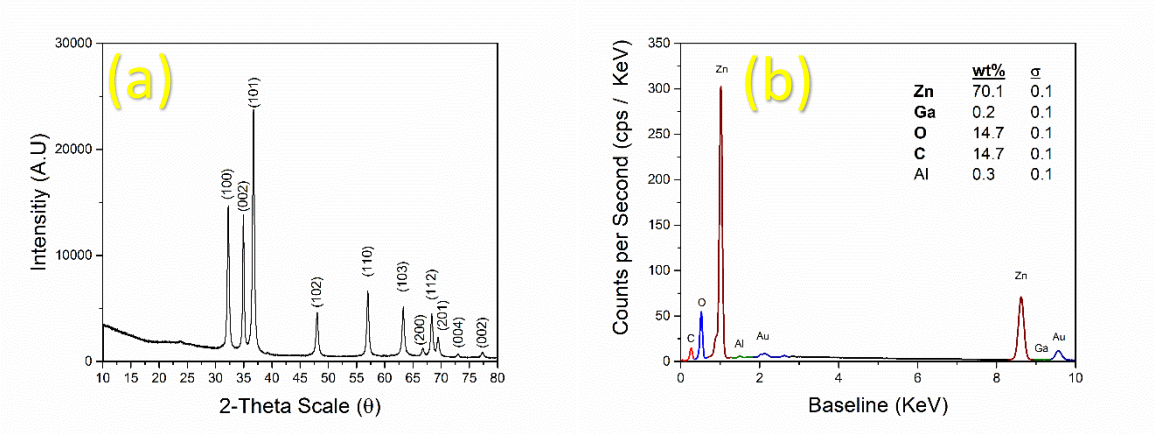

Figure 49 (a) XRD of MW AGZO Powder and (b) Elemental Analysis for MW AGZO Powder

5.2.5 Bulk Resistivities of Conductive Filler

When printing a material, the bulk resistivity of the material is required to determine the maximum conductivity which can be attained. An optimised conductive ink will have a printed resistivity value as close to the value of the bulk as possible while also maintaining good printability. The bulk resistivity value of each powder was taken by making a solid pellet of material, sintering it at the recrystallisation temperature required and then dividing the sheet resistance of the pellet by the thickness of the sample.

Each pellet of material was fabricated by placing a small amount of powder into a pellet die. This die is then placed into a manual hydraulic press (Specac) as shown in Figure 50(a-b). The press is then pumped until the die is under 10 metric tons of pressure and is then left for 1 minute. After one minute of the die being pressed, pressure is relieved, and the pellet is removed from the press.

Figure 50 Pellet making equipment with (a) pellet die and (b) hydraulic press

After the pellets are removed they are then microwave sintered at 650^{O}C. For microwave sintering, the pellets are sandwiched between two silicon carbide tiles which have a high microwave absorption coefficient. The pellets as shown in Figure 51 and the silicon carbide tiles are then placed into the centre of a research grade microwave system (BP-210, 2100W, Microwave Research Applications). The microwave radiation is then absorbed by the carbide tiles transferring the energy into the pellets for sintering. The pellets are removed, and sheet

resistance measurements are taken using a Jandel HM20 four-point probe system. Pellet thickness data is collected using digital Vernier callipers.

Figure 51 Microwave sintered metal oxide pellets

To calculate the bulk resistivity, ρ, in the standard units of Ω.cm, Equation 8 must be used:

$$\rho = R_s T$$

Equation 8 Calculation of Bulk Resistivity

Where R_S is the sheet resistance of the material in ohms per square and T is the thickness of the sample. For each conductive filler material, pellet sheet resistances, sample thicknesses and bulk resistivity values can be found in Table 5.

Table 5 Bulk Resistivities of Conductive Fillers

Conductive Filler	Sheet Resistance	Sample Thickness / cm	Resistivity / Ωcm
Indium Tin Oxide	82.78 $m\Omega\square^{-1}$	0.085	7.04×10^{-3}
GZO (CHFS)	1.516 $\Omega\square^{-1}$	0.095	1.44×10^{-1}
AGZO (MW)	2.893 $\Omega\square^{-1}$	0.09	2.60×10^{-1}
GZO (MW)	210.82 $m\Omega\square^{-1}$	0.105	2.21×10^{-2}

The most conductive material is the indium tin oxide at 7.04×10^{-3} Ω.cm which is to be expected. The AGZO material is less conductive than the both gallium doped zinc oxide powders. This is likely due to the long-term stability issues of co-doping aluminium and gallium. Aluminium is known to leech out of zinc oxides giving lower conductivities over time [282]. The CHFS GZO is also conductive suggesting doping inconsistencies discussed in this chapter can be mitigated for in printed variants with a suitable post processing method.

5.3 Vehicle Materials

5.3.1 Vehicle Overview

In the previous section, four chosen TCO materials were characterised in powder form (the filler and dry component of the ink). For ink formulation, as discussed in Section 2.5.3, a suitable vehicle (the wet component of the ink) needs to be selected. In this section, a breakdown of the three vehicles to be used for the dispersal of conductive filler is given. The first vehicle (Vehicle A) is a commercially available polymeric binder from Gwent Electronic Materials (R2070613P2) developed for screen printing with electro-ceramic materials. The second (Vehicle B) is a nitrocellulose-based vehicle provided by an industrial sponsor which uses the crosslinking nature of nitrocellulose to create highly dense, highly packed printed films. This nitrocellulose-based vehicle uses a mixture of 11.5% nitrated cellulose as a binder and alpha-terpineol and methoxyethanol as solvents. The third vehicle (Vehicle C) is a self-developed formulation based off published literature utilising an alkyd resin binder and provides more flexibility for optimisation.

5.3.2 Vehicle A (Commercial R2070613P2)

A main issue of using a commercially procured vehicle system is that components are trade secrets and are not available for dissemination. An overview of the vehicle is that this polymeric binder is suitable for screen printing pastes, the vehicle is slightly shear thinning changing from 330mPas to 150mPas over a 0 – 230s^{-1} shear rate range and the optimal drying temperature is 130^{o}C for 10 minutes. The polymeric solids content of the vehicle is 36-39% and it is originally designed to print electroluminescent phosphor pastes onto sputter coated indium tin oxide material. Due to this, the vehicle is compatible with metal oxides. The main use of this vehicle will be as a standard, to compare the other vehicles to a commercially available resin.

5.3.3 Vehicle B (Nitrocellulose)

Vehicle B is a nitrocellulose based premade vehicle supplied by an industrial partner. A sought-after property of resins for printed electronics is the ability for the vehicle to crosslink and increase packing density [39]. This crosslinking occurs when functional reactive groups on the polymer undergo further reactions under temperature. As can be seen in Figure 52, the

nitrocellulose monomer unit has branching N^+ - O^- groups along the chain which react together under heating, fusing the monomer units together and creating a densely packed polymer network. With a conductive filler, this crosslinking process pulls resin coated particles together into a densely packed film, enhancing electrical conductivity.

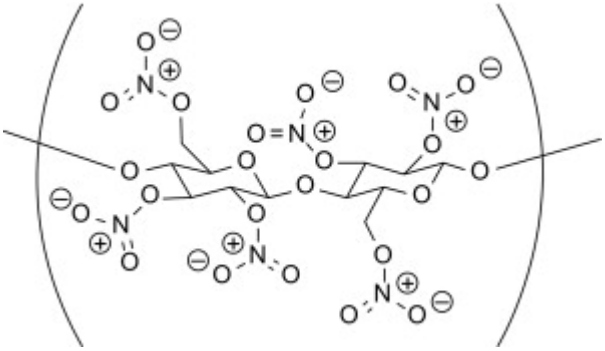

Figure 52 Nitrocellulose Monomer Unit [286]

Nitrocellulose is commonly referred to a guncotton as it is highly explosive above a 13% nitration level of cellulose. The nitrocellulose used here is 11.5% nitrated, giving it the highly reactive properties required for packing the films together while also keeping any inks formulated safe for industrial use near heat. The vehicle also contains terpinol, an oil molecule commonly found in plant oils and acts as a thinner and dispersant for the nitrocellulose resin. Iso-propoxy-methanol is used as the thinning agent and solvent. Polymeric solids content is between 10-30% and the viscosities were measured to be between 380 and 50mPas from 0 to 251.8S-1, indicating that it has non-Newtonian behaviour. This vehicle is manufactured on industrial scales for a wide variety of conducting materials and will be used to give the materials the best possible chance to conduct. Good results with this vehicle will also demonstrate that these materials can be scaled up for industrial processes.

5.3.4 Vehicle C (Alkyd Resin)

As sustainability is an increasingly important factor in printed electronics, a resin was chosen which could potentially be sourced from biological sources. Alkyd resins of differing alkyl chain lengths are typically sourced for ink and paint formulation from Flax (linseed oil), walnuts (walnut oil) or poppy seeds. The particular alkyd resin used for this research is Fischer Scientific Alkyd Resin (70wt%, pure solution in xylene). Following published variations of alkyd resin-based vehicles, Exxon Mobil Flashprint M71a was chosen to be the solvent. This solvent is an

industrially used printing ink solvent and it a high-grade kerosene which is compatible with ceramics. To assess the drying and printability of this vehicle, a study will be performed in Section 5.4.

5.3.5 Additives

For this research two additives will be selected, the first being a curing additive and the second being a surfactant for the avoidance of agglomeration and to aid in ink stability over time. The curing additive to be selected is Eugenol, this is an organic aromatic compound, which is synthesised naturally as an oil in cloves, enabling a sustainable biological source for the ink vehicle. The eugenol acts as an antioxidant, readily oxidising itself in air. This can protect the rest of the wet ink from being oxidised first and acts as an anti-curing additive, enabling the wet ink to stay printable in a screen printer for a longer time. The second additive, the surfactant was chosen to be sodium dodecyl sulphate (SDS). This is a common anionic surfactant, which is typically compatible with metal oxide materials due to the oxygen in the crystal lattice creating a metal – oxygen dipole, enabling the SDS to stabilise surface charge and prevent agglomeration. In the literature, SDS has been shown to be compatible with both zinc oxide and indium tin oxide materials in making suspensions.

5.4 Vehicle and Material Compatibility and Choice

5.4.1 Overview

In this section, three vehicles (A, B and C) will be used for the dispersal of conductive filler and then film densification and conductivity of the screen-printed films are used as criteria for selecting a single suitable vehicle for the remainder of the research. To decide which vehicle has the best properties for printing with metal oxide materials and to determine which metal oxides perform the best a series of studies are performed. Firstly, a series of print quality tests are made with varying formulations of vehicle C in order to optimise it for ink formulation. Then, on the final vehicle C formulation, a curing study is performed in order to determine the correct processing temperatures for printed films. Each vehicle is then tested with a single metal oxide material, curing at different temperatures to determine which one provides the highest conductivity. Scanning electron microscope (SEM) imaging this then performed to analyse film densification caused by each vehicle and to see if this correlates with the conductivity data. The best performing vehicle is then selected for preliminary ink formulation with each metal oxide material. Optical and electrical properties are analysed for all four materials. Two final materials are selected, the one with the highest conductivity and the one with the best performing optical properties.

5.4.2 Optimisation of Vehicle C

Both vehicle A and B are pre-mixed and ready to use, they only require the addition of TCO powder and surfactants / solvents. The investigation for formulating inks was to determine the optimal ratio of solvent to resin in Vehicle C. For this, the quality system designed in Section 4.5.4 – the printing quality of a range of vehicle C based inks was assessed. Prints (13μm thick) were made onto both treated and untreated variants of Melinex ST504 (heat stabilised PET film). The percentage of M71a in vehicle B was altered to change the viscosity of the ink without changing the weight percent content of the filler (75% ZnO for all – AGZO not used for printing assessment).

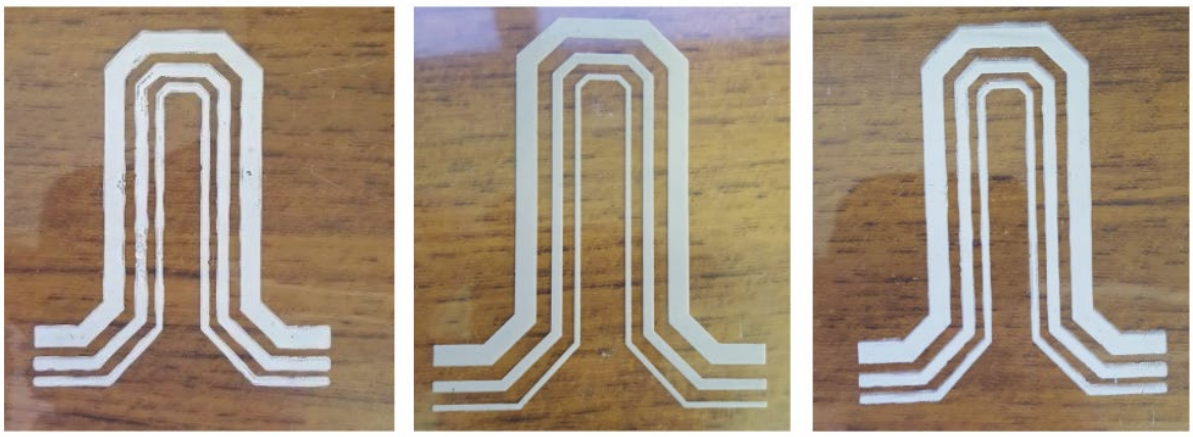

Figure 53 Printing Quality with varying solvent, (a) 40wt%, (b) 20wt%, (c) 0wt%

Between 0 and 10wt% of vehicle containing M71a solvent was used (Figure 53, c) with prints scoring between 0 and 2 on the assessment scale. Inks were too thick to print properly and when they did, ink bleeds out of the lines. Low amounts of solvent in the ink led to long clean up times with particles being stuck in polyester screens. Large amounts of solvent in the vehicle, between 30 – 40wt% (Figure 53, a) created less viscous inks printing in the range of 1 – 3. Particle coverage was good, but ink bleed was high due to high solvent content. The only vehicle variant that consistently gave 3s and 4s on the assessment scale was between 10 and 30wt% solvent (Figure 53, b).

A solvent ratio of 80% Vehicle C to 20% M71a thinner was optimal for high printing quality. After the best ratio was determined, it was required to determine the solvent and binder burn off characteristics for the vehicle curing. For this thermogravimetric analysis was performed on the inks and can be seen in Figure 54.

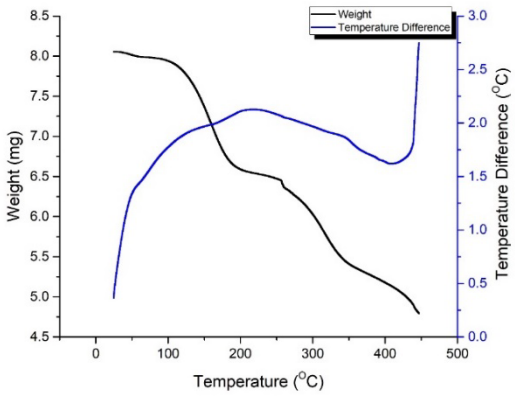

Figure 54 Thermogravimetric Analysis of Vehicle C

As can be seen in Figure 54, looking at the weight versus temperature of the ink displays the curing properties. At 190^{o}C there is a weight drop suggestive of a solvent evaporation taking place. The second drop is gradual and happens at approximately 350^{o}C shows resin burn off. Optimal curing for conductive inks on flexible substrates should occur much lower than these values considering heat stabilised polymer sheets can be used up to a maximum of 250^{o}C.

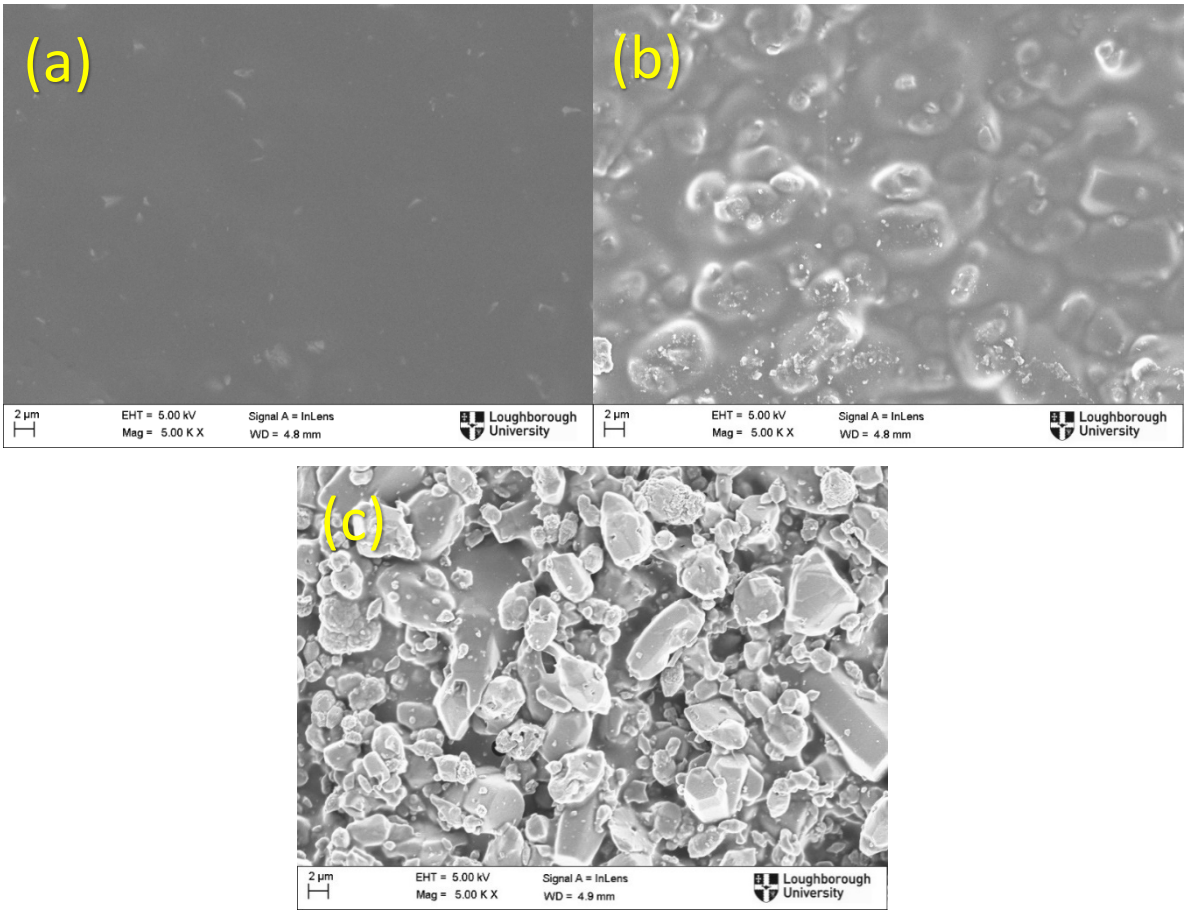

Figure 55 SEM Images for MW AGZO in Vehicle C cured at (a) 150^{O}C, (b) 250 ^{O}C and (c) 350 ^{O}C

The SEM images shown in Figure 55(a-c) where taken on an MW AGZO ink formulated with vehicle C at 150 – 350^{O}C to confirm the solvent and resin burn off. As can be seen in Figure 55(a), at a temperature before full solvent evaporation occurs, there are no details to be seen in the film. This lack of detail and ability to see the particles shows that the particles are covered by a wet layer, in this case the solvent. In Figure 55(b), after solvent burn off particle features can start to be seen, confirming the interpretation of thermogravimetric analysis. The particles appear to have a layer of resin coating them suggesting the polymer content is too high. However, as seen in Figure 53, when polymer content is reduced by thinning with solvent, print quality decreases drastically. At 350^{O}C in Figure 55(c), particles can finally be fully

distinguished in a compact film at a temperature much too high for use in printed electronics. This data suggests vehicle C, may be suitable for other applications such as paints, it is not compatible with the features required for conductive ink formulation.

5.4.3 Effect of Vehicles on Conductivity and Film Densification

In order to select the best vehicle for the metal oxide fillers, microwave synthesised AZGO was selected as the filler, inks were then made with each vehicle varying the conductive filler with data shown in Figure 56. Vehicles A, B and C were all used for this study. Vehicle C is still used although the previous section has shown it is not entirely suitable in order to gain a more complete understanding of why it is not suitable. AZGO was selected as the 1-micron particle size is small enough to not be altered by the three-roll mill and too large for fast agglomeration, allowing for the assessment of any particle size changes the vehicles may alter. Vehicle A, the commercial standard, did not have any conductivity or reach percolation until 60wt% filler was achieved.

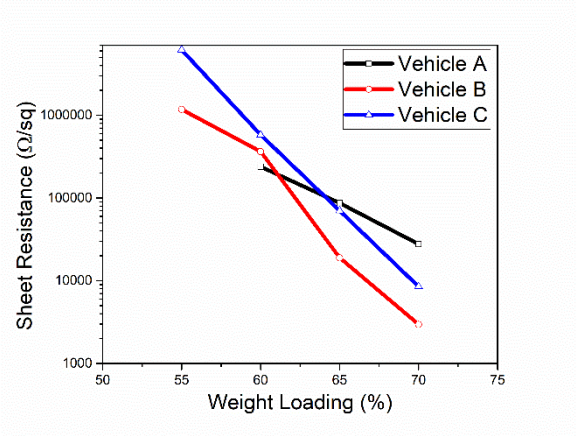

Figure 56 MW AGZO Weight Loading versus Sheet Resistance for each vehicle

Both vehicle B and C displayed percolation at 55wt% with vehicle B providing the best conductivity at higher weight percent values. The three cured vehicles with MW AGZO fillers were imaged with SEM and can be seen in Figure 57. Information about crosslinking quality can be determined from the images. Figures 57 (a) and (b) appear to have highly uniform particle sizes at equal spacings. Particles do not appear to be tightly packed showing that vehicle A has poor crosslinking ability and therefore further studies will not improve

conductivity, this conclusion is reinforced by data shown in Figure 56 which shows curing temperature versus sheet resistance for the vehicle.

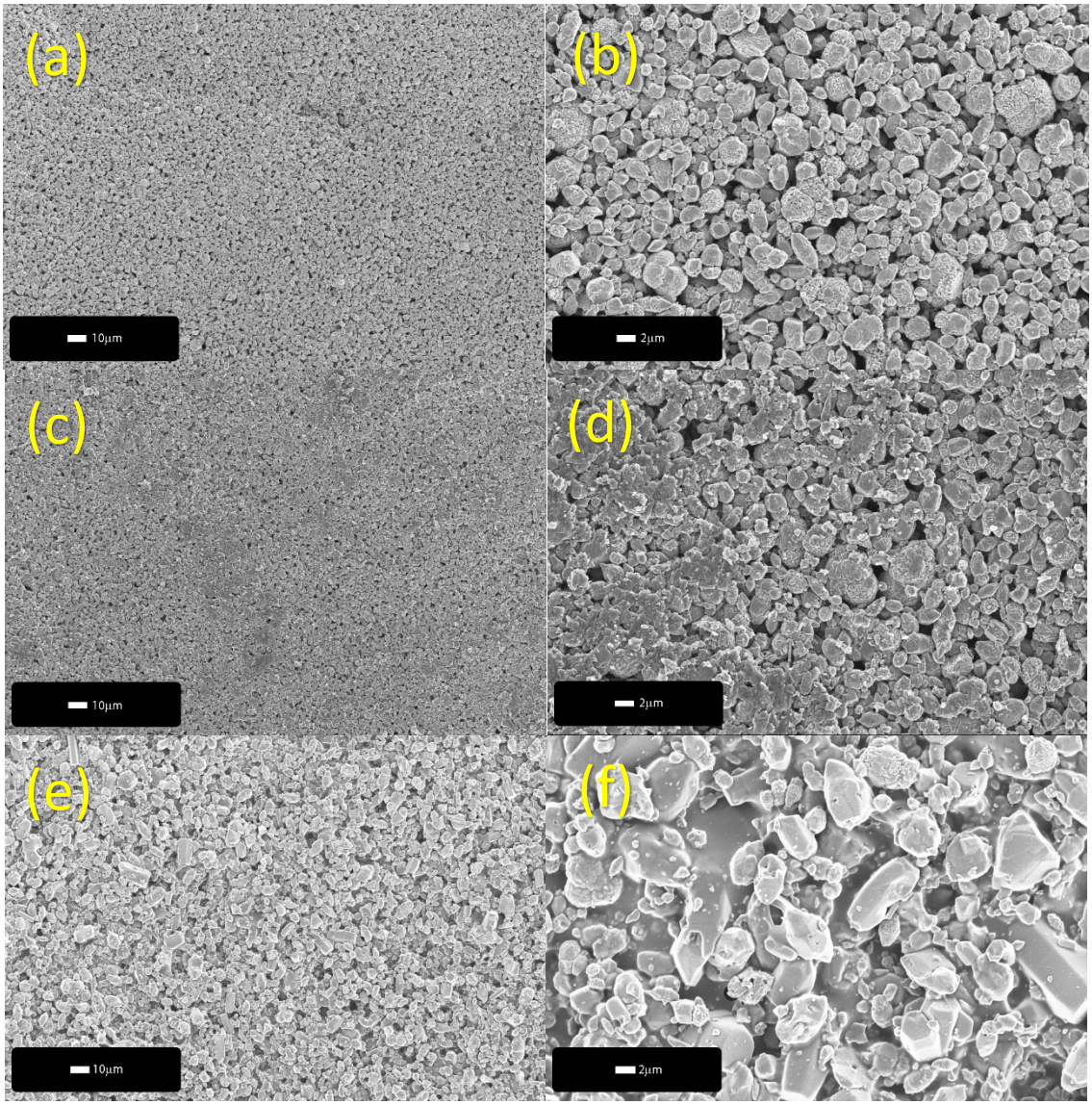

Figure 57 Scanning Electron Microscope Images of cured MW AGZO with (a) Vehicle A (b) Vehicle A, (c) Vehicle B, (d) Vehicle B, (e) Vehicle C and (f) Vehicle C

Vehicle B displays the best film densification ability, as can be seen in Figure 57 (c) and (d) large sections of particles appear to be crushed together, which shows that the vehicle has crosslinked and pulled the particles together. This, including the conductivity data suggests vehicle B is the best vehicle to proceed with metal oxide ink formulation and will be selected for further investigation with each metal oxide material.

As vehicle B has been selected further materials characterisation was performed in order to confirm curing properties and binder quality. To measure the curing profile of the

nitrocellulose based, thermogravimetric analysis (TGA) and differential scanning calorimetry (DSC) was performed. The nitrocellulose vehicle is placed in an Alumina crucible and onto a platinum balance, with a second reference crucible for DSC measurements. The reference crucible is filled with a similar weight to the nitrocellulose in alpha phase alumina. Initially, a temperature scanning range of 25 to 250°C was selected, however, at these temperatures the material fused and destroyed the alumina crucibles, most likely due to alpha-terpineol having an unintentional reaction. Further tests were performed to 150°C, the ramp rate selected was 1°C per minute to provide ample resolution and three replicates were measured. Samples were measured in an air atmosphere to simulate real processing conditions and data is shown in Figure 58(a). From the TGA data, it can be that weight loss drops dramatically between 75 and 105°C, with weight loss stabilising into general evaporation after this point, confirming the standard curing temperature for the vehicle. The DSC data also shows a relatively broad exothermic release of energy at the same point, which is most likely due to the nitrocellulose crosslinking, as polymer crosslinking reactions are generally exothermic and do not occur at a single temperature. The cured vehicle was then analysed via x-ray photoelectron spectroscopy to determine the organic bonding in the cured polymer, data is shown in Figure 58(b).

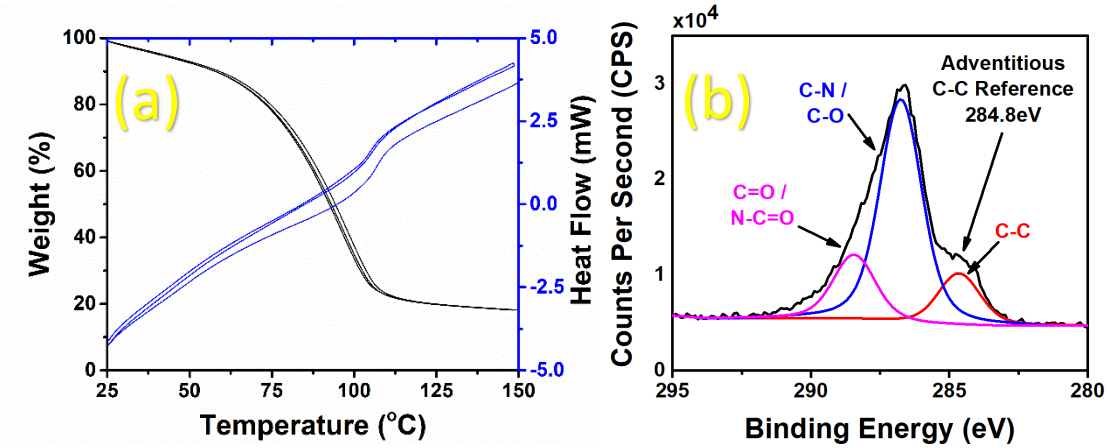

Figure 58 Analysis of Selected Vehicle B via (a) Thermogravimetric Analysis and Differential Scanning Calorimetry and (b) X-ray Photoelectron Spectroscopy

The bond information supplied by the XPS shows a mixture of C = O, N-C=O, C- and C-O bonds for the cured vehicle confirming a change from the original monomer unit described in Figure 58(b). This provides evidence that crosslinking does occur as expected via the formation of nitrogen carbon bonds.

5.4.4 Selection of Metal Oxides for Further Investigation

In the previous section, vehicle B was determined to be the most suitable vehicle. In this section, each of the four metal oxides fillers discussed in Section 5.2 will be formulated into inks with vehicle B. By varying the filler only, information on the conductivity of each material in ink form can be determined. For this study, the weight loadings of each metal oxide were varied from 50% weight loading to the maximum weight loading that could be achieved with still printable rheology. In Figure 59(a) the percolation thresholds for each material can be seen, with sheet resistances being taken from films made with a 12μm wet thick film k bar coaters to simulate a typical screen-printed film thickness. CHFS GZO was the worst performing material with no conductivity observed for any weight loading. Both microwave synthesised zinc oxide materials did show some conductivity, with AGZO performing better than GZO, however, worse than ITO which provided unoptimized sheet resistances between 177.4 to 625.23$\Omega\square^{-1}$between 60 and 75wt% with the 70wt% providing 3.05% of bulk conductivity. Above 75wt%, both the ITO and MW GZO displayed increases in sheet resistance. This phenomenon can be attributed to an increase in filler material loading, lowering the packing density of the film creating a less conductive network than expected. The optical transparencies for each printed material can be seen in Figure 59(b). For screen printed samples both types of GZO had the highest transmittance values with MW GZO peaking at 31T% and CHFS GZO reaching a maximum of 52%T. The ITO and MW AGZO are both below 5T% across the spectrum.

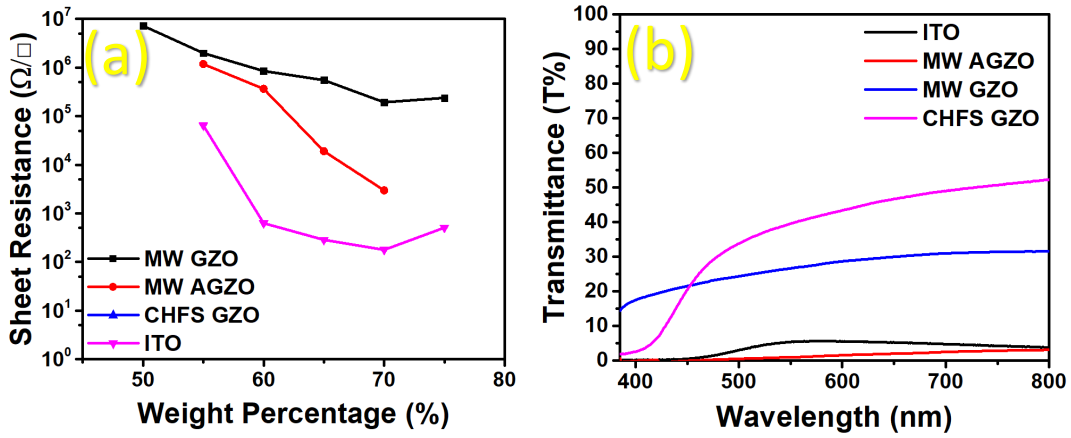

Figure 59 Preliminary Ink Formulation Data for (a) Sheet Resistance versus Weight Percent Loading of Filler and (b) UV/VIS light transmission data for each ink

Taking this into account with the conductivities obtained, the GZO and the ITO will be selected for further investigation. The GZO, is chosen in order to research the optical properties of the material and while the ITO is chosen in order to exploit the relatively high conductivities. As the main focus of this work is to create conductive inks, a design of experiments will be performed on the ITO to investigate the main factors contributing to conductivity and the reproducibility of printed conductive films. For the GZO ink formulation, a study will be performed investigating the effects of weight loading and film thickness on the transparency of films. An investigation into whether adding a secondary conductive material to the GZO alters the electrical properties will be investigated to determine the potential of conductive transparent films.

5.5 Ink Formulation with CHFS GZO

5.5.1 Overview

During preliminary ink formulation studies in the previous sections, gallium doped zinc oxide (GZO) films were found to be the most transparent. As GZO is an n-type semiconductor with a bandgap, highly transparent films of this material may be useful in future applications, especially if conductivity can be induced in post processing studies. In this section, GZO inks between 50 and 70 weight percent are formulated and a weight loading / film thickness versus transparency study is undertaken. Due to the nanoparticle GZO, formulations above 70% could not be manufactured as the rheology became too thick for proper dispersion, even with SDS surfactant.

5.5.2 Materials and Methods

The continuous hydrothermal flow synthesised gallium doped zinc oxide discussed in Section 5.2, is used as the conductive metal oxide. This is dispersed into a nitrocellulose-based vehicle consisting of 11.5% nitrated cellulose, 2-isosproxyethanol and alpha terpineol. The solvent used to thin the ink was also 2-isopropoxyethanol (Sigma Aldrich, 99%). The two additives used were eugenol (Sigma Aldrich, 99.9%) and sodium dodecyl sulphate (SDS, Sigma Alridch, ACS Reagent >99.0%). Samples were printed onto soda lime glass (Thermofisher) using kbar coating tools rated to provide 4 to 100μm wet films.

5.5.3 Transparent GZO Formulations

Transparent GZO ink formulations investigated in order to determine the relationship between weight fraction of TCO to transparency in a printed TCO film. Inks were fabricated at varying weight fractions of GZO with vehicle B and printed via k-bar coating tools at different thicknesses to determine the effect of weight loading and print thickness on the transparency. As can be seem in Figure 60(a-c), there is a small trend of decreasing transparency with an increase in weight loading, however, the difference at the peak is only 4%. GZO 4um films at 50 weight percent show over 84% transmittance. A bandgap absorption can be seen in the UV region of the films, observed by the large decrease in transmission. This bandgap absorption does not appear to be altered by any thickness or weight loading change.

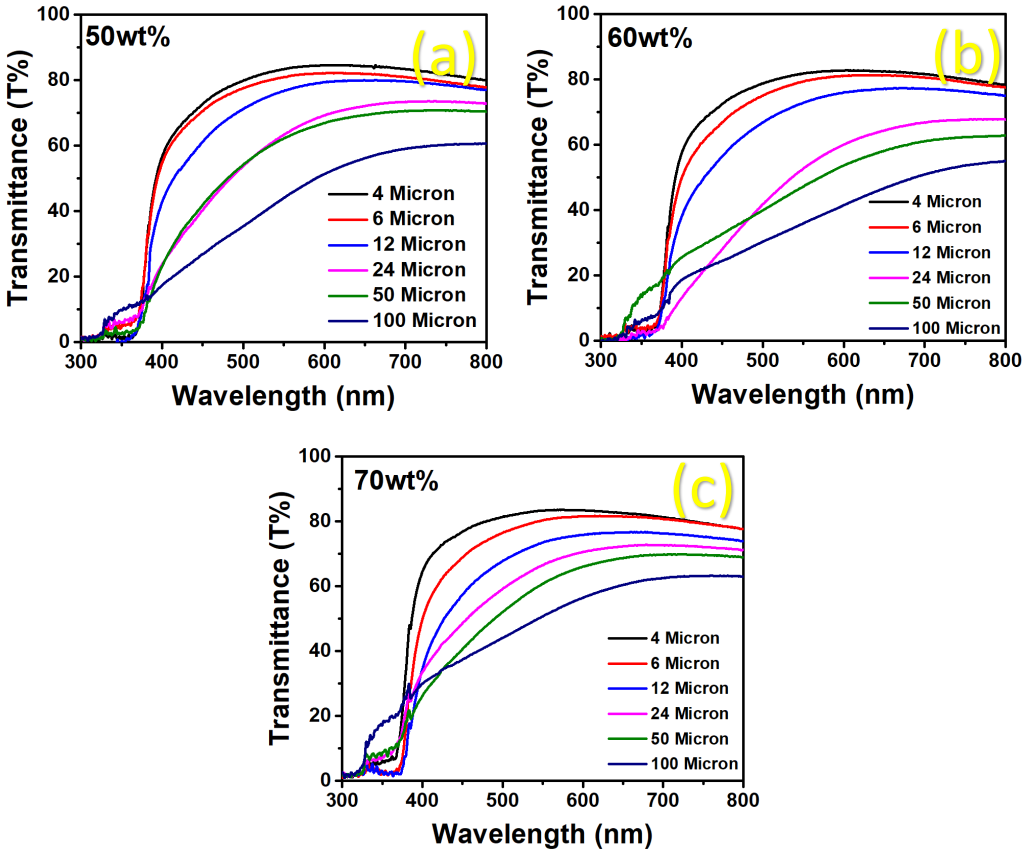

Figure 60 Transparency for GZO printed films at varying film thicknesses for (a) 50wt%, (b) 60wt% and (c) 70wt% inks

An increase in haze with increasing film thickness can be observed. Generally, an increase in the shallow decrease of transmittance with wavelength can be attributed to scattering from haze. Thicker films are less transparent and hazier as there is more material to scatter, reflect

and absorb photons, increasing the opaqueness to the human eye. With these measurements, it has been demonstrated that highly transparent, semiconductor metal oxide films can be printed and retain transparency. However, there is no way to further optimise this material as there is no conductivity observed. A future chapter will investigate a suitable post processing method for this material to determine whether any conductivity can be obtained from the GZO.

5.6 Ink Formulation with Indium Tin Oxide

5.6.1 Overview

Preliminary indium tin oxide (ITO) inks researched in earlier sections provided the highest conductivity levels of any of the metal oxides, with conductivity levels in ranges where printed electronic applications can be developed. This section focuses on investigating the effects of the ink components, printing and processing on the final conductivity of ITO printed films. The main experimental methodology used in the section to do this is the Taguchi L8 experimental design framework. Here, the contribution of seven factors to conductivity, optical and rheological properties and repeatability are assessed so the best ink can be chosen for developing printed electronics applications.

5.6.2 Materials and Methods

Commercial indium tin oxide (ITO, Alfa Aesar, 99.9%) as discussed in Section 5.2, is used as the conductive metal oxide. This is dispersed into a nitrocellulose-based vehicle consisting of 11.5% nitrated cellulose, 2-isosproxyethanol and alpha terpineol. The solvent used to thin the ink was also 2-isopropoxyethanol (Sigma Aldrich, 99%). The two additives used were eugenol (Sigma Aldrich, 99.9%) and sodium dodecyl sulphate (SDS, Sigma Alridch, ACS Reagent >99.0%). Samples were printed onto soda lime glass (Thermofisher) using kbar coating tools rated to provide 4 to 50μm wet films. Films printed with 100μm wet film thickness were could not be reliably measured to a difference in rheology and the ITO inks being much thinner than the GZO inks. Wet films could not be made consistently, and prints were not uniform enough for reliable UV/Vis analysis.

5.6.3 Conductive ITO Formulations

Conductive ITO ink formulations were fabricated at varying weight fractions of ITO with vehicle B and printed at different thicknesses via k-bar coating tools to determine the effect of weight loading and print thickness on the conductivity and optical properties of the films. Films of ITO were printed using K-bar coaters providing wet film thicknesses of 4, 6, 12, 24 and 50 microns. Firstly, UV/VIS spectroscopy (Perkin Elmer, Lambda 35) was performed on the samples between 800 and 300nm using a reflectance standard (spectralon, 99.9%). As can be seen in Figure 61, from 65 to 75 weight percent, transparency decreases as expected with a

larger jump between 65 and 70 than between 70 and 75. All samples follow the general trend of a thicker film creating a less transparent film. Haze increases can be observed, however, these are not as pronounced as the haze increases with the GZO shown in the last section. Indium tin oxide is one of the few materials with both metallic like conductivity and a bandgap, typically between 3.4 to 3.7eV, higher than a doped zinc oxides bandgap of 2.5 – 2.7eV. The bandgap of ITO is therefore further into the UV region of high energy photons below 200nm and therefore cannot be observed with these measurements.

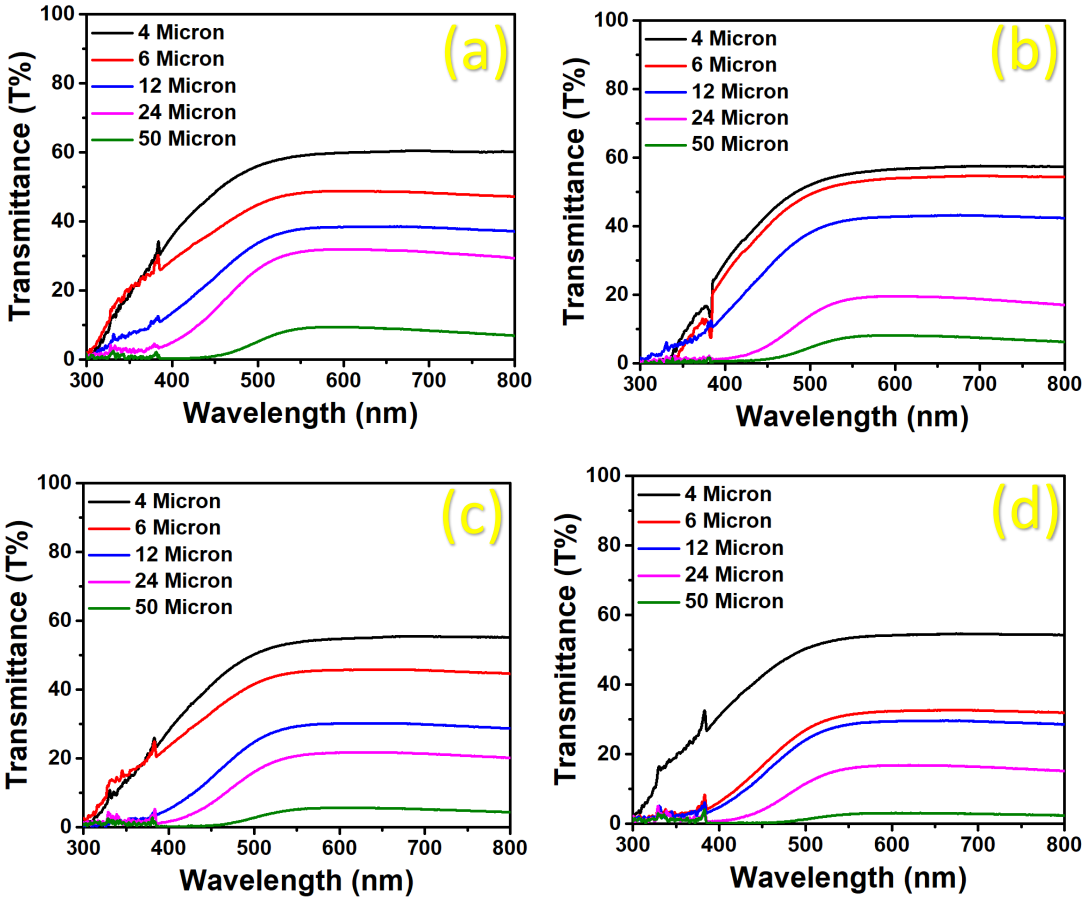

Figure 61 Optical properties for ITO inks at (a) 65wt%, (b) 70wt%, (c) 72.5wt% and (d) 75wt%

The sheet resistances were taken for films of varying weight percentages and thicknesses, shown in Figure 62(a-d). Each point on the graph contains data of three repeats (replicates) of each print, each repeated sample contains the data of nine sheet resistance measurements on the film to determine film uniformity. The standard error of the mean is shown on each point of the graph which is a measure of the film uniformity and repeatability of each coating. Due to the preliminary conductivity research in an earlier section, inks between 65 and 75% percent were measured and followed the same trend of 70wt% being the most conductive.

Films at 65wt% showed a mean sheet resistance of 112.53Ω□$^{-1}$with a standard error of 2.83 in a 50-micron film. This sheet resistance decreased to an average of 57.77Ω□$^{-1}$ with a standard error of 2.42 at 70wt%, moving to 200.04Ω□$^{-1}$and 391.63Ω□$^{-1}$for 72.5 and 75wt% respectively. With increasing film thickness, the standard error also decreases and an increase in film uniformity is observed suggesting for repeatable, conductive films, thicker films should be made.

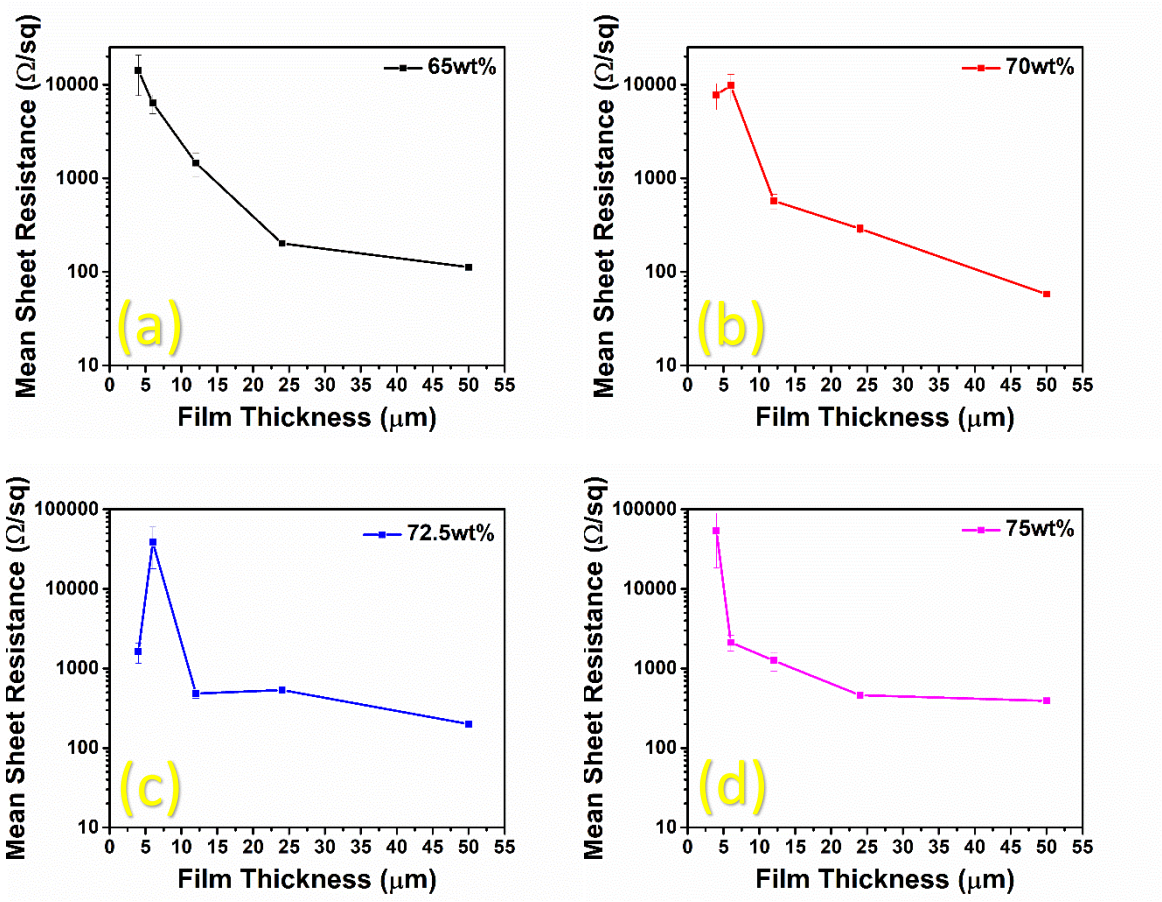

Figure 62 Electrical properties for ITO inks at (a) 65wt%, (b) 70wt%, (c) 72.5wt% and (d) 75wt%

In the next sections, a design of experiments will be performed analysing each formulation and processing parameter with conductivity, optical properties and rheological and ink stabilisation data to determine the main effects of each parameter on the final properties and the reproducibility and reliability of printed ITO films.

5.6.4 Indium Tin Oxide Experimental Design

In order to assess which components and parameters affect the conductivity, transparency and ink rheology the most, a Taguchi L8 design of experiments was performed. In this experimental design, seven individual factors are altered across eight experiments which are repeated three times in order for the experimental design to analyse which factors also affect the standard deviation. The reasoning behind choosing a Taguchi experimental design model is that traditionally selected mixture experiments are known to confound data, this means each parameter is "aliased" and there is no way to extract meaningful information about the parameter effects. However, there is one caveat which needs to be taken into consideration using experimental designs for inks. The total weight of the ink cannot be kept constant, otherwise it is impossible to keep the experimental factors constant and invalidates the experiment. For the indium tin oxide inks, the factors which will be altered are:

- The weight fraction of indium tin oxide filler (ITO @ 6.5 – 8.5g)
- The weight fraction of nitrocellulose binder (NC @ 1.0 – 3.0g)
- The amount of rheology thinning solvent isopropoxymethanol used in the ink (IPM @ 0 – 2.5g)
- Impact of sodium dodecyl sulphate (SDS @ 0 – 0.25g)
- The influence of eugenol curing additive on the conductivity (E @ 0 – 0.25g)
- The film thickness (12 – 24μm)
- The curing temperatures (110 – 200^{o}c)

The final experimental design for ITO ink formulation can be seen in Table 6:

Table 6 Taguchi L8 Experimental Design for ITO Ink Analysis

Run	ITO / g	NC / g	IPM / g	E / g	SDS / g	Curing Temp / ^{o}C	Thickness / μm
1	6.5	1.0	0	0.25	0.25	200	24
2	6.5	3.0	2.5	0	0	200	24
3	8.5	3.0	0	0	0.25	200	12
4	8.5	1.0	2.5	0.25	0	200	12
5	8.5	3.0	0	0.25	0	110	24
6	6.5	1.0	0	0	0	110	12
7	6.5	3.0	2.5	0.25	0.25	110	12
8	8.5	1.0	2.5	0	0.25	110	24

Each experimental run was performed three times with screen printing, with conductivity mapping, UV/VIS spectroscopy and rheology measurements performed. Results for each are discussed in the next sections.

5.6.5 Indium Tin Oxide Parameter Analysis: Conductivity

Sheet resistance measurements, including conductivity maps and replicates were taken for each ink to enable the analysis of factor effect on ink resistivity. The sheet resistance responses range from 218.98 to 7950$\Omega\square^{-1}$, with a ratio of maximum to minimum value of 36.3047. Typically, if the ratio is greater than 10, a mathematical transformation is required to accurately model the data. As resistance cannot be infinite or zero except in the case of a perfect conductor or insulator, a Logit mathematical function was applied to the data in the form of Equation 9 with an upper and lower bound selected as 1MΩ and 1Ω respectively:

$$y' = \ln\left(\frac{y - lower}{upper - y}\right)$$

Equation 9 Logit Mathematical Function

Analysing the main effects of the parameters provides the contribution each factor has towards the final conductivity of the film. The data shown in Table 7, suggests that the three of the factors contribute towards 88.98% of the final sheet resistance.

Table 7 Percentage Contribution of Factors Towards Sheet Resistance

Factor	Standardised Effects	Sum of Squares	Contribution / %
ITO	-0.34	0.71	2.30
NC	0.000758	0.00000345	0.0000113
IPM	0.27	0.44	1.43
E	1.55	14.46	47.09
SDS	-1.00	6.04	19.68
Curing Temp	-0.18	0.20	0.66
Film Thickness	-1.07	6.82	22.21

Modelling the data in this way provides an F-value of 49.67 which suggests the model is highly significant and there is a less than 0.01% chance that the trends seen in the data could occur

due to noise. The predicted R2 value which indicates how well the model predicts the sheet resistance is 0.8607 which is in good agreement of the adjusted R2 of 0.8943. The R2 of the measured data is 0.9127. The signal to noise ratio was calculated to be 21.127 which is much higher than the recommended value of 4 for this experimental design. The top four factors, ITO, Eugenol, SDS and Film Thickness were uses to create response charts showing the effects of each factor on both the resistance and the effect on the standard deviation.

Analysing the factor response charts shown in Figure 63(a-d), the effect of each of the four factors can be seen. For each graph, the sheet resistance is shown on the y-axis, as with normal sheet resistance, a lower value equates to a higher conductivity. As generally expected, the addition of more indium tin oxide into the ink results in a lower sheet resistance. It can also be seen in Figure 63(a) that there is a slight change in the standard deviation of printed films with differing amounts of indium tin oxide. With the eugenol, it is also observed that the addition of this curing additive greatly affects the sheet resistance and the standard deviation. The addition makes the printed films both less conductive and less reproducible.

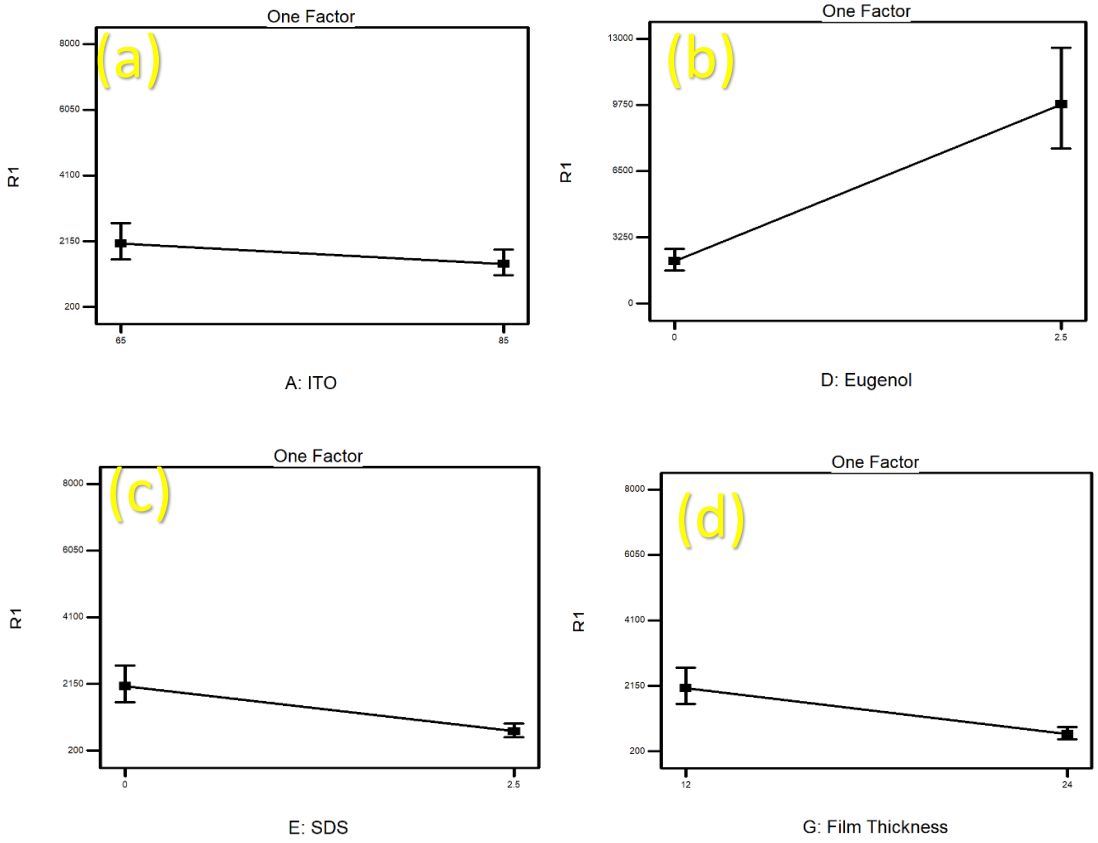

Figure 63 One Factor Response Graphs Showing the Effect of (a) ITO quantity, (b) eugenol, (c) SDS surfactant and (d) film thickness on resistivity

The addition of sodium dodecyl sulphate both makes the printed ITO films more conductive and more reproducible. This can be attributed to the fact that particle sizes should be stabilised, and the formation of agglomerates is hindered, creating better material packing. Increases in film thickness, increase conductivity, which is to be expected, however, this also increases the reproducibility of the printed films.

5.6.6 Indium Tin Oxide Parameter Analysis: Optical Properties

For all UV/VIS spectroscopy transmission measurements, previous experimental procedures described in earlier sections were followed. All measurements were made in reference to a reflectance standard (spectralon, 99.9%). Measurements were taken in the visible and UV spectrum between 800 and 190nm and the absolute values used for the analysis were taken at 550nm, the centre of the visible light wavelength range. Transmissions were measured between 8.89 and 60.24% with a ratio of max to min of 6.77, requiring no mathematical transformation. The three factors of isopropoxymethanol solvent, eugenol curing additive and film thickness were the three main factors, contributing to 85.65% of the final light transmittance at 550nm. The contribution percentages of each factor can be seen in Table 8:

Table 8 Percentage Contribution of Factors Towards Visible Light Transmission

Factor	Standardised Effects	Sum of Squares	Contribution / %
ITO	0.63	2.38	0.043
NC	4.59	126.31	2.26
IPM	17.32	1799.26	32.20
E	12.43	927.37	16.59
SDS	0.47	1.33	0.024
Curing Temp	1.17	8.24	0.15
Film Thickness	-18.53	2060.04	36.86

Modelling the data in this way provides an F-value of 34.55 which, as with the sheet resistance analysis suggests the model is highly significant and there is a less than 0.01% chance that the trends seen in the data could occur due to noise. The predicted R2 value which indicates how well the model predicts the transmission is 0.8072 which is in good agreement of the adjusted R2 of 0.8537. The R2 of the measured data is 0.8791. The signal to noise ratio was calculated

to be 14.859 which again is much higher than the recommended value of 4 for this experimental design. The top four factors, nitrocellulose content, isopropoxymethanol content, Eugenol, and Film Thickness were uses to create response charts showing the effects of each factor on both the transmission and the effect on the standard deviation.

Analysing the factor response charts shown in Figure 64(a-d), the effect of each of the four factors can be seen. For each graph, the percentage of light transmission is shown on the y-axis, with a larger value equating to a more transparent printed film. Firstly, for all four factors there is no appreciable change in standard deviation and therefore reproducibility for any of the factors with regards to optical properties. It can also be seen that for the additions of material into the ink have a general trend of providing an increase in transparency. For the nitrocellulose and eugenol, this is likely due to the fact that the more of this material is in the ink, the lower the effective weight loading of ITO there is, therefore there are fewer ceramic particles scattering, absorbing and reflecting the light. With the isopropoxymethanol this is also the case, however, this viscosity thinning solvent also will evaporate during the curing process, leading to a lower effective film thickness as more material will leave the film.

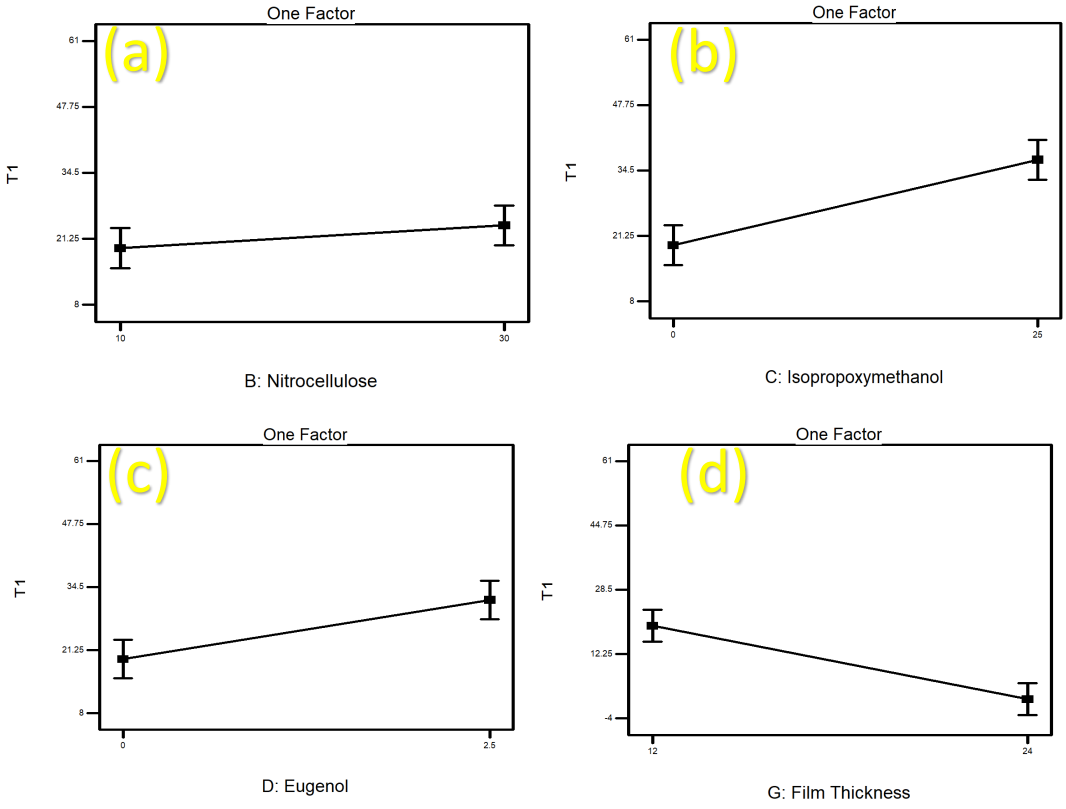

Figure 64 One Factor Response Graphs Showing the Effect of (a) nitrocellulose, (b) IPM, (c) eugenol and (d) film thickness on transparency

Finally, as expected the film thickness has the greatest effect on the film transparency, a thinner film provides a more transparent film as there is less material to disrupt photons of light.

5.7 Composite Nano-Ink Formulations

5.7.1 Overview

As discussed earlier in Chapter 5, transparent conducting oxide nano-powders manufactured via the continuous hydrothermal flow synthesis process have vastly superior optical transparencies, reaching as high as 85% transmittance of visible light. At lower weight percentages, they also have superior rheological properties making them suitable for a wide range of printing processes. However, the correct electrical properties are difficult to obtain due to the number of particle/particle grain boundary resistances that occur with a small particle size. There are many high cost transparent conducting alternative materials to transparent conducting oxides and one of the main motivations for the zinc oxide based TCOs is their low cost. This study investigates the effect of composite ink formulations of gallium doped zinc oxide nano-powders mixed with small quantities of transparent conductors on optical and electrical properties of printed films.

5.7.2 Materials

For this study two transparent conducting oxide materials will be used, with the chosen TCO materials being gallium doped zinc oxide (CHFS) nano-powders and commercial Indium Tin Oxide powder (Alfa Aesar, 99.99% Metals Basis). Eight total formulations will be developed as can be seen in Table 9. Two formulations will be standards for comparison, these are a 50w/w% GZO in nitrocellulose ink and a 70w/w% ITO in nitrocellulose ink. The small weight loadings of secondary material were to eliminate any changes to conductivity being purely from the properties of the secondary material.

Table 9 Composite Nano-Ink Formulations

Ink Code	TCO Material	TCO Weight Loading (wt%)	Secondary Material	Secondary Material Weight Loading (wt%)
LS001	GZO	50	None	**0**
LS002	GZO	50	Carbon Nanotubes	**0.1**
LS003	GZO	50	Graphene Flakes	**0.05**
LS004	GZO	50	Silver Nanowires	**0.1**
LS005	ITO	70	None	**0**
LS006	ITO	70	Carbon Nanotubes	**0.1**
LS007	ITO	70	Graphene Flakes	**0.05**
LS008	ITO	70	Silver Nanowires	**0.1**

For this study two transparent conducting oxide materials will be used, with the chosen TCO materials being gallium doped zinc oxide (CHFS) nano-powders and commercial indium tin oxide powder (Alfa Aesar, 99.99% Metals). The first conductive secondary material selected were carbon nanotubes (Multi-Walled, Sigma-Aldrich) with the hypothesis that small amounts of conductive fibrous material in the film may aid in lowering grain boundary resistance. Single layer graphene flakes (ACS Materials, Hummer Method Manufactured) with a bulk resistivity of $3x10^{-1}$ Ω.cm and a particle size of 0.4-0.5μm length, 1.2nm thickness were also used as a secondary material with the hopes of giving large, highly conducting particle coverage. Silver nanowires (ACS Materials, dispersed in ethanol) were also chosen due to their high conductivities and high transparencies as discussed in Section 5.5, the nanowires had an average width of 70nm and a length ranging between 100-200μm.

5.7.3 Experimental

Inks were formulated using the three-roll mill process discussed in chapter 4. To determine any changes in electrical and optical properties, thick film screen-prints were made onto soda lime glass (NSG) and cured at 105°C. Sheet resistance measurements were taken using the Jandel HM20 four-point probe and transmittance data was collected using the Perkin Elmer

35 UV-VS spectrophotometer. Changes to the rheological properties were measured using the Haake VT550 cone and plate rheometer.

5.7.4 Results

Sheet resistance measurements for each of the inks are displayed in Table 10 measured of the Jandel HM21 Four Point Probe with a measurement error of 0.5%. The data shows that for GZO nano-powders, having a small amount of secondary conducting material can enable conductivity with carbon nanotubes having the largest effect. For ITO, sheet resistances are largely unchanged which is most likely due to the particles being much larger than GZO and therefore particles already have good interconnectivity.

Table 10 Sheet Resistivities of Composite Nano-Inks

Ink Code	TCO Material	Secondary Material	Sheet Resistance
LS001	GZO	None	None
LS002	GZO	Carbon Nanotubes	1.432 $M\Omega\square^{-1}$
LS003	GZO	Graphene Flakes	7.119 $M\Omega\square^{-1}$
LS004	GZO	Silver Nanowires	None
LS005	ITO	None	83.73$\Omega\square^{-1}$
LS006	ITO	Carbon Nanotubes	89.24$\Omega\square^{-1}$
LS007	ITO	Graphene Flakes	74.68$\Omega\square^{-1}$
LS008	ITO	Silver Nanowires	79.56$\Omega\square^{-1}$

To determine whether the change in electronic properties of the materials were due to the mixed conductors having a synergistic effect or are from the secondary materials conducting, inks were formulated using the same secondary material weight loadings seen in Table 9 for carbon nanotubes and graphene. Carbon Nanotube inks with a 0.1wt% loading into nitrocellulose did not conduct, neither did 0.05wt% loadings of graphene into nitrocellulose. This suggests there is a synergistic effect between the mixed materials which warrants further investigation.

Each print had the optical properties of the thick film screen-prints analysed between 385 – 1100nm wavelengths with transmission plots being shown in Figure 65. Thick film pure GZO inks are between 40 – 50% transmissive in the visible light region and it is shown that including

small quantities of secondary material can vastly alter the transmissive properties. GZO mixed with carbon nanotubes drops to a constant 0.5T% while mixing with graphene reduces transmission to <2T% across the spectrum. GZO mixed with silver nanowires provides a transmission of <18T%. This data shows that mixing a highly transparent material with another highly transparent material may not always result in transparent film.

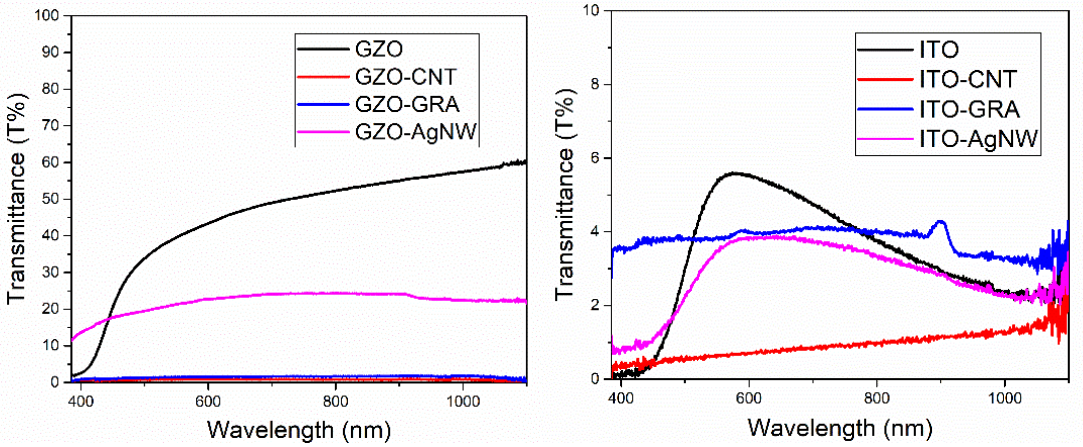

Figure 65 Transmission Plots for (a) GZO Composite Inks and (b) ITO Composite Inks

The indium tin oxide inks were all between 0.5 – 6T% transmissive. Noise can be seen above a wavelength of 1000nm, this is due to ITO being an excellent infrared (IR) absorber [283]. Prints for the pure ITO, the graphene mix and the silver nanowire mix all give similar transmission values suggesting these materials are having a minimal impact on the optical properties of the ITO. However, the carbon nanotube mix gives the lowest transmissions which is to be expected as they are one of the blackest materials currently known [284].

It has been shown that mixing nanomaterials for transparent conductors can have an adverse effect on the optical properties desired. However, Table 10 demonstrates that there is an apparent trade off with potentially improved electrical conductivities which warrants an investigation of whether proper sintering with these can achieve close to bulk resistivity values on printed films.

Although the composite nano-inks have only small quantities of secondary material mixed into the formulation, the rheological properties appeared to change drastically. These were studied via placing a pea sized drop of ink onto a cone and plate rheometer (0.5^0 Incline Cone,

Haake VT550) and measuring viscosity and shear stress vs shear rate. For gallium zinc oxide composite nano-inks, data can be seen in Figure 66.

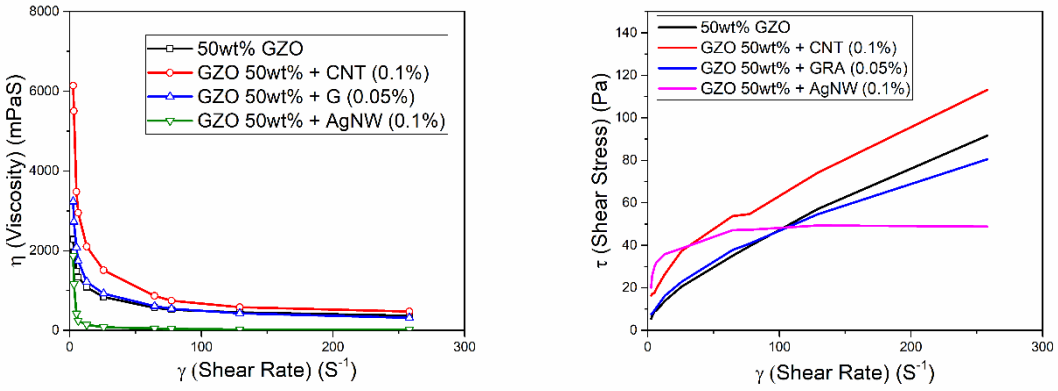

Figure 66 Rheological Data for GZO Composite Nano-Inks

An analysis of the GZO rheology data shows that all the inks are highly stable with no ink film breakdown across Figure 66. The addition of 0.1wt% of carbon nanotubes to the GZO ink results in a tripling of viscosity which is due to a large surface area of the nanotubes. The graphene mix also increases starting viscosity from 2280mPas to 3230mPas, again this is due to the low density of the graphene and high surface area increase the amount of contact zones for the vehicle to disperse. The silver nanowire GZO mix had a much lower starting viscosity, this is due to the silver nanowires already being dispersed in ethanol for the ink formulation which in turn thins the ink relative to pure GZO. Resting and high shear viscosities are shown in Table 11. Figure 66, shows all inks to be Pseudoplastic, confirming the shear thinning properties of each ink. GZO/Silver Nanowire inks appear to be less shear thinning which is due to the extra solvent in the ink giving it more Newtonian fluid like properties.

Table 11 Shear Thinning Viscosity Data for GZO Composite Nano-Inks

Ink Code	Material	Viscosity @ Shear 2.58s^{-1}	Viscosity @ Shear 258.1s^{-1}
LS001	GZO	2280mPas	369mPas
LS002	GZO/CNT	6140mPas	472mPas
LS003	GZO/GRA	3230mPas	315mPas
LS004	GZO/AgNW	1860mPas	17mPas

Rheological data for ITO based composite inks can be seen in Figure 67. All inks show non-Newtonian fluid properties with shear thinning and pseudoplastic behaviour. However, in the shear stress versus shear rate plots the indium tin oxide/graphene mix starts with high stress at low shear. This suggests the material exhibits more plastic flow than pseudoplastic, keeping a more rigid ink film under stress. For the GZO inks, the GZO/CNT had the highest viscosity whereas for the ITO inks, the ITO/GRA inks have the highest starting viscosity.

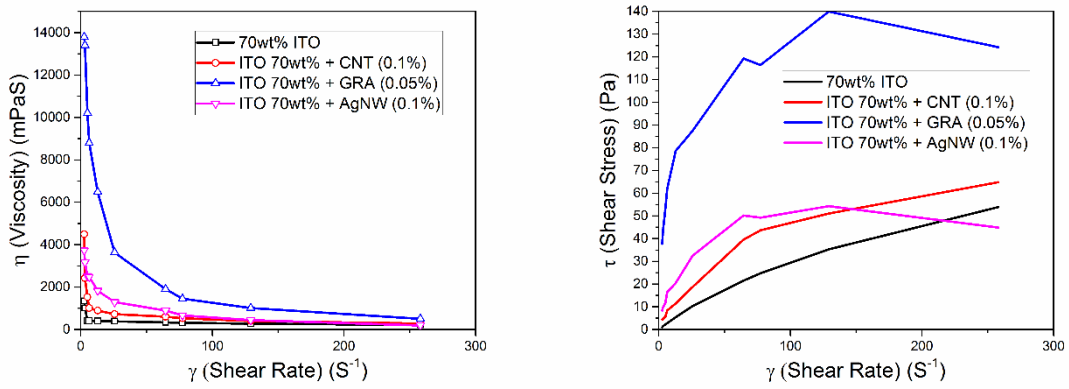

Figure 67 Rheological Data for ITO Composite Nano-Inks

The ITO based inks are highly stable with no ink film breakdown. The ethanol dispersion of the silver nanowires being incorporated into the ITO has little effect on shear thinning compared to the GZO inks, as can be seen in Figure 66, the ITO material is more porous than the GZO which will lead to a better absorption and dispersion of ethanol throughout the ink. The starting viscosity is also higher for ITO/AgNW than GZO/AgNW, showing that even though

there is an increase in thinning solvent in the ink, the ability for it to resist deformation increases. Viscosity is a simple description of a complex system of internal friction and intermolecular forces and this discrepancy can be explained due to a difference in intramolecular force between an ITO-Silver / GZO - Silver network caused by different particle sizes and weight fractions [285].Resting and high shear viscosities are shown in Table 12. All are suitable for printing.

Table 12 Shear Thinning Viscosity Data for ITO Composite Nano-Inks

Ink Code	**Material**	**Viscosity @ Shear 2.58s^{-1}**	**Viscosity @ Shear 258.1s^{-1}**
LS005	ITO	1343mPas	216mPas
LS006	ITO/CNT	4490mPas	279mPas
LS007	ITO/GRA	13810mPas	503mPas
LS008	ITO/AgNW	3730mPas	191mPas

SEM images of the GZO and GZO/CNT inks can be seen in Figure 68. Images show composite GZO CNT inks fully untangle and disperse the carbon nanotubes throughout the ink, a process that is extremely difficult with a pure carbon nanotube ink requiring complicated surfactant-based formulations. SEM images of all ink formulations can be seen in Figure 68(a-e) and Figure 69(a-f).

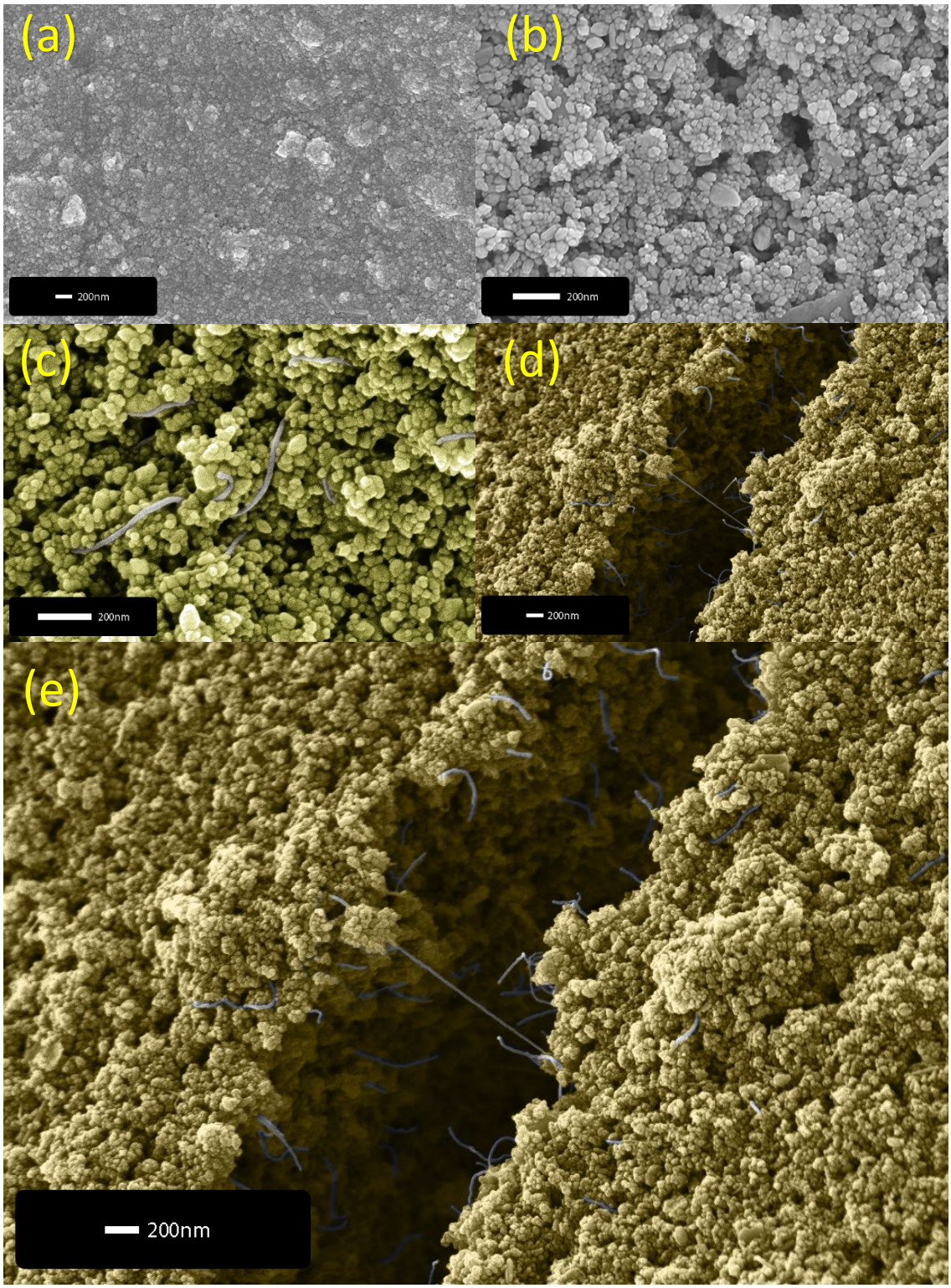

Figure 68 Scanning Electron Microscope Images of printed (a) Pure GZO, (b) Pure GZO, (c) GZO/CNT, (d) GZO/CNT and (e) an enlargement of GZO/CNT displaying CNT dispersion

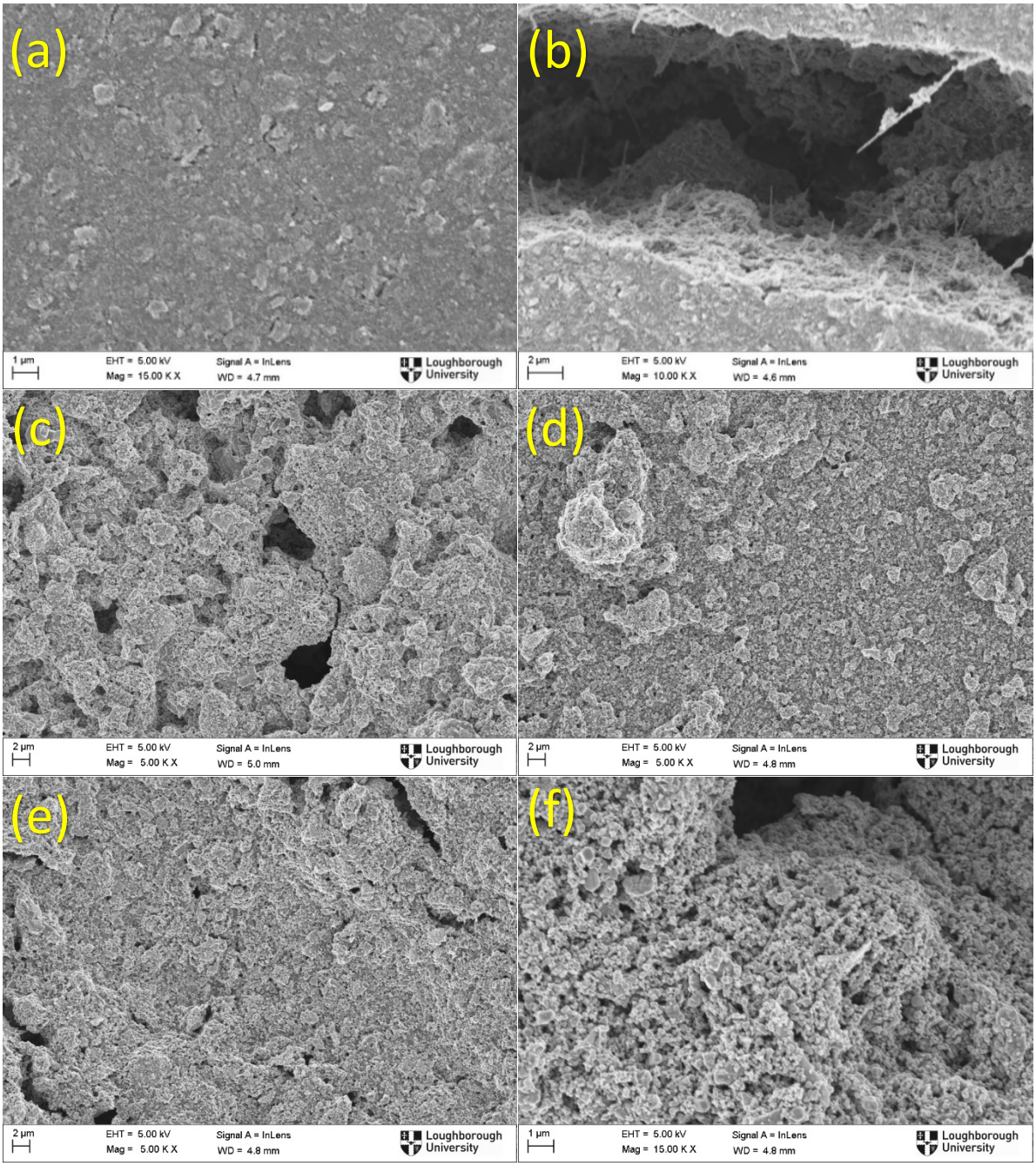

Figure 69 Scanning Electron Microscope Images of printed composite inks showing (a) GZO/Graphene, (b) GZO/Silver Nanowires, (c) ITO, (d) ITO/CNT, (e) ITO/Graphene and (f) ITO/Silver Nanowires

5.8 Chapter Summary

Four metal oxide materials were chosen as candidates for developing conductive metal oxide screen printing inks. Before preliminary ink formulation could occur, a materials characterisation study was performed on the four materials, these being continuous hydrothermal flow synthesised gallium doped zinc oxide (CHFS GZO), microwave synthesised co-doped aluminium gallium doped zinc oxide (MW AGZO) and gallium doped zinc oxide (MW GZO) and finally commercially sourced indium tin oxide (ITO). From the materials characterisation, it suggested the commercially sourced ITO was the highest quality material and showed that the dopants in the zinc oxide materials were unstable resulting in unstable dopant concentrations. Three vehicles were selected and the compatibility with the metal oxides was assessed. The three vehicles, the first a commercial standard from Gwent Electronic Materials, the second an experimental nitrocellulose-based vehicle from an industrial partner and the third being a literature sourced formulation for lithographic and screen-printing applications were assessed in terms of maximum conductivity of a metal oxide. The nitrocellulose-based vehicle provided the highest conductivity and was chosen for the ink formulation studies, characterisation the vehicle in the form of TGA, XPS and cured films via SEM shows the nitrocellulose pulls and densifies the particles together to a larger degree than the others allowing for a more conductive film.

Once the vehicle was selected, inks were formulated at varying weight percentages and the sheet resistance and optical properties were measured. CHFS GZO was found to be non-conducting at all tested weight percentages, however, did show the best light transmission values at 52%T. The MW GZO and AGZO were found to provide some conductivity, with MW AGZO performing better than MW GZO. The best performing conductive ink was indium tin oxide, with values in the range 177.4 to 625.23$\Omega\square^{-1}$, providing the highest conductivity for any metal oxide ink in the literature at this current time at 3.05% of bulk conductivity observed in the film. Of these four materials, the indium tin oxide and CHFS GZO were selected for further investigation, due to the conductive properties of the ITO and the optical properties of the GZO and with the intention of a later post processing method improving the electrical properties of the GZO. With the transparent GZO inks, a film thickness versus transparency study was performed, providing over 84% light transmittances through the film, demonstrating that highly transparent printed metal oxide films are possible. However, as no

conductivity had been observed, no further investigations could be conducted with pure GZO inks in this chapter. As the ITO inks were conductive, this study on film thickness was also repeated, incorporating sheet resistance measurements finding that 70wt% inks were the most conductive with sheet resistances as low as 57.77$\Omega\square^{-1}$. A design of experiments was conducted to provide some insight into how ink formulation components, curing times and film thicknesses affect conductivity, transparency, ink rheology and ink stabilisation in the form of particle size analysis. In terms of conductivity, the biggest factors were found to be quantities of indium tin oxide, the ink stabilisation and curing additives and the printed film thickness. For the optical transparency, the amount of nitrocellulose binder, thinning solvent, curing additive and film thickness had the largest effects.

Finally, for the first time, metal oxide nanocomposite inks were formulated in an effort to see if a secondary quantity of other common transparent conducting materials would increase the conductivity or the transparency of the printed inks. It was found that the secondary materials could induce and provide some synergy with the gallium doped zinc oxide and appeared to slightly increase the conductivity on the indium tin oxide. However, the optical properties suffered greatly. The hypothesis behind this experiment is that a secondary conductor could provide a pathway which decreases the grain boundary resistance in the GZO. However, experiments to confirm this would require a high temperature heat controllable potentiostat and is recommended for future work.

Chapter 6

Laser Processing of Printed Transparent Conducting Oxides

6.1 An Introduction to Laser Sintering of Printed Materials

In Chapter 5, inks were formulated utilising two main conducting oxide fillers alongside a range of composite material inks. The main difficulties encountered in these studies were the compromises required between conductivity, particle size and transparency. As these materials require high processing temperatures, for the low temperature curing of inks a large particle size is required to reduce grain boundary resistances. However, there are issues with printing transparent ceramics due to two factors. Firstly, if the particles are similar in size to the wavelength of light, photons will be either absorbed, reflected or scattering creating opaque films. Secondly, if particles that are sub-wavelength are used, haze is still an issue as scattering effects become dominant in the thick films provided by most printing processes.

For Chapter 6, the effects of post-processing upon metal oxide and metal oxide composite printed films are investigated. The post-processing method researched in this chapter is laser processing which is selected as it is easily integrated into a printing manufacturing process, it enables high temperature processing without any damage to the substrate and it is rapid. For conducting oxide materials, most of the literature in the 2000's is concerned with the pulsed laser deposition of conductive oxides to create films on glass. This has been performed on aluminium doped zinc oxide (AZO) [286] [287], niobium doped titanium dioxide [288] and indium tin oxide [289]. However, due to pulsed laser deposition being difficult to scale up, requiring high vacuums and expensive equipment, research in more recent times has focused on laser treating conductive oxides fabricated by traditional methods such as AACVD, Sol-gel and Pyrolysis. Laser treatments have been used to process sol-gel AZO [290] and sol-gel ITO [291], however, there is little work in the area of laser processing printed conducting oxide films. Recently, gravure printed ITO on PET sheets have been investigated with laser treatments (1.5 – 2.0μm laser wavelength) suggesting improved conductivity post-treatment. However, the groups best conductivity post laser processing is $50\Omega\square^{-1}$, which can already be achieved with non-laser processed ITO inks formulated in Chapter 5.

The main intention of this chapter is to research the effects of laser processing on the printed metal oxides and to perform a full materials characterisation pre and post processing to fully understand how laser processing interacts with printed ceramics. The main motivation behind this is to increase the conductivity of ITO prints, to induce conductivity in the non-conductive GZO prints and to investigate what interactions occurs when laser processing composite inks. In this study, laser processing is to be used as the industrially viable post processing method outlined in research objective 3 in Section 1.3.

6.2 Printing and Laser Processing Optimisation

6.2.1 Experimental Overview

Experimentally, in Chapter 6, the eight inks discussed in Chapter 5 are investigated to determine the effects of laser processing on each material. The main focus is to perform a full materials characterisation study of the pure conductive metal oxide materials pre and post processing to fully gauge any effects the laser is having on the material. Once a complete understanding of the effect of the laser processing is determined, the composite nanoparticle inks formulated in Chapter 5. These materials have been selected for laser processing as the secondary additives can have a potential effect on the final film due to the differing optical properties (light absorption) of the prints. A list of all the materials to be processed in the chapter can be seen in Table 13:

Table 13 Inks to be Laser Processed

Ink Code	Material
LS001	Gallium Zinc Oxide (GZO)
LS002	GZO / Carbon Nanotubes (CNTs)
LS003	GZO / Graphene
LS004	GZO / Silver Nanowires (AgNWs)
LS005	Indium Tin Oxide (ITO)
LS006	ITO / Carbon Nanotubes (CNTs)
LS007	ITO / Graphene
LS008	ITO / Silver Nanowires (AgNWs)

6.2.2 Experimental Design

Due to the large number of parameters involved in laser processing multiple inks, an experimental design programme was coded in R Studio (V.3.5) in the statistical programming language R. The experimental design programme is based on the Box Behnken design of experiments model. This model chosen as the experiments to be carried out are expected to have a second order relationship between parameters and due to the extreme values of each parameter creating possible safety issues. It was picked for the laser processing as, it is expected that low laser powers may not process the film at all dependant on energy absorption, and high laser powers can destroy the film and substrate, yielding no useful information. In traditional experimental designs, parameters to be tested are pinned to the extremes (for example on/off, no power or max power) and as the extremes will yield no information, the centre of the extremes must be explored, hence a second order model has been chosen.

Although this method is well suited to experiments such as laser processing, and other dangerous experiments such as chemical reactions, it does have one issue that needs to be accounted for in this work. As the box-Behnken model does not probe the extremes of each parameter, data is often statistically confounded, so it is not always possible to optimise a system with this method. For this reason, two rounds of process optimisation will be performed, and surface responses analysed. If confounding is observed, the best processing parameters will be selected by the “Pick a Winner” method. This is often used in design of experiments methodology where if the system cannot be modelled, the parameters with the best results can be chosen. For the laser processing experiments, the parameters which yield the lowest resistivity will be chosen.

For both rounds of experiments, there are three parameters that can be and will be tested, with these parameters being laser power (watts / W), laser scanning or raster speed (mm/s) and the amount of passes the laser will make over each print. The first round of process optimisation is the “scoping run” and all materials will be tested within the same ranges. Laser power is to be altered for all eight materials between 5 and 25 watts with 28.1W being the maximum power of the laser. The range of 5 and 25W has been chosen due to the absorbance characteristics of the inks shown in Chapter 5, allowing for a broad range which enables each

material to absorb enough energy to be processed. Laser speed is to be altered between 10 and 50mm/s which alters the energy hit by the sample with respect to time. The range was chosen as if the raster speed is too slow, too much energy can be absorbed destroying the sample and if the speed is too fast, no energy can be absorbed, and the sample won't be processed. The amount of passes the laser makes over each print will also be tested between 1 and 3 passes, providing information whether multiple passes provides any improvement to the electrical or optical properties. The first-round experimental design can be seen in Table 14:

Table 14 Experimental Plan for Laser Sintering Scoping Study

Experiment	**Power / W**	**Laser Speed / mm.s^{-1}**	**Laser Passes**
1	25	10	2
2	5	30	1
3	25	50	2
4	15	10	1
5	15	50	1
6	25	30	1
7	5	50	2
8	5	10	2
9	15	10	3
10	15	30	2
11	15	50	3
12	15	30	2
13	5	30	3
14	25	30	3
15	15	30	2

Each ink is to have 5 tracks printed for each of the 15 experiments giving each ink 75 processed prints for analysis with a total of 600 processed tracks. A further set of 15 experiments will be conducted with parameters changed for each individual material dependant on what the results from the scoping run indicate.

6.2.3 Printing and Laser Processing Equipment

The laser processing in this chapter was performed on a Haecker Automation VICO 520, pictured in Figure 70. The system is originally designed as a pick and place machine for mounting surface mount PCB components, dispensing solder then laser processing the solder. However, any ink can be loaded and processed, allowing for the metal oxide inks to printed.

Figure 70 Haecker Automation VICO 520 [292]

The internals of the Haecker VICO 520 can be seen in Figure 72. In the figure, highlighted in red is the laser head mount which contains a 28.1W 980nm diode. Highlighted in green is the build-plate where substrates are placed for printing onto. Highlighted in blue is the dispensing head where inks are loaded into using 3CC dispensing tubes (Nordson EFD).

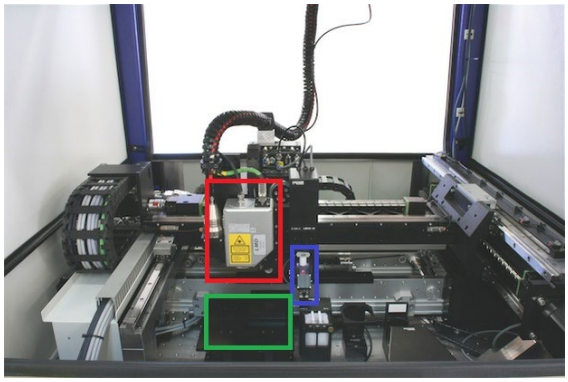

Figure 71 Haecker Automation VICO 520 Internals [293]

The advantages of using micro-dispensing pre-laser processing is that screen printing inks can easily be printed via a direct write method with little to no rheological or formulation alterations. Prints can also be processed in-situ, mitigating any registration issues that may occur from screen printing separately and then inserted into a laser processing system.

6.2.4 Printing Parameter Optimisation

Before laser processing can occurred, printed tracks and thick films must be fabricated for processing. As each ink has different rheological properties, different printing parameters are required for printing consistent, high quality tracks and films. The Haecker system automatically runs a set of self-learning commands, dispensing inks at a variety of flow rates and plunger pressures to determine if the amount of material dispensed matches the amount expected. To optimise each ink, a syringe was placed in the system and the self-learning system was started. The two main parameters measured and optimised are the flow rate of material (mLs^{-1}) and a proprietary 'pressure' unit (measured in mm by the system), optimised dispensing tip sizes, pressures and flow rates can be seen in Table 15.

Table 15 Ideal Printing Parameters for Micro-dispensing of Inks

Ink Code	Material	Dispensing Tip	Pressure / mm	Flow Rate / μLs^{-1}
LS001	GZO	254μm Conical	0.55	0.5
LS002	GZO/CNT	254μm Conical	0.67	0.1
LS003	GZO/GRA	254μm Conical	0.65	0.7
LS004	GZO/AgNW	254μm Conical	0.37	0.2
LS005	ITO	254μm Conical	0.39	0.2
LS006	ITO/CNT	254μm Conical	0.68	0.1
LS007	ITO/GRA	254μm Conical	0.32	0.3
LS008	ITO/AgNW	254μm Conical	0.28	0.3

With the correct parameters in place, high quality printed two and three-dimensional tracks can be printed for laser sintering as can be seen in Figure 72. For this study, all tracks were dispensed to have a 0.1mm layer height staying in the area of 2D printed electronics. One reason micro-dispensing was chosen was that, similar to screen printing, a wide variety of inks and ink rheology can be used with the system, allowing for reliable experimentation. However, there are some differences. The major difference is that the film thickness is typically 50 microns or more (compared to 13 microns with screen printing). Therefore, a caveat is that transferring the laser processing method to a screen-printing manufacturing setup, 50 micron wet film thickness screens should be used in order to achieve the same results.

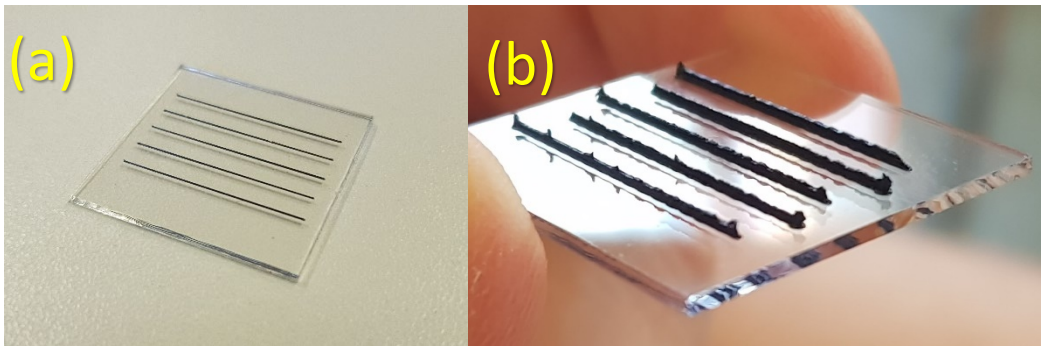

Figure 72 Micro-dispensed tracks for (a) 2D Printing and (b) 3D Printing

All printed tracks using high transparency 24x24x1mm soda lime glass slides (Thermo Scientific) as substrates, the Haecker system was then calibrated to print onto the glass sides. Transparent substrates are required for the laser processing to avoid the laser damaging the substrate. Each glass slide had five printed tracks 2.5mm apart, 20mm in length with a 0.254mm thickness and 0.1mm layer height. In Figure 73, the dispensing process can be seen via a camera fitted to the print head.

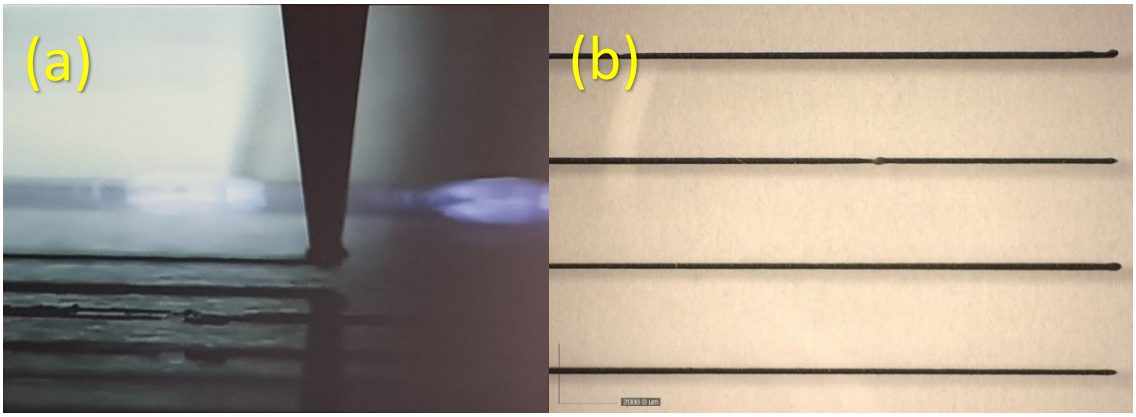

Figure 73 (a) Image of Micro-dispensing in action and (b) Image of Micro-dispensed GZO/CNTs paste at 20x Magnification

An optical microscope image of micro-dispensed GZO/CNT tracks can be seen in Figure 73, demonstrating the quality of the printed tracks. A main issue with this printing method is air bubbles forming in the ink creating small fractures, one such fracture can be seen in Figure 73(b). This is mitigated for by connecting two syringe barrels via a PTFE tube and transferring the ink from one syringe to the other, removing and avoiding the introduction of air bubbles. In total, for two rounds of optimisation for eight inks, 224 total substrates were printed on. This gives a total of 1120 printed tracks for laser sintering.

6.2.4 Printing Parameter Optimisation

The main factor involved when processing materials with laser radiation, is that the material should be able to absorb the energy of the light. As the laser is in the near infrared part of the electromagnetic spectrum, a material which is non transparent and non-white (absorption of part of the visible spectrum) may be transparent in the infrared region. Any transmission of photons through the sample reduces the amount of energy absorbed by the film, this also occurs for reflectance of light. Transmission data for each material has already been discussed in Section 5.4 and 5.6. Reflectance measurements for each material were taken against a spectralon barium titanite reference (99.9% R) between 385 – 1100nm and can be seen in Figure 74(a-b). The laser to be used has a 980nm diode meaning the optical data in this region will affect sintering the most.

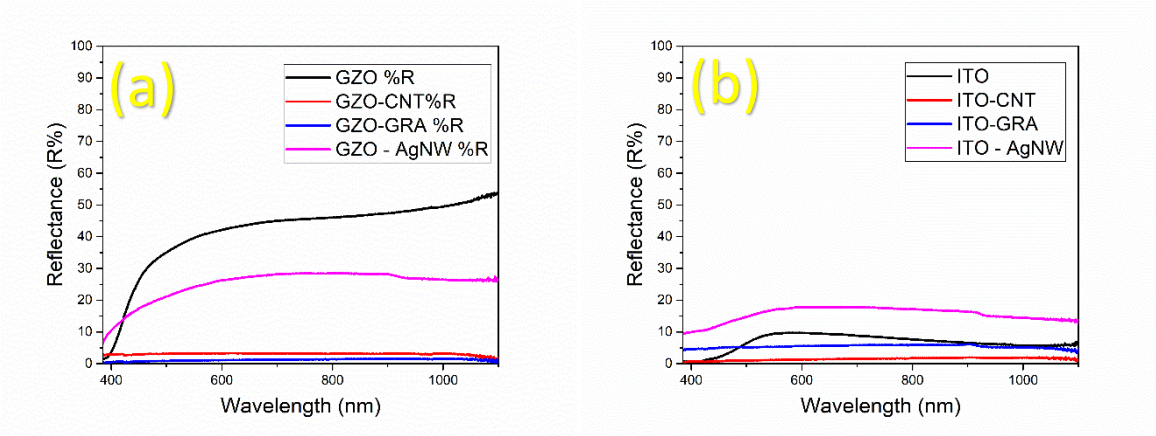

Figure 74 Reflectance Data for (a) GZO Composite Nano-inks and (b) ITO Composite Nano-Inks

Pure GZO is the most reflective material reflecting 48% of photons in the near infrared region. For all carbon mixed inks, reflectivity is below 2% suggesting these materials should give excellent sintering. Pure ITO shows a 5% reflectance, ITO is commonly used as an IR absorber for this reason. Silver nanowires increase the reflectivity of ITO to 10% whereas it decreases GZO reflectivity to 18% suggesting they give an increase in absorption to the GZO while also being reflective.

To calculate the percentage of light absorbed by the material, it can be assumed that any percentage of light that is not transmitted (T) or reflected (R) is absorbed (A) and for 100% of all photons, these three situations will occur in some ratio. For this we can measure transmission and reflectance and calculate absorbance using Equation 10:

$$A_{\%} = 100 - R_{\%} - T_{\%}$$

Equation 10 Calculation of Percentage Absorbance

Calculated percentage absorbance data across the full spectrum can be seen in Figure 75 (a-b) with absorbances at the laser wavelength (980nm) summarised in Table 16. All the ITO based inks absorb light well with carbon nanotubes performing best and silver nanowires performing the worst. The graphene does not appear to change the optical properties much for the ITO which could be due to the size of the flakes compared to the ITO.

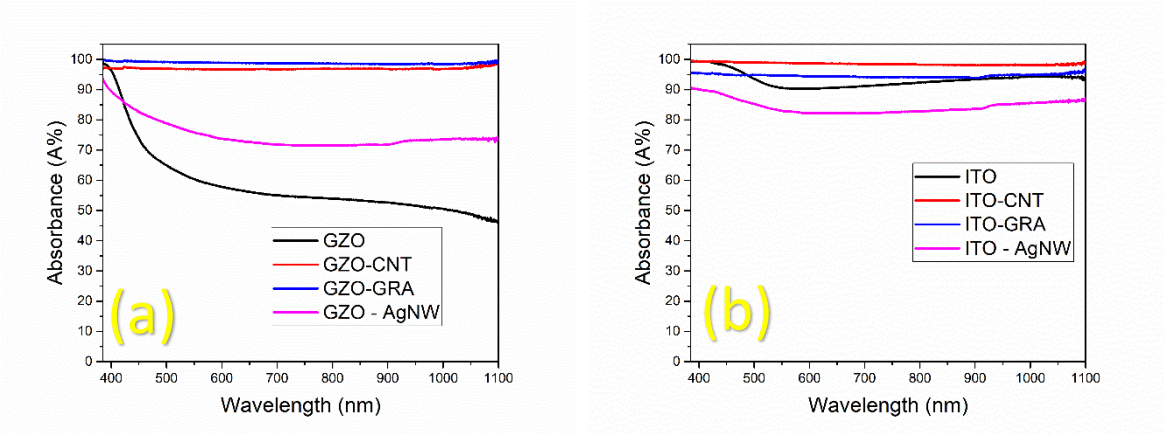

Figure 75 Absorbance Data for (a) GZO Composite Nano-inks and (b) ITO Composite Nano-Inks

Pure GZO is the worst performing light absorber suggesting UV light would be ideal for curing, however, this may not be an issue with the laser at higher powers. All other GZO based inks have percentage absorbances above 70%.

Table 16 Absorbance Data for Laser Sintering at 980nm

Ink Code	TCO Material	Secondary Material	Absorbance at 980nm / %
LS001	GZO	None	50.90
LS002	GZO	Carbon Nanotubes	97.06
LS003	GZO	Graphene Flakes	98.68
LS004	GZO	Silver Nanowires	73.16
LS005	ITO	None	93.98
LS006	ITO	Carbon Nanotubes	98.22
LS007	ITO	Graphene Flakes	94.92
LS008	ITO	Silver Nanowires	85.18

The absorption in the UV region of the electromagnetic spectrum is typically associated with bandgap absorption. A common form of lasers which operate in the region are “excimer” lasers and are used in micromachining. However, these will not be used for this research as they are high cost and difficult to operate in conjunction with printing due to their reliance on halogenated gases to operate.

6.3 Processing of Gallium Zinc Oxide

6.3.1 Thermogravimetric Analysis of GZO Powder

As the laser processing will treat the materials to much higher temperatures than conventional heat treatments, the temperatures involved are often 1000°C plus depending on the laser power. Due to this thermogravimetric analysis (TGA) with differential scanning calorimetry (DSC) measurements were taken in order to determine how the material will react to these thermal conditions. Measurements were performed on the pure gallium doped zinc oxide powder three times in order to eliminate any artefacts. The experiment was performed under air to keep the atmosphere consistent with processing conditions. The data is displayed in Figure 76. Analysis of the weight percentage versus temperature consistently shows a 0.5wt% drop between 25 – 100°C which is associated with water loss.

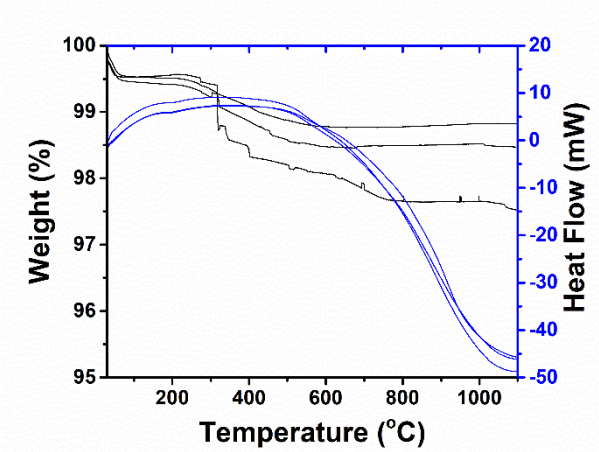

Figure 76 Thermogravimetric (TGA) and Differential Scanning Calorimetry (DSC) data for Gallium Zinc Oxide Powders

A further drop is seen at 320°C, the continuous hydrothermal flow synthesis method used to fabricate these nano-powders only reaches a maximum processing temperature of 300°C, this combined with the heat flow data showing energy releasing exothermically indicates that there is a small amount (0.5 – 1wt%) of precursor material impurity in the sample. Zinc acetate has been shown in other work to decompose between 110 and 350°C [294]. After this drop the weight percentage stabilises as is expected with a ceramic powder. There is a slight difference in weight loss over 350°C of approximately 1wt%, however, the same trend is seen overall indicating this is from experimental error or artefacts. At approximately 650°C a switch

from exothermic energy release to endothermic energy absorption can be seen in the heat flow DSC data to 1100°C. This shows that the ideal processing temperatures are 650°C plus which enables the material to begin to fuse, sinter and allow to recrystallisation.

6.3.2 Optimisation of Printing Parameters Via Printed Tracks

Stylus profilometry analysis was performed on the most conductive GZO tracks. The stylus moves across all five lines, three times. Profile 1 is the end of the laser sintered track, profile 2 is the centre of the track and profile 3 is the start of the tracking where the laser first powers up for raster.

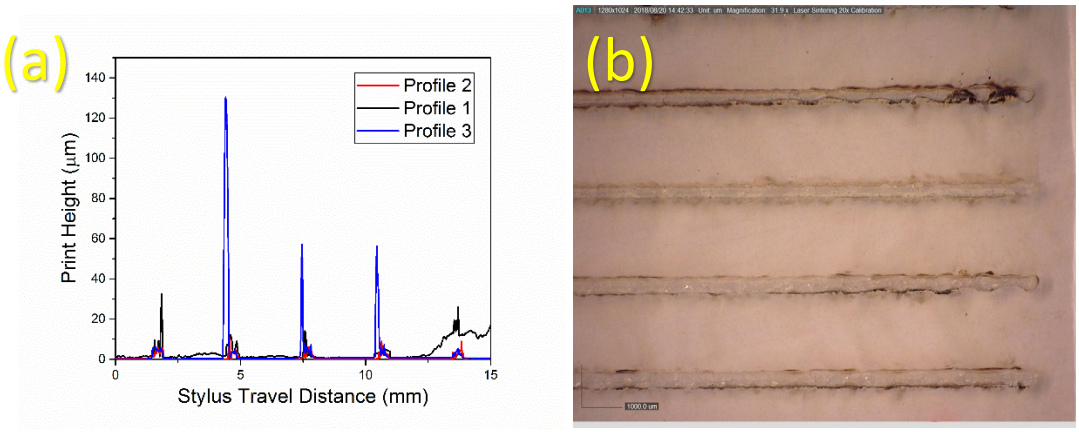

Figure 77 Profilometry Analysis of Printed GZO Tracks

Mean track thickness and resistivity values per track can be seen in Table 17, laser sintering has provided some conductivity to the GZO material, however, the values collected are still not useable in most electronic applications other than printed resistors. This poor sintering is most likely due to the optical properties not being conducive to near visible / near IR photonic sintering as discussed in Chapter 3.

Table 17 Laser Processed Resistivity Data for GZO Composite Nano-Inks

Printed Track	Sheet Resistance	Mean Track Thickness / µm	ρ Resistivity / Ωcm
1	678910	1.87	$1.27x10^{2}$
2	162421	1.67	$2.71x10^{1}$
3	389442	1.81	$7.05x10^{1}$
4	124891	2.51	$3.13x10^{1}$
5	535252	2.41	$1.29x10^{2}$

From the data shown in Table 17, the average resistivity of GZO processed tracks is $7.70x10^{1}\Omega cm$ which is 0.187% the resistivity of the bulk material discussed in Chapter 5. For thick, large area films the parameters of 40mm/s raster speed and 1 pass of the laser will be chosen and varied with laser power so conductivity versus laser power can be isolated and analysed.

6.3.3 Electrical Properties

After optimal raster speed and lass pass amount parameters where determined, 18 thick films where printed. Three of these were processed in the oven for 10 minutes at $110^{O}C$ to provide a baseline reference. The remaining 15 were then laser processed at 5, 10, 15, 20 and 25 watts with three samples per laser power. To determine the effect this has on the electrical properties, sheet resistance and hall effect measurements were taken as shown in Figure 78(a-b).

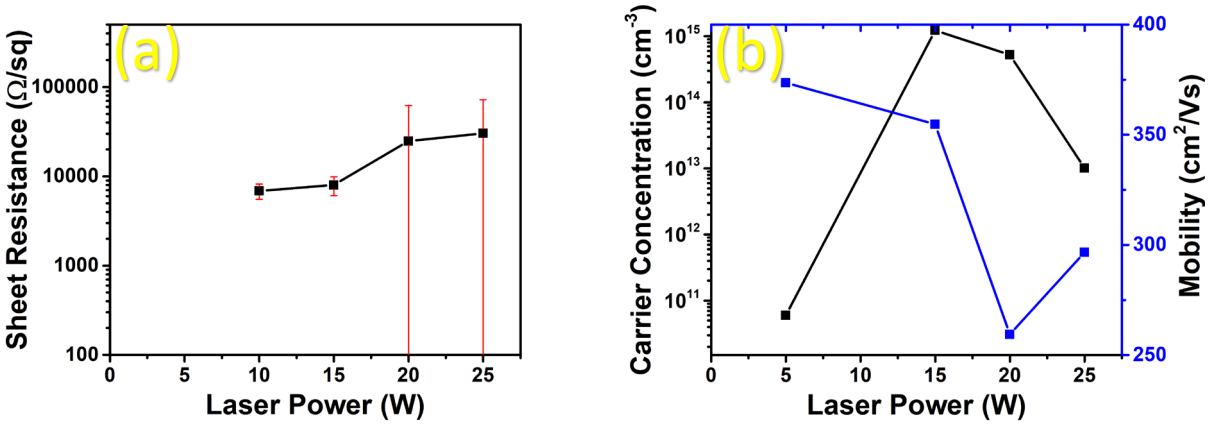

Figure 78 Electrical properties of laser processed gallium zinc oxide (a) Sheet resistance versus power, (b) carrier concentration and mobility versus laser power

Analysing the sheet resistance, it can be observed that the oven cured gallium zinc oxide and 5W processed GZO does not conduct. Once the laser power reaches 10 and 15W, conductive uniform films are formed with an increase in carrier concentration and decrease in mobility. These GZO films have high mobilities compared to typical films, due to the polycrystallinity of the nanoparticles. Their low carrier concentration can be attributed to large grain boundary resistances with each individual particle having a high electron mobility.

6.3.4 Optical Properties

UV-Visible spectroscopy was performed on the GZO films to determine whether the laser processing has any effect on the transmittance of the films or the bandgap of the material. Transmittance measurements were performed by scanning between wavelengths 800 – 200nm with a 2nm slit width in a diffuse reflectance configuration. All measurements were performed blanking for the glass (referencing with substrate to prevent interference) with a spectralon reflectance standard (>99% reflectance, Labsphere). Transmittance data (Figure 79) showed that no laser treatment provided the highest transparency for a micro-dispensed thick film (100μm), transparency then decreases from 5 to 10 watts of processing power and then increasing again. Films with 20- and 25-watt processing treatments showed similar transmittance plots. A lower the angle of slope in transmittance plots can be associated with haze and increased scattering showing that laser treatment causes more disorder in the films. The increase in transparency with 20- and 25-watt treatments can be associated to a thinner film caused by laser ablation from high energy densities.

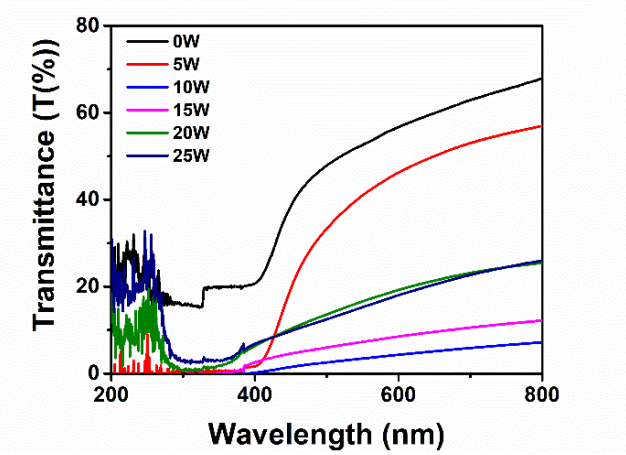

Figure 79 UV-Visible Transmittance Data for Laser Treated GZO Thick Films

For the calculation of the bandgaps, Tauc plots (Figure 80(a)) were used by converting the transmittance data into absorbance using Equation 10. Where the energy of light is enough for electrons to be excited from the valence to conduction band, a straight line can be observed on a plot of photon energy versus quantity of light absorbed. This can then be extrapolated as demonstrated via the red line in Figure 80(b) to find the bandgap of the material. Zinc oxide materials are direct bandgap semiconductors, therefore bandgap calculations were made for allowed direct electron transitions only.

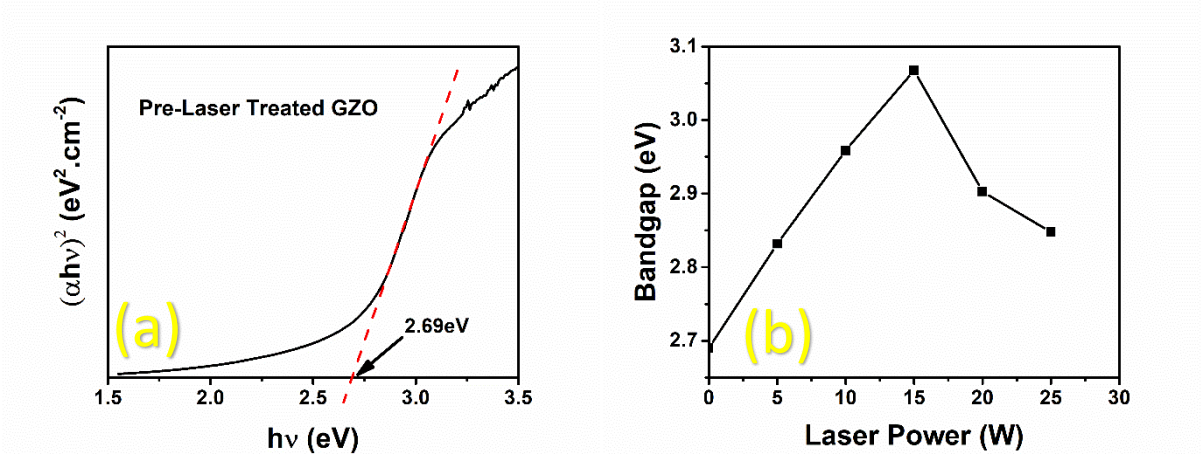

Figure 80 (a) An example of a Tauc Plot and (b) Bandgap data for non-laser treated GZO thick film

The bandgaps were calculated for GZO thick films processed at differing laser power levels and can be seen in Figure 80. The data shows the bandgap appearing to increase with a peak with films processed at 15-watts. Typically, the decreasing of a bandgap will result in an increase of semiconductor conductivity. However, this increase also occurs with an increase in conductivity. This can be attributed to the Moss-Burstein effect where a material becomes conductive enough to have electrons resting in the conduction band (ref). Due to this, electrons must be excited to a state higher than the conduction band creating an apparent increase in the bandgap. The peak at 15-watts matches the peak in carrier concentration observed in Section 6.3.3, confirming the conductivity versus increase in bandgap relationship. This apparent rather than actual bandgap change is just as useful for optical devices and demonstrates that the bandgap of the material can be altered via laser processing.

6.3.5 SEM Analysis

Field emission gun scanning electron microscopy was performed on the laser processed samples with images shown in Figure (81). The unprocessed material (a) can be seen as a dense highly polycrystalline film with the particle size remaining the same but the film becoming denser with a 5-watt laser treatment (b). In Figure 81(c) at 10 watts, the particle size visibly increases from 25 – 50nm to 75 – 100nm with an underlying dense film, matching the point where films begin to see conductivity.

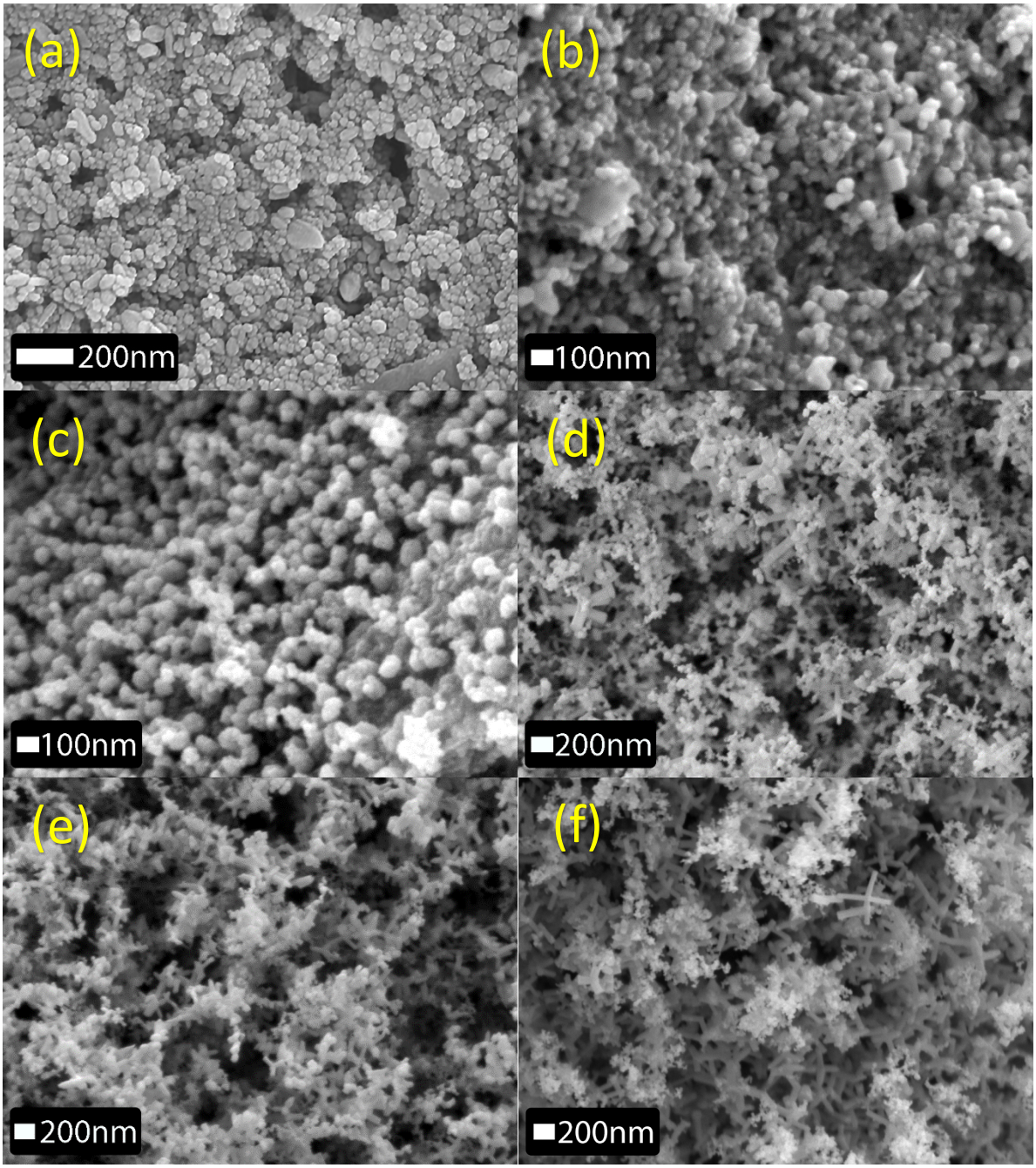

Figure 81 FEG-SEM images of (a) un-processed GZO, (b) GZO processed at 5W, (c) GZO processed at 10W, (d) GZO processed at 15W, (e) GZO processed at 20W and (f) GZO processed at 25W

At 15 watts (d), the particle size increases again with the film becoming less dense and the microstructure changing from spherical particles to dendrites (branching structures) and small zinc oxide nanorods and tetrapods. Moving to higher laser powers of 20 and 25 watts the film density remains the same. However, an increasing amount of nanorods and tetrapods can be seen with growth in crystallite size increase with laser power. The dendrites appear to convert into the rods with GZO processed at 25W. The large change in microstructure is unexpected

as the fabrication of ceramic nanorods typically require high temperature traditional thin film deposition methods.

6.3.6 EDX Characterisation

Energy dispersive X-ray analysis was performed in tandem with scanning electron microscope imaging to determine the effect of the laser processing on the overall composition of the film. In the EDX spectrum of the laser processed gallium doped zinc oxide, shown in Figure 82, a total loss of gallium dopant was observed. Most likely due to zinc oxide doping being typically unstable, especially under high temperatures.

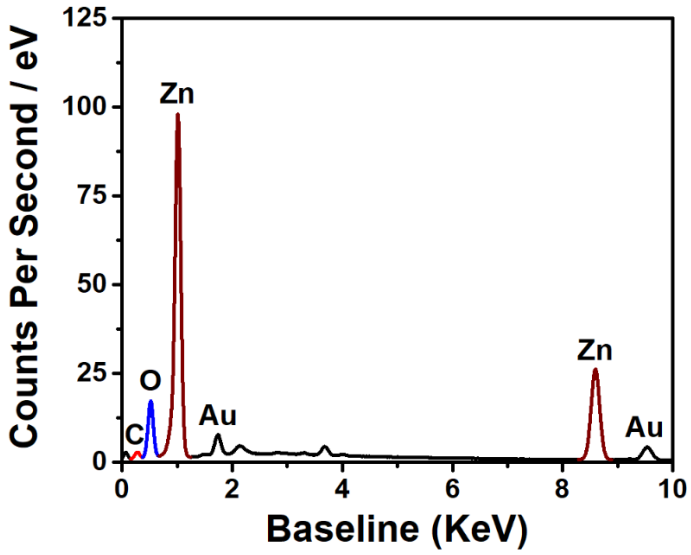

Figure 82 EDX Spectrum for Gallium doped Zinc Oxide (GZO) at 25W

If the gallium has left the material, a crystal structure change may have occurred requiring x-ray diffraction analysis.

6.3.7 XRD Characterisation and Crystal Structure Analysis

Films processed at different power levels were analysed via x-ray diffraction to determine the effect of laser processing on the crystal structure of the gallium doped zinc oxide and to look for evidence of mechanisms for nanorod and tetrapod growth. X-ray diffraction patterns can be seen in Figure 83(a) and it can be observed with an increasing laser processing power that there is no clear change in crystal structure pre or post processing. The largest change is a change in relative intensity between the (100) and (101) reflections. In the literature, zinc oxide nanorod growth is typically associated with the (002) reflection plane, however, here it is observed that the (100) plane is increasing which is associated with tetrapod growth. Therefore, the majority of the film is GZO tetrapods rather than nanorods which clarifies the SEM images seen in Section 6.3.5, for a clearer picture of the tetrapods, transmission electron microscopy is required. The only other difference observed in the XRD patterns are highlighted in red in Figure 83(a) and expanded in Figure 83(b).

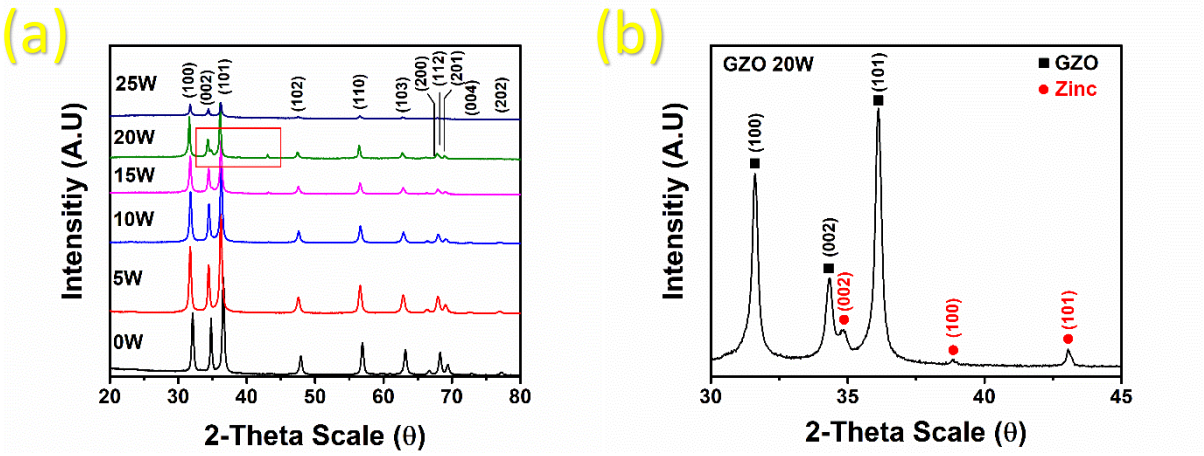

Figure 83 X-ray Diffraction Patterns for (a) Processed Gallium Zinc Oxide Films and (b) Enhanced 20W Laser Processed Gallium Zinc Oxide Displaying Evidence of Material Reduction

For the films processed at 20-watts laser power, three small peaks are observed between 30 and 45 degrees on a 2-theta scale. These peaks in the literature and open crystal databases are generally associated with the (002), (100) and (101) reflections of pure zinc metal. This demonstrates a phase separation occurring in the film between doped zinc oxide and zinc metal, indicating that the laser is inducing some sort of reduction of the zinc oxide associated with the growth of the tetrapods. The most likely type of reduction occurring is a carbothermal reduction process considering the carbon heavy nature of the inks being processed. In the

literature, this reduction process is also commonly associated with the fabrication of zinc oxide tetrapods.

From x-ray diffraction patterns, the crystallite size can be calculated giving indication of whether the laser induces crystal growth or particle fusion. Crystallite size differs from particle size, the crystallite size is the size of single crystals in the system and are also known as grains. In polycrystalline materials such as these, particles are made up of multiple single crystals being fused together, therefore, to achieve lower grain boundary resistances for higher conductivity, larger crystallite sizes are required. Calculation of the size of the single crystal is achieved by measuring the full-half-width maximum of an XRD peak and using the Scherrer equation as shown in Equation 11:

$$D_p = \frac{k\lambda}{\beta cos\theta}$$

Equation 11 The Scherrer equation

Where crystallite size (Dp) can be calculated from the shape factor constant (k) which is assumed to be 0.9 for most particle morphologies, β is the line broadening in radians, θ is the angle of reflection and λ is the wavelength of x-rays used (1.541874 Å). An internal reference such as alumina can be added to the material for more accurate crystallite size measurement, however, as a secondary material can affect the optical properties and therefore the crystal structure changes post laser processing, crystallite size in this context is being used as a comparison to GZO powder. This method assumes that the material adheres exactly to its shape factor, adding error to the calculated data. However, it is useful for determining trends internally within a dataset. Calculated crystallite size data for the GZO is displayed in Table 18:

Table 18 Crystallite Size Data for GZO

	Crystallite Size per Reflection		
Sample	***(100) /nm***	***(002) /nm***	***(101) /nm***
GZO Powder	22.77	28.44	23.21
GZO Ink	17.81	22.85	20.61
GZO 5W	21.72	25.10	20.94
GZO 10W	22.15	25.51	22.22
GZO 15W	24.38	24.52	24.23
GZO 20W	31.27	23.18	29.79
GZO 25W	40.32	23.17	34.92

Analysing the crystallite size data, a decrease in crystallite size can be observed from powder form to ink form. As no processing has occurred on the powder, this is most likely due to an increase in lattice strain. An increase in lattice strain can be attributed to impurities in the film such as organics or the crystalline structure being defective. Both of these are likely to be the case in unprocessed printed GZO as the majority of organics have not burned off while the film is polycrystalline and compact giving rise to crystal defects.

After laser processing, looking at the main reflection planes (100), (002) and (101) growth is observed mainly in the (100) and (002) planes moving from 0 to 5-watts. Growth in the (002) plane peaks at 10-watts while at 25-watts processing power the (100) and (101) planes give 40.32nm and 34.92nm respectively. The lattice planes are shown in Figure 84.

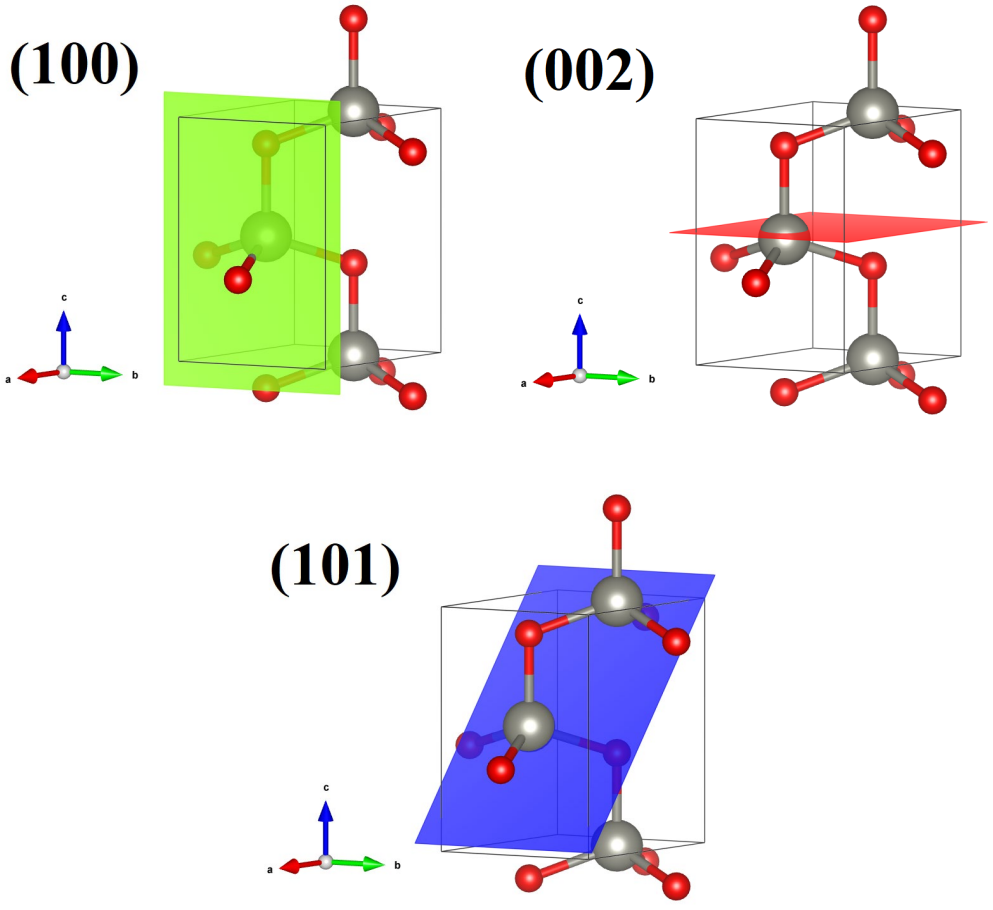

Figure 84 Three Primary Lattice Planes for Zinc Oxide Single Crystals

As the (002) plane is associated with a join in the tetrapod structure, as the intersections do not show any signs of growth in the SEM images, the (100) and (101) planes growing indicates a lengthening of the ZnO in the rod and tetrapod morphologies.

6.3.8 XPS Analysis

X-ray diffraction analysis suggests a reduction process involving the metal oxide is involved while giving no indication on how either the gallium dopant or the carbon has interacted with the system. X-ray photoelectron spectroscopy was performed to gather information on these aspects of the laser processing with Figure 85 detailing XPS data for printed and unprocessed GZO and for GZO processed at 20-watts. The 20-watt processed sample was chosen due to it having a clear zinc metal phase in the XRD. The high resolution XPS scans were performed for Carbon, Zinc, Gallium and Zinc Oxygen bonding electrons with all scans being referenced to adventitious carbon at 284.4eV. In Figure 85(a), a high-resolution scan pre and post processing for carbon is shown suggesting a majority of the carbon and organic binders have been removed as the C-N, C-O peaks have disappeared, the two main bonding configurations of the nitrocellulose binder.

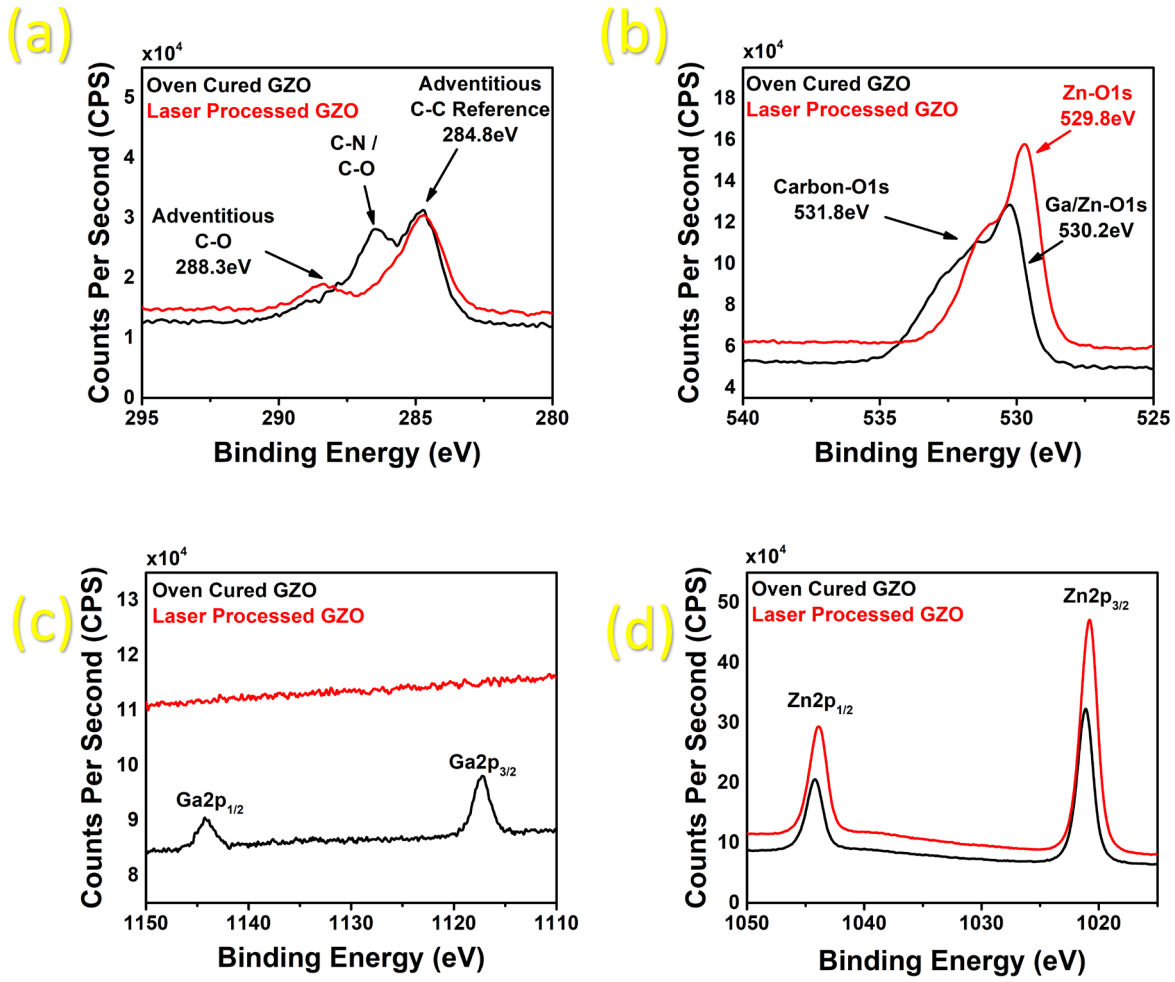

Figure 85 XPS Spectra for Pre and Post Processed GZO detailing (a) Carbon, (b) Zinc and Gallium, (c) Gallium and (d) Zinc

For the zinc-gallium-oxygen bonding scan, a shift of 0.4eV between pre and post processed material is observed. Comparing to literature values, this suggests a conversion of Gallium and Zinc oxygen bonds converting into purely zinc oxygen bonds and that a removal of the gallium dopant has occurred. Analysing the pure gallium content in the film pre and post processing, it is clear that the gallium dopant has been completely removed via the laser treatment suggesting that the gallium doping is not temperature stable. In Figure 85, (d) the high-resolution scan fails to provide extra evidence of the reduction process occurring as no appreciable amount of zinc metal is found. However, XPS is a surface only technique, only penetrating a few nanometres into a sample and any exposed zinc metal in an atmosphere of air will rapidly grow an oxide layer.

6.3.9 TEM Analysis

Transmission electron microscope (TEM) imaging was performed on a 25-watt laser processed gallium doped zinc oxide sample. The 25-watt sample was analysed via TEM due to it being the only set of GZO samples to display nanorod growth with TEM required to analyse the growth mechanism. The imaging confirms what can be seen in the SEM analysis, suggesting that there is not one overall morphology but a mixture of fine dendrite structures and particles, tetrapods and nanorods. As can be seen in Figure 86 (a -b) there is a large amount of differing particle structures with not one structure being in excess with a large and varied amount of particle sizes.

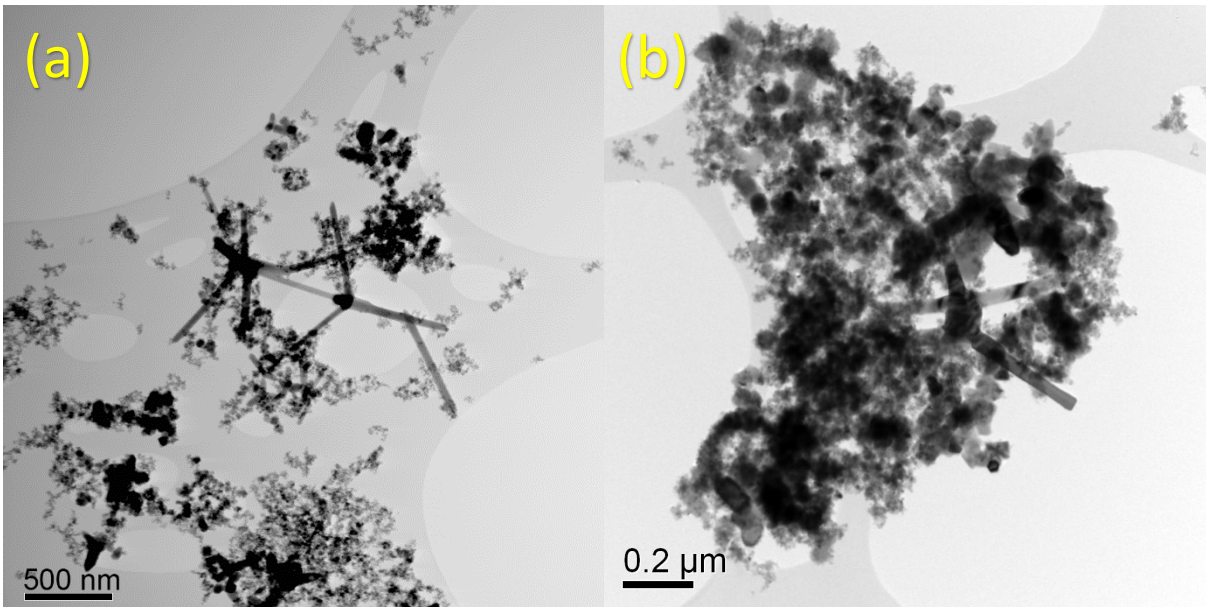

Figure 86 Transmission Electron Microscope Images for Processed at 25 Watts Gallium Zinc Oxide Films showing (a) Particle Morphology Mixture and (b) Typical mixture of Sample Particles Including Dendrites, Rods and Tetrapods

This provides evidence that for the GZO, the laser cannot selectively fabricate a single crystal structure. During processing the laser power has a ramp up and ramp down for each 300-micron line processed meaning the film experiences differing amounts of energy across the print in a non-uniform manner. This combined with the rich array of structures zinc oxide crystals can form creates a situation where many particles are experiencing many different processing conditions on one film, creating no consistent morphology.

Due to the large number of different microstructures, energy dispersive x-ray spectra were taken for each morphology found including a map in a region of the sample displaying a large variation of structures. Oxygen, zinc and gallium content were analysed for each particle using a point and identification EDX setup, providing highly accurate compositional data for a small region of space. Although this method provides more accurate data than mapping, the point and ID beam spot is 80μm in diameter so overlap with nearby particles is possible. Figure 87 (a), displays a transmission electron microscope image with six particles for compositional analysis labelled and numbered in red. The corresponding EDX spectra for the labels can be seen in Figure 87(b).

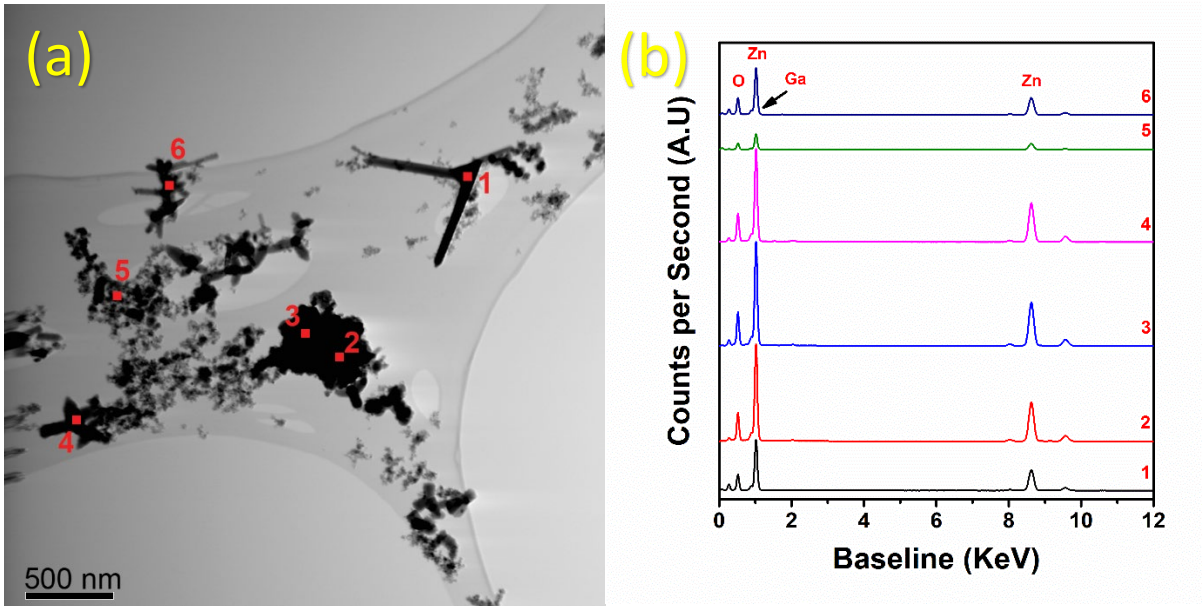

Figure 87 Point and ID Elemental Analysis Data Showing (a) TEM of Particles and Analysis Sites and (b) EDX Data for Corresponding Analysis Sites

Compositional data in the form of both weight and atomic percentages for the EDX point and ID samples shown in Figure 87 (a) is shown in Table 19. From the elemental analysis, it is clear that the gallium has mostly been removed from it's original 2at% dopant concentration for all morphologies. In terms of atomic percent, literature values of zinc oxide show a 50:50 ratio between zinc and oxygen atoms. The particle at site 2 in the absence of 2% gallium shows an approximate 47:53 ratio between zinc and oxygen. This data suggests this is a particle which has not reached the energy required to undergo a laser induced change but absorbed enough energy for the gallium to leave the crystal structure and to be replaced with oxygen.

Table 19 Point and ID Elemental Analysis Data Corresponding with Figure 87

Site	Morphology	Zn (wt%)	O (wt%)	Ga (wt%)	Zn (at%)	O (at%)	Ga (at%)
1	Nanorod	76.42	23.51	0.06	44.29	55.68	0.03
2	Spherical	78.46	21.54	0	47.13	52.87	0
3	Spherical	77.36	22.6	0.03	45.58	54.41	0.02
4	Tetrapod	77.93	21.99	0.08	46.43	53.52	0.04
5	Fine	72.39	27.61	0	37.23	62.71	0.06
6	Nanorods	72.39	27.61	0	39.08	60.92	0

Site 2, therefore, is the closest particle found to the completely unreacted starting GZO and can be used as a reference to compare every other particle to. Each of the other particles show zinc atomic percentages between 37 and 46% implying an oxidation of the zinc greater than pure zinc oxide. When zinc metal oxidises, the oxygen forms a crystal lattice with the zinc in a 50:50 ratio, however, during this process it has been reported in the literature that chemisorption of extra oxygen can occur, trapping excess oxygen in the lattice structure. This provides evidence that particles with excess oxygen content not explained via loss of the gallium dopants, must have been formed via reduction of the zinc oxide, then re-oxidation in the presence of air. It appears that during this re-oxidation, a recrystallisation occurs forming the variety of microstructures observed in SEM and TEM measurements.

Selective area electron diffraction patterns were taken for particles of unprocessed gallium zinc oxide in order to calculate the d-spacings and therefore the unit cell volume of the material pre and post processing and can be seen in Figure 88(a-d). Calculated d-spacings before and after laser processing are shown in Figure 89(a-b) which are consistent again with the gallium doping leaving the zinc oxide crystal.

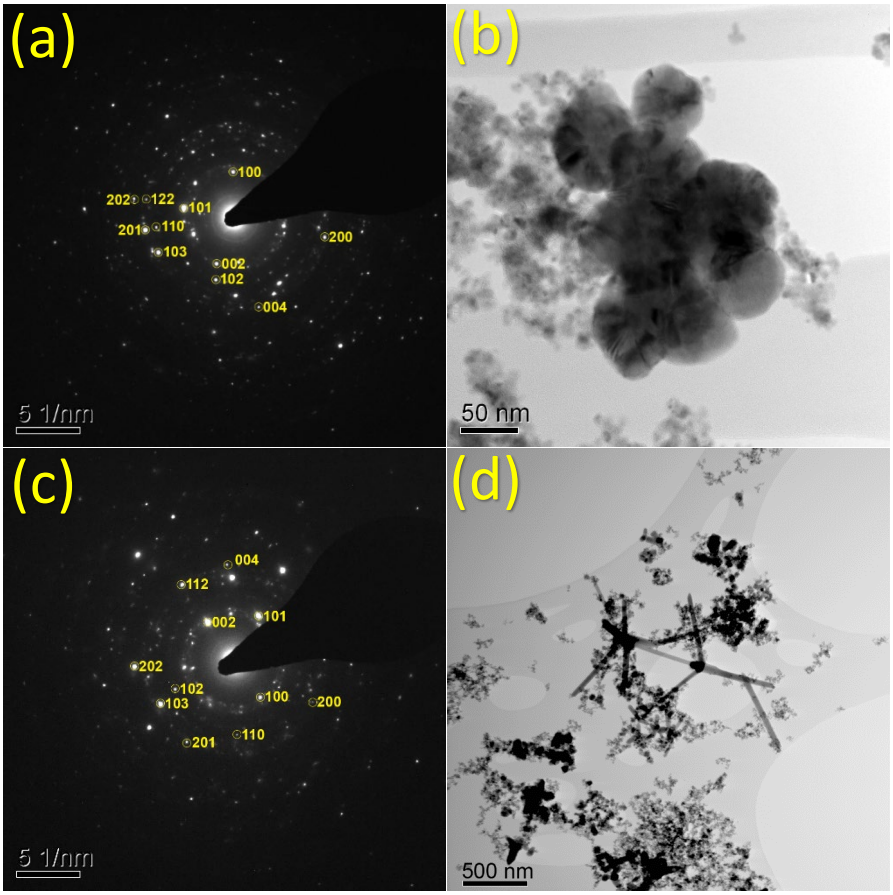

Figure 88 Transmission Electron Microscope Images for Processed at 25 Watts Gallium Zinc Oxide Films showing (a) Selected area electron diffraction pattern for pre-processed GZO (b) TEM image of unreacted GZO particles, (c) selected area electron diffraction pattern for nanorods and (d) TEM image of the analysed GZO rods

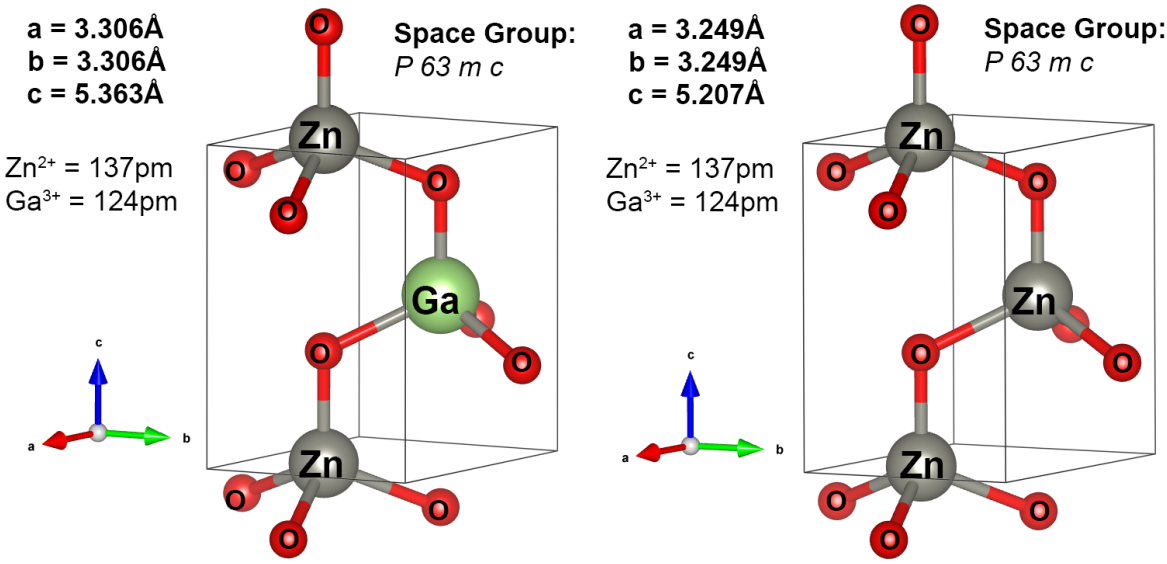

Figure 89 (a) GZO and (b) ZNO crystal structure with measured and calculated d-spacings and ionic dimensions

6.4 Processing of Indium Tin Oxide

6.4.1 Thermogravimetric Analysis of Indium Tin Oxide Powder

For the indium tin oxide, data showing weight percentage change and heat flow from differential scanning calorimetry is shown in Figure 90. The indium tin oxide was measured from 20 to 1200°C with a ramp rate of 5 degrees per minute which provides high resolution for ceramics. Samples were measured in air as laser processing is performed in air it provides more realistic information. Analysis of the weight percentage change with regards to increasing temperature shows a general trend of rising across the measurement. For two of the samples there is a drop at 300°C of approximately 1wt%, a literature search of potential precursor materials suggest this could be due to indium nitrate which shows similar weight loss behaviour between 250 – 300°C in literature TGA data [295]. For the sample which shows no drop, as the powder was mixed and randomly taken pre-measurement, it is possible no left-over precursors were in the sample, the DSC data is also highly repeatable suggesting no error with the experimental equipment.

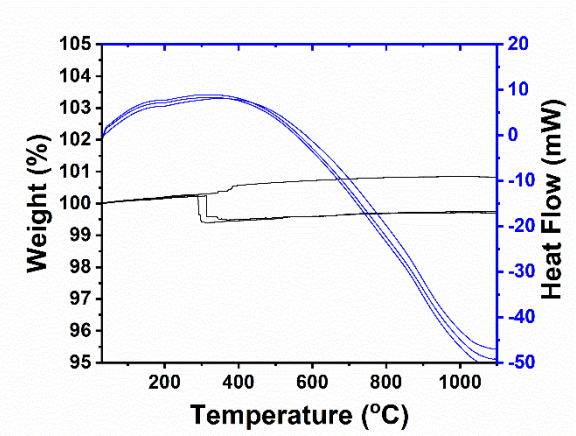

Figure 90 Thermogravimetric (TGA) and Differential Scanning Calorimetry (DSC) data ITO Powders

Typically, the increase in weight demonstrated in Figure 90 could be due to further oxidation of the indium tin oxide, or chemisorption of oxygen in air filling the oxygen vacancies in the crystal structure. As the material absorbs more oxygen, the weight will slightly increase. The DSC data shows an exothermic plateau between 100 and 500oC, this is most likely due to partial melting of any inorganic precursors (Tin Chloride, Indium Nitrate) and the melting of any non-oxidised metallic impurities. Both indium and tin melt at 156°C and 231.9°C

respectively. Towards the end of the measurement, a large trend towards an endothermic peak is shown. This is due to reaching the recrystallisation temperature of the indium tin oxide material.

6.4.2 Optimisation of Printing Parameters Via Printed Tracks

Stylus profilometry analysis was performed on the most conductive ITO tracks. The stylus moves across all five lines, three times. Profile 1 is the end of the laser sintered track, profile 2 is the centre of the track and profile 3 is the start of the tracking where the laser first powers up for raster.

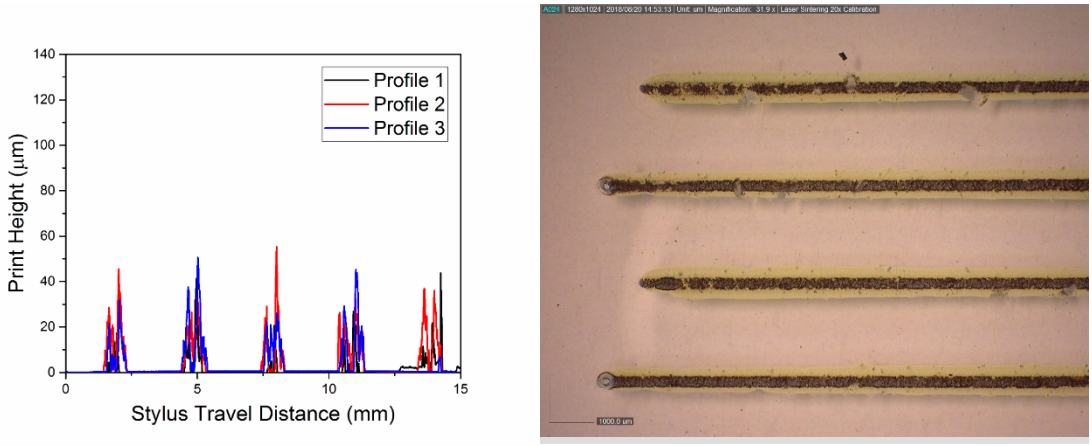

Figure 91 Profilometry Analysis of Printed ITO Tracks

As the indium tin oxide absorbs much more light energy than the GZO, good sheet resistance values can be achieved with a lower laser power. For 250micron thick tracks, sheet resistance values are on par with oven cured bulk samples from Chapter 5. The processed tracks are also much more uniform than the GZO, with tracks averaging between 9.58- and 12.4-micron layer heights.

Table 20 Laser Processed Resistivity Data for ITO Composite Nano-Inks

Printed Track	Sheet Resistance	Mean Track Thickness / µm	ρ Resistivity / Ωcm
1	184.52	12.2	2.25×10^{-1}
2	192.88	11.5	2.22×10^{-1}
3	247.3	9.58	2.37×10^{-1}
4	181.23	12.4	2.25×10^{-1}
5	87.42	11.9	1.04×10^{-1}

From the data shown in Table 20, the average resistivity of ITO processed tracks is 2.03×10^{-1}Ωcm which is 3.46% the resistivity of the bulk material discussed in Chapter 5. For thick, large

area films the parameters of 30mm/s raster speed and 1 pass of the laser will be chosen and varied with laser power so conductivity versus laser power can be isolated and analysed.

6.4.3 Electrical Properties

After optimal raster speed and lass pass amount parameters where determined, 18 thick films where printed. Three of these were processed in the oven for 10 minutes at 110^{O}C to provide a baseline reference. The remaining 15 were then laser processed at 2.5, 5, 7.5, 10 and 15 watts with three samples per laser power. To determine the effect this has on the electrical properties, sheet resistance and hall effect measurements were taken as shown in Figure 92(a-b).

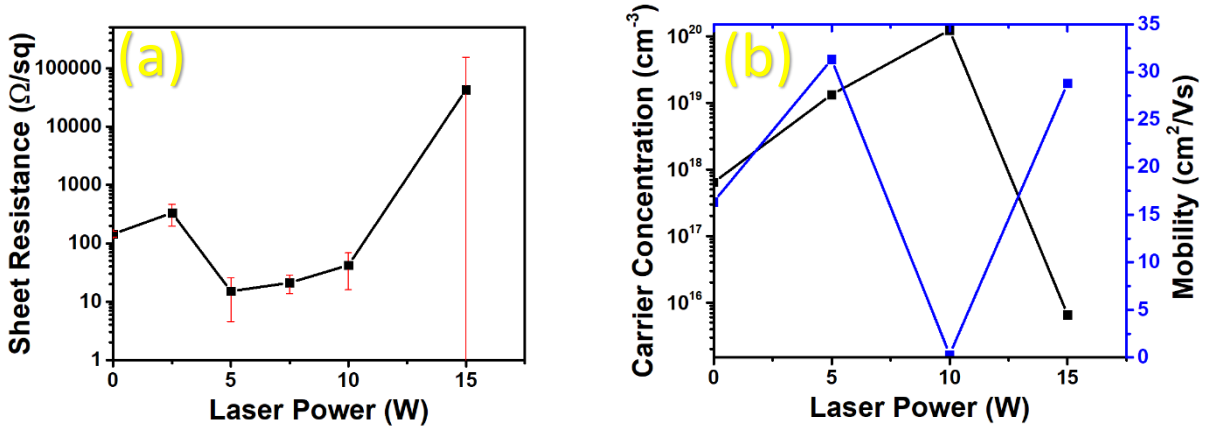

Figure 92 Electrical properties of laser processed GZO (a) Sheet resistance versus power, (b) carrier concentration and mobility versus laser power

Initially, a laser treatment performed at 2.5W leads to an increase in sheet resistance and decrease in film uniformity, this can be associated with the laser only outputting peak power after a rise and fall time delay. At 5W the most conductive films are created with an average sheet resistance of 15Ω□$^{-1}$ being formed. This is also associated with an increase in carrier concentration of 1.33x10^{19}cm^{-3} and the highest average mobility of all processed films at 31.3cm^2/Vs. Between 5 and 10 watts sheet resistances and film uniformity is improved while at the highest power, film uniformity becomes worse with sheet resistance ranging between 10Ω□$^{-1}$ and 1.07MΩ□$^{-1}$ due to laser ablation of material creating a non-uniform layer thickness. As nanowires begin to form, a large drop in mobility is observed which is associated with smaller crystallite size, with nanowire growth at 15W carrier concentration decreases with electron mobility increasing.

6.4.4 Optical Properties

Transmission measurements were taken of the ITO films at different processing powers. Due to the bandgap absorption of ITO being further into the high energy UV region, bandgap values could not be determined, therefore it is inconclusive whether the bandgap can be tuned for the ITO. Reflectance measurements were also taken in the hopes of employing the Kubelka-Munk method of derterming band gap from reflectance spectroscopy, however, this was also unsuccessful. Due to film uniformity issues in the 15W laser processed sample, absorbance, reflectance and transmittance data were too noisy for accuracte measurement. However, the data for 0 to 10W its shown in Figure 93.

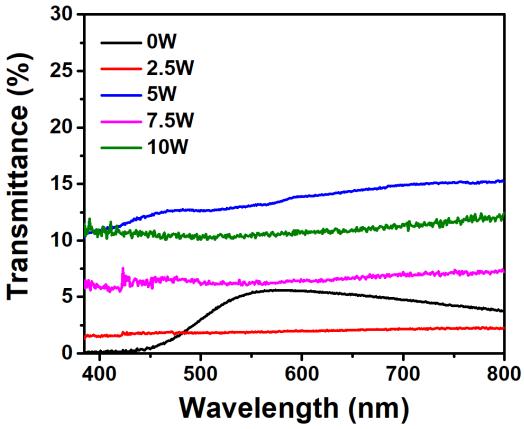

Figure 93 Transmittance Data for ITO films processed between 0 to 10W

Transmittance values at 550nm were 5.35%, 1.90%, 13.06%, 6.24% and 10.29% for 0, 2.5, 5, 7.5 and 10W processed films respectively. Therefore the data appears to match the SEM evidence in the next section, where for 2.5W films, a densification occurs without a large particle size change, lowering the transmittance. For 5W, the particle size decreases in a similarly dense film, allowing for more light to pass through, then a dual action of particle sizes increase with particle size increases allow for more light to pass through at higher powers. However, all of the transmittance values are still well below anything that would be transparent to the human eye and therefore it can be concluded that for ITO laser processed samples, in this experiment the processing does not alter the transparency in any meaningful way.

6.4.5 SEM Characterisation

Field emission gun scanning electron microscopy was performed on the laser processed samples with images shown in Figure 94. The unprocessed material (a) can be seen as a relatively porous polycrystalline matrix. The particle size drastically reduced and resulted in a denser film with a 2.5-watt laser treatment in Figure 94(b), the particle morphology continues to be a mixture of spherical and cubic crystals. In Figure 94(c) at 5 watts, the sample with the lowest sheet resistance, counterintuitively a highly porous, dendritic nanostructure has formed from cubic indium tin oxide crystals with small needle like particles seen in the background of the micrograph.

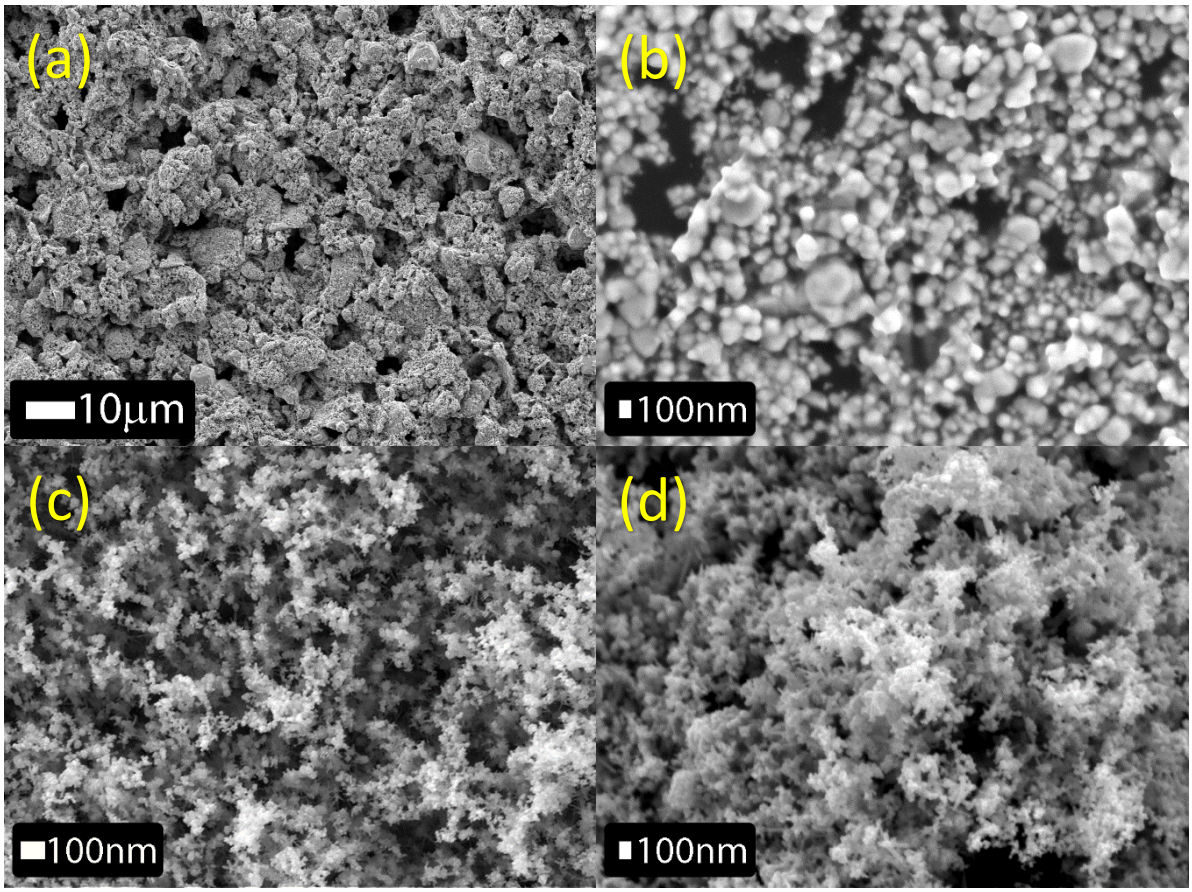

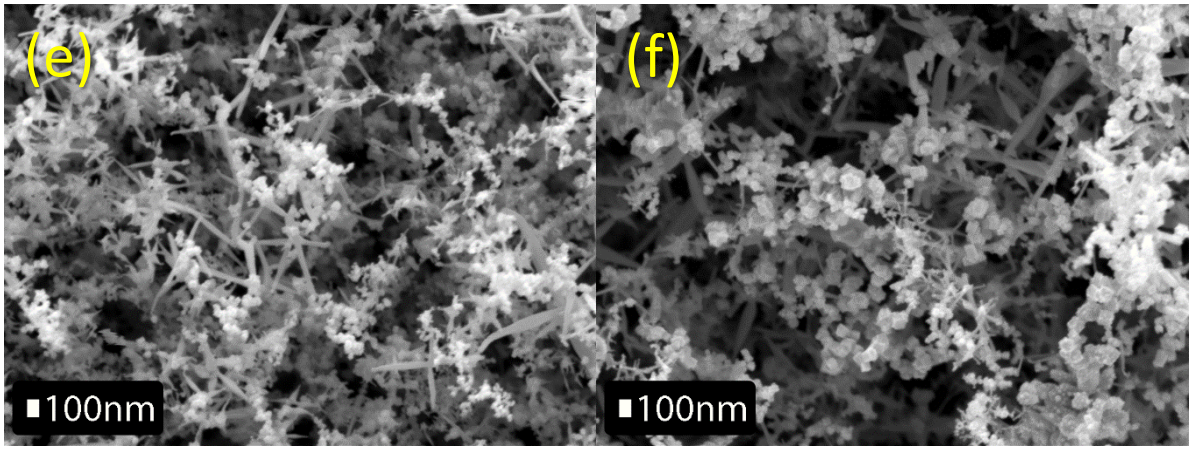

Figure 94 FEG-SEM images for printed thick films, showing (a) oven cured ITO, (b) ITO processed at 2.5W, (c) ITO processed at 5W, (d) ITO processed at 7.5W, (e) ITO processed at 10W and (f) ITO processed at 15W

At 7.5 watts (d), the overall structure and mix of morphologies is not dramatically changed, a smaller increase in particle size is observed suggesting a breakdown and recrystallisation of the material in a similar fashion to the gallium zinc oxide material discusses in Chapter 6. Moving to higher laser powers of 10 and 15 watts it can be seen that the majority of the film converts into cubic dendritic structures with a large amount of indium tin oxide nanowires and tetrapod wires. With increasing laser power, it can be observed that the length and width of the nanowires increases suggesting a relationship between the growth of these structures and laser power.

6.4.6 EDX Characterisation

EDX characterisation was performed on the nanowire structures, however, due to the high energy required for EDX and the small size of the nanowires, clear matching SEM's were difficult to obtain as shown in Figure 95. The counts for the EDX spectrum are also quite low, due to the high magnification imaging required. Looking at the EDX spectrum, the weight percentages of oxygen, indium and tin have increased from 22.1, 68.2 and 9.7wt% to 18.97, 62.92 and 18.2wt% respectively. Therefore, a relative decrease of indium and oxygen has occurred followed by an increase in the amount of tin. As the indium and tin cannot convert or disappear from the crystal without another phase being detected, suggesting a migration of tin from the inside to the surface of the particles. The decrease in oxygen suggests another reduction process occurring, similarly to the GZO discussed earlier.

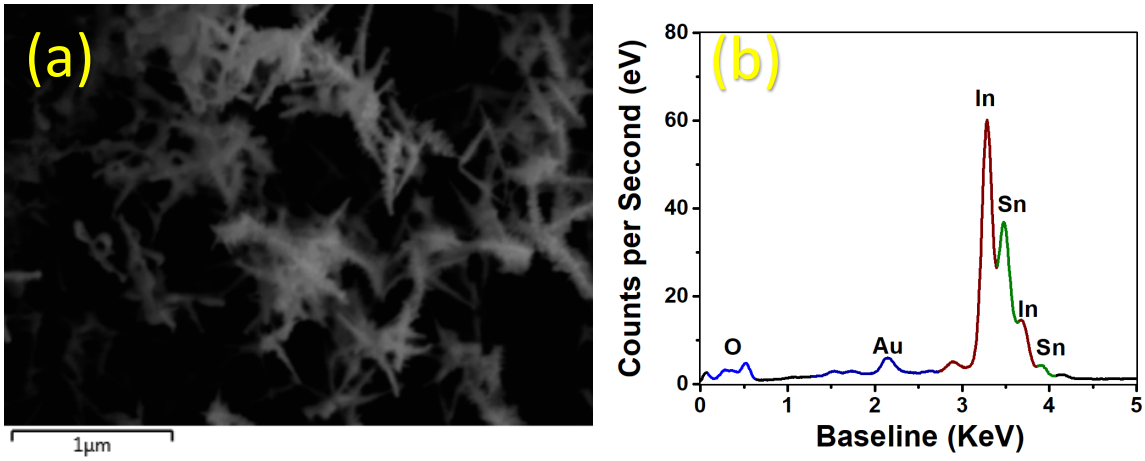

Figure 95 EDX Data showing (a) EDX image for ITO Nanowires and (b) EDX Spectra of the nanowires

6.4.7 XRD Characterisation

X-ray diffraction patterns were taken for the printed and processed films to determine any changes in crystal structure with regards to laser power (Figure 96(a-b)). Pure phase ITO is seen with inks cured in the oven, whereas after laser processing at any power a varying amount of corundum type indium oxide and tin metal as can be seen in Figure 96(b). This suggests the laser is causing a small phase separation in the indium tin oxide with a reduction of the tin oxide metal occurring. As the tin oxide doping is less than 10%, the tin oxide phase cannot be detected via XRD.

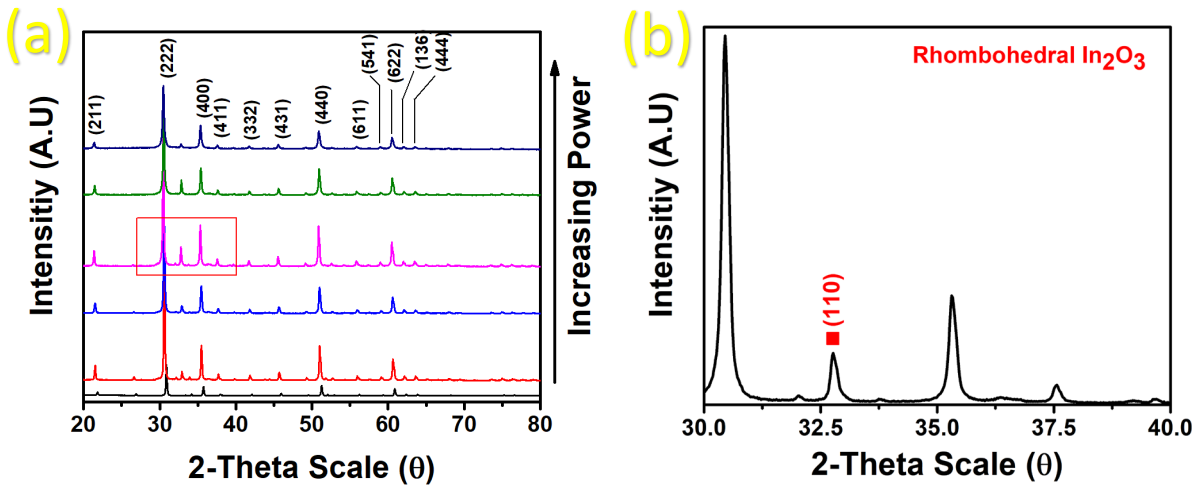

Figure 96 X-ray diffraction patterns for (a) indium tin oxide processed at various laser powers and (b) an enhanced area of 7.5-watt laser processed ITO diffraction pattern highlighting compositional change

A relative intensity change is also seen with increasing laser power. At powers were nanowires begin to form there is a 10% increase in the ratio between the (222) and (400) plane which is typically associated with an increasing level of oxygen vacancies in the ITO crystallites. This again provides evidence that the laser treatment is creating a reduction reaction within the material.

Calculated crystallite size data for the ITO is displayed in Table 21:

Table 21 Crystallite Size Data for ITO

	Crystallite Size per Reflection			
Sample	***(222) /nm***	***(400) /nm***	***(440) /nm***	***(662) /nm***
ITO Powder	43.74	44.36	42.46	44.12
ITO Ink	48.60	48.31	47.67	46.40
ITO 2.5W	46.68	42.65	36.65	32.47
ITO 5W	38.02	37.16	32.47	29.02
ITO 7.5W	45.76	43.40	35.79	32.15
ITO 10W	79.63	77.02	67.10	61.91
ITO 15W	65.82	65.10	52.63	51.18

Analysing the crystallite size data, an important note must be made about using the Scherrer equation to calculate the crystallite size between two different morphologies. As ITO processed at 10 and 15 watts has become wire like and as the crystal is cubic with a rectangular cross section of the wire, a different shape factor must be used for 10- and 15-watt materials for an accurate comparison. In the literature, the shape factor for nanowires is proportionate to the aspect ratio of the wires, the length to width ratio. For a majority of particles, a shape factor (k) of 0.9 is adequate. However, for nanowires resulting from a 10-watt laser process, the aspect ratio was estimated to be 10:1 as analysing SEM images provided an average width of 50nm and a typical length of 500nm. For 15-watt laser processed ITO, this 10:1 aspect ratio also appeared to be the case, with a widths between 50 – 100nm and lengths between 500nm and 1μm. In the literature, assuming these aspect ratios are correct considering the small sample area seen via SEM images, the shape factor is 1.8 rather than 0.9 for 10:1 aspect ratio cubic crystal structure-based nanowires [296]. The associated lattice planes are shown in Figure 97 (a-d).

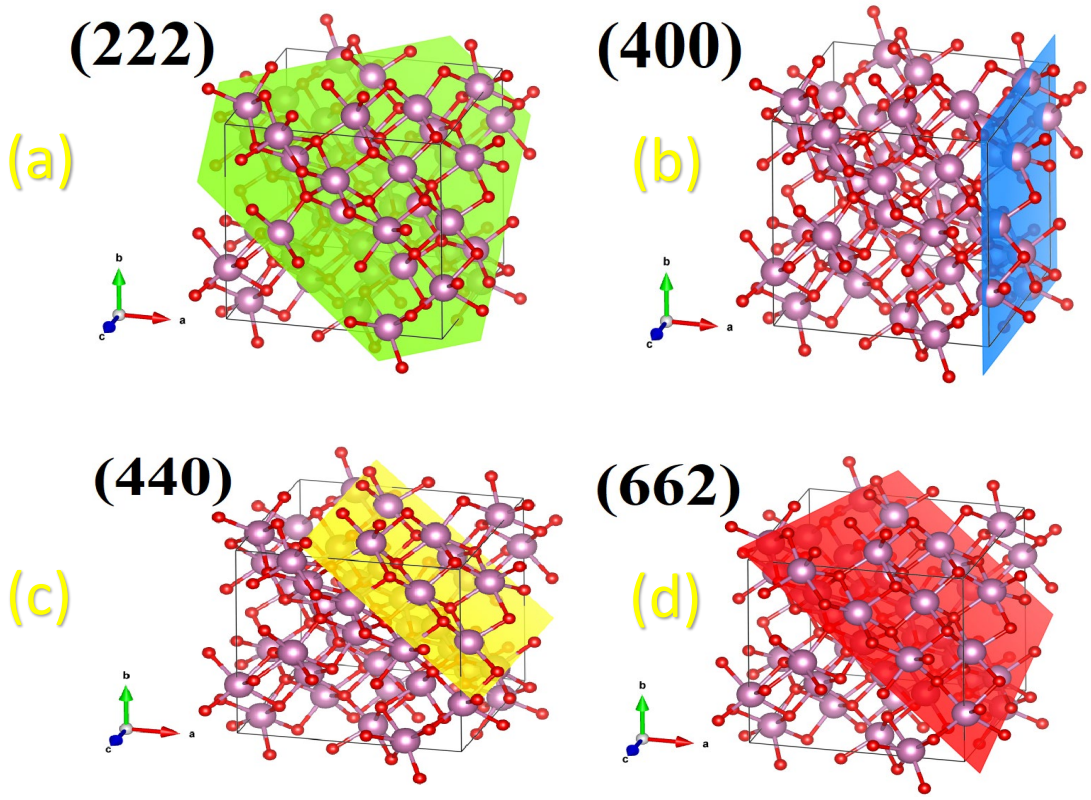

Figure 97 ITO crystal structure and lattice planes for (a) 222 plane, (b) 400 plane, (c) 440 plane and the (662) plane

Analysing the data, the crystallite sizes appear to agree with the SEM images until ITO processed with a 15-watt laser, this suggests it can be assumed that the approximation of aspect ratio and therefore shape factor is therefore not accurate. Initially with a 2.5-watt laser treatment, the crystallite size decreases and decreases yet again for a 5-watt treatment. This is also confirmed via SEM evidence which shows a decrease in particle size. Crystallite sizes then continue to grow with the 7.5- and 10-watt laser treatments with large amounts of growth in the (400) plane. In the literature, a growth in this particle reflection has been associated with an increase in ITO conductivity which is backed up with the electron mobility and carrier concentration shown in Chapter 6. Considering the conductivity data, a decrease in carrier concentration and conductivity is shown for the 15-watt laser processing samples which suggests the shape factor estimation discussed earlier may actually be correct. Due to the decrease in crystallite size for the 15-watt laser processed samples can account for the Hall effect measurements as also the nanowires are larger, there are also more dendrites seen in the SEM.

6.4.8 XPS Analysis

X-ray photoelectron spectroscopy (XPS) was performed on oven cured ITO ink versus a laser processed nanowire to determine any compositional or structural changes to the material. Surveys were performed across the spectrum with high resolution scans performed for O1s, C1s, Sn3d, In3d and InMN1 regions referenced to the adventitious carbon 1s peak. Comparing the two samples (Figure 98 (a-d)) shows large differences between the samples. It is clear that upon post processing, only adventitious carbon remains on the sample, providing clear evidence of the laser removing all of the remaining carbon vehicle. Due to this, the oxygen peak shifts 3.3eV (Figure 98(a)), signifying a removal of C=O bonds associated with the nitrocellulose binder, moving to a pure metal-oxygen bond. Although evidence of metallic tin has been detected in small quantities with the XRD, there is no suggestion of surface level tin via the XPS with measurements being consistent with tin oxide.

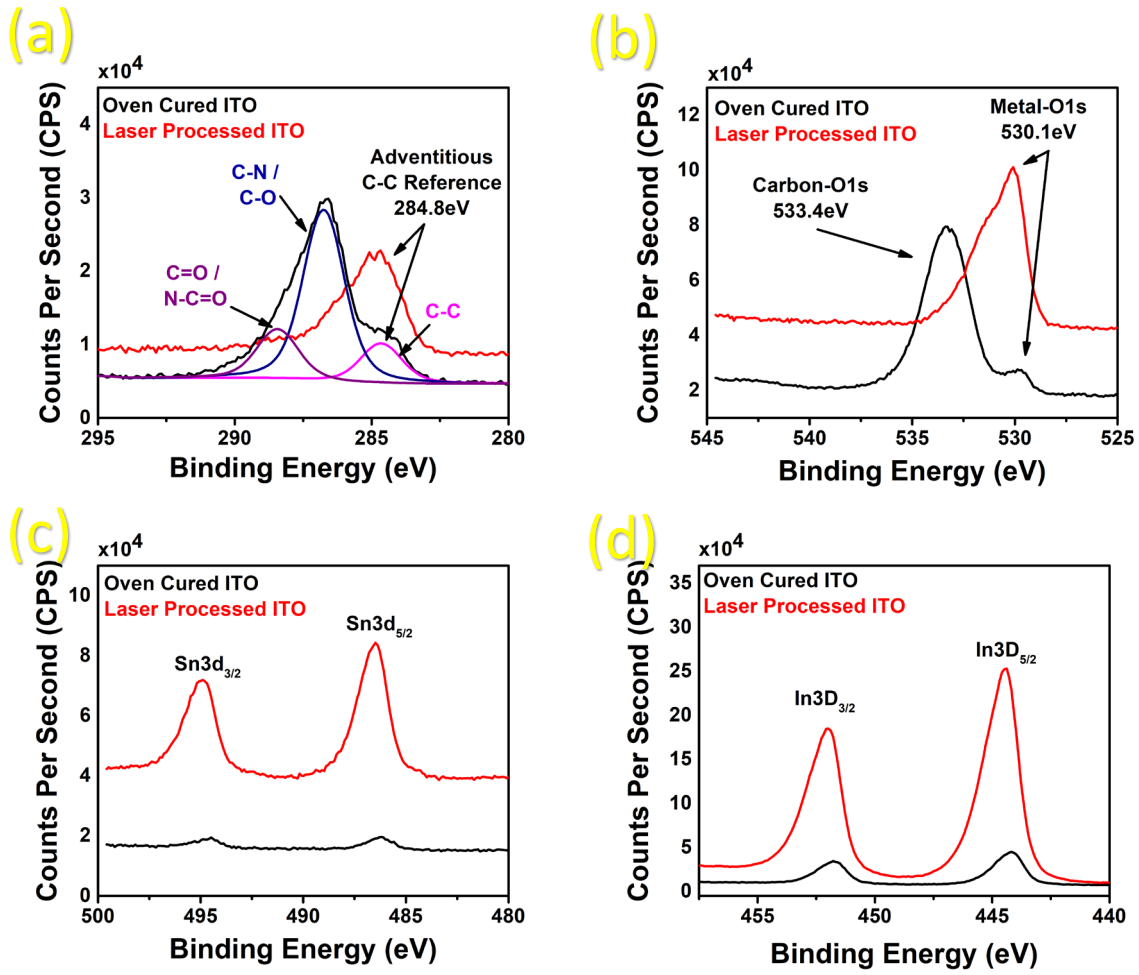

Figure 98 XPS spectra for (a) high resolution C1s scans (b) high resolution O1s scans, (c) high resolution Sn3d1 and (d) high resolution In3d1 scans

The indium 3d peaks are also broad providing evidence that the bulk of the indium is in the In2O3 configuration. The indium auger peaks InMN1 also provide no evidence of metallicity or reduction, however, surface metals will oxidise readily in air. The atomic percentage ratios of indium to tin on the oven cured sample are respectively, 8.25:1 to 5.5:1 in the laser processed sample. This provides evidence of a migration of tin from the particle interior to the exterior with the possibility of SnO2:In2O3 phase separation.

6.4.9 TEM Analysis

From the TEM analysis, it can be seen that a typical nanowire at 10W processing power had a width of approximately 10 - 20nm with lengths of 500 – 800nm, with a mixture of branching needles. These are shown in Figure 99(a-b). To determine the actual phase, composition change and crystal structure of the formed ITO nanowires, and to provide insight into the formation process, transmission electron microscopy was performed on the nanowires. As the nanowires in the 15W laser processed samples were too large for good TEM, the 10W sample was chosen. TEM imaging, elemental analysis and selected area diffraction patterns were taken for the ITO nanowires (Figure 100(a-c). From the TEM analysis, it was clear most of the film had converted to nanowires of varying amounts with dendrites and nanocubes being relatively difficult to find.

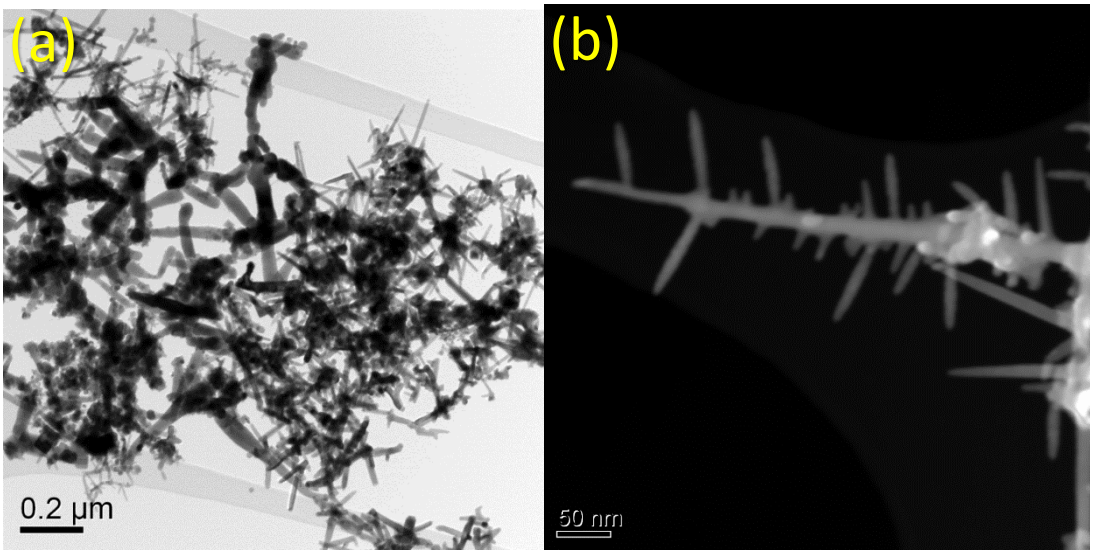

Figure 99 Transmission Electron Microscope Images for Processed at 10 Watts ITO Films showing (a) Particle Morphology Mixture and (b) close up branching nanowire

Unlike the GZO, it appears the ITO prefers to fabricate a single morphology of particles providing a much more uniform film of particles overall. This suggests that the laser processing is much more effective for materials with a smaller variety of particle morphologies as it can then consistently convert material into a single morphology.

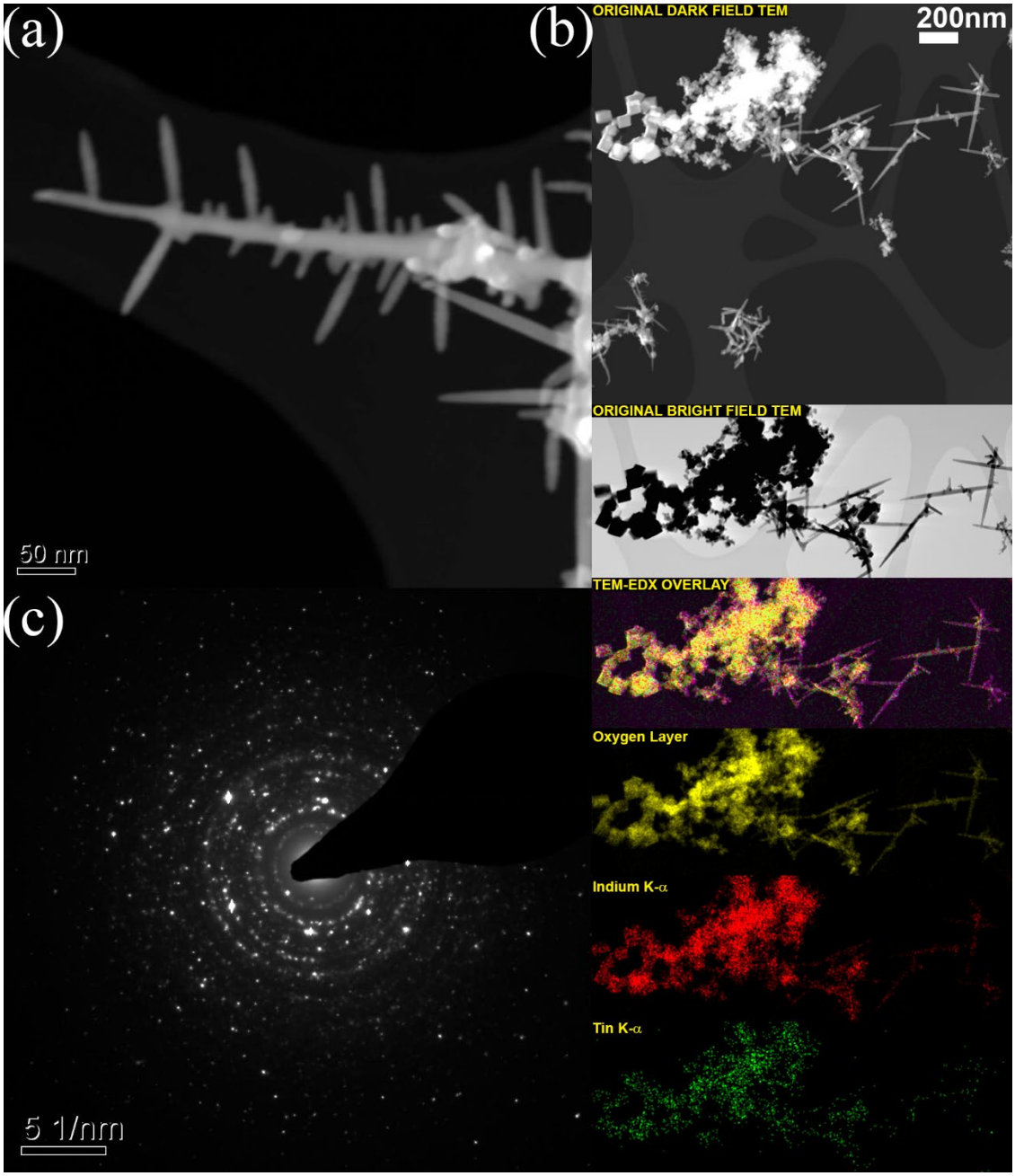

Figure 100 Transmission Electron Microscope Images for (a) 10W Laser Processed ITO Nanowire Structure (b) TEM-EDX mapping analysis of ITO nanowires and (c) Selected Area Electron Diffraction Pattern for ITO Nanowires

For the ITO nanowires, EDX mapping (Figure 100(b)) was performed on a selection of nanoparticles which show the growth process of the nanowires in action. From this TEM it can

be observed that the original cubic microparticles convert into smaller dendrite structures, these then reform into wire and whisker like structures. Point and ID EDX analysis was performed on each of these structures displayed in Table 22.

Table 22 Elemental Compositions of Laser Grown ITO Morphologies

Area	Sn (at%)	In (at%)	O (at%)
Nanowires	5.14	32.99	61.86
Cubic	8.72	56.09	35.19
Fine	5.59	35.99	58.42

As suggested in the XRD data, there is evidence of a reduction process taking place during the laser processing, driven by a carbothermal reduction of the metal oxides via the carbon heavy ink vehicle. The elemental data for the cubic particles provide more evidence for this, compared to the fine or nanowire structures, the material is oxygen deficient. The fine structures then increase in oxygen content with the nanowires containing the most amount of oxygen. During laser treatments of 10 watts or more with the indium tin oxide, the pyrometer used to measure material temperature displays greater than 1200^{O}C (the maximum limit of detection), this combined with the organic heavy ink vehicle creates an environment where the carbon acts as a reducing agent. This then reduces the metal oxide particles into oxygen deficient or metallic intermediates, burning the carbon and oxygen off as CO_2. As the ITO undergoes a re-oxidation into it's previous state, the fine particles combine into nanowires and heirarchical 3D nanowhiskers. The proposed carbothermal reduction is shown in Equation 12.

$$3In_2O_{3(s)} + 3C_{(s)} \rightarrow 3In_{(s)} + 3CO_{2(g)}$$

$$3In_{(s)} + 4^1/_2O_{2(g)} \rightarrow 3In_2O_{3(s)}$$

Equation 12 Proposed carbothermal reduction mechanism for laser induced ITO nanowire growth

Selected area diffraction patterns were taken of the ITO nanowires to determine whether the rods are formed through sintering, fusing or crystal growth. As can be seen in Figure 100(c) the selected area electron diffraction (SAED) pattern displays polycrystalline behaviour showing that the rods are not single crystal. This polycrystallinity suggests fusion of the fine particles into the branching structures.

6.5 Laser Processing of GZO Composite Inks

6.5.1 Optimisation of Printing Parameters Via Printed Tracks GZO/CNT Tracks

As discussed earlier in Section 6.3.2, GZO tracks were initially optimised for conductivity via the printing of tracks. This was also performed on the ITO/CNT and ITO/Graphene inks, resulting in in a final conductivity values of 15.96% and 1.85% of the bulk respectively. The GZO/Silver Nanowires inks provided the best results for printed tracks with a conductivity of 18.2%. After optimisation via the printed tracks, the parameters with the highest values were selected. For the GZO composites, the optimal parameters for bulk film and track fabrication are shown in Table 23:

Table 23 Optimal Parameters for the Laser Processing of GZO Composites

Ink	Laser Power / W	Speed / mm/s	Passes
GZO/CNT	2.5	40	5
GZO/Graphene	2.5	50	5
GZO/AgNW	1	30	1

Furthermore, both the conductivity and best processing parameters show that much less power is required than pure GZO attributed to the better absorbance properties of the composite ink. Therefore, less power is required to supply an adequate amount of energy to induce conductivity.

6.5.2 Optical Properties of Laser Processed GZO Composites

Once bulk films had been fabricated and processed, transmittance measurements were taken; shown in Figure 101(a-b). One observation for the bulk films is that the CNT and Graphene composites had a large decrease in film adhesion, with the top of films becoming powdery. For GZO/CNT inks, the transmittance improved, increasing from 0.854% to 7.56% at 550nm. The GZO/Graphene ink improved substantially from 1.426% to 39.21% which is still not transparent to the human eye but could be optimised more with further work. Finally, the GZO/Silver Nanowire ink reduced from 21.285% to 9.432% which is likely due to the reflectivity of the silver decreasing. SEM imaging is required to determine whether this is the case. Overall, although these differences are quite large, the increases in transmission are not enough to warrant this printing and processing method as a way to create any transparent electronics.

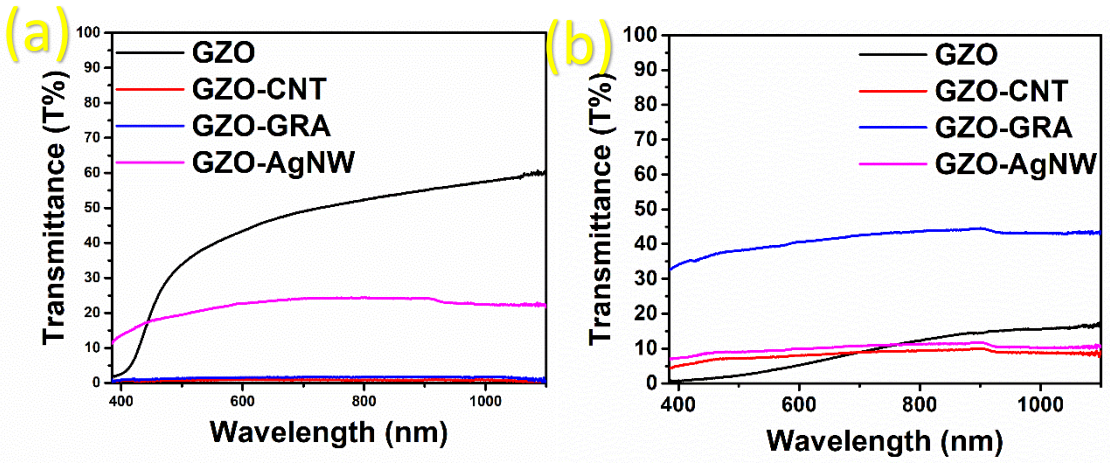

Figure 101 Optical Transmittance Data for GZO composites (a) pre laser processing and (b) post laser processing

6.5.3 Scanning Electron Microscope Analysis of Laser Processed GZO Composites

Scanning electron microscopy was used to determine what happens to the composite inks post processing with images for GZO/CNT, GZO/GRA and GZO/AGNW shown in Figure 102(a-c). It can be seen that for both the GZO/CNT and GZO/GRA, no large changes to the actual particle morphology were observed unlike the pure GZO. The GZO/GRA film is much more porous with finer particles than the GZO/CNT, explaining the transmission increase observed and the decrease in film adhesion.

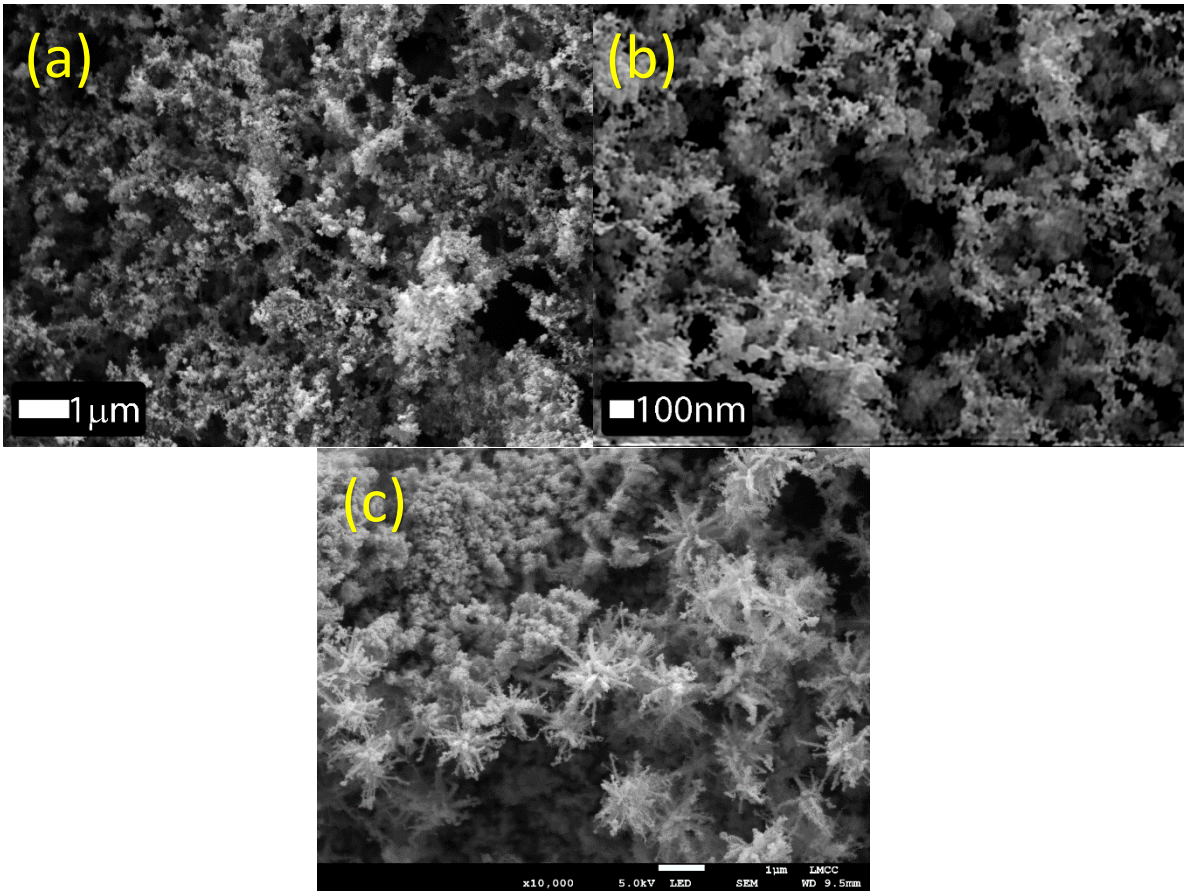

Figure 102 FEG-SEM Images of laser processed (a) GZO/CNT inks, (b) GZO/Graphene inks and (c) GZO/Silver Nanowire inks

Analysing the GZO/ Silver Nanowire film, another nanoparticle morphology is observed, adding to the tetrapods, nanorods and nanowires discussed earlier in the chapter. The laser appears to have created flower like sphere particles 1 to 2 microns across. EDX analysis is required to determine what these actually are but a preliminary suggestion is that silver nanowires have fused together and been coated in the GZO particles. XRD analysis is also required to determine if there are any crystal structure changes.

6.5.4 Energy Dispersive X-ray Analysis of Laser Processed GZO Composites

Firstly, to determine whether the flower like structures in the GZO/AgNW are in fact some zinc oxide silver amalgamation, EDX mapping was performed at high magnification and is shown in Figure 103. Due to the high magnification there is some noise, however, it can clearly be seen that the characteristic zinc Lα, silver Mα and Oxygen Ka electrons overlay with the electron image. No gallium can be seen suggesting a loss of dopant similar to what is observed with pure GZO. The resulting structure has a weight percent composition of 25.01, 72.67 and

2.33wt% for oxygen, zinc and silver respectively. This is slightly oxygen rich compared to the pure GZO, suggesting the silver has oxidised during the process in the air atmosphere or the zinc oxide has had oxygen vacancies filled in the crystal structure.

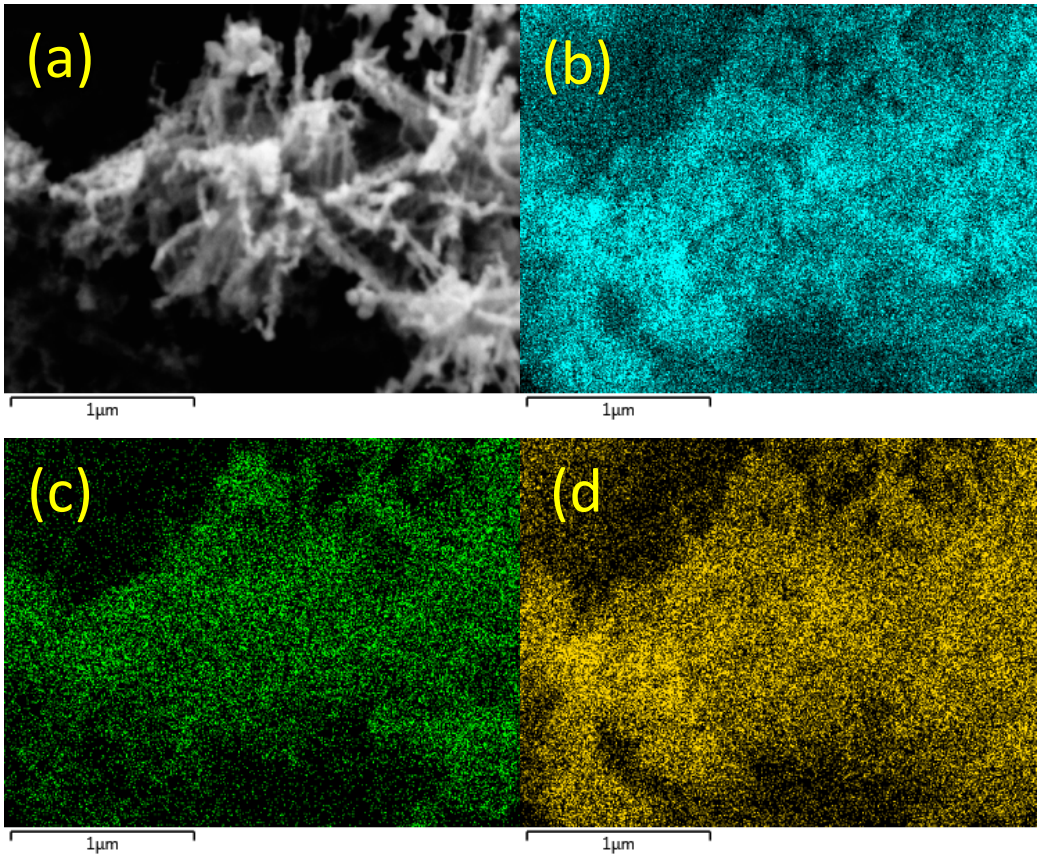

Figure 103 EDX Mapping of GZO/Silver Nanowires showing (a) the SEM for mapping, (b) the zinc map, (c) the silver map and (d) the oxygen map

It appears the silver nanowires no longer exist as no clear wire structure can be seen on the silver EDX map. There have been reports in the wider literature of silver doped zinc oxide including “micro-flower” particle structures, however, XRD analysis is required to determine whether any doping has actually taken place. With regards to the CNT/GZO ink, the final material was similar in composition to pure GZO with weight percentages of 2.36, 75.47 and 22.17wt% for gallium, zinc and oxygen respectively. The dopant being retained may explain the high conductivity relative to the pure GZO of the laser processed GZO/CNT inks. For the GZO/Graphene inks, a loss of dopant occurred with weight percentages of 81.96 and 18.04wt% of zinc and oxygen respectively. This is slightly oxygen poor again providing evidence a reduction process may occur.

6.5.5 X-ray Diffraction Analysis of Laser Processed GZO Composites

In the x-ray diffraction patterns for the processed GZO composites, shown in Figure 104(a-d), no large changes are observed other than a loss of carbon for GZO/CNT and GZO/GRA inks. A slight shift to the right in the GZO/GRA is shown which is typical of dopant loss, confirming the EDX data. Performing a Reitveld refinement on the GZO/AgNW composites, the calculated unit cell volume is the same as pure ZnO suggesting the silver has not doped into the zinc oxide and the structures must be a ZnO/Silver composite structure.

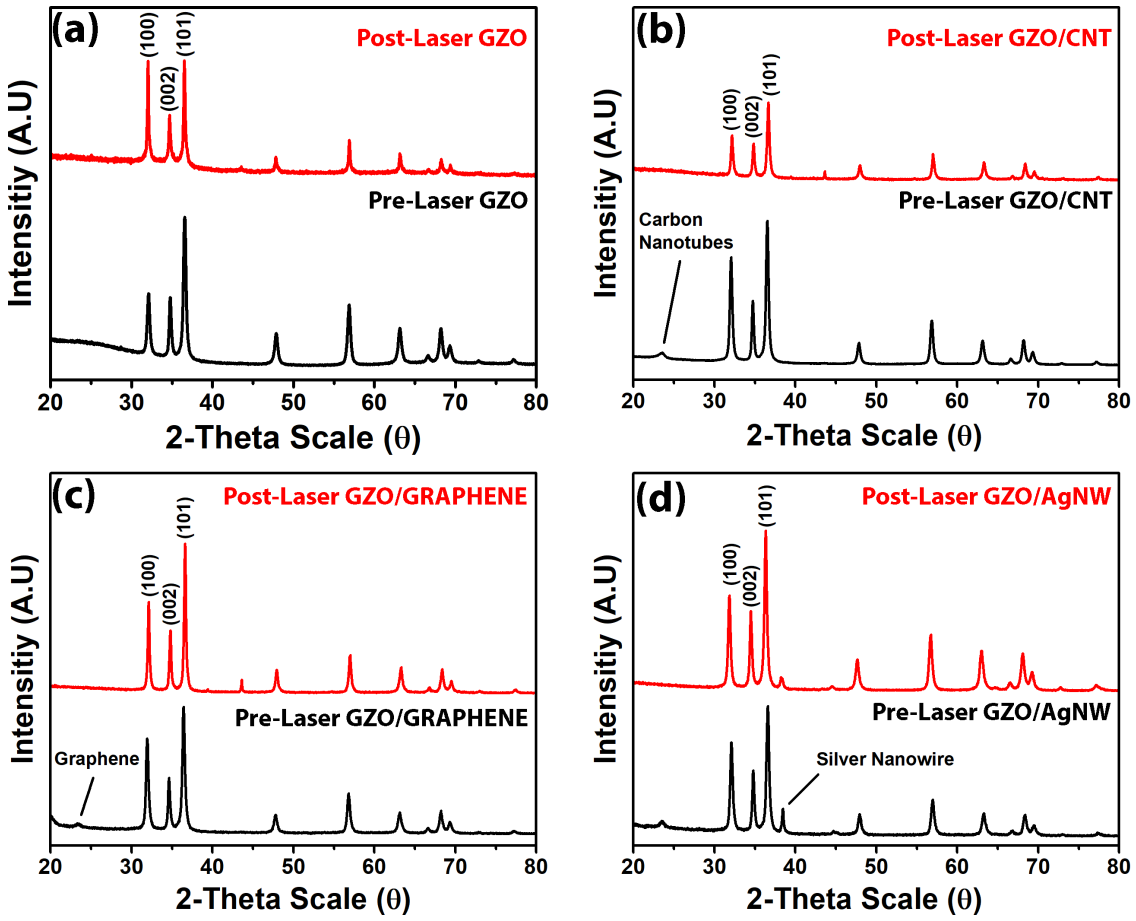

Figure 104 XRD Data for pre and post processed (a) GZO, (b) GZO/CNTs, (c) GZO/Graphene and (d) GZO/Silver Nanowires

6.6 Laser Processing of ITO Composite Inks

6.6.1 Optimisation of Printing Parameters Via Printed Tracks

As with the pure metal oxide inks and earlier GZO composite inks, optimisation was initially performed with printed tracks. For the ITO/CNT and ITO/Graphene inks, this resulted in a final conductivity values of 1.75% and 2.36% of the bulk respectively. The ITO/Silver Nanowires inks provided the best results for printed tracks with a conductivity of 13.9% of the bulk which provides a large 250μm track conductivity improvement compared to pure ITO at 3.46%.. After optimisation via the printed tracks, the parameters with the highest values were selected. For the ITO composites, the optimal parameters for bulk film and track fabrication are shown in Table 24:

Table 24 Optimal Parameters for the Laser Processing of ITO Composites

Ink	Laser Power / W	Speed / mm/s	Passes
ITO/CNT	2.5	30	3
ITO/Graphene	0.5	40	1
ITO/AgNW	5	30	2

6.6.2 Optical Properties of Laser Processed ITO Composites

Once bulk films had been fabricated and processed, transmittance measurements were taken; shown in Figure 105(a-b). For ITO/CNT inks, the transmittance became slightly better, increasing from 0.653% to 2.465% at 550nm. Comparatively, both the ITO/GRA and ITO/AgNW became marginally worse decreasing from 3.832% and 3.477% to 0.327% and 0.2138% respectively. These differences are small are therefore it can be concluded that the optical properties cannot be improved for these materials via laser processing.

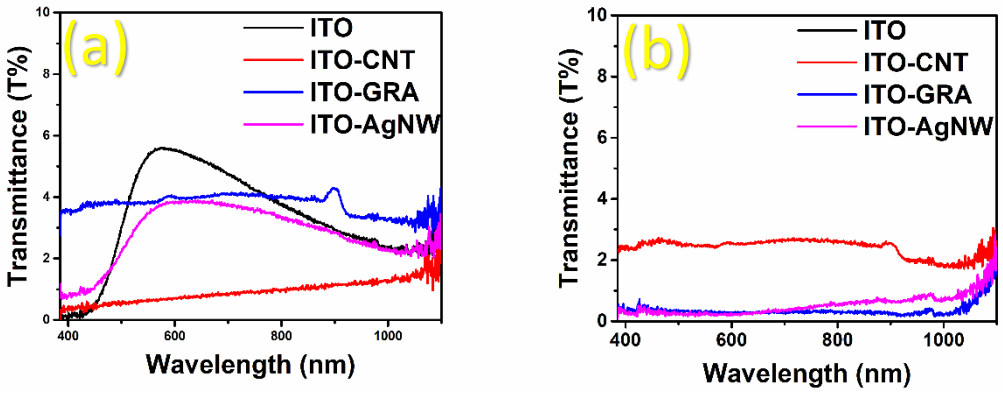

Figure 105 Optical Transmittance Data for ITO composites (a) pre laser processing and (b) post laser processing

6.6.3 Scanning Electron Microscope Analysis of Laser Processed ITO Composites

Scanning electron microscope images; shown in Figure 106(a-c) were taken of each sample providing insight to the structure differences provided by each secondary material. For the ITO/CNT composite, a dense film of shard like nanoparticles have formed. Interestingly, indium tin oxide does not form non-cubic crystals suggesting this is a new phase that has formed, possibly from a reduction process occurring however XRD and EDX will be needed to determine this. ITO/Graphene films are quite porous, with many cracks. No new nanostructures have formed, however, the macrostructure appears flake like which may be due to ITO particles coating graphene flakes. Finally, the ITO/Silver Nanowire films have resulted in a dense, nanoparticle film which is relatively highly conducting, EDX will be required to see whether this is a pure ITO film, or the silver nanowires are still present.

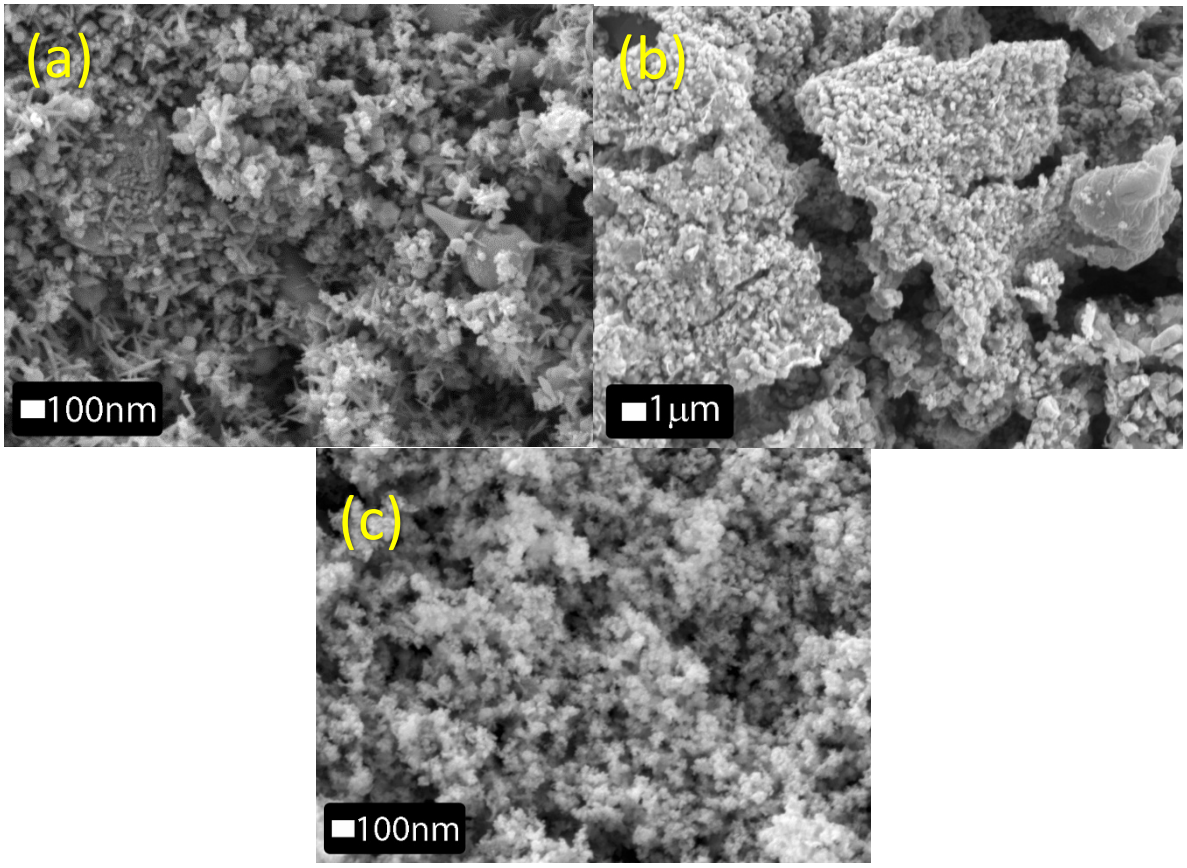

Figure 106 FEG-SEM Images of laser processed (a) ITO/CNT inks, (b) ITO/Graphene inks and (c) ITO/Silver Nanowire inks

6.6.4 Energy Dispersive X-ray Analysis of Laser Processed ITO Composites

EDX analysis of the processed films provided some insight into how the laser processes materials. Looking at the ITO/CNT ink, laser processing resulted in weight percentages of 13.83, 74.98 and 11.18wt% of tin, indium and oxygen respectively. This is highly oxygen deficient and quite tin rich, providing further evidence of the reduction process hypothesised earlier in the chapter. For the ITO/Graphene composite, the EDX compositional data remained unchanged from the starting ITO. Finally, analysing the ITO/Silver Nanowire composites, it is found that the silver nanowires stay in the film with weight percentages of 2.29, 14.47, 59.42 and 23.82wt% for silver, tin, indium and oxygen respectively. Again, it appears that a migration from tin from the internal structure to the external surface has occurred, this combined with the silver is the most probably cause for the relatively high track conductivity.

6.6.5 X-ray Diffraction Analysis of Laser Processed ITO Composites

X-ray diffraction patterns were taken before and after laser processing for each ITO composite material shown in Figure 107(a-d). For the ITO/Graphene and ITO/Silver Nanowires, no additional phases were detected post processing suggesting no large change in crystal structure for the bulk of the film. However, an addition phase of indium tin alloy (In_3Sn) was detected in the ITO/CNT laser processed films, consequently proving the carbothermal reduction process hypothesised to be occurring earlier in this chapter. The In_3Sn alloy is derived from a complete and total reduction of part of the film with a complete stripping of the oxygen from the SnO_2:$In2O_3$. Furthermore, this alloy has been detailed in the wider literature as being a superconductive material at temperatures below 73K, perhaps providing an alternative route to any future printed superconductive applications.

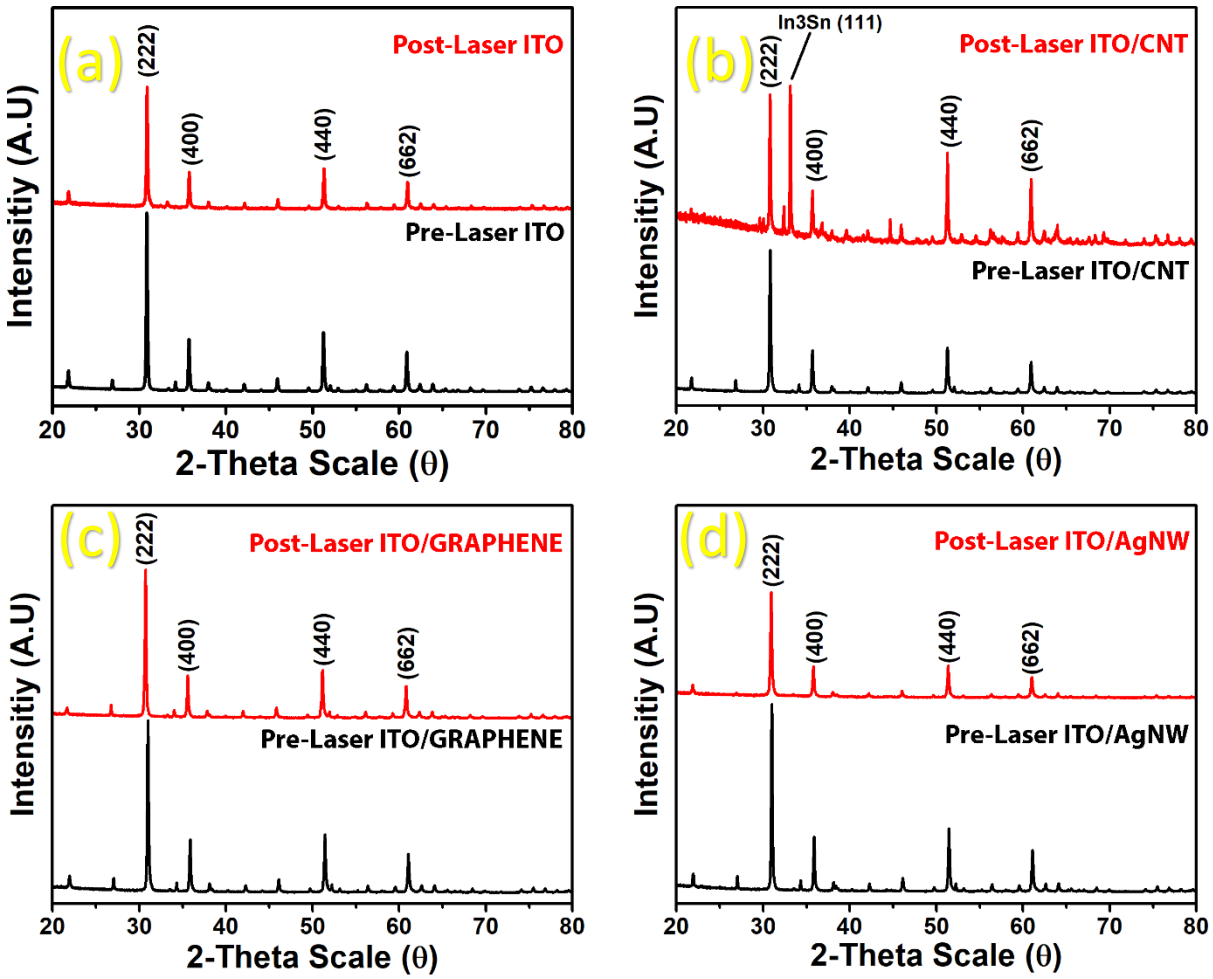

Figure 107 XRD Data for pre and post processed (a) ITO, (b) ITO/CNTs, (c) ITO/Graphene and (d) ITO/Silver Nanowires

6.7 Theory of Processing Mechanism

6.7.1 Classical Carbothermal Reduction of Metal Oxides

A common method for producing ceramic nanorod structures in the literature is by using a carbothermal reduction reaction. This method is based on a classical metal forming reduction reaction used in the mining industry. In this classic process, a metal-oxide ore will be crushed and mixed with carbon (generally graphite or coke) and heated at temperatures exceeding $800^{O}C$, the carbon then acts as a reducing agent, stripping the oxygen from the metal oxide and burning off as CO_2. This is driven by entropy as the conversion of a solid (carbon) to a gas (CO_2) is favoured by a decrease in order. An example of this chemical reaction for a typical metal-oxide (Iron ore smelting) can be seen in Equation 13:

$$2Fe_2O_{3\,(s)} + 3C_{(s)} \rightarrow 4Fe_{(s)} + 3CO_{2\,(g)}$$

Equation 13 Carbothermal Reduction of Iron Ore

The main advantages of this process are that often a higher yield of final product can be obtained, if the amount of carbon is matched to the minimum quantity needed, a high conversion rate with minimal waste can be realised. These reactions are also easy to setup, requiring only a vestibule and furnace offering a one-step, low cost process for metal reductions [297].

With a major obvious disadvantage being the liberation of CO2 and CO from the material, which has adverse effects on human health and the environment if produced in large enough quantities. However, typically due to the lower amount of material required for conversion, greenhouse gas emission can actually be lower. A second disadvantage is that if there is an excess of carbon, metal carbides can be formed as an unwanted by-product. However, in the form of steel, these excess carbons can be beneficial by giving the material extra strength.

6.7.2 Carbothermal Reduction for the Fabrication of Structured Nanoparticles

Materials research in recent years has focused on fabricating new types of ceramic nanostructures based thin films have investigated adapting carbothermal reduction processes into the chemical vapour deposition (CVD) process with successes for both zinc oxide and indium tin oxide. The growth mechanisms in this reaction have been shown to occur via both

vapour-liquid-solid and vapour-solid reactions [298]. In the vapour-liquid-solid reaction, the metal oxide is stripped of its oxygen in the form of CO_2, the reduced metal then forms a liquid metal droplet acting as a nucleating medium where liquid metals re-oxide and grow. This central nucleation is often why tetrapods are favoured with the nucleation occurring from the centre of the tetrapod. In the vapour-solid reaction, parts of the metal oxide essentially sublimate with exposed metallic elements re-oxidising, this can happen in a way where particles can fuse together [298].

The second method of forming these nanostructures can be via a furnace, it has been reported for example that ZnO tetrapods can be synthesised via this process. Graphite and ZnO is simply mixed into a furnace under a nitrogen atmosphere and heated to 1100^{o}C [299]. In this process the tetrapod properties should as size could be controlled through the flow of nitrogen. It has been detailed that the formation of tetrapods is the preferred growth pathway for nanoparticles formed via carbothermal reductions [300].

6.7.3 Laser Induced Carbothermal Reduction of Printed Metal Oxide Films

With regards to whether the laser processing method researched in this chapter is inducing a carbothermal reduction or not, the majority of the evidence gathered in this section suggests it is happening. The main sources of evidence are trace amounts of reduced zinc metal and tin in x-ray diffraction patterns. The largest piece of XRD evidence being a large amount of pure In3Sn alloy phase in the XRD pattern for the processed ITO/CNT. Secondary evidence mainly rests in EDX, SEM and TEM analysis. In energy dispersive x-ray analysis, both the gallium doped zinc oxide and the indium tin oxides are shown to be typically oxygen deficient, suggesting an incomplete re-oxidation. SEM and high magnification TEM analysis also shows a large proportion of tetrapods formed, a common characteristic of a carbothermal reduction. As to whether a vapour-liquid-solid or vapour-solid mechanism is actually occurring, it is unclear. The evidence in my opinion tends towards a vapour-solid mechanism as vapour-liquid-solid reactions typically produce single crystal structures. From the TEM selected area electron diffraction patterns, it can be seen that the particles are more single crystalline but not completely. For example, this essentially means that a wire may be made up of 10 crystallites instead of either a single crystallite or 100's. Therefore, a mechanism which involves the fusion of single crystals, i.e. vapour-solid; rather than the growth of a single crystal seems more likely.

The only way to actually determine this is to perform in-situ TEM, however, the technology for laser based in-situ TEM appears to not currently exist in the literature and is something that can be recommended for future work.

6.7.4 Processing Homogeneity

Lasers, particularly the InGaAs 980nm diode laser used for this research typically have a distribution of energy across the beam, with the highest energy density forming in the centre and the edges of the beam being weak. This distribution was detailed earlier in Chapter 6. To assess bulk film homogeneity, energy dispersive x-ray mapping was performed and is shown in Figure 108(a-d). The analysis was performed via low magnification SEM imaging of 5W laser processed ITO as higher powers did yield porous yet apparently homogeneous films.

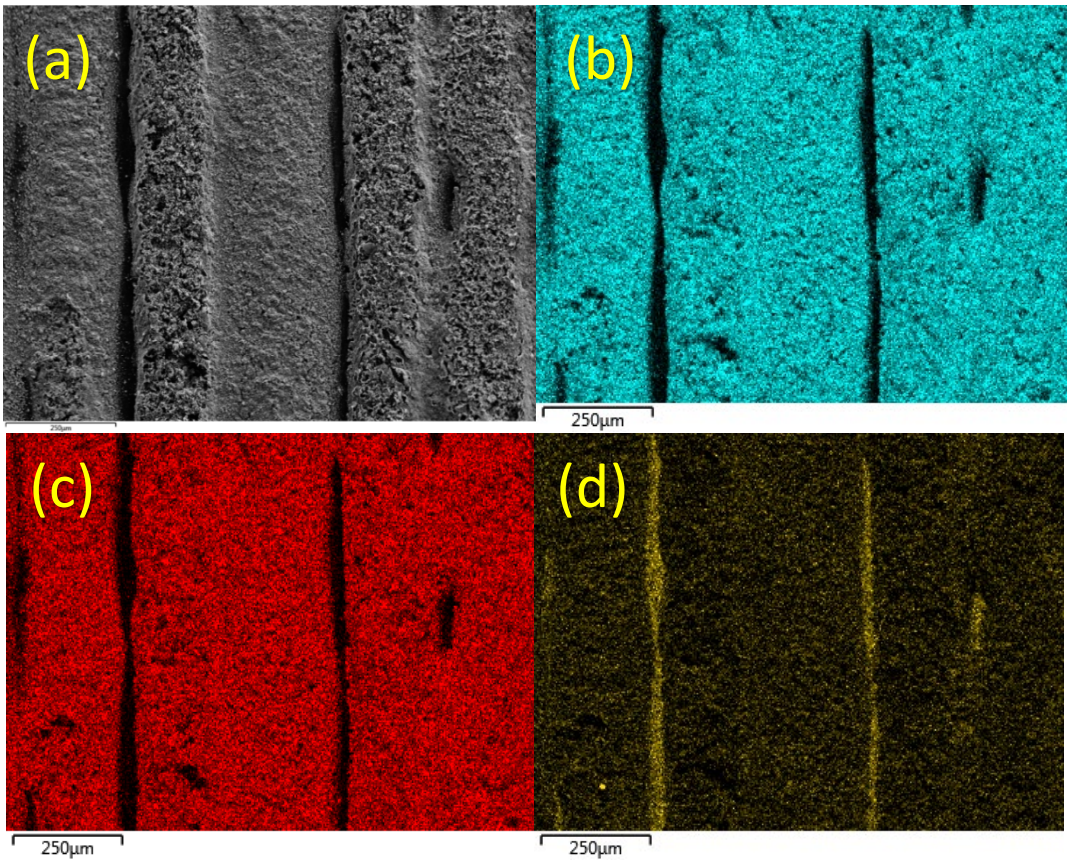

Figure 108 EDX Mapping of ITO Tracking showing (a) SEM image for mapping, (b) a map of indium, (c) a map of tin and (d) the oxygen map

The EDX compositional mapping evidence shows an even distribution of ITO across the film with a homogenous atomic percent distributions of the ITO. The films larger morphology however is quite uneven with gaps shown in the film, highlighted by oxygen rich areas which

are likely due to the underlying glass. These gaps are most likely artefacts from the micro dispensing process. For the larger morphology, dense tracks can be seen with porous surround areas. It is not clear whether these porous areas are the centre of the track which has been hit with the most laser energy, or it is settled debris shifted from the dense inner region.

6.8 Chapter Conclusions

A variety of metal oxide and metal oxide composite inks were printed, and laser processed using the micro-dispensing printing method and laser processed for the first time at a laser wavelength of 980nm. The initial hypothesis would be that laser treatments would be able to enable the indium tin oxide and gallium doped zinc oxide inks to reach their recrystallisation temperature and therefore induce grain growth increasing conductivity and optical transparency. Initially, both indium tin oxide and gallium doped zinc oxide processing parameters were optimised through the sheet resistance of printed 250μm wide tracks, inducing $7.70x10^{1}\Omega cm$ which is 0.187% the resistivity of the bulk material in the GZO and $2.03x10^{-1}\Omega cm$ which is 3.46% the resistivity of the bulk material for ITO. Once the optimal speed and amount of laser passes had been determined, squares were printing for laser processing between 2.5 and 25W. It was found that this processing method is an effective way of rapidly inducing conductivity in the metal oxide inks with conductivities increasing to 10.21% and 40.47% for GZO and ITO respectively. It was hoped that transparency of the printed films would increase as this would provide a further set of applications of the metal oxide inks, however, it was found that the laser processing did not improve the optical properties in any meaningful way. It was also found that the doping stability of the metal oxide is important to the process with the gallium in GZO being removed after laser processing. However, this means high conducting n-type zinc oxide was fabricated with a tuneable bandgap dependant on laser processing power which adds to the number of methods for creating conducting ZnO which are currently of interest in the wider literature. Due to the typical bandgap absorption energy of ITO being far into the UV, the bandgap tunability of this material could not be determined.

An unexpected but remarkable outcome of this processing is that the nanoparticle morphologies of the materials can be altered with the laser processing. With the pure metal oxide inks, the materials characterisation data provided hints that a induced a carbothermal reduction process occurred in the film. Therefore, allowing for a new rapid manufacturing process for simple creation of metal oxide nanostructures that typically require long and complex synthesis. This carbothermal reduction process was properly confirmed after processing the nanocomposite inks, namely in the processing of the indium tin oxide/carbon

nanotube inks where a large quantity of In_3Sn alloy was detected via XRD. It was also found that the addition of these secondary materials into a metal oxide ink, due to their alteration of the optical properties can alter the final nanoparticle morphologies of the film. One issue is that the adhesion, due to the carbon removal is quite poor for the printed bulk films suggesting this process should mainly be used in the form of tracks and grids for future applications. This is the first known application of a laser induced carbothermal reduction reaction, and the first manufacturing process to rapidly print tracks and films and convert them into nanowire and nanorod materials with enhanced properties.

Chapter 7

Resistive and Capacitive Applications of Metal Oxide Materials

7.1 Introduction

In the previous chapters, metal oxide inks were formulated with the main focus on achieving conductivity, it was found that the indium tin oxide (ITO) inks were relatively highly conductive for a printed n-type semiconductor. Gallium doped zinc oxide (GZO) inks were also formulated, these were found to be highly transparent, but this transparency due to the small particle sizes were also hindered by large grain boundary resistances preventing conductivity. Composite inks were also formulated using carbon nanotubes, graphene and silver nanowires. A printing and laser processing method was then developed, and it was found that conductivity in GZO could be induced and the conductivity of the ITO drastically increased.

In this chapter, using the knowledge gained from the previous chapters, passive electronic components in the form of resistive interconnect and capacitors will be fabricated and characterised. This is towards research objectives four and five to develop and characterise printed interconnect and passive devices and to also develop components which have functionality for printed electronics applications.

For the resistors, both oven cured, and laser processed, tracks will be measured for GZO, ITO and composite materials. For the capacitors, micro-dispensing and screen printing will be used as fabrication processes using ITO only as conductivity is required without laser processing. For the screen-printed capacitors, a multi-layer parallel plate design will be used to take advantage of the multi-layer advantages of the screen-printing process and to utilise materials with higher dielectric constants than plastic or glass substrates. Micro-dispensed capacitors will be printed with interdigitated structures, this is due to an inability of the printed system to print multilayer, but also to take advantage of the direct write functionality of the printing and laser processing system. Resistors will be electrically characterised through sheet resistance measurements while the capacitors will be characterised through a combination of

LCR measurements and impedance spectroscopy. Finally, capacitors will be inserted into an RC circuit to see if the function properly and as an application of printed conductive oxides.

7.2 Resistive Properties of Metal Oxide Tracks

7.2.1 Using Laser Processing as a Means Towards Tuneable Resistive Properties

There are three primary passive components that can be made with conductive materials, resistors, capacitors, and inductors. In the previous chapter, a design of experiments was performed on the metal oxide and composite printed 250mm tracks varying laser power (W), processing speed (mm/s) and the amount of laser passes. Here, that data is analysed in the form of track end to end two-point resistance measurements. In industry, resistors are typically screen printed and laser trimmed to reach a certain value, however, a single print will have a single resistance, requiring a different ink per resistance value. The trimming is then used to ensure everything is within a certain tolerance. Typically, tuneable resistors focus on the fabrication of resistor / transistor hybrids where the resistance can be altered by an electrolyte saturated active channel, with the resistance being tuned by altering the electrolyte solution during the manufacturing process, something not currently achievable with printing technology [301]. The aim of this study is to determine whether a single ink, by varying laser processing parameters can yield tuneable printed resistors.

7.2.2 Materials and Methods

The inks used in this section this chapter are the same inks formulated in Chapter 5 and used in Chapter 6. Inks were printed into 20x0.025mm tracks onto soda lime glass (Thermoscientific Plain Glass, 24x24mm) with 5 replicates of each laser processing. Printing and laser processing was performed on the Haecker VICO 520 using a 980nm diode InGaAs laser. Two-point resistance measurements were taken using a calibrated Fluke 179 multi-meter with resistance measurements being taken end to end so a comparison could be made between resistors. The limits of detection for the multimeter are a lower limit of 0.01Ω and the upper limit is 50MΩ. Sheet resistance measurements were also taken from the centre of each track using a Jandell HM10 Four-Point Probe. Measurements were taken in the centre to account for any non-uniformity in the resistance due to the rise and fall time of the laser. Optical microscopy images were taken using a Dino-Lite USB optical microscope.

7.2.3 Laser Tuneable Resistivity GZO and GZO Composite Tracks

A total of 140 tracks were printed for the GZO and each of the GZO composites as part of a Box-Behnken design of experiments. These experiments varied the laser power, the laser speed, and the amount of passes the laser makes over the tracking. Examples of laser processed tracks can be seen in the optical microscopy images in Figure 109(a-d). The samples were laser processed with powers between 0.5 – 28W, speeds of 5 – 100mm/s and 1 to 5 passes of the laser depending on the optical properties and limits of the material. It was found in Chapter 6 that for the composite materials, due to their higher absorbance of light, that faster and lower powers could be used to process tracks. Whereas for pure GZO, a higher power and number of passes was required due the GZO's low absorbance of light.

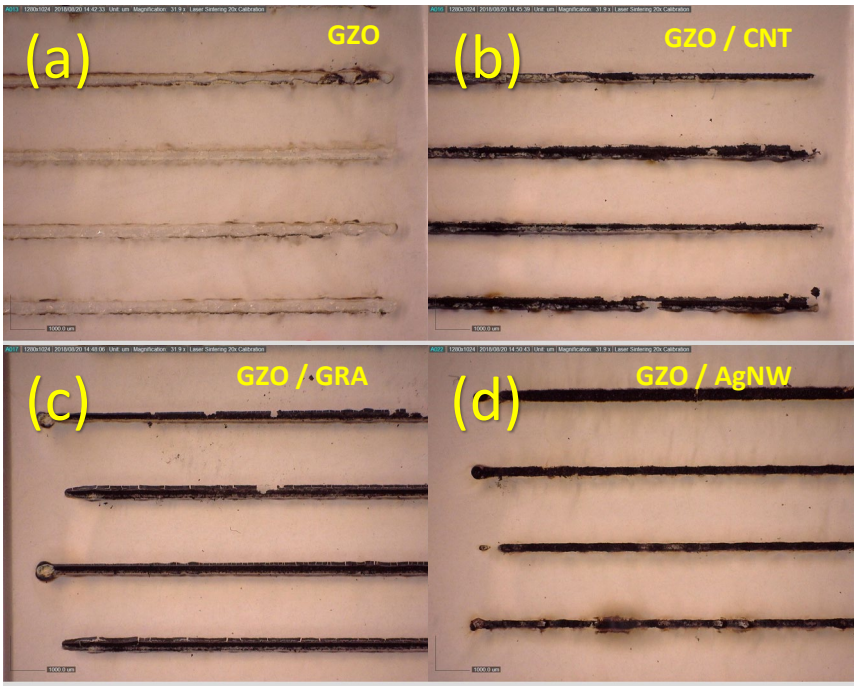

Figure 109 20X Magnified optical microscopy of laser processed (a) GZO, (b) GZO/CNT, (c) GZO/Graphene and (d) GZO/Silver Nanowires

Once all the resistance data had been collected, it was clear that the resistance of the tracks could be altered with via changing the laser parameters. The energy density supplied by the laser was tuned between 1.41×10^3 W/cm^2 and 7.95×10^4W/cm^2, taking into the beam size, the laser powers and assuming a top-hat laser profile. The average minimum resistance and average maximum resistance were plotted in the form of a floating column chart so the tuneable resistance range of each ink can easily be observed; shown in Figure 110. As can be seen, the pure GZO had the smallest range out of the four inks, ranging between 0.732MΩ

and 27.736MΩ also having the worst minimum resistance. GZO/AgNW inks gave the best minimum average track resistance of 799.86Ω, however, the second smallest range with an upper maximum value of 1.518MΩ. The GZO/Graphene inks has a range of 7.181kΩ to 6.419MΩ, providing the second highest range but the second worst minimum resistance. The GZO/CNT inks provided the largest tuneable resistance range from 1.107kΩ to 33.456MΩ, essentially enabling 1kΩ to 1MΩ resistive structures to be fabricated with the printing and laser processing manufacturing method.

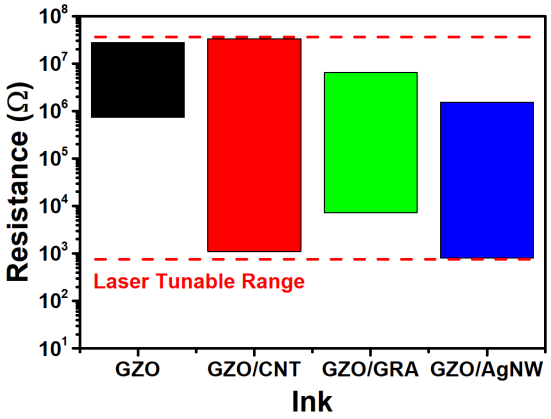

Figure 110 Laser tuneable resistance ranges for each GZO ink

7.2.4 Laser Tuneable Resistivity ITO and ITO Composite Tracks

The experiments were repeated for the ITO based inks and composite inks, with optical microscopy images of shown in Figure 111(a-d).

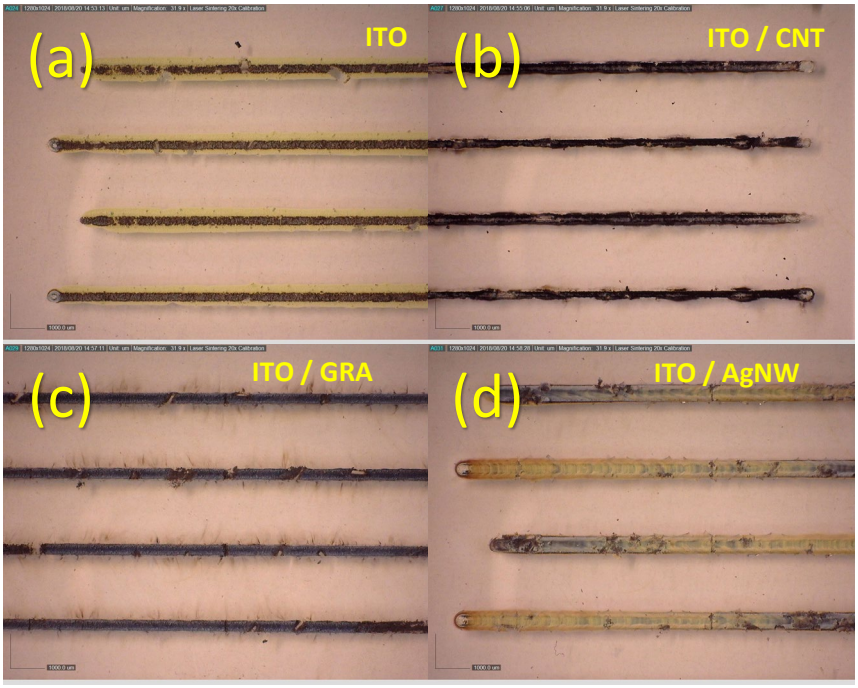

Figure 111 20X Magnified optical microscopy of laser processed (a) ITO, (b) ITO/CNT, (c) ITO/Graphene and (d) ITO/Silver Nanowires

For the indium tin oxide-based inks, laser power was varied by 0.5 – 25W, laser speed between 5 – 100mm/s and 1 to 3 laser passes. As can be seen by the floating column plot in Figure 112, all of the inks showed a large range of tuneable resistances. The smallest range is the ITO/CNT inks, with a minimum average resistance of 329.05Ω and a maximum of 8.19MΩ. The second smallest range is the ITO/Graphene composite inks, with a minimum resistance of 369.73Ω and maximum of 12.72MΩ observed. The second-best material is the pure indium tin oxide ranging between 178.67Ω to 18.16MΩ. However, the material with both the best conductivity and largest tuneable resistance range is the ITO/Silver nanowire inks with a minimum average resistance of 50.86Ω and a maximum of 23.53MΩ. Therefore, it has been demonstrated that by laser processing 250-micron thick tracks, it is possible to tune resistors using the ITO/AgNW ink between 50Ω to 20MΩ, allowing for a method of printing resistors using a single ink and then tuning them with a laser in one process.

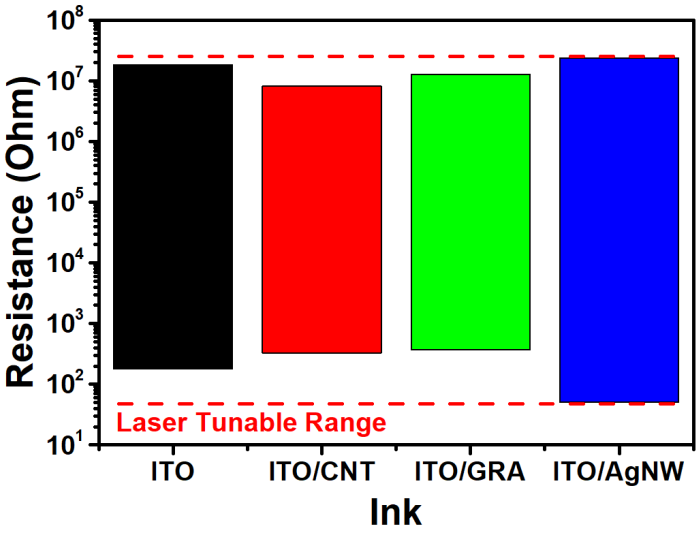

Figure 112 Laser tuneable resistance ranges for each ITO ink

7.3 Design and Fabrication of Micro-dispensed ITO Capacitors

7.3.1 Designing a Printed Interdigitated Capacitor

The printing and laser processing system can only print a single material in 2D, it uses a direct write syringe dispensing system. Due to this, interdigitated capacitive structures were designed considering the limitations of the printing system and glass substrates used. The design, as shown in Figure 113 has a 0.5mm track and gap, considering the 0.254mm nozzles used for printing, this was determined to be the best track and gap to achieve a good capacitance while preventing shorts between fingers.

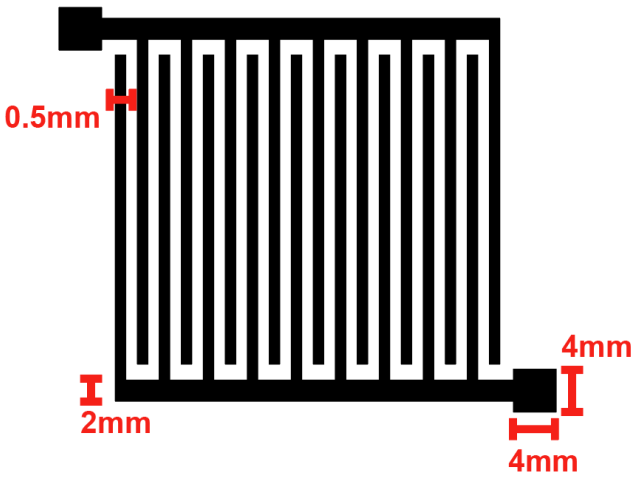

Figure 113 Gerber Design for Interdigitated Capacitors

The capacitor was designed for 24x24mm soda lime glass slides with a literature reported dielectric constant of 7.45 at 1MHz. The design has 18 fingers of 15mm length, with the entire structure encompassing a 20x20mm area.

7.3.2 Materials and Methods

The indium tin oxide (ITO) in used in this chapter is the same indium tin oxide ink formulated in Chapter 5 and used in Chapter 6, the ink code being LS005. Capacitance measurements were taken using a UNI-T 612 LCR meter, measuring the capacitance at 1000Hz. Printing and laser processing was performed on the Haecker VICO 520 using a 980nm diode InGaAs laser.

7.3.3 Capacitor Fabrication and Electronic Characterisation

The indium tin oxide ink used in chapter 6, was printed using a 254mm conical dispensing tip (Nordson) with a printing pressure of 0.39mm and a flow rate of 0.2μLs^{-1}. Ten samples in total were made with five being oven cured (110^{o}C, 10 minutes) and five being laser processed (980nm, 5W). Both oven cured and laser processed samples can be seen in Figure 114.

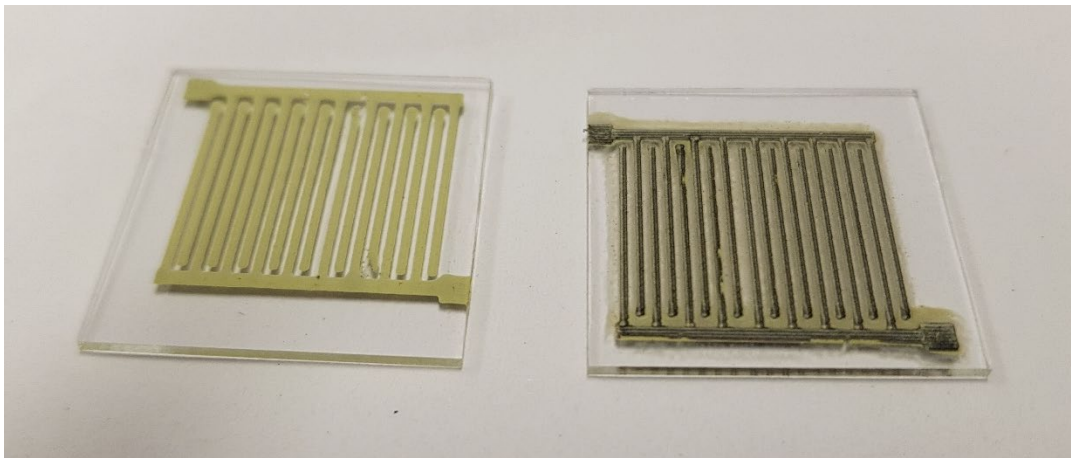

Figure 114 Printed Oven Cured and Laser Processed ITO Interdigitated Capacitors

A major issue was found during the printing process was the machine and printing itself, the printing system's inaccuracy provided a large challenge in relation to the small track and gaps required for the design. This caused shorting in nine of the ten samples printed. The one sample to not short circuit and to provide a capacitance value, was a laser processed sample giving a capacitance of 73.92pF, with a measurement error of +/- 1.0%. A decision was made not to continue with this fabrication process for the capacitors due to the high failure rate. It

is recommended that this be further investigated in the future with machinery that can provide finer detail, or a system be set up where the screen printing and laser processing can be performed in tandem.

7.4 Design and Fabrication of Screen-Printed ITO Capacitors

7.4.1 Designing a Printed Parallel Plate Capacitor

Next, screen printed parallel plate capacitors were designed and purely oven cured as it is not possible to currently integrate the screen-printing multilayer process with the laser processing system available. The design of the parallel plate capacitor can be seen in Figure 115. Originally, a commercial polymer UV curable dielectric was printed, UV cured, then printed on top of again. However, material compatibility issues occurred between the indium tin oxide ink and the polymer dielectric, preventing it's use in this work. Due to these stability issues, a dielectric metal oxide material was chosen for the dielectric layer. Aluminium oxide was chosen due to it being an extremely inert material, while also being low cost, having a low loss tangent (0.001) and a relatively high dielectric constant (9.6). Zinc Oxide was also tested, however, due to the ZnO being a semiconductor, capacitance readings were unstable, therefore insulating Al_2O_3 was selected.

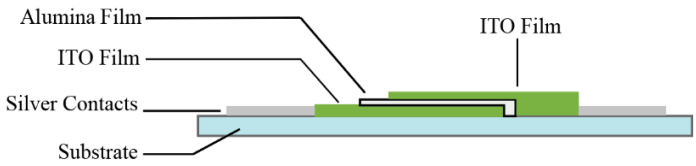

Figure 115 Printed Parallel Plate Capacitor Design

During the design process, multiple prototypes were fabricated and the design where the ITO electrodes are offset from each other was chosen. This design was chosen to prevent short circuits from the electrodes touching each other or the silver contacts as this ink tends to solvate the inks below and leech into the film.

7.4.2 Materials

Indium Tin Oxide (ITO) (99.99% metals basis, Alfa Aesar) powder was used to formulate a conductive metal-oxide screen printing ink for printed electrodes. As discussed in Chapter 5, the nitrocellulose vehicle combined with indium tin oxide powder provides the highest low temperature conductivities and ink LS005 used for this research. Aluminium Oxide (<50nm nano-powder, Sigma Aldrich) was used to formulate a metal-oxide dielectric ink. The vehicle

for the dielectric ink was the same nitrocellulose-based vehicle used for the ITO in order to maximise compatibility. The flexible substrate used in this research was clear Melinex ST504 Heat-Stabilized polyethylene terephthalate (PET) and was donated by Dupont Teijin Films. Silver contacts were printed using a Silver screen printing ink (C2131014D3, Gwent Electronic Materials).

7.4.3 Capacitor Fabrication

Indium tin oxide (~50Ω/□) electrodes were printed onto PET substrates with varying electrode areas ranging from 1cm^2 to 9cm^2 (Figure 116). All screen prints were performed using stainless steel screens using 230 (75/36) meshes on a DEK 1202 screen printer. ITO electrodes were cured in a box oven at 105^{O}C before having alumina dielectric ink printed on top.

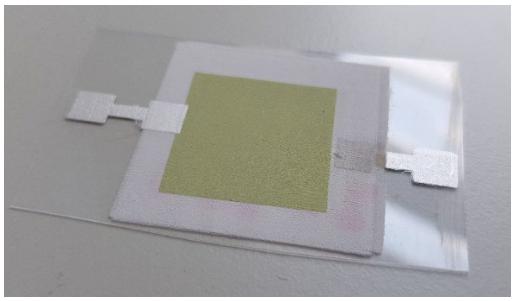

Figure 116 Fully Screen-Printed ITO Capacitor

To eliminate pinholes in the dielectric film, multiple printing passes of dielectric were performed, ranging from 1 to 6 passes. The print is once again placed in a box oven at 105^{O}C to cure the alumina dielectric ink. A final ITO electrode and silver contacts are printed onto the structure, the capacitor goes through a final curing stage at 105^{O}C in a box oven for 5 minutes.

7.4.4 Measurement Equipment

Capacitance measurements were taken using a UNI-T digital LCR meter (UT612), these measurements were taken using the LCR meter connected to a PC using the UNI-T digital multimeter software provided. Sheet resistance measurements were taken using a Jandel HM21 four-point probe. Impedance spectroscopy measurements were taken using a Metrohm Autolab Instruments multi-channel potentiostat / galvanostat (PGSTAT12) using Metrohm's Frequency Response Analyzer software (v4.7.900). Data analysis of complex

impedance data was performed using Autolab Nova (v2.0). Impedance measurements were taken using 100 measuring steps between 1MHz and 100Hz with an amplitude of 0.01V. Profilometry measurements were performed on a Talysurf CLI 2000 and data was analyzed in the Talymap Platinum (v5) software package. R-C circuit analysis was performed using a GWInstek 2072-A Oscilloscope in combination with a GWInstek AFG-2000 Arbitrary Function Generator.

7.5 Electronic Characterisation of ITO Capacitors

7.5.1 Dielectric Layer Thickness and Properties

An initial study was undertaken into the change in dielectric properties versus the amount of printing passes undertaken. All capacitors with one to two printing passes of dielectric would short circuit, giving a resistive reading on the LCR meter. The most likely explanation for this is the presence of pinholes in the printed layer [302]. To create a full coating with no pinholes at least three printing passes of dielectric ink are required. Capacitors with a $2cm^2$ area were printed with printing passes of dielectric ink ranging from 3 – 6 layers. Profilometry measurements (Figure 117) were taken each sample and the average dielectric layer thickness per printing pass (Table. 25).

Table 25 Average Dielectric Thickness Per Printing Pass

Printing Passes	Layer Thickness / μm
3	51.4
4	67.6
5	83.2
6	92.8

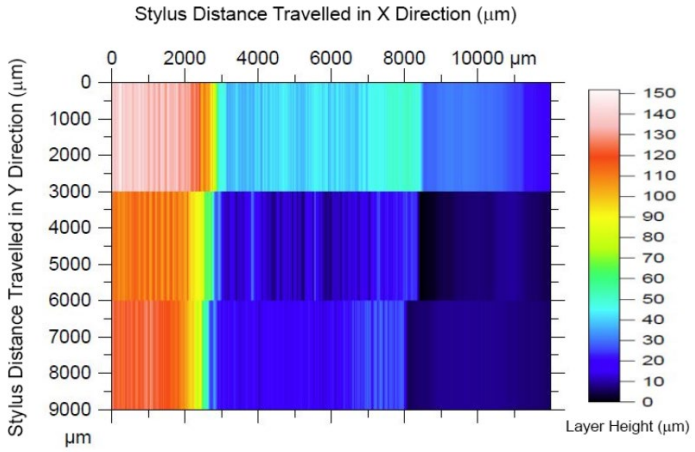

Figure 117 Profilometry Data for Printed ITO Capacitors

The profilometry measurements show that the layer thickness increases as expected with each printing pass, reducing each time. This is most likely due to the screen printer compressing the underlying film with each pass. To determine the effect this layer increase

has on the dielectric properties of the aluminium oxide film, dielectric impedance spectroscopy was performed from 100Hz to 1MHz. From the real and imaginary components of the impedance analysis, the capacitance, dielectric constant and loss tangent can be extracted if the layer thickness of the dielectric is known. As can be seen in figure 118, three printing passes is the optimum amount for printing capacitors with ITO and Alumina, this is the optimal dielectric thickness were the dielectric constant remains at it's highest while being the minimum amount of material required to prevent pinholes and short circuits. The larger amount of capacitance could also be caused from thinner sections of the dielectric overriding the thicker sections of dielectric, creating an overall higher capacitance on average.

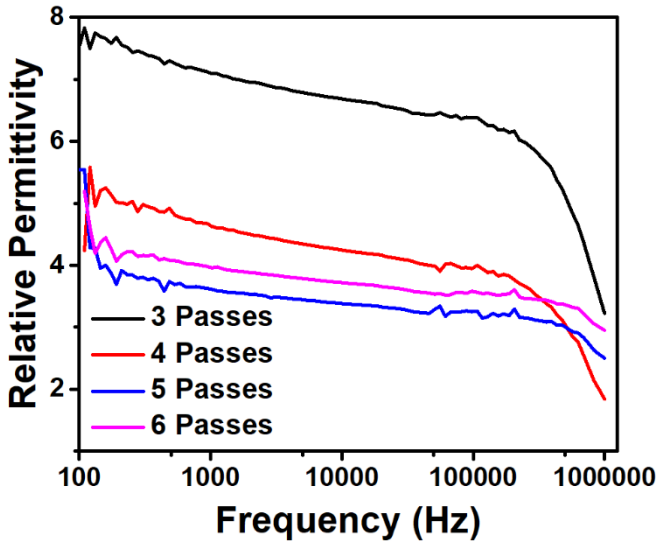

Figure 118 Permittivity versus Frequency with regards to dielectric thickness

Between four and six printing passes the dielectric constant keeps within a relatively tight range with a dielectric constant between 4 and 5. With an increasing layer thickness in a polycrystalline material the dielectric constant is expected to increase. The decrease in dielectric constant could be due an increase in trapped organics and binders in the thicker film, reducing the polycrystallinity. Curing was also performed after each printing pass meaning organics from lower layers could leech out through the top layers disrupting the polycrystallinity. From this study three printing passes of dielectric ink was selected as the optimum amount for all future capacitors in this research.

EDX cross sectional mapping was performed on a capacitor which contained one ITO printing pass followed by 3 printing passes of dielectric to confirm the accuracy of the profilometry

data and to determine how pinholes can form. The layered EDX SEM image is shown in Figure 119 (a-f) with its separate components. The alumina dielectric layer appears to be compact with scattered particles of ITO.

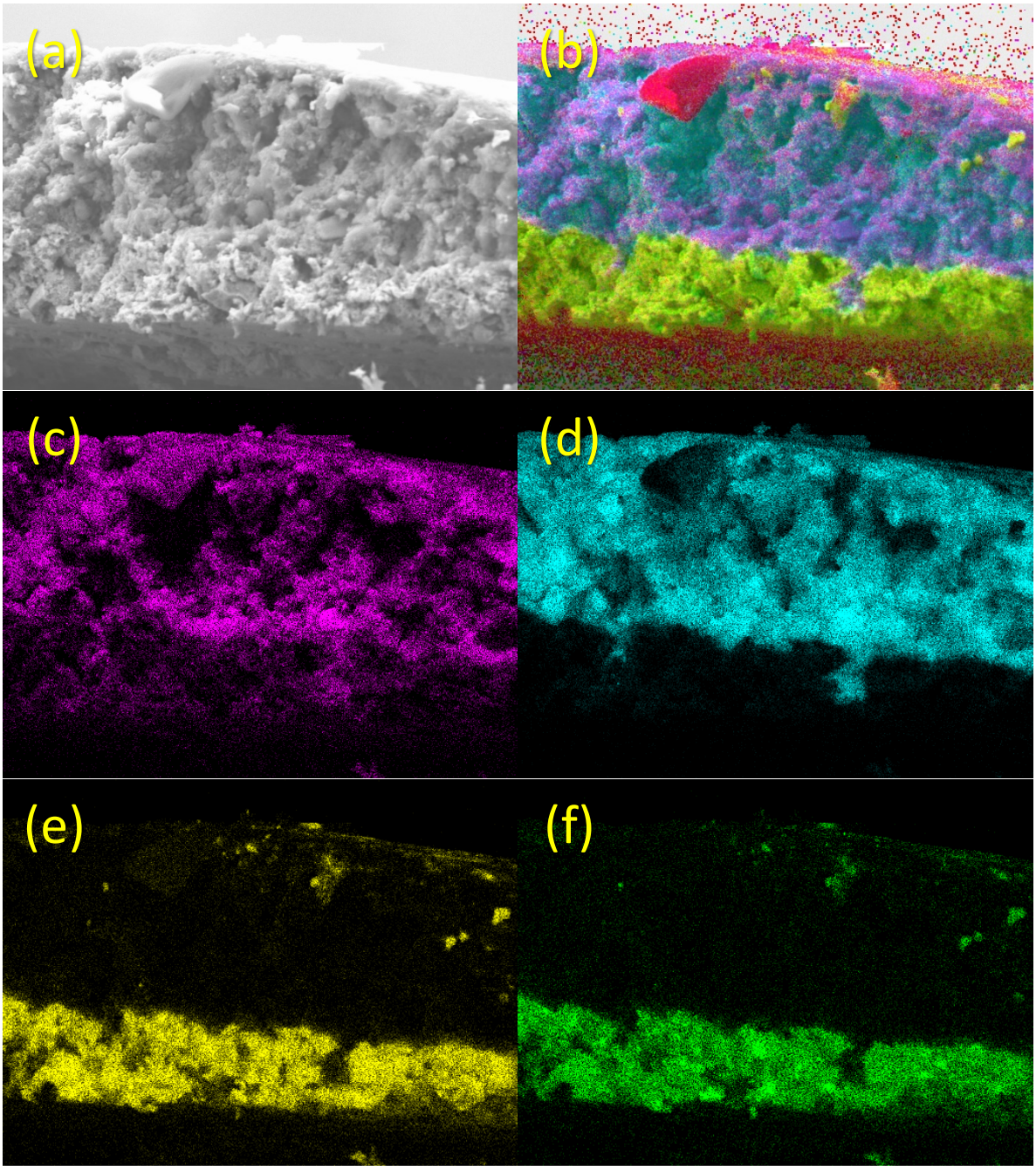

Figure 119 Cross Sectional EDX Mapping Data with (a) Original SEM, (b) Layered Map, (c) Oxygen Layer, (d) Aluminium Layer, (e) Indium Layer and (f) Tin Layer

Some Aluminium seeps into the ITO layer, this suggests the phenomenon of pinhole formation can be attributed seeping of the top ITO layer through the bottom layer. Only one needs to

occur for a short circuit. The layer height in this cross-sectional EDX SEM corresponds to the profilometry data at approximately 50 microns thickness.

7.5.2 Capacitance Density and Tolerances

Capacitance density (capacitance per unit area) was found to decrease with an increasing electrode area (Figure 120). The biggest decrease was measured between 1cm^2 and 4cm^2. Between 4cm^2 and 9cm^2 capacitors a further decrease was measured, however, both electrode area measurements are within the same standard deviation of each other. This suggests after 4cm^2 the capacitance density of the capacitors stabilizes.

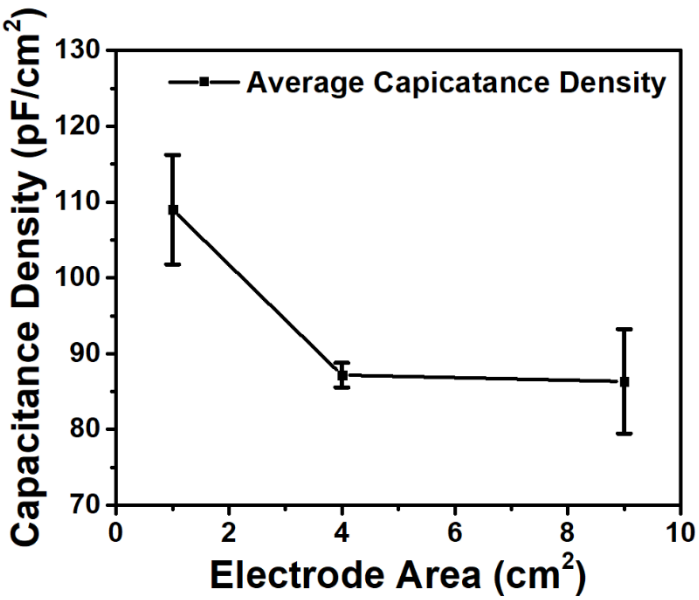

Figure 120 Capacitance Density vs Electrode Area

The tolerance of the capacitors was measured (as shown in Table 26) with 4cm^2 capacitors having the smallest tolerance window.

Table 26 Average Dielectric Thickness Per Printing Pass

Electrode Area / cm^2	Average Capacitance Density / pFcm^{-2}	Tolerance
1	109	-5% / +7%
4	87.15	-1.5% / +2%
9	86.34	-7.6% / +8%

7.5.3 Capacitance versus Frequency Analysis

With an increasing frequency the ability for the capacitor to react to the AC signal (it's reactance XC) decreases. This decreases the ability of the capacitor to store electric charge in an electric field. Figure 121(a) shows this expected capacitance decrease with frequency increase. The large drop off in the kilohertz range can be attributed to the increase in electric field loss shown in Figure 121(b). As the electric field loss increases, the capacitors ability to store charge in an electric field decreases.

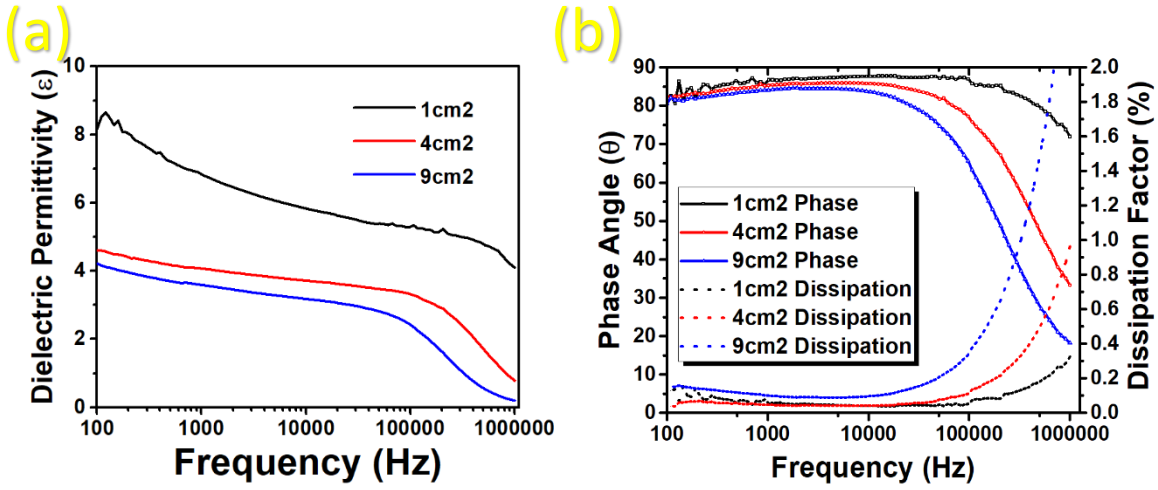

Figure 121 Frequency sweep data for (a) capacitance versus frequency with respect to electrode area and (b) phase angle (bode plot) and dissipation factor (loss tangent) versus frequency

The relationship between the phase shift and frequency (Figure 120(b)) correlates with the magnitude of capacitance drop off in Figure 121(a). At a higher capacitance the cut-off frequency is lower and creates a more well-defined cut-offs point. The dissipation factor and dielectric field loss of the material increases with frequency in Figure 121(b), contributing to the decrease in capacitance. Dissipation factors of the capacitors range from 0.05 to 0.2% up to 90kHz. The $1cm^2$ capacitors increase up to 0.2% at 1MHz, whereas the $4cm^2$ increase to 1% and the $9cm^2$ capacitors increase to a 2% dissipation factor. The loss is high compared to solid, sintered alumina, up to 2% compared to 0.001% literature value. As the dielectric has not been through a binder removal and sintering process requiring high processing temperatures (1100 – 1600°C) the increase in electric field loss at KHz frequencies can be attributed to leftover organics and air voids artificially altering the dielectric properties.

7.5.4 Impedance Analysis

Impedance analysis was performed on the capacitors between 100Hz and 1MHz. As can be seen in Figure 122, an increase in electrode area creates a lower overall impedance. The results appear to show a straight line which is expected of capacitors. An ideal capacitor would give a straight line at 90° to the X axis. As no real capacitor has perfect ideal behaviour the degree of non-ideality can be measured from how close the data is to 90 degrees. With an increasing electrode area, the ideality of the capacitor decreases, this corresponds with the increase in electric field loss with regards to an increasing capacitor area discussed earlier in Chapter 7.

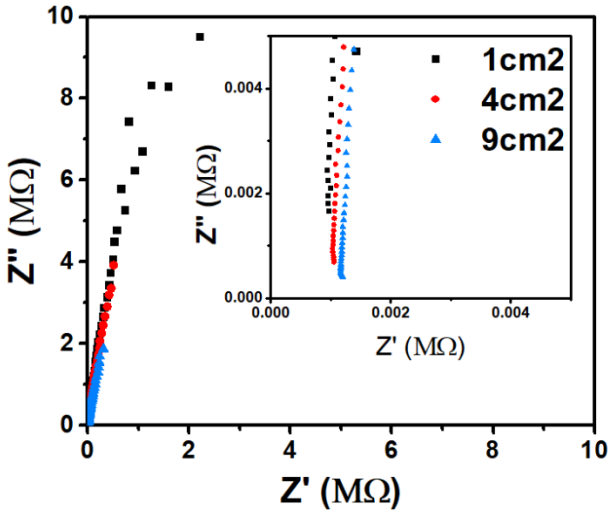

Figure 122 Impedance analysis of capacitors with varying electrode areas

With an increasing electrode area, a shift right in the real impedance is shown. As the ESR can be attributed to a cross in the real impedance axis, this suggests an ESR increase with increasing area. Actual ESR is typically calculated by extrapolating the highest frequency points across the real impedance Z' axis (x-axis). Extrapolating the data, it can be seen that the ESR of the 1cm^2 capacitors is 9.6kΩ, 10.5kΩ for 4cm^2 capacitors and 11.8k Ω for 9cm^2 capacitors. This is high compared to commercial ceramic parallel plate capacitors and can be attributed due to the conductivity of the ITO compared to metallic contacts and the un-sintered alumina dielectric.

7.5.5 Flexibility of Printed ITO Capacitors

Impedance spectroscopy was performed on the printed capacitors under bending. Capacitors were measured before flexing. Samples were then clamped into a strained position with 30% strain applied. The strain applied was calculated using Equation 14, where the percentage of strain (ε) is defined as the difference in the initial length of the component (l_0) and the flexed length of the component (l_1) divided by the initial length (l_0).

$$\varepsilon = \frac{l_o - l_1}{l_o}$$

Equation 14 Calculation of strain

Impedance spectroscopy was performed on the printed capacitors under a 30% strained bend as can be seen in Figure. 123(a – d).

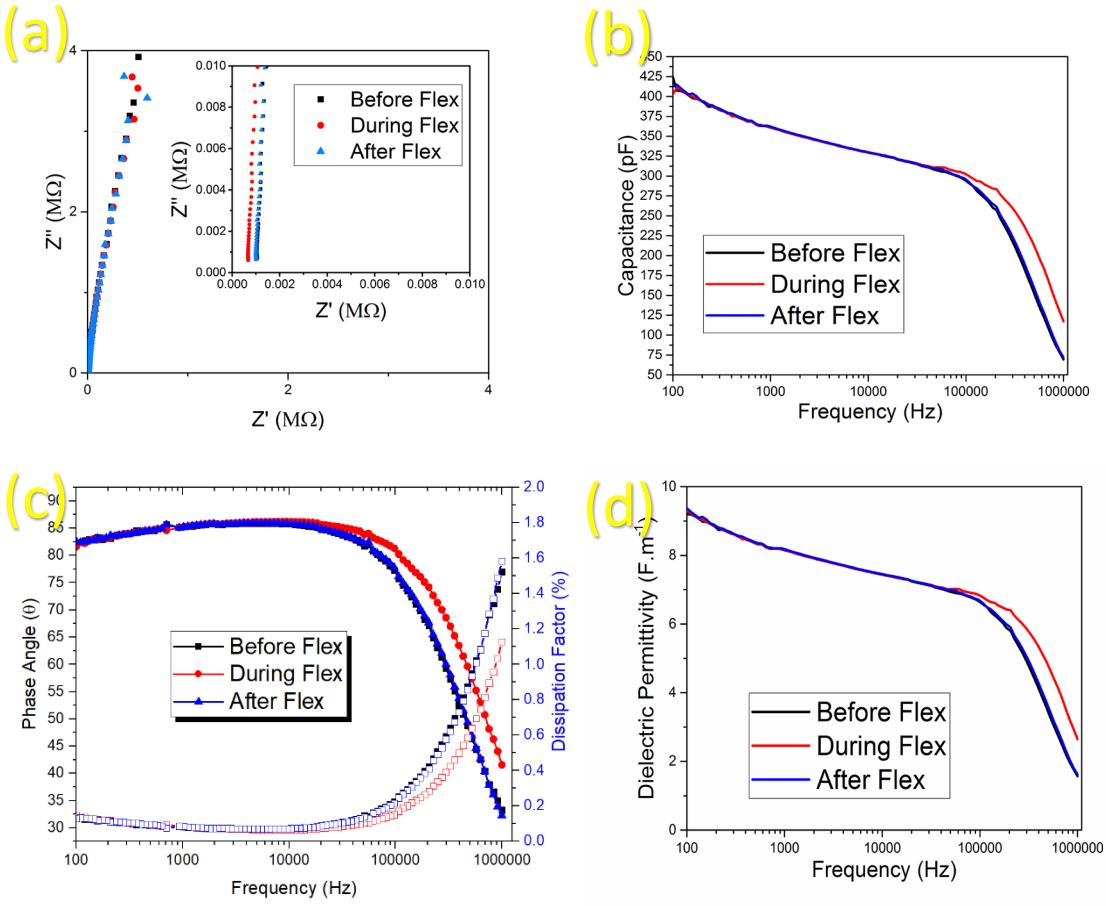

Figure 123 Electrical characterisation of capacitors under a 30% strained bend flex with (a) impedance measurements, (b) capacitance vs frequency, (c) bode plot with dielectric loss and (d) relative permittivity vs frequency

The Nyquist plots in Figure 123(a) for the pre and post flexed positions are completely overlaid demonstrating minimal hysteresis in the capacitors. The flexed samples showed a shift to the left in the real impedance axis suggesting a lowering of effective series resistance during the bend. The capacitance also increases in the in the high frequency region (as shown in Figure 123(b)) and remains unchanged in the low frequency region. Analysing the bode plot (Figure 123(c)) shows that the phase shift occurs at higher frequencies during bending while once again remaining the same at lower frequencies. The dielectrics ability to store electric energy in the electric field increases at higher frequencies (Figure 123(c-d)) along with a decrease in the dielectric loss factor. This explains why capacitance increases in the higher frequency regions.

7.6 R-C Filter Applications of Printed ITO Capacitors

Typically, the capacitance of ceramic capacitors is quite small (<1μF) and due to this, it is not possible to use them as a source of energy in most applications. Instead, the ability to store and manipulate electric fields is used to manipulate DC and AC electricity. Common uses include coupling/decoupling capacitors, which help convert couple AC and DC circuits together in electronic devices. Another use, which is typical of capacitors with capacitance values similar to the printed ITO capacitors, is in filter circuit applications which filter AC waves allowing or blocking certain frequencies in electronics. This section investigates the use of the printed ITO capacitors in an R-C filter circuit, this circuit containing both a resistor and capacitor are used to develop low pass and high pass filters which respectively allow frequencies to pass below or above a particular frequency through the circuit. Applications of these include amplification, noise reduction and frequency equalisation and the ability for printed capacitors to work in a system like this enables these applications to be introduced into printed electronics.

7.6.1 R-C Circuits with 1cm^2 Capacitors

Capacitors fabricated with a 1cm^2 form factor were found over the course of the study to delaminate easily from the PET substrate causing reliability issues. This is due to the thickness of the printed film being quite large in relation to the size of the capacitor and is a common issue with thick film printed electronics. This became apparent mainly during the experimental setup for the R-C circuit analysis where the delamination occurred on all original and repeated samples providing data which suggests the capacitance was greatly decreased. The data in the section shows that the capacitor still functions even after damage, providing a much lower cut-off frequency than theoretical suggested in a low-pass filter circuit.

For analysing the use of the printed capacitors in an RC circuit, a low pass filter was built using printed capacitors with commercial 1Megohm resistors and measured using the oscilloscope and function generator detailed in Chapter 4. The current response of the capacitor was measured in relation to the voltage supplied by the function generator. The voltage peak to peak ($V_{p\text{-}p}$) supplied was $1V_{p\text{-}p}$ which in an unfiltered state (below the cut-off frequency of the low pass filter) provides a current peak to peak ($I_{p\text{-}p}$) of $1A_{p\text{-}p}$ through the system. The frequency was scanned in hertz from 10Hz to 5Mhz with 5MHz being the upper limit of the

function generator. Data for the 1cm^2 capacitors can be seen in Figure 124 with the caveat that the capacitance is lower than suggested in Section 7.4.3 due to the delamination issues. As can be seen in Figure 124 (a-c), no useful data could be collected for the 1cm^2 capacitors. Therefore, it appears that due to the film thickness being so thick, 1cm^2 capacitors can be fabricated but are not reliable for future use. Further research will not be conducted with them.

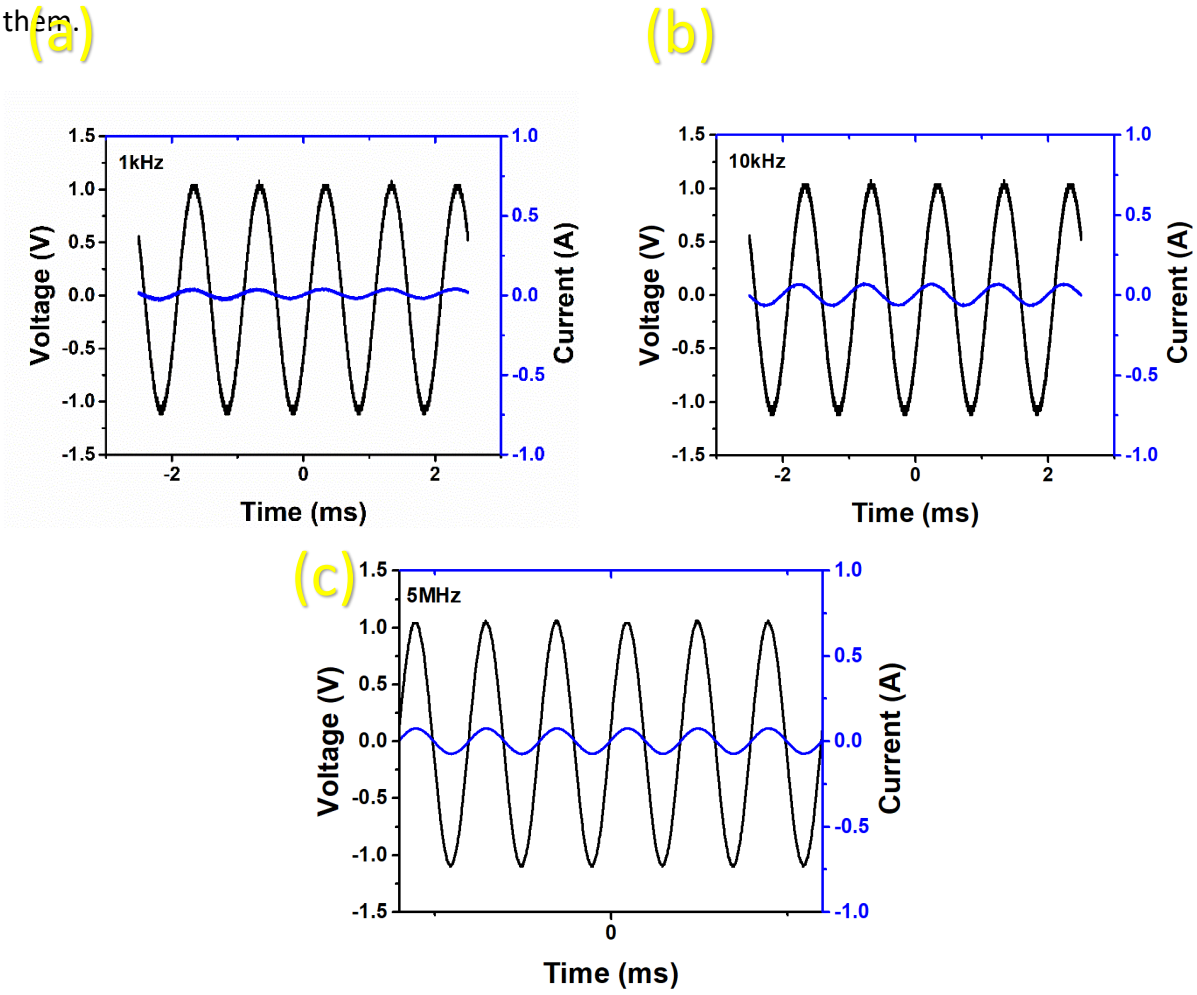

Figure 124 High Pass Filter Data for 1cm^2 capacitors at generated frequencies of (a) 1kHz, (b), 10kHz, (c) 5MHz

7.6.2 R-C Circuits with 4cm^2 Capacitors

Capacitors with electrode areas of 4cm^2 were more mechanically stable than the 1cm^2 counterparts. The circuit filtering capabilities of the capacitors were measured in an R-C circuit in a high pass filter configuration. The reasoning behind selecting a high pass setup is so if the resonant frequency is approached, it can be seen as the AC wave will not be cut off at higher frequencies.

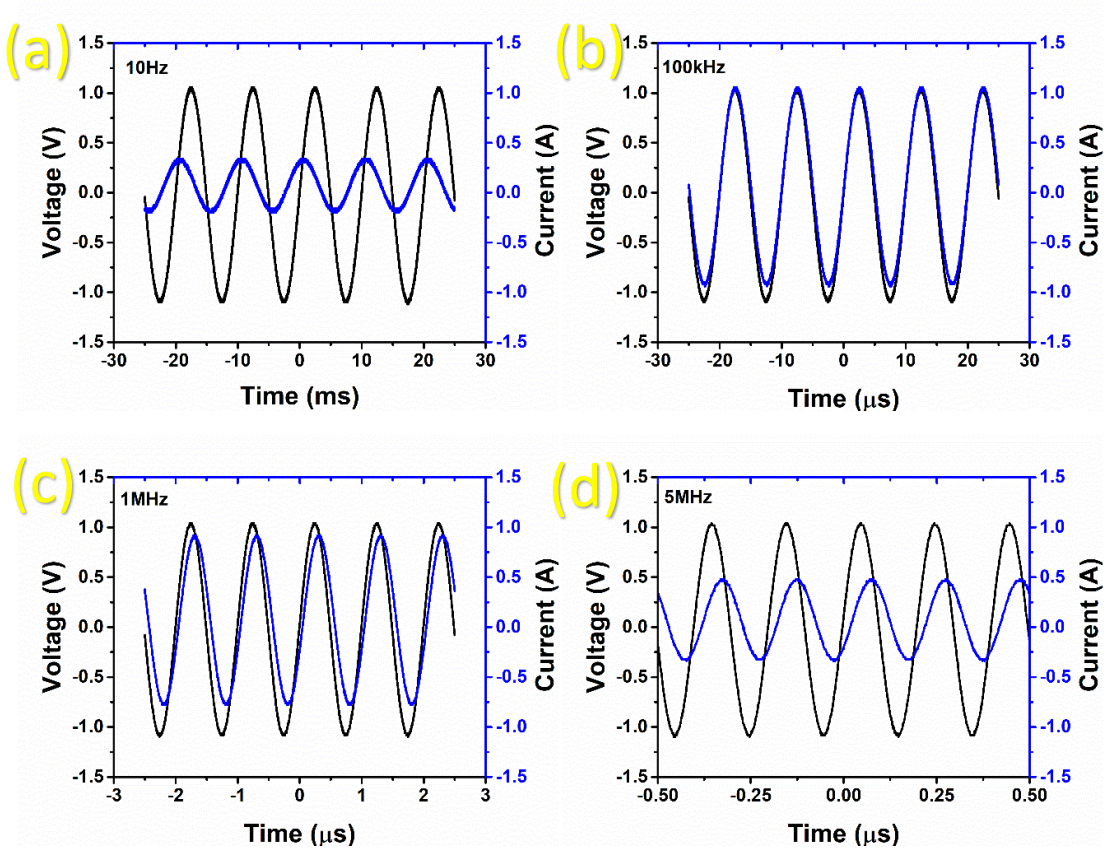

Figure 125 High Pass Filter Data for 4cm^2 capacitors at generated frequencies of (a) 10Hz, (b), 100kHz, (c) 1MHz and (d) 5MHz

The theoretical cut-off point for the 4cm^2 capacitors in either high pass or low pass configuration is calculated to be 456.79Hz +/- 32.2Hz considering the tolerance of the capacitors and resistor (gold band, 5%). This is the point where the AC current will be allowed or denied from flowing through the system at a cut-off gain of -3dB. The -3dB cut-off point was found to be an average of 634.67Hz, 145Hz higher than the upper expected limit. This suggests a lower capacitance in reality than is measured via the LCR meter and impedance spectroscopy, perhaps due to a change in the dielectric constant from environmental conditions such as humidity. Equipment limitations only allowed for measurements of frequencies up to 5MHz however, as can be seen in Figure 126(a-b) the response of the capacitor with respect to frequency is decreasing. As the capacitor has a parasitic inductance, the circuit will have a resonant frequency (f_R) in Hertz (Hz) calculated using Equation 15 where L is the inductance in Henries (H) and C is the capacitance in farads (F):

$$f_R = \frac{1}{2\pi\sqrt{LC}}$$

Equation 15 Calculation of Resonant Frequency

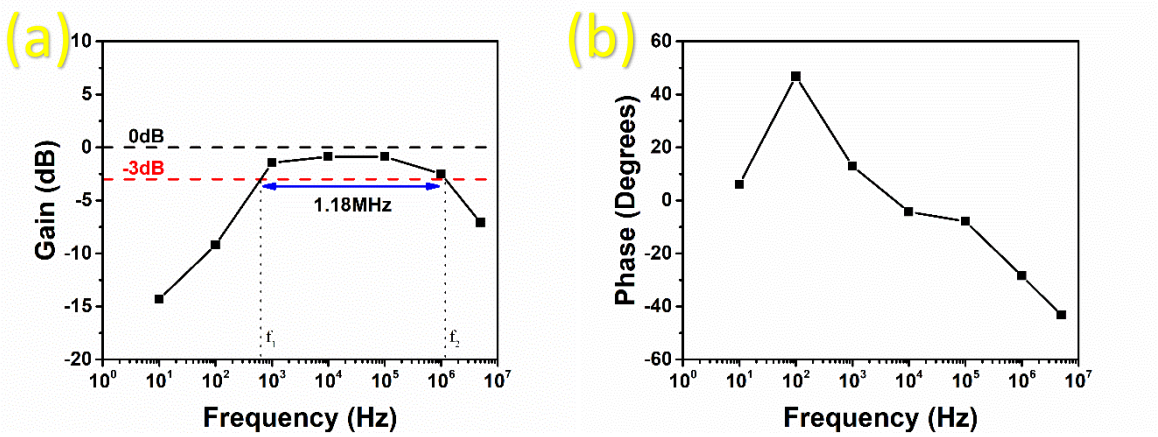

Figure 126 High Pass Filter bode plots for 4cm^2 capacitors displaying (a) frequency response magnitude and (b) phase response of the system

As can be seen in Section 7.4.3, the permittivity and capacitance of the system is decreasing as it tends to 1MHz. If it was possible in the scope of this research to sweep greater frequencies, a minima peak could be seen in capacitance, permittivity and the phase response bode plots in Figure 126 when the resonant frequency is reached. Knowing the self-resonant frequency of the capacitor is important as it dictates the usable frequency range since when operating above the resonant frequency, the capacitor acts as an inductor and creates an open circuit leading to voltage spikes [303]. To attempt to predict a range the self-resonant frequency might be in, the parasitic inductance of the 4cm^2 capacitors was measured using the LCR meter between 100Hz and 100KHz and can be seen in Figure 127.

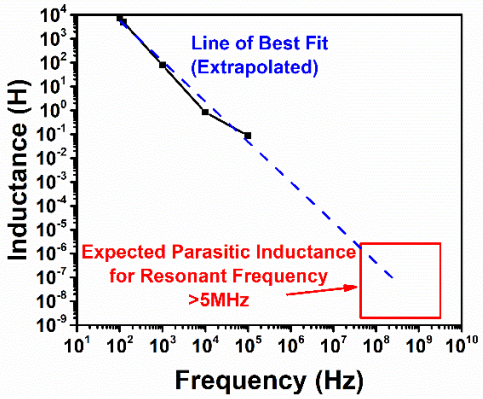

Figure 127 Measurement and Extrapolation of Parasitic Inductance

The RC data suggests the resonant frequency of the capacitor is >5MHz which is outside of the measurement range available.

7.6.3 R-C Circuits with 9cm^2 Capacitors

As with 4cm^2 capacitors, 9cm^2 capacitors were also tested in the RC circuit in a high pass configuration. Measurements at 10Hz were too noisy with a clean signal only occurring 30Hz or more. Most likely due to it acting with a high DC resistance at low frequencies. Measurements for 30Hz, 100kHz, 1MHz and 5MHz are shown in Figure 128(a-d). The average capacitance of the tested capacitors was 777.06pF +/- 62.16pF with the filter using a 1MΩ resistor.

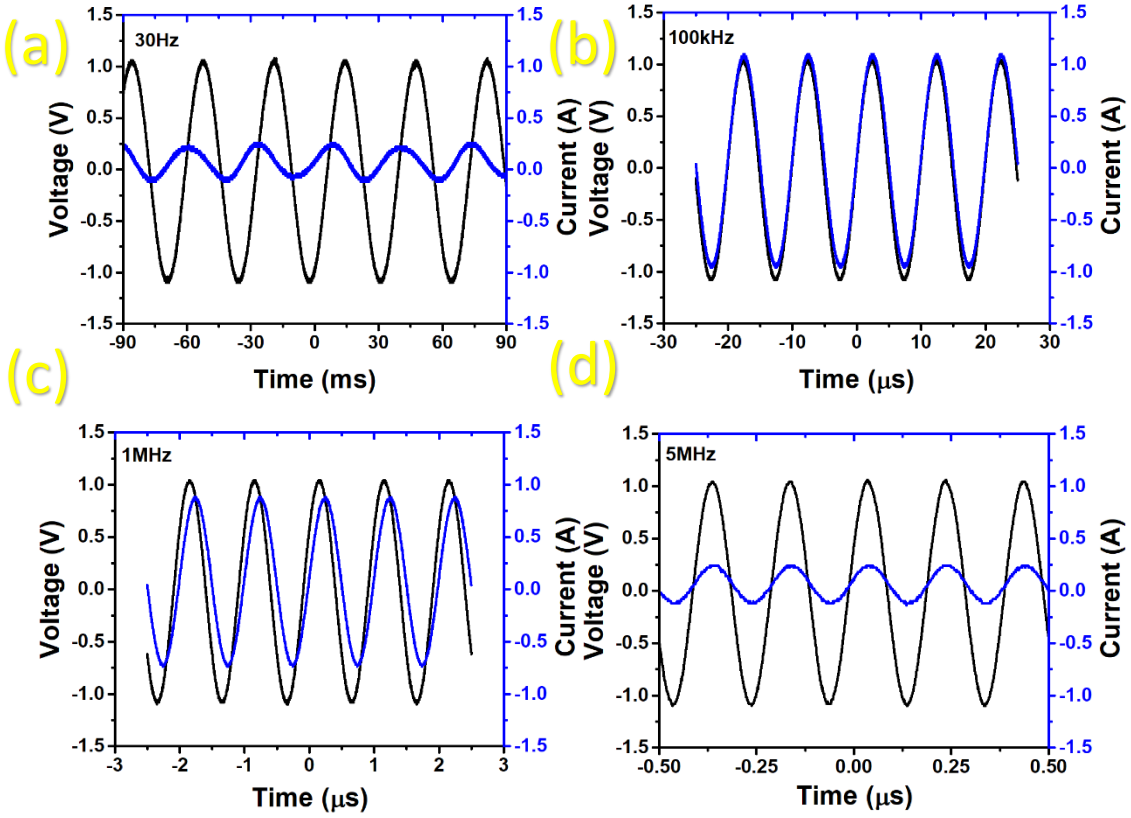

Figure 128 High Pass Filter Data for 9cm^2 capacitors at generated frequencies of (a) 30Hz, (b), 100kHz, (c) 1MHz and (d) 5MHz

The theoretical cut-off point for the 9cm^2 capacitors in either high pass or low pass configuration is calculated to be 204.9Hz +/- 36.4Hz calculating the value with the tolerances of the capacitors considered. The -3dB cut-off point was found to be 298.79Hz, much closer to the theoretically predicted value than the 4cm^2 capacitors. Looking at the impedance

spectroscopy Nyquist plots in Chapter 4. This is most likely due to a much lower effective series resistance, which can be seen by the extrapolating a straight line through the x-axis (real part of impedance). Analysing the bode plots of the capacitors seen in Figure 129(a-b), these feature a slightly larger bandwidth than the 4cm^2 capacitors, by approximately 78000kHz. Therefore, the data suggests a slight increase in the resonant frequency which is to be expected. The dielectric thickness is unchanged, which is the main factor in altering the resonant properties of a capacitor. However, a change in electrode area does appear to have a slight effect on resonance.

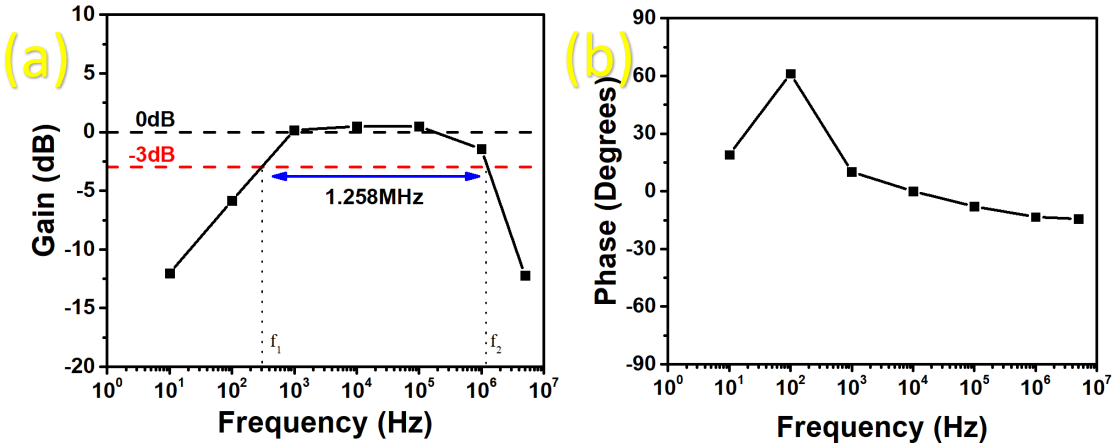

Figure 129 High Pass Filter bode plots for 9cm^2 capacitors displaying (a) frequency response magnitude and (b) phase response of the system

The phase response follows a much shallower trend compared to the 4cm2 capacitors. Once the phase hits -90 degrees, the capacitor will switch to an inductor, suggesting a larger range in which the capacitor is usable. However, higher frequency measurement equipment in future work would be needed to characterise this.

7.8 Conclusions

In conclusion, this chapter demonstrated that printed conductive oxides can be used for printed electronic applications. Firstly, printed and laser processed resistors was characterised, and it was found that laser processing could be used to tune the conductivity of the tracking between 50Ω to 20MΩ using the indium tin oxide / silver nanowire composite ink.

Capacitors were fabricated, initially interdigitated capacitors fabricated through micro dispensing, these were both oven cured, and laser processed. The micro-dispensing system available did not have the ability to repeatably print track and gaps with the widths required. All but one of the samples fabricated short circuited. Due to the inability to properly print interdigitated metal oxide capacitors, this has been left for future work at a time when better technology is available. The next design which can be used for capacitors is the parallel plate setup. As the micro-dispensing system could not be used for multi-layer and multi-material printing, screen printing was chosen as the fabrication method. An aluminium oxide dielectric ink was formulated for the parallel plate. Unfortunately, due to the two separate printing methods, the printed and laser processed resistors could not be integrated into fully printed RC circuits, however, this would be a good route to pursue in future work.

For the first time, fully printed, functional metal oxide capacitors were fabricated and characterised proving that conductive metal oxide inks can be used in electronic systems. The printed capacitors were found to be stable upon flex up to the tested strain of 30% and the capacitance can be tuned by changing the area of the electrodes. Analysis in RC circuits demonstrated they function as any commercially manufactured capacitor would, allowing for more advanced applications to be developed.

Chapter 8

Transparent Conducting Oxides as Sensing Devices

8.1 An Introduction to Humidity Sensing

As demonstrated in Chapter 7, screen-printed parallel plate capacitors can be developed using indium tin oxide (ITO) inks and a variety of dielectrics. One of the main applications of capacitors are humidity sensors. Chapter 8 will investigate the use of printed and sputter coated indium tin oxide films as humidity sensors. Characterising both in this way gives an opportunity to see how the material reacts under temperature and humidity and gives insight into how electrical properties may be affected by use in the general atmosphere.

Humidity is an important factor in many electrical, industrial and environmental systems and therefore it is as essential as temperature to monitor with ease and accuracy [1], [2]. Environmental monitoring, agriculture and manufacturing of electronics require wide range, accurate and high response humidity sensors to ensure data is reliable [2]. Most personal electronic devices in recent times are now equipped with humidity sensors and domestic applications such as smart buildings for human comfort are becoming more popular.

In this chapter, sputter coated, transparent, flexible ITO films and printed ITO capacitors are investigated for their humidity sensing properties. For the sputter coated ITO, a screen-printed dielectric polymer was incorporated into the sensor structure to develop a wide range of detectable relative humidity. Whereas the printed sensors follow the same structure as the capacitors in Chapter7. The sensors are characterised in terms of sensitivity, response times, the sensing stability of the sensors, and the mechanism of sensing is determined using complex impedance measurements. Investigating the humidity sensing properties of ITO gives insight into the ability of the material to withstand humidity and helps determine potential failure points for future transparent and printed electronics.

8.2 Design and Fabrication of Sputter-Coated ITO Capacitors

8.2.1 Sensor Fabrication

Dielectric ink was printed onto a 7.5cm^2 area of a 10cm^2 indium tin oxide film using the DEK1202 screen printer. The screen used has a polyester thread with a thread count of 305 threads per inch (TPI). A second 10cm^2 indium tin oxide film with 1cm^2 removed was then placed on top of the wet dielectric layer leaving both sections of the ITO film and dielectric layer exposed while forming a parallel plate capacitor as seen in Figure 130(a-b).

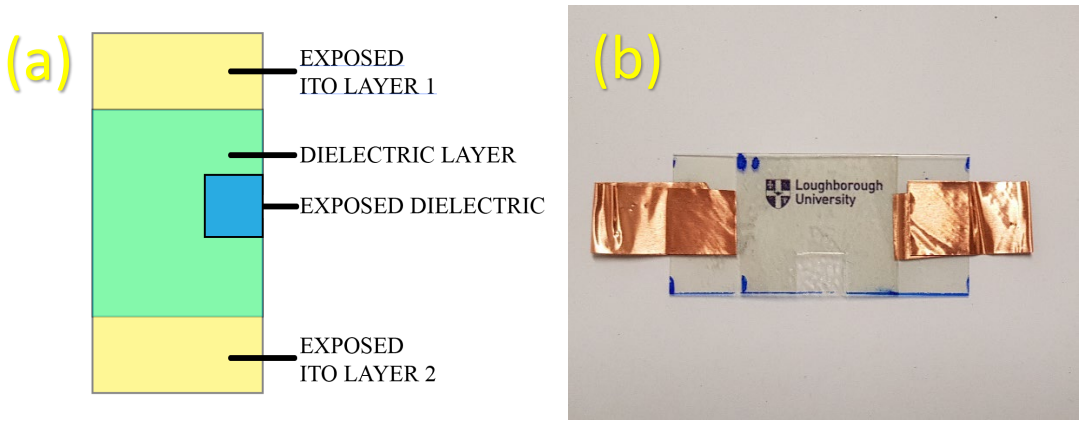

Figure 130 (a) Schematic of Sputter Coated Humidity Sensor and (b) image of fabricated sensor

The sensor was then cured for five minutes under a UV lamp (365nm, 38W) and removed. Copper tape was placed on the exposed ITO to create sturdier electrical contacts for measurements to be taken. The total area of the parallel plate capacitor after fabrication where ITO/Dielectric/ITO layers directly overlap is 5cm^2. Five sensors were fabricated with 10Ω□$^{-1}$ ITO, five more prepared with 20Ω□$^{-1}$ ITO and a final five prepared with 50Ω□$^{-1}$ ITO. The end contacts of the ITO film were exposed alongside a central dielectric square. This is to allow for the characterization of how the water molecules interact with the dielectric and the ITO film. These samples were also compared to sensors with the ITO film encapsulated, leaving only the dielectric exposed and compared to pure ITO film. The contribution of each part of the structure can then be determined.

8.2.2 Materials for Sputter Coated Parallel Plate ITO Capacitors

Indium tin oxide (ITO) films were prepared by magnetron sputter coating onto Dupont Teijin Films Melinex O (125μm, 89.5% transmittance) polyethylene terephthalate film (PET) at Diamond Coatings LTD. ITO films where prepared at varying sheet resistances (Ω/sq or $\Omega\square^{-1}$), sputter coated PET was prepared at 10, 20 and 50$\Omega\square^{-1}$. As can be seen in Figure 131, the films were highly polycrystalline with grain sizes ranging from 25 – 200nm.

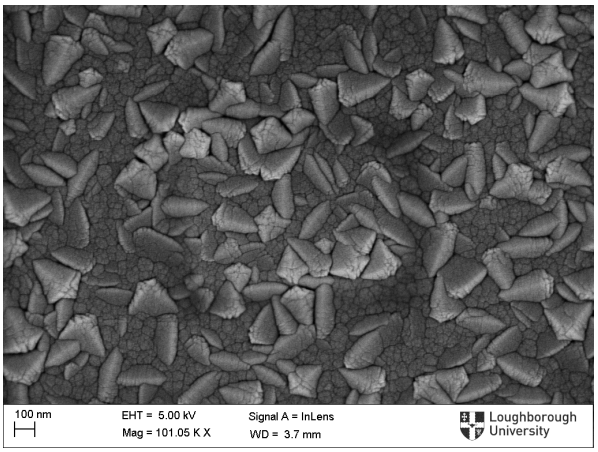

Figure 131 SEM of Sputter Coated ITO @ 10$\Omega\square^{-1}$

Gwent Electronic Materials supplied UV-curable, screen printable transparent dielectric ink D2150901D1 which is polymer based. Initially the alumina dielectric ink developed in chapter 7 was tested, however, a bond could not be formed between the two sputter coated plates. For comparison purposes, the polymer dielectric was also attempted to be used with the printed ITO capacitors, however, material compatibility issues occurred prevent fabrication. This is not an issue due to the sensing mechanism analysis via impedance spectroscopy allowing each component of the sensor to be electronically analysed for it's purpose in the humidity sensing.

8.2.3 Measurement Equipment

Capacitance measurements were taken using a UNI-T digital LCR meter (UT612), these measurements were taken using the LCR meter connected to a PC using the UNI-T digital multimeter software provided. Measurements of capacitance were taken with the LCR meter set to a frequency of 1KHz. Humidity measurements were taken using a Rotronic Instruments

HygroGen humidity and temperature measurement chamber. The software controller for the chamber was the Eurotherm 2704 temperature and humidity controller.

Scanning electron microscope (SEM) images were taken using a Leo 1530 VP field emission gun scanning electron microscope (FEG-SEM). The accelerating voltage used for all SEM images was 5kV and the working distance ranges between 5.00mm and 6.1mm. Sheet resistance measurements were taken using a Jandel HM21 four-point probe. Transmittance data for the humidity sensors were taken using a Perkins Elmer Lambda 35 UV/VIS spectrophotometer with a 100% reflectance standard and the software package used was UV Winlab.

Impedance spectroscopy measurements were taken using a Metrohm Autolab Instruments multi-channel potentiostat / galvanostat (PGSTAT12) using Metrohm's Frequency Response Analyzer software (v4.7.900). Data analysis of complex impedance data was performed using Autolab Nova (v2.0). Impedance measurements were taken using 50 measuring steps between 100kHz and 0.1Hz with an amplitude of 0.01V.

8.4 Humidity Sensing Properties of Sputter-Coated ITO Capacitors

8.4.1 Determination of Dielectric Layer Thickness and Dielectric Constant

Typically, printed layer thickness is determined by the screen with the caveat that the printed ink will shrink. As UV inks do not contain evaporating solvents which are normally required for curing, no loss of mass occurs. To determine the layer thickness of dielectric polymer after printing, the polymer was printed onto soda lime glass (NSG, cleaned in ultrasonic bath with acetone, deionized H2O and ethanol). These prints were then cured via UV (365nm) and cut with a diamond tipped blade for cross-sectional SEM, shown in Figure 132.

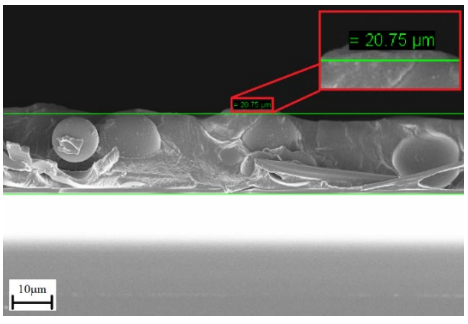

Figure 132 Cross Sectional SEM of Printed Polymer Dielectric Layers

The cross-sectional SEM shows that the printed dielectric layers had uniform layer thicknesses of 20.98μm and 20.75μm, respectively. To ensure the accuracy, the average of these two values are used to calculate the dielectric constant of the ink. Once again, Equation 16 can be used to determine the dielectric constant for each sample.

$$K = \frac{Cd}{\varepsilon_0 A}$$

Equation 16 Calculation for Dielectric Constant

Taking the dielectric thickness to be an average of the samples measured in Section 8.4.1 the dielectric constant for each sample can be determined. For the sensors using polymer dielectric ink, the average distance of separation was an average of 20.87μm, average capacitance was 522pF for sensors using the 10Ω□$^{-1}$films and area of the coated electrodes was 7.5cm^2. This gives an average dielectric constant of 1.63 for the polymer. Typically, standard polymers have a dielectric constant between 1.5 and 3 [304].

8.4.3 Optical Properties of the Sputter Coated ITO Films and Capacitors

Humidity sensors fabricated using the thickest ITO films (10Ω□$^{-1}$) were found to have a minimum transmittance of 75% in the visible spectrum (Fig.133). Sensors fabricated using the thinnest ITO films (50Ω□$^{-1}$) had a minimum transmittance of 82% in the visible spectrum.

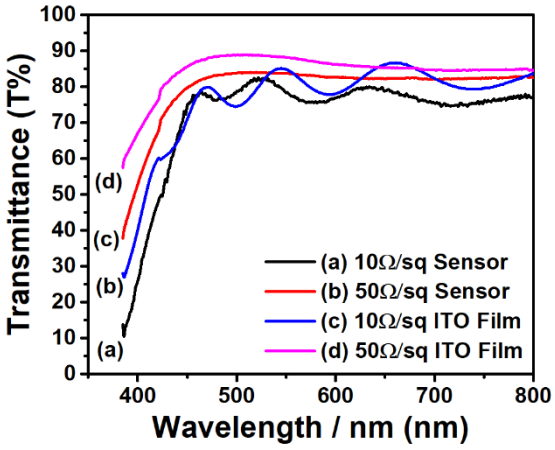

Figure 133 Transmittance Data for films and sensors between 10 and 50Ω□$^{-1}$

Due to the UV absorbing nature of the dielectric polymer ink, UV/VIS spectrophotometry measurements contained noise below 385nm. There is a 7% difference in transmittance

between the thickest and thinnest films used for sensing. For comparison, the literature value given for the Melinex O PET film used is 89.2% transmittance [305].

8.4.4 Humidity Sensing Characteristics

Capacitance versus relative humidity was measured at three different frequencies, 100Hz, 1kHz and 100kHz. (Fig.134a-d). Capacitance increases with an increase in relative humidity for all frequencies. Measurements at 100Hz show a 152% increase in capacitance between 5 - 95% relative humidity. At 1kHz a more linear 116% increase in shown and for measurements at 100kHz, the increase for the full range was 105%.

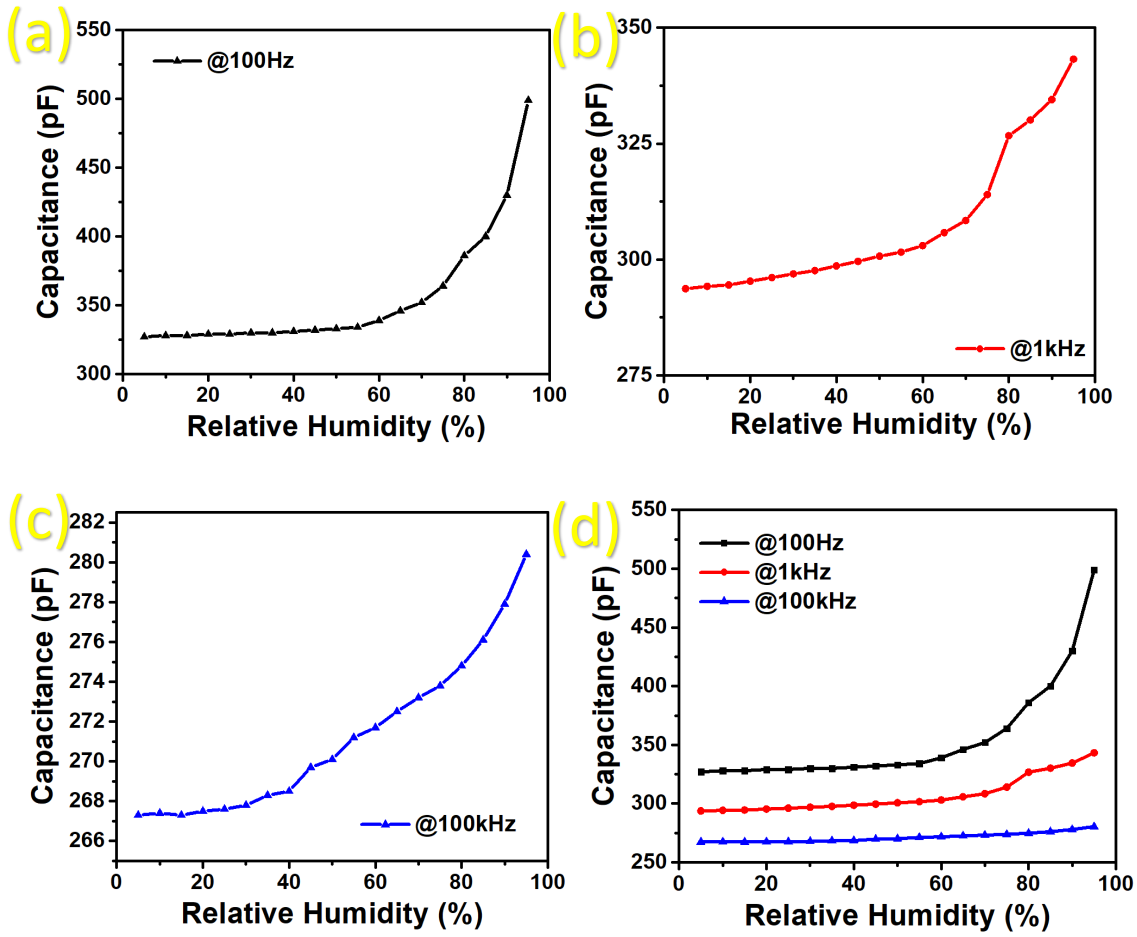

Figure 134 Humidity measurements for 10Ω□$^{-1}$sensors at 25°C, Capacitance VS Relative Humidity for humidity sensor @ (a) 100Hz, (b) 1kHz and (c) 100kHz, (d) data overlay of (a – c)

For all sensors, capacitance versus relative humidity measurements could follow a linear approximation up to 75% relative humidity. These large changes in capacitance suggest the interactions with the water have a larger effect on either the dielectric permittivity of the

polymer or conductivity of the electrode between 75 – 100% RH. This shows that if measuring humidity above the cut-off frequency of the capacitor, a different trend should be expected. The sensitivity changes depending on the sheet resistance, essentially a smaller capacitance has less range for sensing. For the 10Ω□$^{-1}$ sensors for the full humidity range, sensitivities are 2.19pF/RH%, 0.75pF/RH% and 0.31pF/RH% for 100Hz, 1KHz and 100KHz respectively. If only the linear part of the curve is considered, the data changes to 0.55pF/RH%, 0.25pF/RH% and 0.09pF/RH% for 100Hz, 1KHz and 100KHz respectively which gives a sensitivity range typically of off the shelf commercial humidity sensors. As can be seen in Fig. 135(a-d), three sensors were measured simultaneously with the general trend that the lower the sheet resistance, the higher the capacitance. Capacitors generally have a wide tolerance and the sensors are no exception.

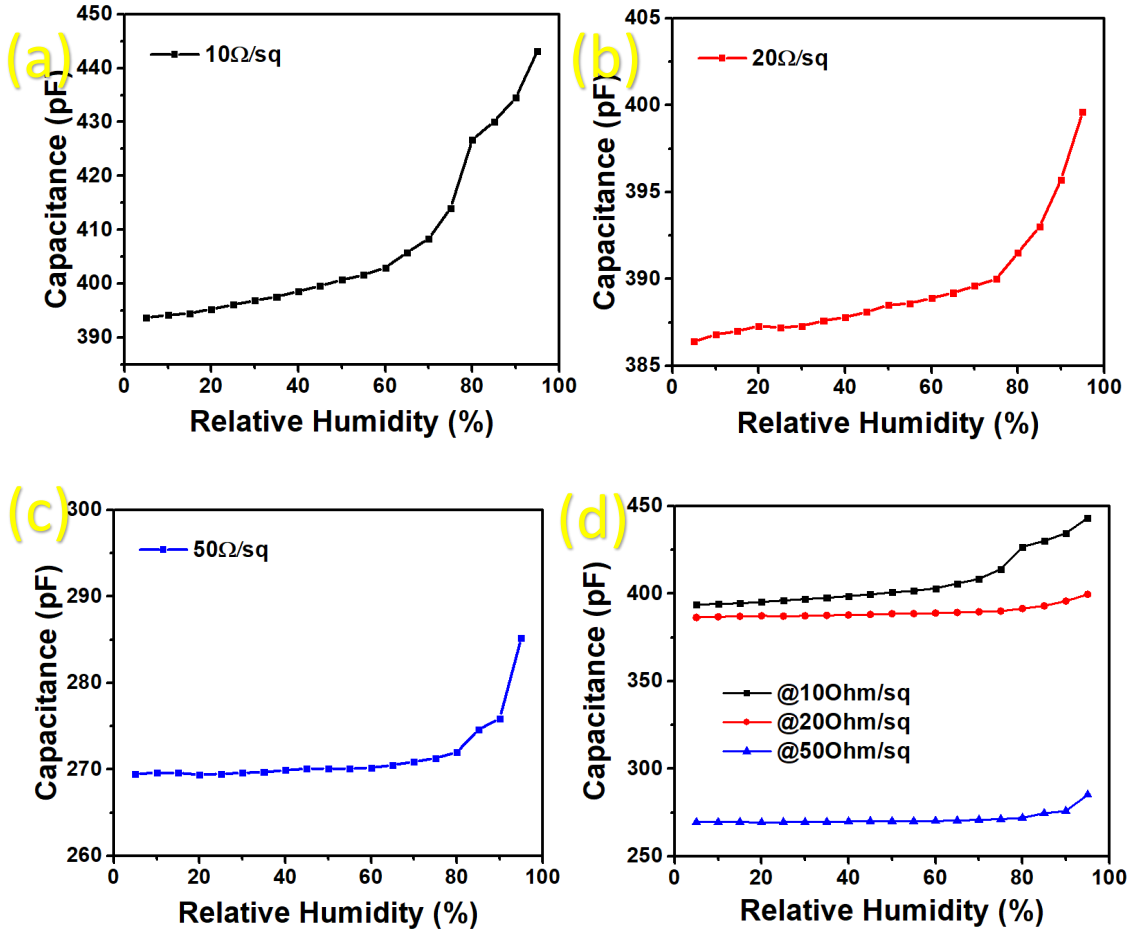

Figure 135 Capacitance VS Humidity of the sensor at varying sheet resistances, (a) 10Ω□$^{-1}$sensor, (b) 20Ω□$^{-1}$, (c) 50Ω□$^{-1}$measured @ 1kHz, (d) data overlay of (a – c)

Capacitance measurements between 10Ω□$^{-1}$ and 20Ω□$^{-1}$often overlapped in terms of values. However, 10Ω□$^{-1}$ sensors gave larger changes in capacitance compared to 20Ω□$^{-1}$sensors of a similar base value. This suggests a thicker and more conductive ITO film will give more sensitive readings. For all film thicknesses, sensors give a linear response up to 75% relative humidity. The 50Ω□$^{-1}$ sensors had minimal 0.1 – 0.2pF changes until a relative humidity of 20% had been achieved. The lower conductivity of the film affects the overall capacitance creating a less sensitive sensor. Due to the poor performance of the 20 and 50 Ω□$^{-1}$sensors, the 10Ω□$^{-1}$ sensors are chosen for further studies into their dynamic response times. This demonstrates they could be used for sensing and although they do not display higher performance, they are transparent providing an advantage over commercially available sensors.

8.4.5 Dynamic Response of Sensors

To measure dynamic response and hysteresis effects, a sweep was performed between 60% and 80% relative humidity. The sweep would stabilize at 60% RH, hold for 30 seconds, move up to 80% RH, hold for another 30 seconds and then repeat the cycle. As can be seen in Fig. 6, capacitance of the sensor vs time is plotted against relative humidity vs time. The 10Ω□$^{-1}$ITO sensor shows an average hysteresis effect of 0.8pF per cycle. Response times were measured as the time for the capacitance to peak after the humidity level reaches 80%. The 10Ω□$^{-1}$ITO sensor shows an average response time of 31.5 seconds and average recovery time of 31 seconds as seen in Figure 136.

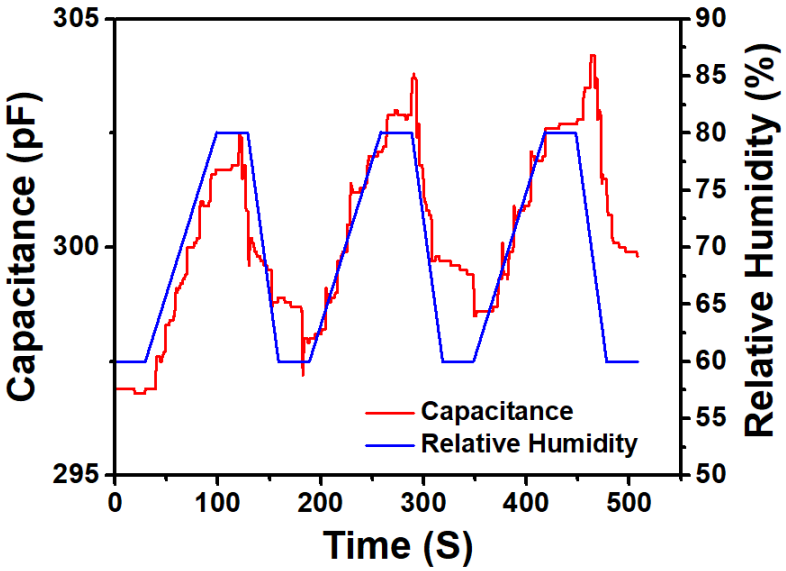

Figure 136 Capacitance VS Time against Relative Humidity VS Time for a range of 60 – 80% relative humidity

The hysteresis in the sensors can be explained using both indium doped tin oxide and the dielectric polymer. Doped oxides contain oxygen vacancies in the crystal structure and contact with open air can lead to surface alteration via oxygen containing species. When taking capacitive measurements, the dielectric polymer introduces hysteresis to the capacitance. When a water molecule absorbs onto the surface of the polymer, it can either diffuse into the polymer or desorb. Hysteresis is affected by a failure of water molecules to desorb back into the atmosphere. Another potential contribution to the hysteresis is capillary condensation where water can absorb into the pores of materials and is not always reversible, trapping the water [306].

8.4.6 Stability of Sensors

Stability measurements were taken over seven days for 10Ω□$^{-1}$, 20Ω□$^{-1}$ and 50Ω□$^{-1}$ sensors and can be seen in Fig 137(a-c). These were taken to see if material degradation had taken place over the week of measurements.

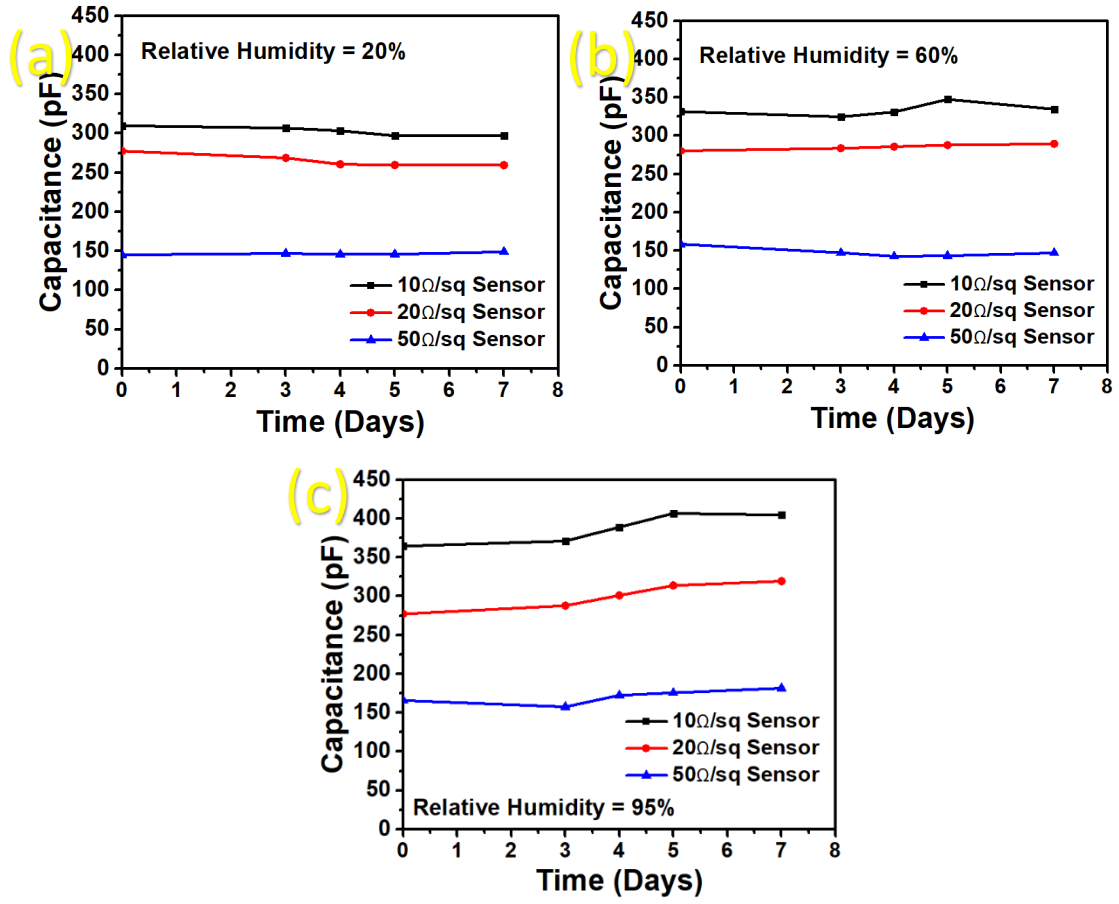

Figure 137 Stability of sensors over 7 days taken at (a) 20% relative humidity, (b) 60% relative humidity and (c) 95% relative humidity

At 20% relative humidity sensors were at their most stable with day to day changes in capacitance kept in a small range. At 60% relative humidity the average trend over the seven days was also linear with any changes in capacitance staying within a certain range. However, for sensors at 95% relative humidity, a general rising trend can be seen over the seven days with larger fluctuations in humidity. This suggests that the high levels of moisture create an ongoing hysteresis effect at this humidity and the changes in capacitance match the data seen in Fig 134(a-c).

As can be seen in Figures 134(d) and 1355(d), after 80% relative humidity, a non-linear increase in capacitance is recorded. Combining this with the data from Figure 1377(a-c) suggests that a point in relative humidity has been reached were water is more likely to be trapped into the dielectric layer, changing the dielectric constant with greater effect leading to a jump in capacitance.

In Figure 137(b) for the most conductive and highest capacitance sample a variation can be seen at the 4 – 5 days region. In Figure 137(c) this can also be seen on all the samples, suggesting this is an artefact of increased humidity and sensitivity. In Figures 134 and 135, capacitance changes become larger and the sensor becomes more susceptible to humidity changes at higher humidity's and higher ITO conductivities. Therefore, this variation is most likely due to a combination of higher sensor sensitivity and this sensitivity giving the hysteresis a more prominent effect on measurements. This data suggests the sensors are more stable within a 5 – 75% relative humidity range and that the most transparent, least conductive sensors are the most reliable.

8.4.7 Complex Impedance and Sensing Mechanism Analysis

Impedance measurements were taken at six different relative humidity levels, ranging from 5% to 95% relative humidity. The sensor response was measured from 0.1Hz to 100kHz. As seen in Fig 138(a) the impedance spectra are altered with increasing humidity. An increase in relative humidity is associated with an observed shrinking of the high frequency semi-circle on the Nyquist plot (Fig. 138(a)). This semi-circle corresponds to the bulk resistance of the dielectric layer and is seen to decease as the humidity level increases. The semicircle can be modelled seen in Fig 139(a-b), using a parallel Resistor (R) – Constant Phase Element (CPE) circuit (R-CPE circuit) and this typically represents adsorption levels in humidity sensors [307] [308]. The CPE in this section of the circuit is a near ideal capacitor where if n = 1 is an ideal capacitor, modelling demonstrates a consistent $1 > n > 0.972$ for these sensors.

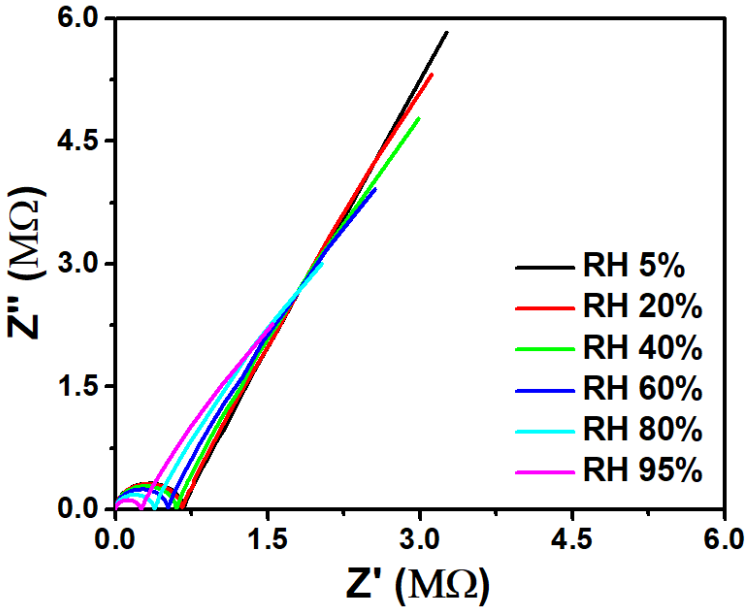

Figure 138 Nyquist plots for 10Ω□$^{-1}$ sensors at 5%, 20%, 40%, 60%, 80% and 95% relative humidity

At lower frequencies, another feature is seen in the Nyquist plot, after the high frequency semi-circle. A straight line is seen (at low humidity) which seems to transform I to a second semi-circle at higher humidity. This can be attributed to a double layer capacitance forming on the exposed dielectric, this occurs from the diffusion of the water into the polymer, changing the dielectric permittivity and therefore capacitance of the sensor. The largest change in both the straight line and the semi-circle also is confirmed by the capacitance vs humidity measurements in Fig 134(a-c). Polymer dielectric based humidity sensors tend to have a greater response to relative humidity changes between 75% and 100% [309] [310].

Typically, capacitors in complex impedance spectroscopy rarely behave ideally, instead acting as a constant phase element (CPE) or non-ideal capacitor. In a Nyquist plot this generally represents a charge transfer reaction and in a humidity sensor can be attributed to both ionic diffusion and double layer capacitance. As seen in Fig 9(a-b) the change in dielectric permittivity of the dielectric can be modelled as a parallel CPE – RW circuit. In the CPE – RW section represents both ionic diffusion into the dielectric of the sensor and a double layer capacitance forming via a layer of adsorbed water molecules onto the water surface.

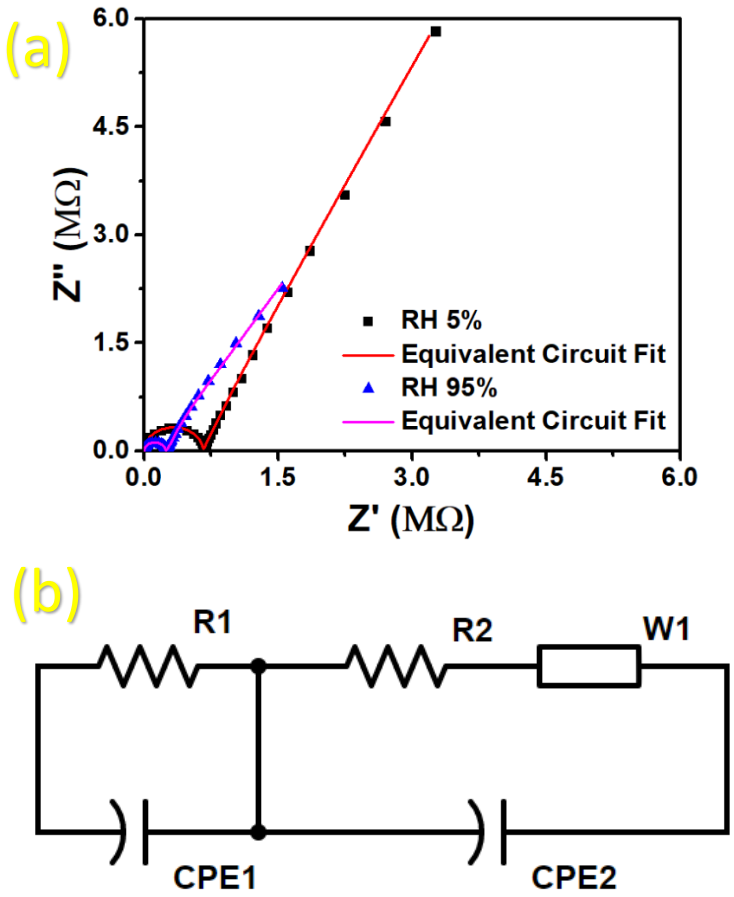

Figure 139 (a) Simulated and Nyquist plots for sensors at 5% and 95% relative humidity and (b) equivalent circuit diagram for the sensors

At a higher relative humidity, the straight-line is shown to curve which indicates it is the start of a larger semi-circle, rather than a straight line. This can also be modelled with Warburg impedance which can be associated with a charge transfer element in the sensor. This suggests that at higher humidity levels, ionic diffusion begins to occur. At a higher relative humidity, the ionic conductivity increases as more H+ and OH- ions complex with the surface, lowering the bulk resistance of the dielectric and increasing the capacitance [310] [311].

8.5 Humidity Sensing Properties of Printed ITO Capacitors

8.5.1 Printed Parallel Plate Capacitors as Humidity Sensors

The design of the printed humidity sensors remains unchanged from the capacitors used in Chapter 7, due to the alumina dielectric already being exposed to the air, allowing for water absorption. Indium tin oxide in the literature has also been investigated for it's humidity sensing properties. To determine whether the dielectric or the conductive material or a combination of the two provide the humidity sensing mechanism, impedance spectroscopy can be used.

8.5.2 Materials

The materials used in this section are the same as described in Section 7.4.2.

8.5.3 Measurement Equipment and Experimental Setup

Capacitance measurements were taken using a UNI-T digital LCR meter (UT612), these measurements were taken using the LCR meter connected to a PC using the UNI-T digital multimeter software provided. Measurements of capacitance were taken with the LCR meter with varying frequencies of 100Hz, 1KHz, 10KHz and 100KHz, the default setting of the LCR meter is 1KHz. Humidity measurements were taken using a Rotronic Instruments HygroGen humidity and temperature measurement chamber. The software controller for the chamber was the Eurotherm 2704 temperature and humidity controller. Impedance spectroscopy measurements were taken using a Metrohm Autolab Instruments multi-channel potentiostat / galvanostat (PGSTAT12) using Metrohm's Frequency Response Analyzer software (v4.7.900). Data analysis of complex impedance data was performed using Autolab Nova (v2.0). Impedance measurements were taken using 50 measuring steps between 100kHz and 0.1Hz with an amplitude of 0.01V.

8.6 Humidity Sensing Properties of Printed ITO Capacitors

8.6.1 Humidity Sensing Characteristics of 4cm^2 Capacitors

Capacitance versus relative humidity was measured at four different frequencies, 100Hz, 1kHz, 10kHz and 100kHz as shown in Figure 140 for three replicates. Capacitance increases with an increase in relative humidity for all frequencies as expected due to water absorption altering the dielectric properties of the metal oxides. The sensors were measured between 5 and 95% relative humidity, the limits of the environmental chamber used, with temperature kept constant at 25°C. The average sensitivity of the sensors and the standard errors of the mean were calculated for each measurement frequency. For measurements at 100Hz, the average sensitivity of the sensors are 3.8pF/RH% with a standard error of the mean of 0.42pF/RH%. For measurements of 1kHz, the average sensitivity is 2.11pF/RH% and the standard error of the mean is 0.23pF/RH%. This then further reduces to 1.185pF/RH% and 0.85pF/RH% with errors of 0.12 and 0.092 for 10kHz and 100kHz respectively. A decrease in sensitivity with an increasing frequency is to be expected as data shown in Chapter 7 details that the dielectric constant of the capacitor decreases with decreasing frequency. In the literature, most of the shelf capacitive humidity sensors have a typical sensitivity of <0.5pF/RH% [312]. This means the 4cm^2 capacitive humidity sensors in comparison to the literature are classified as high sensitivity alongside being highly linear.

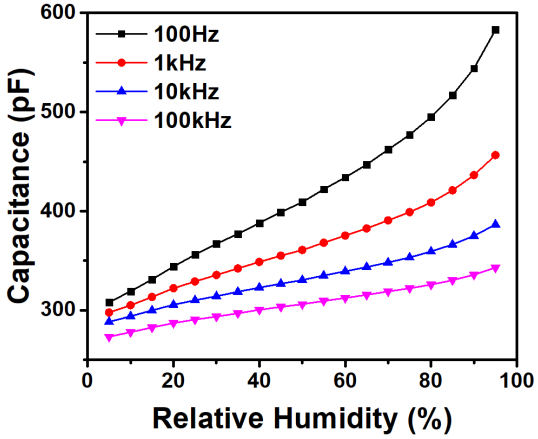

Figure 140 Relative Humidity Sensing Characteristics of a 4cm^2 Sensor at Different Frequencies

Analysing the data, it can be seen that although the sensors follow the typical non-linear pattern, the degree of linearity is exceptionally high for a humidity sensor. Plotting lines of

best fits for each replicate and repeat results in an average R2 value of 0.9772 with a standard error of the mean of 0.004822 allowing for the use of a linear approximation in the programming for any device utilising these printed sensors. The percentage minimum to maximum are 204%, 164%, 140% and 127% for 100Hz, 1kHz, 10kHz and 100kHz respectively.

8.6.2 Hysteresis Analysis of 4cm^2 Capacitors

Measurements of hysteresis were taken via two methods, firstly, due to the environmental chamber used, the rate of humidity increase is highly controllable, however, the decrease of humidity is not due to an immediate venting of chamber caused by the control unit. The first measurement, therefore, is a measurement of increasing relative humidity from 5 to 95%, the chamber is then left at 95% for 10 minutes to reach a full saturation and then decreased in 5% intervals to 5% to see how closely the sensors return to their original value. The second method repeatably increases and decreases between two relative humidity values and to determine whether the sensor returns to its base position. The first method, hysteresis loops can be seen in Figure 141(a-d) and as can be seen in each loop, the final capacitance is generally quite close to the initial starting capacitance. For sensors at 100Hz, a 6pF difference is observed between the start and end of the loop. For 1kHz, 10kHz and 100kHz, differences of 4.1pf, 3.2pF and 13.5pF are observed.

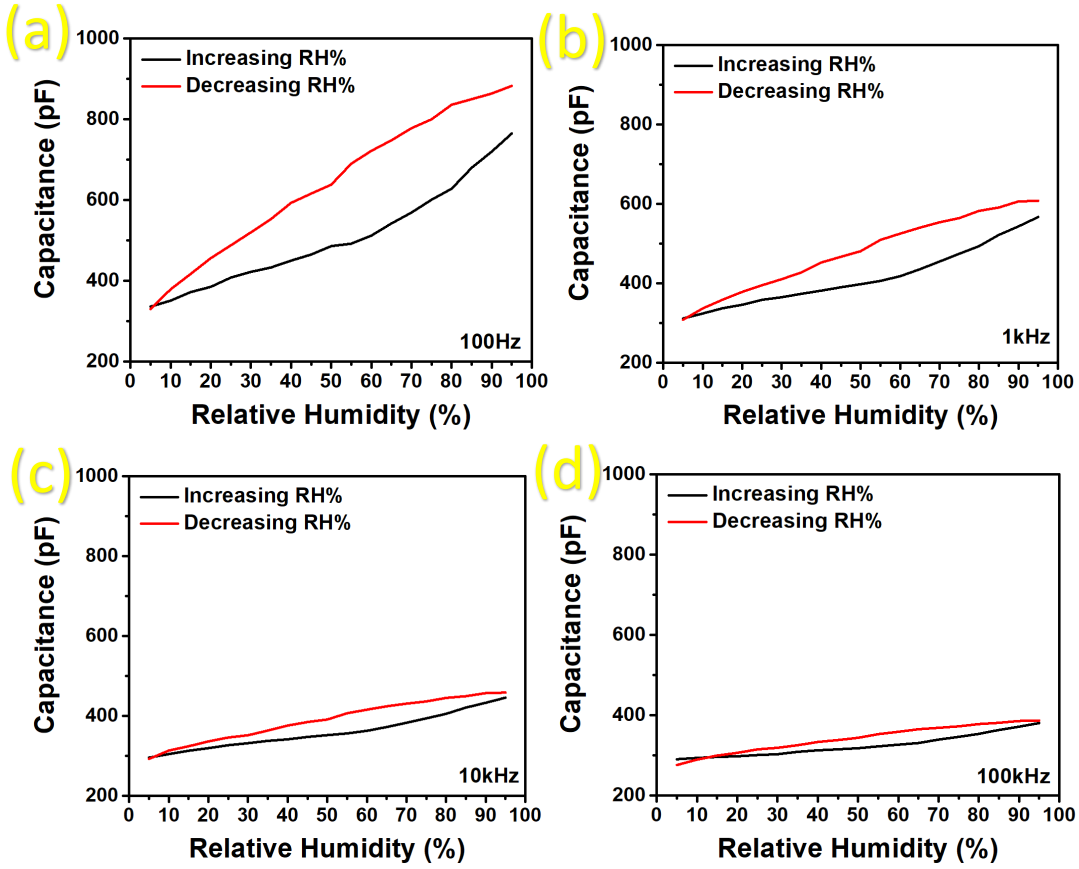

Figure 141 Hysteresis curves for humidity sensors at (a) 100Hz, (b), 1kHz, (c) 10kHz and (d) 100kHz

Analysing the data, it can be seen that although the sensors follow the typical non-linear pattern, the degree

8.6.3 Humidity Response Characterisation of 4cm^2 Capacitors

Sensors were measured for the response and recovery times in a controlled temperature (Constant 25^{o}C) and humidity chamber. Response and recovery times were measured between four ranges of humidity, these being 15 – 30%, 15 – 50%, 15 – 70% and 15-90%. The upper and lower limits of 90% and 15% were selected due to the chamber time to reach relative humidity below 15% or above 90% taking longer than the sensors response and recovery time. The response time is calculated by measuring capacitance and relative humidity with time and shown in Figure 142. Once the humidity reaches its maximum value, the response time is measured as the time taken for the sensor reading to plateau. Again, for the response time, it is measured as the time taken for the humidity sensor to plateau once the humidity chamber has reached its targeted humidity.

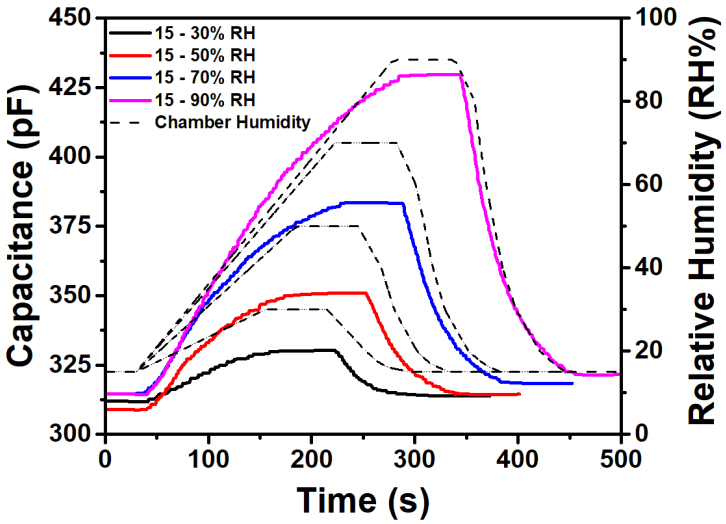

Figure 142 Humidity Response Curves of Humidity Sensors

The average recovery and response time was 20.88 seconds and 4.63 seconds respectively. Alumina has been commonly used in various humidity sensors in the literature however, never in a fully printed capacitive humidity sensor before. Analysing the literature, the structure of the alumina is considered to provide a major contribution to the response and recovery time. Metal oxides sense primarily through diffusion so typically have slower response times than some other materials with a range in the observed literature of 28 seconds to >240 minutes. Therefore, these sensors display faster response times than previously reported work. Any recovery or response time below <5 seconds is considered fast, demonstrating that the sensors have a typical response time but a fast recovery time at 4.63 seconds, most likely due to the printed films allowing for quick diffusion out of the films.

8.6.4 Humidity Sensing Characteristics of 9cm^2 Capacitors

For the 9cm^2 humidity sensors, the average sensitivity of the sensors and the standard errors of the mean were calculated for each measurement frequency. For measurements at 100Hz, the average sensitivity of the sensors are 7.76pF/RH% with a standard error of the mean of 1.04pF/RH%. For measurements of 1kHz, the average sensitivity is 3.69pF/RH% and the standard error of the mean is 0.51pF/RH%. This then further reduces to 2.76pF/RH% and 1.93pF/RH% with errors of 0.28 and 0.018 for 10kHz and 100kHz respectively. This follows the same trend as 4cm^2 sensors while providing much greater sensitivity. The average linearity for each response curve is an average R2 of 0.9738 with a standard error of the mean of 0.002793.

Therefore, although the system has just as good linearity as the 4cm^2 capacitors with the added benefit of an even higher, excellent sensitivity as shown in Figure 143.

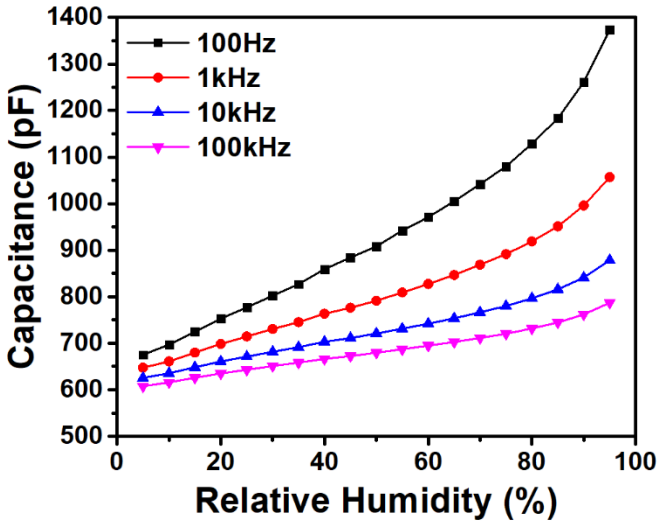

Figure 143 Relative Humidity Sensing Characteristics of a 9cm^2 Sensor at Different Frequencies

From the data it can be seen that these sensors can provide good, sensitive humidity sensing across the entire relative humidity spectrum. The percentage increase in humidity compared to the 4cm^2 sensors also follow the same trend, with percentage changes increasing by only 3 – 11%. The percentage increases are 215%, 168%, 143% and 131% for 100Hz, 1kHz, 10kHz and 100kHz respectively, indicating that the larger increased capacitance only has a minimum effect on relative sensing range but a large effect on the sensitivity.

8.6.5 Hysteresis Characterisation of 9cm^2 Capacitors

The hysteresis loops for the 9cm^2 sensors are shown in Figure 144(a-d) which show different properties to the 4cm^2 loops. In the waiting and stabilisation period once the increasing RH% has reached 95%, there appears to be a drop in the capacitance which could indicate the increased capacitance in the 85 to 95% range is due to some migration of water through the ITO layer also adding some sort of contribution to the capacitance, after a migration via diffusion of the water into the alumina, the capacitance then decreases. Below 85% RH, typical hysteresis loop behaviour is seen. Measurements at 100Hz show a difference of 82pF which is much more than the 4cm^2 sensors. This is due to the primary water absorption method being slow diffusion and stability measurements discussed in a later section will analyse whether the sensors return to their true value.

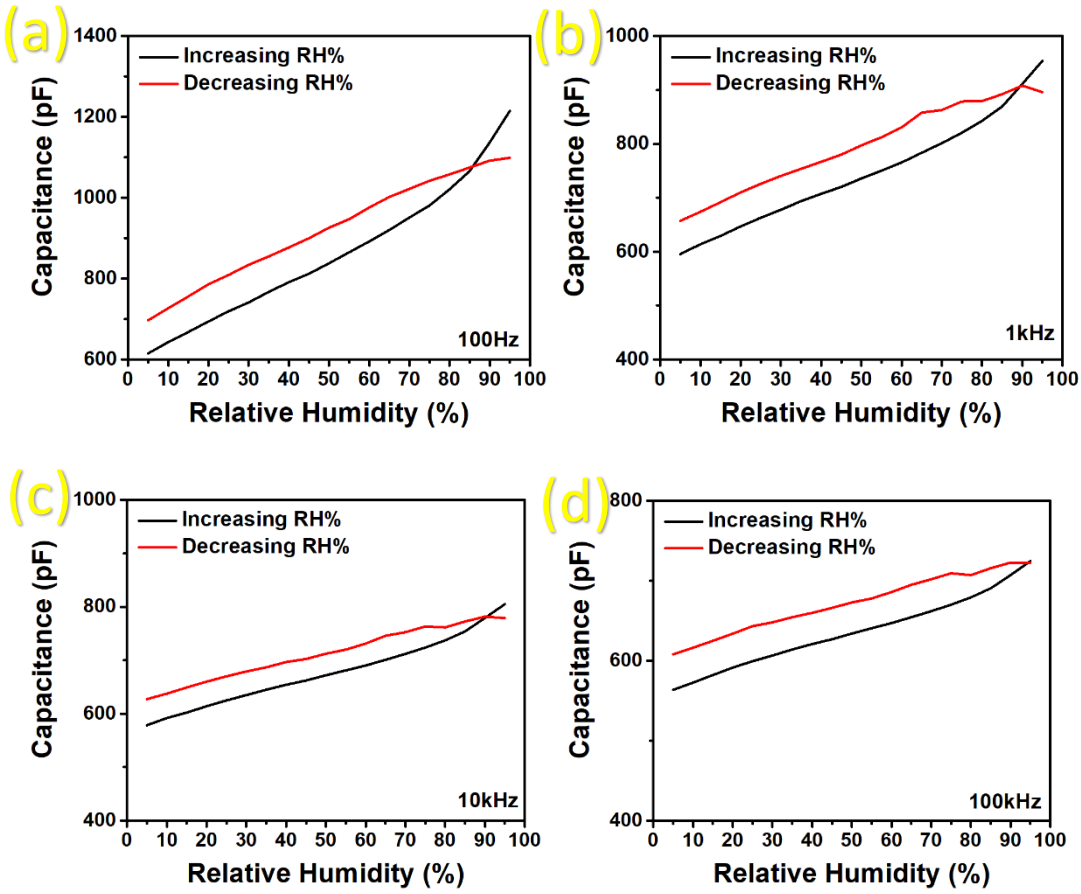

Figure 144 Hysteresis curves for humidity sensors at (a) 100Hz, (b), 1kHz, (c) 10kHz and (d) 100kHz

At 1kHz, the difference in the start and end capacitance is 61.8pF and for 10kHz and 100kHz it is 48.7pF and 44.5pF respectively. Therefore, there is greater hysteresis in the larger sensors which, due to the diffusion process is to be expected.

8.6.6 Humidity Response Characterisation of 9cm^2 Capacitors

As shown in Figure 145, compared to the smaller 4cm^2 sensors, the larger 9cm^2 sensors plateau much later in the sensor cycle. It appears that due to the larger sensor area, a longer time is taken for the dielectric to reach a saturation point where water diffusion is so slow, over realistic timespans a plateau is formed. Both response and recovery times are much slower suggesting a compromise to be considered when altering sensor size between response and recovery time and then sensitivity depending on the application. For the sensor in the range of 15 – 30% relative humidity the response time is 51.5 seconds with a recovery time of 49 seconds. Moving up to a 50% relative humidity, the response time changes to 56 seconds and a recovery time of 76.5 seconds. At 70% relative humidity, response times were in the same range as previous measurements at 45 seconds and the recovery time 68.5

seconds. Finally, for measurements at 90% relative humidity a peak was reached at 43 seconds and the response minimum measured at 72.5 seconds.

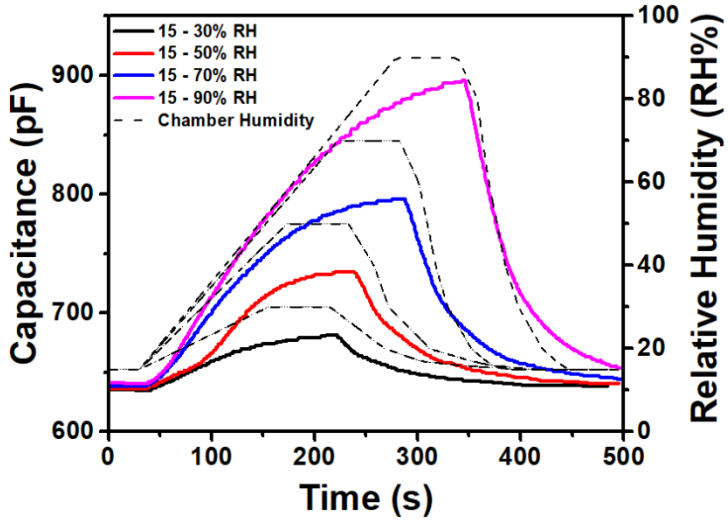

Figure 145 Humidity Response Curves of Humidity Sensors

Therefore, the average response time of the sensor is 48.8 seconds and the recovery time is 66.63 seconds. The response times measured indicates some sort of linear relationship between capacitor area and response time, considering the 9cm^2 sensor is 2.25x larger than the 4cm^2 and the response time is 2.34x larger. However, the recovery time is much larger than the 4.63 seconds of the smaller sensors, suggesting the water diffusion process out of the film is much slower with an increasing film.

8.6.7 Dynamic Response and Environmental Stability of Humidity Sensors

Dynamic response was measured by alternating between 60% and 80% relative humidity and the time between peaks. The sensors and humidity were measured in real time to provide capacitance and humidity plots and data can be seen in Figure 146. The sensors follow the humidity plot very closely due to their reasonable response and recovery times. An initial observation of hysteresis is made between the first and second peak. However, there is very little hysteresis between the second and third peak suggesting once an initial saturation point has been reached, due to the delay in diffusion out of the film, the hysteresis becomes minimal as water is only absorbed into easily accessible parts of the film.

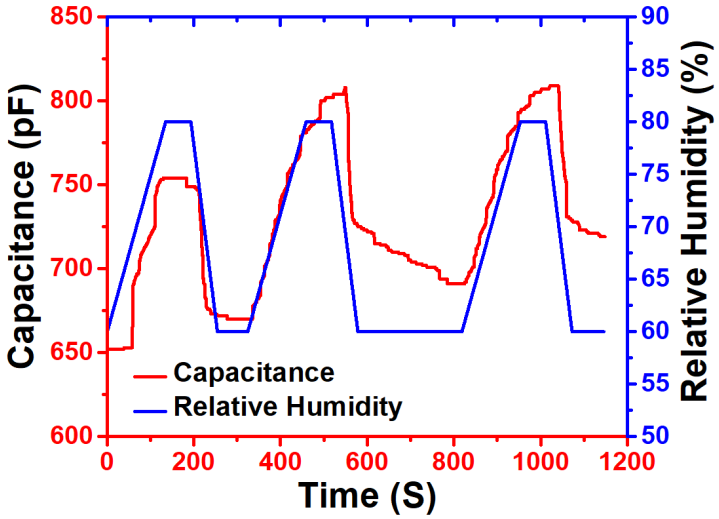

Figure 146 Humidity Sensor Dynamic Response

Stability measurements were taken at three different humidity levels, a low humidity level of 20% RH, a medium humidity level of 60% RH and a high humidity level at 95% RH. The first measurement was taken an hour after placement into the chamber to allow it to acclimatise to the new humidity. Stability measurements were taken until readings became stable and can be seen in Figure 147(a-c). For both 20% and 60% RH experiments, stability was observed approaching 7 days. With regards to measurements at 20% RH for the 4cm^2 sensors, a decrease from 312.7pF to 307.4pF was observed and for the 9cm^2 sensors a decrease from 582.5pF to 572.5pF was observed. As this humidity level is lower than typical environmental humidity's, it is possible this is caused by the long-term diffusion of any leftover water in the sensor's pre-measurement.

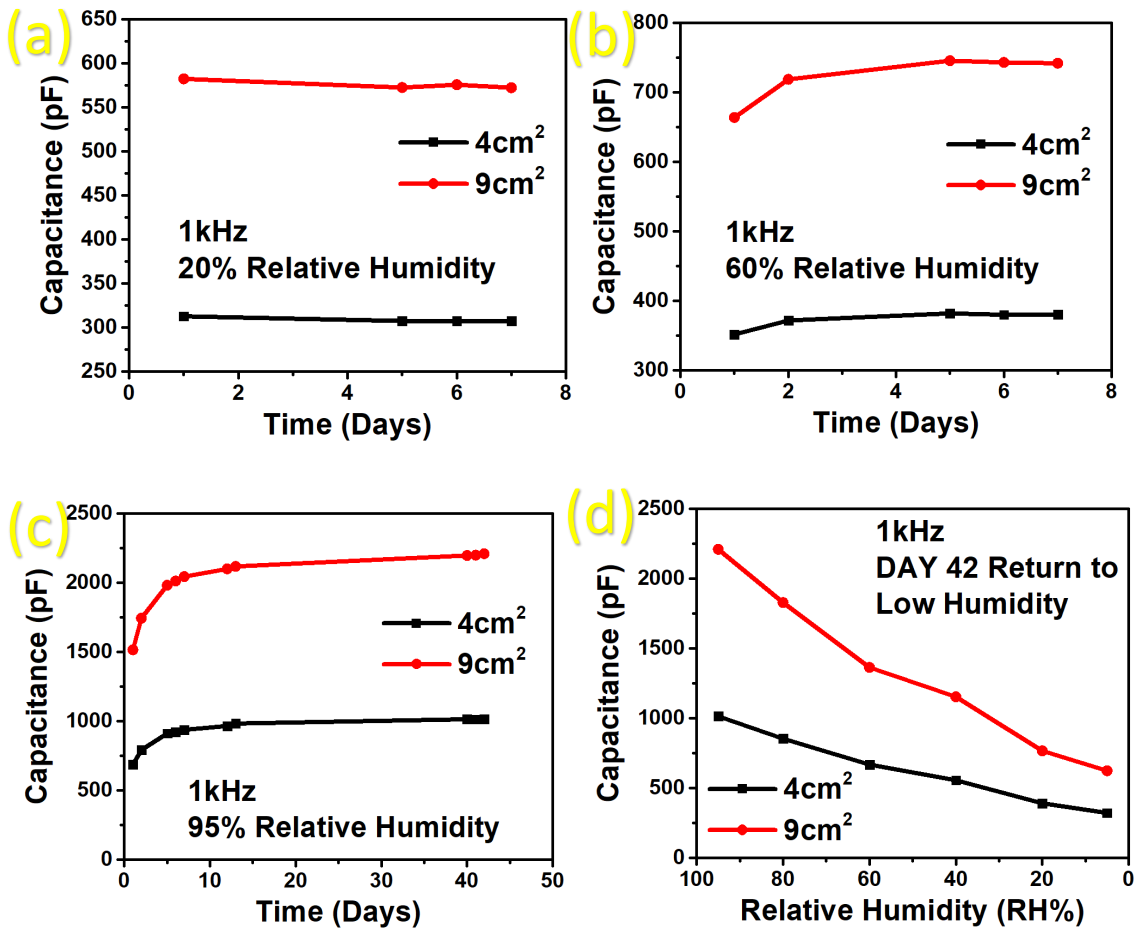

Figure 147 Environmental stability of sensors at (a) 20% RH, (b) 60%RH and (C) 95%RH with the (d) return profile from 95% to 5%

For the sensors measured at 60% RH, a general increase in capacitance is shown over the first five days of measurement before stabilisation. The most likely explanation is due to the diffusion of water becoming more difficult after an initial absorption phase, taking days instead of seconds to fully saturate the dielectric. The initial 4cm^2 capacitance was 351.6pF with a final stable capacitance of 380.4pF, whereas the 9cm^2 sensor had a capacitance of 664.1pF moving up to 742.1pF. The 95% RH high humidity stability measurements were initially taken for 2 weeks, then left for a further 30 days to account for a full saturation of the dielectric film. Capacitance was found to increase from 686.9pF to 1014.6pF for the 4cm^2 sensor and from 1516.3pF to 2211pF for the 9cm^2 sensor. For the 95% RH sensor measurements, to determine whether the high humidity for 45 days had any lasting effects, the humidity was lowered back to 5% relative humidity with data shown in Figure 147(d). For the 9cm^2 sensor measurements, the sensor moved back to a 5% RH of 623.8pF whereas the 4cm^2 sensor dropped to 321.9pF. After leaving the sensors in for another 24 hours, final

capacitances of the 4cm^2 sensor were 308.1pF and 594.5pF for the 9cm^2 which is exceptionally close to the original values. Impedance measurements were also taken post stability measurements to see the effects of long-term moisture exposure on the sensors. Nyquist plots are shown in Figure 148(a-b).

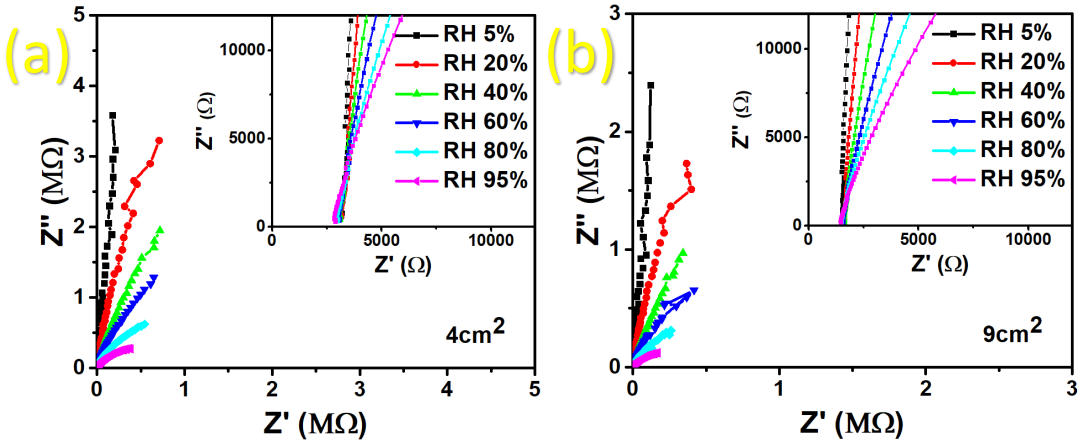

Figure 148 Nyquist plots post-stability measurements at varying relative humidity's for (a) 4cm^2 and (b) 9cm^2 sensors

Analysing the Nyquist plots, it appears there is no lasting effect on the sensor at 5% RH for both the 4 and 9cm^2 sensors other than a slight drop in imaginary impedance. At 95%, the start of a semi-circle can be observed which is typical of ionic conductivity, showing that so much water has been absorbed into the film that OH-, H+ and impurities in the water are acting to aid in the electric field generation and the conductivity of the dielectric material. Looking at the inset for both Figure 148 (a-b), the ESR increases with a decreasing humidity, proving that the water is increasing the conductivity of the system.

8.6.8 Humidity Sensing Mechanism Analysis

Analysing the relative permittivity of the sensors (Figure 149) at different humidity levels shows that the water vapour is indeed being absorbed into the alumina dielectric and enabling the sensing. Bulk alumina has a permittivity of 9.6, whereas water has a bulk permittivity of 80, therefore and increase in water absorption essentially increases the permittivity and then the capacitance. At 750 – 850Hz, a spike can be seen in each measurement, this is most likely due to the fact that the humidity measurements could not be performed in a faraday cage and is most likely noise from parasitic electromagnetic waves at that frequency. Another dip can

be seen at 120Hz, a common frequency used in consumer electronics. There appears to be minimal effect at higher frequency

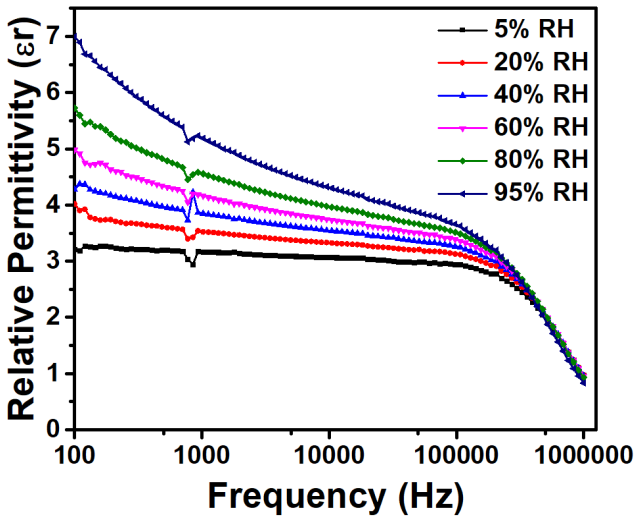

Figure 149 Relative permittivity of sensors at varying relative humidity percentages

From the impedance analysis shown in Figure 150, it can be seen that the non-ideal from behaviour of the capacitor is increasing. A perfect capacitor will have a Nyquist plot with no changing real impedance, and only a change in the imaginary impedance, essentially a 90^{O} angle to the x-axis. The increasing humidity levels are creating and increasing amount of ionic conductivity in the film and beginning to create a semi-circle characteristic of the phenomena. This is also interpreted as the capacitor moving away from being a perfect capacitor and that the water absorption / ionic conductivity is creating a more imperfect capacitor with the water increasing the dissipation factor and the dielectric permittivity in tandem.

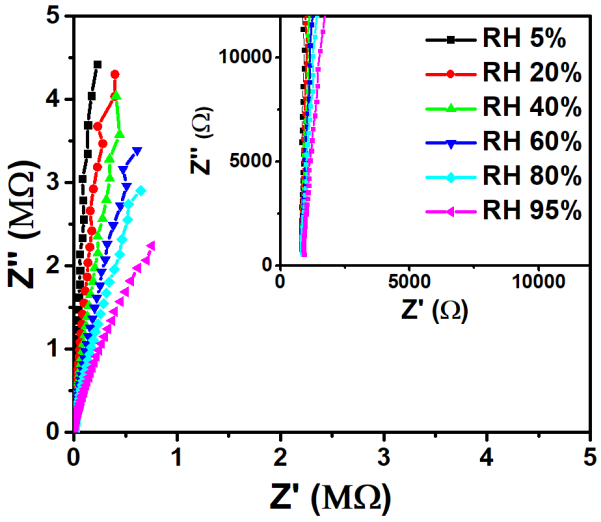

Figure 150 Nyquist plot of sensors at varying relative humidity percentages for a freshly fabricated sample

When simulating, knowledge about the design of the electrical is required. With the printed parallel plate capacitors, the structure is resistive film of ITO, resistive dielectric film of alumina where the electric field is generated with polarisation and a second resistive film of ITO. Due to this, the 0% humidity system, or in this case the 5% humidity model, can be described in equivalent circuit terms as a resistor connected to a resistor (ITO) and capacitive element in parallel (Alumina) connected to a resistor. Since no capacitor can be ideal, the capacitive element is chosen as a constant phase element, which models as a capacitor with an ideality (n) between 0.9 and 0.99. In the literature, the true physical meaning of the constant phase element (CPE) has been discussed.

One ample explanation for capacitive devices of porous materials such as this system, each dielectric particle-particle boundary in the dielectric can create an electric field having a capacitive element, with the particle itself also being resistive. Therefore, the dielectric layer can be modelled as an essentially infinite amount of RC circuits, each with their imperfect capacitance. To represent this as one circuit component, the CPE is used. For the sensing mechanism analysis, the sensor is modelled at both 5% and 95% humidity, the minimum and maximum that can be measured in the experimental setup. We can then observe the system with no water absorption and the system with maximum water absorption. The two chosen equivalent circuit diagrams can be seen in Figure 151(a-b).

For the no water absorption system, the circuit matches the 5% relative humidity with the constant phase element showing a near perfect capacitor where N = 0.988. Adding a second CPE to one of the ITO part of the equivalent circuit diagram at shows the N value of the ITO section at 0.945 and the N value of the Alumina at 0.93 showing the capacitance is becoming more imperfect due to water absorption into both films.

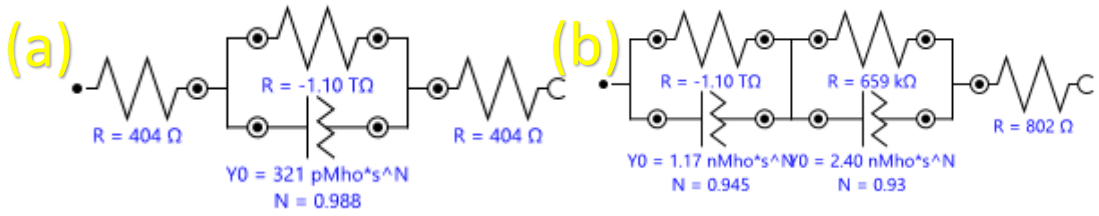

Figure 151 Equivalent circuit diagrams at (a) low humidity and (b) high humidity

With these equivalent circuit diagrams, Nyquist and bode plots are simulated. The simulation of 5%RH equivalent circuit diagram provides a near perfect fit to the experimental data, however, it does not fit the 95% RH data, proving that a new element is required to describe the sensing system. The simulated circuit diagram for the system at 95%RH, with the added CPE to the ITO part provides again a near perfect simulated bode plot and Nyquist plot as shown in Figure 152 (a-b).

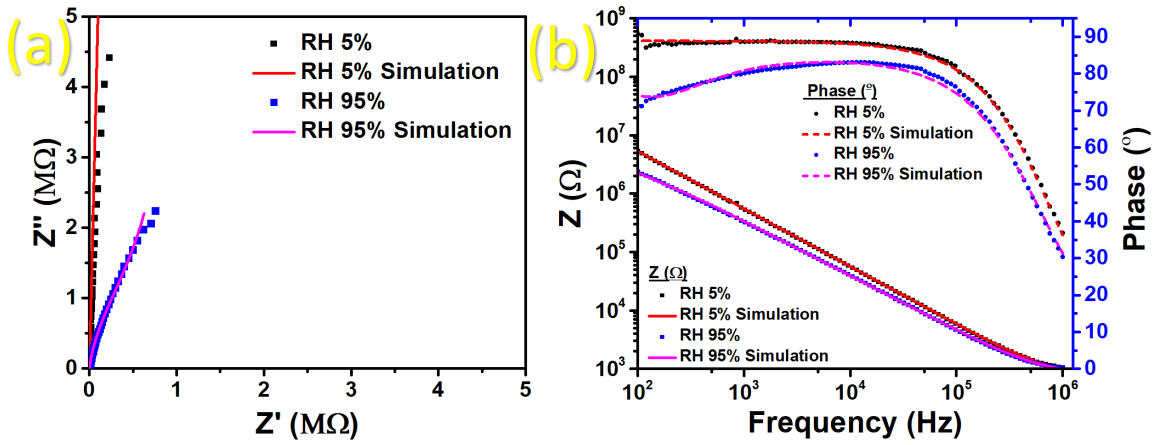

Figure 152 (a) Simulated versus measured impedance responses at low and high humidity and (b) the corresponding bode plots

As can be seen in both the Nyquist and bode plot, the simulated equivalent circuit data provides a good fit. Using the knowledge from the sputter coated capacitors, it can be assumed that at the 95% relatively humidity point, the water is causing a semi-circle to be

created, a sign of ionic conductivity in the dielectric which is typical of humidity sensing. Simulations were performed for each impedance measurement to determine at which humidity the indium tin oxide starts contributing, it was found that the ITO electrode provided no contribution to the humidity sensing until 80% relative humidity. This humidity percentage is the point where the system becomes nonlinear in the humidity versus capacitance data in Figure 140. This suggests the mechanism of the humidity sensor is the absorption of water into the alumina pores, increasing ionic conductivity and the dielectric constant essentially creating a Helmholtz electrical double layer.

8.7 Conclusions

The humidity sensing properties of sputter coated indium tin oxide were investigated by the design and fabrication of parallel plate capacitors. Sensors were transparent with a range of 75 – 82% transmittance in the visible region. The relative humidity range tested was between 5% and 95% RH. Response and recovery times were measured for both modes. In capacitive mode response times were on average 31.5 seconds with an average recovery time of 31 seconds. Complex impedance spectroscopy was performed on the sensors at different humidity levels to determine the sensing mechanism. The sensing mechanism was found to be a combination of ionic diffusion and ionic conductivity increasing in the dielectric layer, a double layer capacitance forming on the dielectric layer altering dielectric permittivity. These results provide insight into the use of transparent conducting oxides as electrodes for dielectric based capacitive transparent humidity sensors.

For the first time, fully printed all metal oxide humidity sensors were printed and characterised and were found to perform better than their counterparts made with materials manufactured via traditional manufacturing processes. The sensors had excellent stability which could be altered with a change in sensor size, ranging from 0.85pF/RH% to 7.76pF/RH%, all much higher than commercially available discrete humidity sensors which are typically in the 0.2 – 0.5pF/RH% range. The response time of the sensors again altered with a changing size with the smaller 4cm^2 sensors having a great response time of 20.8 seconds and an excellent, fast average recovery time of 4.63 seconds. The sensing performance was highly linear (R2 >0.97) for sensors of different sizes for the entire humidity range. Again, this provides a large advantage over commercially available capacitors which only demonstrate linearity across a small humidity range, for example 10 – 75% is quite typical. The sensing mechanism was found to be primarily due to the properties of the alumina, with the water absorption of ITO contributing in a minor way at high humidity above 80%.

Chapter 9

Conclusions and Future Work

9.1 Thesis Overview

This chapter will provide an overview of the research conducted in this body of work with some final remarks on the successes, the limitations, the key contributions to knowledge and some direction for future work. In this thesis, the research has focused on the development of conducting oxide electro-ceramic inks for printed electronics applications. It has outlined the challenges faced in enabling these generally highly structured, crystalline materials to perform in the high energy, disordered world of printing. After succeeding in developing usable inks, various passive components were fabricated in the two and three-dimensional printing domains leading to viable integration of these novel materials to traditional manufacturing methods.

9.2 Key Findings and Contribution to Knowledge

9.2.1 Considering the Key Findings with Regards to the Research Questions

The overall aim of this research was:

To progress the field of manufacturing conductive oxide based electronic devices with the long-term aim of improving sustainability via reduction of waste and harmful halogenated chemical processing. For this to be attained, there is a need for a method of depositing TCOs in complex patterns. Any post-processing method must be industrially viable.

From this overall aim, five research questions were formulated in Chapter 1:

(RO1) Identify and determine the characteristics of ITO and ITO Alternatives

This research objective was completed by the literature review and was motivated by the environmental and economic concerns of using indium. By distilling the most recent data at the start of this research in Section 3.3.4, it was determined that aluminium/gallium co-doped zinc oxide and gallium doped zinc oxide were the most promising indium free candidates for replacing ITO. This was due to their similar conductivities and visible light transparencies for

thin film coatings. Due to a lack of literature for these materials in the field of printed electronics, four materials were selected. These were:

- Commercial indium tin oxide
- Microwave synthesised aluminium/gallium doped zinc oxide
- Microwave synthesised gallium doped zinc oxide
- Continuous hydrothermal flow synthesised gallium doped zinc oxide

Materials characterisation was performed on these materials to determine the qualities and properties of the powders. Inks were then formulated for electrical and optical characterisation.

(RO2) To formulate and optimise conductive oxide-based inks and characterise the properties of printed films

Research objective 2 was completed in Chapter 5, which was based on the ink formulation of the conductive oxide materials. Three vehicles were tested to find the most suitable for developing TCO based inks. Inks were formulated for low temperature curing ($110^{O}C$) which created highly conducting prints ($50\Omega\square^{-1}$) and highly transparent prints (<85%T) however, it was discovered that there is a large trade-off between the conductivity and transparency achieved which was mainly due to particle size differences. Inks with larger particles suffered from a large decrease in transparency while having much higher conductivities due to larger grain sizes and particle overlap. Inks which provided transparent layers were found to not recrystalise at these lower temperatures and therefore did not exhibit grain growth contributing to large grain boundary resistances. It transpired during the research that optically clear, highly conductive electro-ceramics were not possible. A decision was made to prioritise the conductivity of metal oxide inks due to their wide range of applications, however, transparency was still measured throughout post-processing out of interest.

The most transparent ink and the most conductive ink were selected for further trials which studied the effect of mixing other transparent conducting materials on optical, electrical and rheological properties. ITO and GZO inks had additions of:

- Carbon Nanotubes
- Single Layer Graphene Flakes

- Silver Nanowires

It was determined that there was an apparent change in conductivity for the GZO based inks which warranted further investigation with regards to the post-processing experiments.

(RO3) To investigate an industrially viable post-processing technique for optimisation

This research objective was completed in Chapter 6. Laser processing was selected as the post-processing method to be investigated. The laser to be used was a 980nm diode InGaAs laser which is combined with the Haecker micro-dispensing system which is generally used in industry for pick and place PCB manufacturing. The two main and six composite inks developed in Chapter 5 were used. It was found that the post processing method significantly increased the conductivity of the ITO and GZO. For the ITO, the conductivity increased from 3.08% to 40.45% of the bulk which is a dramatic increase. With regards to the GZO, the original films were non-conductive, however, conductivities of 10.12% of the bulk could be observed post laser treatment. It was also discovered during the laser processing that the laser could convert particles into different morphologies, not only developing an industrially viable post processing method of curing, but also developing a rapid, industrially viable method of fabrication of particles which are typically difficult to fabricate quickly.

(RO4) Develop and Characterise Printed Interconnect and Passive Devices

This research objective was completed in Chapter 7, where both laser processing and traditional screen-printing techniques were used to create a range of tuneable printed interconnects and capacitors respectively. Using the laser processing and micro-dispensing method developed in Chapter 6, 250μm tracks were printed, and laser processed using a variety of inks. It was found that by changing the laser processing parameters, the two-point resistance of the tracks could be altered dramatically, allowing for a tuneable resistance range observed between 50Ω and 20MΩ.

Then, due to the multilayer advantages of the screen-printing technique, fully metal oxide printed capacitors were fabricated and characterised. The capacitors were found to be highly stable and relatively low loss for printed devices with capacitances in the range of 100 – 1000pF, they were tested in RC circuits and were found to perform as expected, showing no difference to commercially available capacitors.

(RO5) Characterise Printed 2-D Applications Utilizing the Printed Passive Components

In chapter 8, this research objective was completed by the development of the printed capacitors into humidity sensors. These humidity sensors were characterised by analysing the humidity versus capacitance curves, the sensitivity, response times and sensing mechanism. They were found to have excellent sensitivity compared to commercially available humidity sensors, the response and recovery times were also good compared to other ceramic based sensors. The sensor humidity response was found to be linear across the whole humidity range measured (5 – 95%RH) which again proves to better than the majority of sensors available currently. Transparent humidity sensors were also fabricated using sputter coated ITO which provided results on par with commercial sensors with the added benefit of being optically transparent.

9.2.2 Main Contributions to Knowledge

Contribution 1 – Conducting Oxide Based Screen Printing Inks

Firstly, in Chapter 5, indium tin oxide inks were formulated and achieved 3.08% of the bulk conductivity of the indium tin oxide resulting in the most conductive indium tin oxide inks at the time of writing. The resulting ink films observed had a sheet resistance of 57.7$\Omega\square^{-1}$, which is on par with carbon but not as conductive as silver, this work provides a foundation for a relatively highly conducting n-type semiconductor material to be integrated into printed electronics. This is currently the most conductive, printed and low temperature cured oxide material, enabling the integration of metal oxides into functional printed electronics.

Contribution 2 – Laser Processing Greatly Improves the Conductivity of Both ITO and GZO

Originally, research objective three set out to investigate how a post processing method other than conventional heat-treatment could affect the final optical and electrical properties of the metal oxide-based inks. Laser processing was selected for this and, while the optical properties were not improved, with regards to the indium tin oxide inks, a conductivity of 40.47% of the bulk was achieved. For the gallium zinc oxide, a conductivity of 10.21% of the bulk could be gained, demonstrating that with laser processing, the conductive properties of the inks could be greatly improved. This provides a post-processing method for metal oxides which enables highly conductive, and chemically stable printed electronics.

Contribution 3 – Discovering a New Manufacturing Method for the Rapid Production of Oxide Nanostructures

During the laser processing, a full materials characterisation study was performed revealing that a carbothermal reduction process occurred, converting standard spherical metal oxide particles into a variety of nanoparticle morphologies. This is the first time this has been performed (according to the literature) using lasers, and, allows for large amounts of further work into testing and developing this method for a wide variety of metal oxide materials. In the future, with better printing technology, the mass production of printed, exotic ceramic morphology structures with high performance can be rapidly manufactured and patterned using this technique.

Contribution 4 – Development of Fully Metal Oxide Based Printed Electronic Components

For the first time, fully printed conductive metal oxide resistive and capacitive components have been developed for the field of printed electronics. This demonstrates and creates the potential for manufacturers of printed electronics to use more materials than the traditional carbon and silver. For the printed humidity sensors, due to the fact the electrodes are all metal oxide and more environmentally stable, more of the sensor can be exposed to the environment rather than being encapsulated. Furthermore, with the experiments performed in this thesis, there was no evidence of lasting damage or degradation for any of the conductive samples

9.3 Main Limitations of the Research

There are some limitations to the research performed in this thesis which it is important to discuss. Reviewing the work in Chapter 5, one of the main limitations is that with ink optimisation, there are many routes one can take, all of them with disadvantages. Here, a standard Taguchi framework design of experiments was used. This is better than the traditionally used mixture experiment as there is no statistical confounding meaning the determination of the effects of parameters on the ink is accurate. However, in a mixture experiment, the relative ratios of material are controlled, all components of an ink must add up to 100% and a mixture design divides this percentage between the components. In the Taguchi method, this forgoes component fractional percentage consistency for the sake of higher quality main effects analysis. It was felt it is more important to know the effects of each factor on the ink, however, some may prefer a traditional mixture design route.

In Chapter 6, the main limitation is not one of methodological choice, but a limitation of the evidence that can be collected to prove the final theory of the chapter. It is theorised that from all the evidence collected from an extensive materials characterisation experiment that the material is undergoing a carbothermal reduction synthesis. However, there is currently no experimental method which can observe this process in-situ. It could be indirectly inferred with an in-situ laser processing of the material within a transmission electron microscope. However, this would still not be definitive proof as it would have to be performed under high vacuum. Also, the integration of a laser processing system into a transmission electron microscope is beyond the remit of this research. Therefore, it can be said that according to the analysis performed in this thesis, the most likely mechanisms for the formation of the nanowires is a carbothermal reduction process, although this cannot be said for certain.

Another main limitation of the thesis is in Chapter 8, namely, the sensing mechanism analyses for both humidity sensors. Focussing on the modelling of the impedance spectra through the use of equivalent circuit diagrams, it is often the case that multiple models can fit a measured system. With regards to both of the sensors, the development of the equivalent circuit diagrams were formed through the knowledge of the constituent materials and the structure of the materials. By considering the structure of the dielectric material, the sensor structure, particle sizes, apparent porosity etc. the equivalent circuit diagrams were made. Although

these models fit the measured experimental data well, it must be said that there could perhaps be another equivalent circuit that could fit. However, the reasoning behind each model has been discussed, and it is with knowledge of the systems developed that these are close to a real description of the process. Another limitation with the humidity sensors is that although aging and stability testing was performed, accelerated aging does not always reflect upon the real-world performance.

9.4 A Reflection of the Research and Future Work

After an initial development of printed electronics from the late 1990's to the late 2000's, it became apparent that for mass, high value and worthwhile integration of printed electronics into existing products, devices have to be fully printed. However, until now the majority of printed electronics research has focussed on silver and carbon-based conductive elements. Overall, this research has laid some foundations for further research into integrating new materials into printed electronics. It has highlighted some of the challenges and compromises required to develop functional inks using new materials. For example, spherical nanoparticles of silver and carbon can provide enhanced properties but for ceramics, it vastly increases the amount of grain boundaries, creating a compromising situation between conductivity and transparency. For future metal oxide ink formulations, two routes of future work seem promising. The first route is to expand this current research in developing conductive, n-type and p-type inks for thick films which can conduct in the sub-kilohm sheet resistance range. With this, particle size and optical properties do not matter, however, these can further advance printed resistive and capacitive devices, sensors and perhaps even potentially printed logic in the future. The second route of potential future work is to focus on developing the manufacturing technology to print and crystallise the materials through solution processing. The challenges with this are likely to be altering pre-cursor solution rheology with additives and developing the manufacturing and processing technology.

During this research, a new manufacturing method for printing and converting materials into interesting and useful nanostructures has been developed. For future work, there is a lot of potential for this method. As demonstrated, the laser processing of printed metal oxides can be performed with at least two common metal oxide materials and due to the processing mechanism, there is no reason why it would not work with others. It can be foreseen that there is much potential in printing and processing a wide range of metal oxide materials and characterising the final resulting products. It would also be extremely useful to focus on the printing and processing mechanism, manufacturing equipment and secondary optical additives on the ability to control the rates of growth. This would be towards the manufacture of highly uniform nanostructure films where the size and structure of every single particle can be controlled within a small standard deviation.

9.5 Some Concluding Remarks

Overall, the original goal of introducing conductive metal oxide materials into the world of printed electronics has been achieved. The conductive metal oxides chosen were of the transparent conducting oxides (TCO) family of materials, with the hope that some transparent electronics may be able to be printed. It transpired that this was not achievable, and a decision was made to pursue these materials considering conductivity alone. Due to this, major advances in the printing of this material has been achieved by focusing on the conductive aspects. In this research, the most conductive metal oxide inks at of the time of writing this, processed at low temperatures have been developed. This enables indium tin oxide, a degenerate n-type semiconductor to be integrated into printed electronics for the development of electronic components. This has been demonstrated by the three applications (resistors, capacitors and sensors) discussed in this thesis. To overcome some of the difficulties in working with this material (i.e. high temperature processing), a laser processing method was introduced into the printing process. This shows excellent future potential in manufacturing metal-oxide based electronics and by using heavily organic based vehicles, it allowed for the carbothermal reduction process to take place, allowing for nanoparticle morphologies to be manufactured post printing. The two techniques developed were then utilised to developed resistive and capacitive components that are tuneable and outperform others in the literature. Now that the groundwork has been laid for the use of the materials in printed electronics, it will be exciting to see how they can be integrated further and what types of applications can be fabricated with them.

Works Cited

[1] IDTechEx, “Transparent Conducting Films (TCF) 2016-2018 Forecasts, Markets, Technologies",” IDTechEx, 2016.

[2] A. Elshkaki, T. E. Graedel, L. Ciacci and B. K. Reck, “Resource Demand Scenarios for the Major Metals,” *Environmental Science and Technology,* vol. 52, no. 2, pp. 2491-2497, 2018.

[3] UNITED STATES GEOLOGICAL SURVERY, “Tin,” USGS, 2017.

[4] itri, “2016 Report on Global Tin Resources and Reserves,” ITRI, 2016.

[5] A. Stadler, “Transparent Conducting Oxides—An Up-To-Date Overview,” *Materials,* vol. 5, no. 4, pp. 661-683, 2012.

[6] R. A. Vogel, “Fine Line Printing for Consumer Electronics,” *Solid State Technology,* pp. 51 - 54, 1972.

[7] J. S. Chang, A. F. Facchetti and R. Reuss, “A Circuits and Systems Perspective of Organic/Printed Electronics: Review, Challenges, and Contemporary and Emerging Design Approaches,” *IEEE Journal on Emerging and Selected Topics in Circuits and Systems ,* vol. 7, no. 1, pp. 7 - 26, 2017.

[8] H. Kipphan, Handbook of Print Media, vol. 6, Germany: Springer, 2001.

[9] J. A. Jeong and H. K. Kim, “Characteristics of inkjet-printed nano indium tin oxide particles for transparent conducting electrodes,” *Current Applied Physics,* vol. 10, no. 4, pp. 105-108, 2010.

[10] K. S. Kwon, Y. S. Choi and J. K. Go, “Inkjet jet failures and their detection using piezo self-sensing,” *Sensors and Actuators A: Physical,* vol. 20, no. 1, pp. 335-341, 2013.

[11] L. T. Creagh and M. McDonald, “Design and Performance of Inkjet Print Heads for Non-Graphic-Arts Applications,” *MRS Bulletin,* vol. 22, no. 11, pp. 807-811, 2003.

[12] T. Minami, “Transparent conducting oxide semiconductors for transparent electrodes,” *Semiconductor Science and Technology,* vol. 20, no. 4, 2005.

[13] J. Puetz and M. Aegerter, “Direct gravure printing of indium tin oxide nanoparticle patterns on polymer foils,” *Thin Solid Films,* vol. 516, no. 14, pp. 4495-4501, 2008.

[14] L. Blessing and A. Chakrabarti, DRM, a Design Research Methodology, Springer, 2009.

[15] E. Wilson, An Introduction to Scientific Research, Dover Publications, 1952.

[16] A. Pike, D. Hoffman, M. Diez-Garcia, P. Pettitt, J. Alcolea, R. Balbin, C. Gonzalez-Sains, C. Heras and e. al, “U-Series Dating of Paleolithic Art in 11 Caves in Spain,” *Science,* vol. 336, no. 6087, pp. 1409-1413, 2012.

[17] J. H. Liu, “Research on the Developmental Venation of Calligraphy Seal Cutting Art Form from the Perspectives of Chinese Traditional Culture and Art Form,” in *2nd Internation Conference on Social Science, Management and Economics*, Shanghai, 2016.

[18] American Printing History Association, “History of Printing Timeline,” [Online]. Available: printinghistory.org/timeline. [Accessed 23 08 2017].

[19] J. Pan, “On the origin of printing in the light of new archaeological discoveries,” *Chinese Science Bulletin,* vol. 42, no. 12, pp. 976-981, 1997.

[20] E. Wilkinson, Chinese History, Harvard University Press, 2015.

[21] Xinhua English, “Woodblock printing workshop in E. China,” 2012. [Online]. Available: english.sina.com/life/p/2012/0425/461785.html. [Accessed 23 08 2017].

[22] M. Polo, The Travels of Marco Polo, a Venetian, in the Thirteenth Century: Being a Description, by that Early Traveler, of Remarkable Places and Things, in the Eastern Parts of the World, 1818.

[23] T. H. Barrett, The Woman Who Discovered Printing, Great Britain: Yale University Press, 2008.

[24] T. Christensen, “Gutenberg and the Koreans: Did East Asian Printing Influence the European Renaissance?,” in *River of Ink: Literature, History, Art, Counterpoint*, 2014.

[25] PREPRESSURE, “The History of Print frm 1400 - 1499,” [Online]. Available: https://www.prepressure.com/printing/history/1400-1499. [Accessed 25 08 2018].

[26] L. Febvre and H. J. Martin, The Coming of the Book: The impact of printing 1450 - 1800,, London: Verso, 1997.

[27] M. McLuhan, The Gutenberg Galaxy: The Making of Typographic Man, Toronto: University of Toronto Press, 1962.

[28] T. Schlossberg, “Literacy Rates,” The State of Publishing, 2011.

[29] UNESCO, “Education: Literacy Rates,” UNESCO, 2017.

[30] J. Dittmar, “Information Technology and Economic Change: The Impact of the Printing Press,” *Quarterly Journal of Economics,* 2010.

[31] D. P. Nord, J. S. Rubin and M. Schudson, The History of the Book in America, Chapel Hill: University of North Carolina Press, 2009.

[32] P. Bravo, “6 Perks of Offset Lithography,” *My Poll UX,* p. 4.

[33] C. Sullivan, The History of Screen Printing, Jane Turner Print Museum, 2011.

[34] “The Historic Background of Screen Printing Machines and Digital Printing Technology,” 2017. [Online]. Available: https://screenprintingmachine.net/historic-background-screen-printing-machine-and-digital-printing-technology/. [Accessed 25 08 2018].

[35] A. Kent and J. G. Williams, “Epson: A history,” in *Encyclopedia of Microcomputers*, New York, Marcel Decker INC, 1990, p. 298.

[36] H. G. Greig, “Electrostatic printing”. United States of America Patent US2874063A, 1959.

[37] F. Galembeck and T. A. L. Burgo, Electrostatic Processes and Products. In: Chemical Electrostatics, Springer , 2017.

[38] G. West and J. Kuk, “The Complementarity of Openess: How MakerBot Leveraged Thingiverse in 3D Printing,” *Technological Forecasting and Social Change,* vol. 102, pp. 169-181, 2016.

[39] S. L. Roig, White 3D Printed Piece, 2017.

[40] B. Berman, “3D Printing: The new industrial revolution,” *Business Horizons,* vol. 55, no. 2, pp. 155-162, 2012.

[41] R. M. Scarisbrick, “Electrically Conducting Mixtures,” *Journal of Applied Physics D,* vol. 6, p. 2098, 1973.

[42] A. Nag and E. al, “Printed Electronics: Present and Future Opportunities,” in *Ninth International Conference on Sensing Technology*, Palmerston North, New Zealand, 2015.

[43] E. Coatanea, V. Kantola and E. al, Printed Electronics, Now and Future, Helsinki: Helsinki University Print, 2009.

[44] R. A. Vogel, “Fine Line Printing for Consumer Electronics,” *Solid State Technology,* pp. 51-54, 1972.

[45] B. Lunt, Marvels of Modern Electronics: A Survey, Dover Publications, 2013.

[46] A. Blavo and B. Pineaux, “Printing Processes and their Potential for RFID Printing,” in *Joint sOc-EUSAI Conference*, Grenoble, 2005.

[47] H. Kang, R. Kitsomboonloha, J. Jang and V. Subramanian, “High-Performance Printed Transistors Realized Using Femtoliter Gravure-Printed Sub-10 µm Metallic Nanoparticle Patterns and Highly Uniform Polymer Dielectric and Semiconductor Layers,” *Advanced Materials,* vol. 24, no. 22, pp. 3065-3069, 2012.

[48] M. Li, Y. Li and E. al, “Recent developments and applications of screen-printed electrodes in environmental assays—A review,” *Analytica Chimica Acta,* vol. 734, pp. 31-44, 2012.

[49] L. Xie, G. Yang and E. al, “A system-on-chip and paper-based inkjet printed electrodes for a hybrid wearable bio-sensing system,” in *IEEE Engineering in Medicine and Biology Society*, San Diego, 2012.

[50] D. Southee, G. Hay, P. Evans and D. Harrison, “Printed Electronics and Offset Lithography,” in *Innovative Electronics Manufacturing Seminar*, 2007, 2007.

[51] J. S. Sagu, N. York, D. J. Southee and K. G. U. Wijayantha, “Printed electrodes for flexible, light-weight solid-state supercapacitors – a feasibility study,” *Circuit World,* vol. 41, no. 2, pp. 80-86, 2015.

[52] J. Steimle, “Printed Electronics for Human Computer Interaction,” in *MPI for Informatics*, Sarrbrucken, 2015.

[53] A. Sridhar, T. Blaudeck and R. R. Baumann, “Inkjet Printing as a Key Enabling Technology for Printed Electronics,” *Material Matters,* vol. 6, 2011.

[54] Fujifilm, “Deposition Products: Diamatix,” [Online]. Available: http://www.fujifilmusa.com/products/industrial_inkjet_printheads/deposition-products/index.html. [Accessed 28 08 2017].

[55] S. C. Chang, J. Liu, J. Bharathan and E. al, “Multicolor Organic Light Emitting Diodes Processed by Hybrid Inkjet Printing,” *Advanced Materials,* vol. 10, no. 9, 1999.

[56] E. Sowade, E. Ramon, K. Y. Mitra and E. al, “All-inkjet-printed thin-film transistors: manufacturing process reliability by root cause analysis,” *Scientific Reports (Nature),* vol. 6, 2016.

[57] S. Bidoki, J. Nouri and A. Heidari, “Inkjet deposited circuit components,” *Journal of Micromechanics Engineering,* vol. 20, p. 55023, 2010.

[58] S. Jung, A. Sou, K. Banger, D. H. Ko, P. Chow and E. al, “All inkjet printed, all air processed solar cells,” *Advanced Energy Materials,* vol. 14, no. 14, 2014.

[59] N. Marjanovic, “Inkjet printing and low temperature sintering of CuO and CdS as functional electronic layers and Schottky diodes,” *Journal of Material Chem,* vol. 21, p. 13634, 2011.

[60] P. Lorwongtragool, E. Sowade, N. Watthanawisuth and E. al, “Novel Wearable Electronic Nose for Healthcare Based on Flexible Printed Chemical Sensor Array,” *Sensors,* vol. 14, pp. 19700-19712, 2014.

[61] IDTechEx, “Printed and Flexible Sensors 2017 - 2027: Technologies, Players, Forecasts,” IDTechEx, 2017.

[62] H. W. Lin, C. P. Chang, W. H. Hwu and M. D. Ger, “The rheological behaviors of screen-printing pastes,” *Journal of Materials Processing Technology,* vol. 197, no. 1 - 3, pp. 284-291, 2008.

[63] XIAMEN LINGTIE, “Xiamen Lingtie Machinery Auto roll to roll screen printing,” [Online]. Available: https://i.ytimg.com/vi/KOAogI47vbg/maxresdefault.jpg. [Accessed 28 08 2017].

[64] S. Khan, L. Lorenzelli and R. S. Dahiya, “Technologies for Printing Sensors and Electronics Over Large Flexible Substrates: A Review,” *IEEE Sensors,* vol. 15, no. 6, pp. 3164-3185, 2015.

[65] K. Honeychurch and J. Hart, “Screen-printed electrochemical sensors for monitoring metal pollutants,” *Trends in Analytical Chemistry,* vol. 22, no. 7, pp. 456-469, 2003.

[66] K. Yamanaka, M. Vestergaard and E. Tamiya, “Printable Electrochemical Biosensors: A Focus on Screen-Printed Electrodes and Their Application,” *Sensors,* pp. 1-16, 2016.

[67] H. Hannebaur, T. Falcon, R. Hesse and E. al, “18.9 %-EFFICIENT SCREEN-PRINTED SOLAR CELLS APPLYING A PRINT-ON-PRINT PROCESS,” in *26th European Photovoltaic Solar Energy Conference and Exhibition*, Hannover.

[68] A. T. Aijazi, Printing Functional Electronic Circuits and Components, Michigan: Western Michigan University, 2014.

[69] S. C. Lim, S. H. Kim, Y. S. Yang and E. al, “Organic Thin-Film Transistor Using High-Resolution Screen-Printed Electrodes,” *Japanese Journal of Applied Physics,* vol. 48, no. 8R, 2009.

[70] D. Southee, G. Hay, P. S. A. Evans and D. Harrison, “Lithographically printed voltaic cells – a feasibility study,” *Circuit World,* vol. 33, no. 1, pp. 31-35, 2007.

[71] G. Hay, P. S. A. Evans, D. Harrison, D. Southee, G. Simpson and P. Harrey, “Characterization of lithographically printed resistive strain gauges,” *IEEE Sensors,* vol. 5, no. 5, 2005.

[72] R. Withnall, J. Silver, G. Fern, P. Marsh, T. Ireland, P. S. A. Evans, D. Southee, G. Hay, D. Harrison and K. Breen, “Low Cost, Flexible Electroluminescent Displays with a Novel Electrode Architecture Printed by Offset Lithography,” *Society for Information Display,* vol. 37, no. 1, pp. 1491-1494, 2006.

[73] S. Kim, H. Soioudi, H. Zhao and E. al, “Ultrathin high-resolution flexographic printing using nanoporous stamps,” *Science Advances,* vol. 2, no. 12, 2016.

[74] CPI, “New Printed Electronics - Bringing Interactivity to Print,” CPI, 2012.

[75] N. Board, Handbook on Printing Technology (Offset, Gravure, Flexo, Screen), National Institute of Industrial Research, 2002.

[76] G. Grau, J. Cen, H. Kang and E. al, “Gravure-printed electronics: recent progress in tooling development, understanding of printing physics, and realization of printed devices,” *Flexible and Printed Electronics,* vol. 1, no. 2, 2016.

[77] M. Hambsch, K. Reuter and M. Stanel, “Uniformity of fully gravure printed organic field-effect transistors,” *Materials Science Engineering,* vol. 170, no. 93, 2010.

[78] D. Sung, A. Vornbrock and V. Subramanian, “Scaling and optimization of gravure-printed silver nanoparticle lines for printed electronics,” *IEEE Transactions on Components and Packaging Technologies,* vol. 33, no. 44, p. 105.

[79] E. Secor, S. Lim, H. Zhang and E. al, “Gravure printing of graphene for large-area flexible electronics,” *Advanced Materials,* vol. 26, no. 8, p. 4533, 2014.

[80] ASTM, “Standard Terminology for Additive Manufacturing Technologies - F2792 12a,” ASTM, 2015.

[81] S. Mansour and R. Hague, “Impact of Rapid Manufacturing on Design for Manufacture for Injection Moulding,” *Journal of Mechanical Engineering Science,* vol. 217, no. 4, pp. 453-461, 2003.

[82] I. Shin and M. Park, “3D printed conductive patterns based on laser irradiation,” *Applications and Materials Science,* vol. 214, no. 7, 2017.

[83] S. Leigh, R. Bradley, C. Purssell and E. al, “A Simple, Low-Cost Conductive Composite Material for 3D Printing of Electronic Sensors,” *PLOS ONE,* vol. 7, no. 11, 2012.

[84] E. MacDonald, R. Salas, D. Esplain and E. al, “3D Printing for the Rapid Prototyping of Structural Electronics,” *IEEE Access,* vol. 2, pp. 234-242, 2014.

[85] W. Li, A. Ghazanfari, M. Leu and R. G. Landers, “Methods of Extrusion-On-Demand for High Solids Loading Ceramic Paste in Freeform Extrusion Fabrication,” in *Solid Free-form Fabrication Symposium*, Austin, 2015.

[86] SCULPTEO, “3D Printing for Electronics Industry - What is the Next Revolution,” 07 12 2016. [Online]. Available: https://www.sculpteo.com/blog/2016/12/07/3d-printing-for-electronics-industry-whats-the-next-revolution. [Accessed 28 08 2017].

[87] A. Coniglio, M. Daoud and H. Herrmann, “Conductivity and diffusion near the percolation threshold,” *Journal of Physics A: Mathematical and General,* vol. 22, no. 19, 1989.

[88] L. Xia, D. Zhang and G. Jia, “Spinning and drawing of PLA filament,” *Journal of Tianjin Polytechnic University,* vol. 1, 2007.

[89] L. Lei, J. Qiu and E. Sakai, “Preparing conductive poly(lactic acid) (PLA) with poly(methyl methacrylate) (PMMA) functionalized graphene (PFG) by admicellar polymerization,” *Chemical Engineering Journal,* vol. 209, pp. 20-27, 2012.

[90] X. Wei, D. Li, W. Jiang and E. al, “3D Printable graphene composite,” *Scientific Reports,* vol. 5, p. 11181, 2015.

[91] S. Kesner and R. Howe, “Design Principles for Rapid Prototyping Forces Sensors Using 3-D Printing,” *IEEE Transactions on Mechatronics,* vol. 16, no. 5, pp. 866-870, 2011.

[92] J. Muth, D. Vogt, R. Truby and E. al, “Embedded 3D Printing of Strain Sensors within Highly Stretchable Elastomers,” *Advanced Materials,* vol. 26, no. 36, pp. 6307-6312, 2014.

[93] S. Zhang, W. G. Wittow and J. C. Vardaxoglou, “Additively manufactured artificial materials with metallic meta-atoms,” *IET Microwaves, Antennas and Propagation,* vol. 11, no. 14, pp. 1955-1961, 2017.

[94] X. Wang, M. Jiang, Z. Zhou and E. al, “3D printing of polymer matrix composites: A review and prospective,” *Composites Part B,* vol. 110, pp. 442-458, 2017.

[95] Y. H. Cho, I. H. Lee and D. W. Cho, “Laser scanning path generation considering photopolymer solidification in micro-stereolithography,” *Microsystem Technologies,* vol. 11, no. 2, pp. 158-167, 2005.

[96] J. Z. Manapat, Q. Chen, P. Ye and R. C. Advincula, “3D Printing of Polymer Nanocomposites via Stereolithography,” *Macromolecular Materials and Engineering,* vol. 302, no. 9, 2017.

[97] Q. Wang, A. Jackson, Q. Ge and E. al, “Lightweight Mechanical Metamaterials with Tunable Negative Thermal Expansion,” *Physical Review Letters,* vol. 117, no. 17, 2016.

[98] V. Bhavar, P. Kattire, V. Patil and E. al, “A review on powder bed fusion technology of metal additive manufacturing,” in *4th International conference and exhibition on Additive Manufacturing Technologies*, Bangalore, 2014.

[99] M. S. Hossain, J. A. Gonzalez and R. M. Hernandez, “Fabrication of smart parts using powder bed fusion additive manufacturing technology,” *Additive Manufacturing,* vol. 10, pp. 58-66, 2016.

[100] B. E. Carroll, T. A. Palmer and A. M. Beese, “Anisotropic tensile behavior of Ti–6Al–4V components fabricated with directed energy deposition additive manufacturing,” *Acta Materialia,* vol. 87, pp. 309-320, 2015.

[101] J. Chang, J. He, M. Mao and E. al, “Advanced Material Strategies for Next-Generation Additive Manufacturing,” *MDPI Materials,* vol. 11, no. 166, pp. 1 - 19, 2018.

[102] Z. Cui, Applications and Future Prospects of Printed Electronics," in Printed Electronics: Materials, Technologies and Applications, Singapore: John Wiley and Sons, 2016.

[103] D. Savastano, “Research Institutions in Flexible and Printed Electronics,” Printed Electronics Now, 2016.

[104] IDTechEx, “Printed and Flexible Sensors 2017 - 2027: Technologies, Players, Forecasts,” IDTechEx, 2017.

[105] Sensors Online, “Flexible-Printed Electronics Applications Grow,” Sensors Online, 2013.

[106] ARM / PragmatIC, “PlasticARM,” IDTechEx Europe, Berlin, 2017.

[107] Encyclopaedia Britannica, Resistor Definition, Encyclopaedia Britannica Inc.

[108] M. J. Peterson, Sputtering of Thin Film Resistors, Arizona : University of Arizona Library , 1969.

[109] E. Giani and J. P. Mathurin, “Screen Printed Thick Film Resistors — Better Yields with Shorter Set-up Times,” *Microelectronics International,* vol. 6, no. 3, pp. 28-34, 1989.

[110] P. Leon, “Carbon-Composition Resistor”. United States of America Patent US2347795A, 02 05 1944.

[111] J. W. Jira, “Metal Film Resistor”. United States of America Patent US2281843A, 05 05 1942.

[112] S. J. Jung, A. Sou, E. Gili and H. Sirringhauss, “Inkjet-printed resistors with a wide resistance range for printed read-only memory applications,” *Organic Electronics ,* vol. 14, no. 3, pp. 699-702, 2013.

[113] A. Ostfeld, I. Deckman, A. M. Gaikwad and E. al, “Screen printed passive components for flexible power electronics,” *Scientific Reports,* vol. 5, p. 15959, 2015.

[114] Elceram, “Technical Characteristics and Design Rules of Thick Film Printed Ceramic Substrates Production,” Elceram, Prague, 2017.

[115] M. Oakes, “An Introduction to Thick Film Resistor Trimming by Laser,” *Optical Engineering ,* vol. 17, no. 3, pp. 173-217, 1978.

[116] T. Bartush and J. Curtin, “Active Resistor Trimming by Differential Annealing”. United States of America Patent US5233327A, 03 08 1993.

[117] D. J. Southee, G. I. Hay, P. S. A. Evans and D. J. Harrison, “Flexible dot-matrix display manufacture by offset lithography,” *Journal of Engineering Manufacture,* vol. 222, no. 8, pp. 943-948, 2008.

[118] G. I. Hay, P. S. A. Evans, D. J. Harrison, D. J. Southee, G. Simpson and P. M. Harrey, “Characterization of lithographically printed resistive strain gauges,” *IEEE Sensors Journal,* vol. 5, no. 5, pp. 864 - 871, 2005.

[119] D. Janczak, M. Sloma, G. Wroblewski and E. al, “Screen-Printed Resistive Pressure Sensors Containing Graphene Nanoplatelets and Carbon Nanotubes,” *MDPI Sensors ,* vol. 14, no. 9, pp. 17304-17312, 2014.

[120] H. Andersson, A. Manuilskiy, T. Unander and E. al, “Inkjet Printed Silver Nanoparticle Humidity Sensor With Memory Effect on Paper,” *IEEE Sensors ,* vol. 12, no. 6, pp. 1901-1905, 2012.

[121] B. Huber, J. Schober, A. Kreuzer and E. al, “Inkjet-printed resistive memory cells for transparent electronics,” *Microelectronic Engineering,* vol. 194, pp. 85 - 88, 2018.

[122] M. Jayalakshmi and K. Balasubramanian, “Simple Capacitors to Supercapacitors,” *International Journal of Electrochemical Science,* pp. 1196-1217, 2008.

[123] J. F. Scott, “High-Dielectric Constant Thin Films for Dynamic Random Access Memories (DRAM),” *Annual Review of Materials Science,* pp. 79-100, 1998.

[124] H. S. Athab and D. Lu, “A High-Efficiency AC/DC Convertor with Quasi-Active Power Factor Correction,” *IEEE Transactions of Power Electronics,* pp. 1103 - 1109, 2010.

[125] T. M. Zeeff, T. H. Hubing, T. Doren and D. Pommerenke, “Analysis of Simple Two-Capacitor Low-Pass Filters,” *IEEE Transactions on Electromagnetic Compatibility ,* pp. 595 - 601, 2003.

[126] P. M. Harrey, P. S. A. Evans and D. J. Harrison, “Integrated capacitors for conductive lithographic film circuits,” *IEEE Transactions on Electronics Packaging Manufacturing ,* vol. 24, no. 4, pp. 333-338, 2001.

[127] M. Jung, J. Kim, J. Noh and E. al, “All-Printed and Roll-to-Roll-Printable 13.56-MHz-Operated 1-bit RF Tag on Plastic Foils,” *IEEE Transactions on Electronic Devices,* vol. 57, no. 3, pp. 571-580, 2010 .

[128] B. J. Kang, C. K. Lee and J. H. Oh, “All-inkjet-printed electrical components and circuit fabrication on a plastic substrate,” *Microelectronic Engineering,* vol. 97, pp. 251-254, 2012.

[129] B. S. Cook, J. R. Cooper and M. M. Tentzeris, “Multi-Layer RF Capacitors on Flexible Substrates Utilizing Inkjet Printed Dielectric Polymers,” *IEEE Microwave and Wireless Components Letters,* vol. 23, no. 7, pp. 353-355, 2013.

[130] P. J. Lin, C. Chang, Y. Yuan and E. al, “Fabrication and characterization of passive devices on flexible substrates,” in *International Conference on Electronic Materials and Packaging*, Taipei, 2008.

[131] Y. T. Yen, T. H. Fang and Y. C. Lin, “Optimization of screen-printing parameters of SN9000 ink for pinholes using Taguchi method in chip on film packaging,” *Robotics and Computer-Integrated Manufacturing,* vol. 27, no. 3, pp. 531-537, 2011.

[132] Du Pont Electronics, “Void Elimination in Screen Printed Thick Film Dielectric Pastes,” DuPont Electronics , 1996.

[133] B. Chen, T. Cui, Y. Liu and K. Varahramyan, “All-polymer RC filter circuits fabricated with inkjet printing technology,” *Solid-State Electronics,* vol. 47, no. 5, pp. 841-847, 2003.

[134] P. M. Harrey, B. J. Ramsey, P. S. A. Evans and D. J. Harrison, “Capacitive-type humidity sensors fabricated using the offset lithographic printing process,” *Sensors and Actuators B: Chemical,* vol. 87, no. 2, pp. 226-232, 2002.

[135] S. H. Lee, H. Seo and S. Lee, “Fabrication of a printed capacitive air-gap touch sensor,” *Japanese Journal of Applied Physics,* vol. 57, 2018.

[136] N. J. Callan, “On a New Galvanic Battery,” *Philosophical Magazine,* vol. 9, no. 3, pp. 472-478, 1836.

[137] E. L. Rich, “Printed Circuit Inductor”. United States of America Patent US3484731A, 16 12 1969.

[138] R. L. Remke and A. B. Glenn, “Spiral Inductors for Hybrid and Microwave Applications,” in *Proceedings of Electronic Components Conference*, 1974.

[139] S. M. Jenei, “ANALYSIS AND OPTIMIZATION OF PLANAR THICK FILM NI-FERRITE INDUCTOR,” *COMPEL - The International Journal for Computation and Mathematics in Electrical and Electronic Engineering,* vol. 14, no. 4, pp. 291-295, 1995.

[140] K. Fairchild, G. Morcan, T. Lenihan and E. al, “Reliability of flexible thin-film embedded resistors and electrical characterization of thin-film embedded capacitors and inductors,” in *47th Electronic Components and Technology Conference*, San Jose, 1997.

[141] S. Pranonsatit and S. Lucyszyn, “Self-assembled screen printed microwave inductors,” *Electronics Letters,* vol. 41, no. 23, 2005.

[142] S. Stalf, “Printed inductors in RF consumer applications,” in *International Conference on Consumer Electronics*, Los Angeles, 2001.

[143] D. Redinger, S. Molesa, S. Yin and E. al, “An ink-jet-deposited passive component process for RFID,” *IEEE Transactions on Electronic Devices,* vol. 51, no. 12, pp. 1978-1983, 2004.

[144] V. Subramanian, P. C. Chang, D. Huang and E. al, “All-printed RFID tags: materials, devices, and circuit implications,” in *19th International Conference on VLSI Design held jointly with 5th International Conference on Embedded Systems Design (VLSID'06)*, Hyderabad, 2006.

[145] N. Lim, J. Kim, S. Lee and E. al, “Screen Printed Resonant Tags for Electronic Article Surveillance Tags,” *IEEE Transactions on Advanced Packaging,* vol. 32, no. 1, pp. 72-76, 2009.

[146] Y. Kim, H. Kim and H. J. Yoo, “Electrical Characterization of Screen-Printed Circuits on the Fabric,” *IEEE Transactions on Advanced Packaging,* vol. 33, no. 1, pp. 196-205, 2010.

[147] B. S. Cook, C. Mariotti, J. R. Cooper and E. al, “Inkjet-printed, vertically-integrated, high-performance inductors and transformers on flexible LCP substrate,” in *2014 IEEE MTT-S International Microwave Symposium (IMS2014)*, Tampa, 2014.

[148] Y. Yan, C. Ding, K. D. T. Ngo and E. al, “Additive manufacturing of planar inductor for Power Electronics applications,” in *2016 International Symposium on 3D Power Electronics Integration and Manufacturing (3D-PEIM)*, Raleigh, 2016.

[149] R. A. Henle and J. L. Walsh, “The Application of Transistors to Computers,” in *Proceedings of the IRE*, 1958.

[150] P. Yadav, K. Pandey, B. Tripathi and E. al, “An effective way to analyse the performance limiting parameters of poly-crystalline silicon solar cell fabricated in the production line,” *Solar Energy,* vol. 122, pp. 1-10, 2015.

[151] R. J. Waltman and J. Bargon, “Electrically conducting polymers: a review of the electropolymerization reaction, of the effects of chemical structure on polymer film properties, and of applications towards technology,” *Canadian Journal of Chemistry,* vol. 64, no. 1, pp. 76-95, 1986.

[152] P. S. Heljo, C. Schmidt, R. Klengel, H. S. Majumdar and D. Lupo, “Electrical and thermal analysis of frequency dependent filamentary switching in printed rectifying diodes,” *Organic Electronics,* vol. 20, pp. 69-75, 2015.

[153] M. Yoshida, K. Suemori, S. Uemura and E. al, “Printed Electrode for All-Printed Polymer Diode,” *Japanese Journal of Applied Physics,* vol. 50, no. 4S, 2011.

[154] K. E. Lilja, T. G. Backlund and D. Lupo, “Printed organic diode backplane for matrix addressing an electrophoretic display,” *Thin Solid Films,* vol. 518, no. 15, pp. 4385-4389, 2010.

[155] N. Sani, M. Robertsson, P. Cooper and E. al, “All-printed diode operating at 1.6 GHz,” *Proceedings of the National Academy of Sciences of the USA,* vol. 111, no. 33, pp. 11943-11948, 2014.

[156] D. H. Kim, G. W. Kang and H. J. Shin, “Electrically engineered polymer-carbon hybrid heterojunction for high-performance printed transistors,” in *SPIE Organic Photonics and Electronics* , San Diego, 2014.

[157] G. Grau, R. Kitsomboonloha, S. Swisher and E. al, “Printed Transistors on Paper: Towards Smart Consumer Product Packaging,” *Advanced Functional Materials,* vol. 24, no. 32, pp. 5067-5074, 2014.

[158] J. Kwon, Y. Takeda and K. Fukada, “Three-Dimensional, Inkjet-Printed Organic Transistors and Integrated Circuits with 100% Yield, High Uniformity, and Long-Term Stability,” *ACS Nano,* vol. 10, no. 11, pp. 10324-10330, 2016.

[159] S. Zambou, B. Magunje, S. Rhyme and E. al, “Solid State Electronics,” *Variable temperature performance of a fully screen printed transistor switch.*

[160] P. Andersson, D. Nilsson, P. O. Svensson and E. al, “Active Matrix Displays Based on All-Organic Electrochemical Smart Pixels Printed on Paper,” *Advanced Materials,* vol. 14, no. 20, pp. 1460-1464, 2002.

[161] P. Tehrani, L. O. Hennerdal, A. L. Dyer and E. al, “Improving the contrast of all-printed electrochromic polymer on paper displays,” *Journal of Materials Chemistry,* vol. 19, no. 13, pp. 1799-1802, 2009.

[162] J. Jensen, H. F. Dam and J. R. Reynolds, “Manufacture and demonstration of organic photovoltaic-powered electrochromic displays using roll coating methods and printable electrolytes,” *Journal of Polymer Science B,* vol. 50, no. 8, pp. 536-545, 2012.

[163] J. P. Coleman, A. T. Lynch, P. Madhukar and E. al, “Printed, flexible electrochromic displays using interdigitated electrodes,” *Solar Energy Materials and Solar Cells,* vol. 56, no. 3, pp. 395-418, 1999.

[164] B. H. Chen, S. Y. Kao and C. H. Hu, “Printed Multicolor High-Contrast Electrochromic Devices,” *ACS Applied Materials and Interfaces,* vol. 7, no. 45, pp. 25069-25076, 2015.

[165] X. Cao, C. Lau, Y. Liu and E. al, “Fully Screen-Printed, Large-Area, and Flexible Active-Matrix Electrochromic Displays Using Carbon Nanotube Thin-Film Transistors,” *ACS Nano,* vol. 10, no. 11, pp. 9816-9822, 2016.

[166] B. Yoon, D. Y. Ham, O. Yarimaga and E. al, “Inkjet Printing of Conjugated Polymer Precursors on Paper Substrates for Colorimetric Sensing and Flexible Electrothermochromic Display,” *Advanced Materials,* vol. 23, no. 46, pp. 5492-5497, 2011.

[167] Y. Yang, S. C. Chang, J. Bharathan and J. Liu, “Organic/polymeric electroluminescent devices processed by hybrid ink-jet printing,” *Journal of Materials Science: Materials in Electronics,* vol. 11, no. 2, pp. 89-96, 2000.

[168] S. L. Park, Y. Xiong, R. H. Kim and E. al, “Printed assemblies of inorganic light-emitting diodes for deformable and semitransparent displays,” *Science,* vol. 325, no. 5943, pp. 977-981, 2009.

[169] S. G. R. Bade, J. Li, X. Shan and E. al, “Fully Printed Halide Perovskite Light-Emitting Diodes with Silver Nanowire Electrodes,” *ACS Nano,* vol. 10, no. 2, pp. 1795-1801, 2016.

[170] Y. L. Kong, I. A. Tamargo, H. Kim and E. al, “3D Printed Quantum Dot Light-Emitting Diodes,” *ACS Nano Letters,* vol. 14, no. 12, pp. 7017-7023, 2014.

[171] D. L. Dexter, “A Theory of Sensitized Luminescence in Solids,” *The Journal of Chemical Physics,* vol. 21, p. 836, 2004.

[172] K. Vanheusden, W. L. Warren, C. H. Saeger, D. R. Tallant and J. A. Voight, “Mechanisms behind green photoluminescence in ZnO phosphor powders,” *Journal of Applied Physics,* vol. 79, p. 7983, 1996.

[173] R. Withnall, J. Silver and G. R. Fern, “Low Cost, Flexible Electroluminescent Displays with a Novel Electrode Architecture Printed by Offset Lithography,” *Society for Information Display International Symposium Digest of Technical Papers,* vol. 37, no. 1, pp. 1491-1494, 2006.

[174] R. J. H. Young, P. S. A. Evans, G. I. Hay, D. J. Southee and D. J. Harrison, “Electroluminescent light sources via soft lithography,” *Circuit World ,* vol. 34, no. 3, pp. 9-12, 2008.

[175] S. Magdassi, The Chemistry of Inkjet Inks, Israel: The Hebrew University of Jerusalem, 2009.

[176] C. Englund and A. Verikas, “Ink Flow Control by Multiple Models in an Offset Lithographic Printing Process,” *Computers and Industrial Engineering,* vol. 55, no. 3, pp. 592-605, 2008.

[177] M. Rentzhog, “Print quality and resistance for water-based flexography on polymer-coated boards: Dependence on ink formulation and substrate pretreatment,” *Progress in Organic Coatings,* vol. 57, no. 3, pp. 183-194, 2006.

[178] H. W. Lin, C. P. Chang, W. H. Hwu and D. M. Ger, “The rheological behaviors of screen-printing pastes,” *Journal of Materials Processing,* vol. 197, no. 1, pp. 284-291, 2008.

[179] J. K. Fink, The Chemistry of Printing Inks and their Electronics and Medical Applications, Wiley, 2014.

[180] S. S. Bhore, Formulation and Evaluation of Resistive Inks for Applications in Printed Electronics, Michigan: Western Michigan University, 2013.

[181] Business Wire, “Global Conductive Inks Market Driven by Rising Demand for Advanced Compact Electronic Devices,” Technavio, 2017.

[182] L. Huang, “Graphene-Based Conducting Inks for Direct Inkjet Printing of Flexible Conductive Patterns and Their Applications in Electric Circuits and Chemical Sensors,” *Nano Research,* vol. 4, no. 7, pp. 675-684, 2011.

[183] IDTechEx, “Printed, Organic and Flexible Electronics 2013 - 2023,” IDTechEx, 2013.

[184] V. Karthik, “Conductive silver inks and their applications in printed and flexible electronics,” *RSC Advances,* vol. 5, no. 95, pp. 77760-77790, 2015.

[185] A. White and L. Germer, “The Rate of Oxidation of Copper at Room Temperature,” *Journal of the Electrochemical Society,* vol. 81, no. 1, pp. 305-319, 1942.

[186] H. Mbarek, “Screen printied ITO films for NHS gas sensing,” *Materials Science and Engineering,* vol. 26, no. 2, pp. 500-504, 2006.

[187] R. W. Stowe, “High-power UV lamps for industrial UV curing applications,” in *Internation Symposium on Optical Science, Engineering and Instrumentation*, Denver, 1996.

[188] R. W. Stowe, “Practical Aspects of Irradiance and Energy in UV Curing,” Fusion UV Systems, Gaithersburg, 1998.

[189] C. Decker, F. Masson and R. Schwalm, “How to speed up the UV curing of water-based acrylic coatings,” *Journal of Coatings Technology and Research,* vol. 1, no. 2, pp. 127-136, 2004.

[190] S. Luo and C. P. Wong, “Effect of UV/ozone treatment on surface tension and adhesion in electronic packaging,” *IEEE Transactions on Components and Packaging Technologies,* vol. 24, no. 1, pp. 43-49, 2001.

[191] G. Grau and E. al, “Gravure-printed electronics: recent progress in tooling development, understanding of printing physics, and realization of printed devices,” *Flexible and Printed Electronics,* vol. 1, pp. 1 - 65, 2016.

[192] M. Peil and A. Langensheidt, “Radiation curing: Getting on the right wavelength: How different variables affect crosslinking of inks by UV LEDs,” *European Coatings Journal,* no. 2, pp. 22-27, 2012.

[193] DuPoint Teijin Films, “MELINEX ST504 - PRODUCT DESCRIPTION,” Dupoint Teijin, 2016.

[194] H. J. Hwang, K. H. Oh and H. S. Kim, “All-photonic drying and sintering process via flash white light combined with deep-UV and near-infrared irradiation for highly conductive copper nano-ink,” *Scientific Reports,* vol. 6, p. 196696, 2016.

[195] J. Perelae, R. Abbel, S. Wunscher and E. al, " Roll-to-Roll Compatible Sintering of Inkjet Printed Features by Photonic and Microwave Exposure: From NonConductive Ink to 40% Bulk Silver Conductivity in Less Than 15 Seconds," *Advanced Materials,* vol. 24, pp. 2620-2625, 2012.

[196] E. Balliu, H. Andersson and M. Engholm, "Selective laser sintering of inkjet-printed silver nanoparticle inks on paper substrates to achieve highly conductive patterns," *Scientific Reports,* vol. 8, p. 10408, 2018.

[197] W. M. Cranton, S. L. Wilson, R. Ranson and E. al, "Excimer laser processing of inkjet-printed and sputter-deposited transparent conducting SnO2:Sb for flexible electronics," *Thin Solid Films,* vol. 515, no. 24, pp. 8534-8538, 2007.

[198] M. J. Renn, M. Shrandt, J. Renn and J. Q. Feng, "Localized Laser Sintering of Metal Nanoparticle Inks Printed with Aerosol Jet® Technology for Flexible Electronics," *Journal of Microelectronics and Electronic Packaging,* vol. 14, pp. 132-139, 2017.

[199] S. Magdassi, M. Grouchko, O. Berezin and A. Kamyshny, "Triggering the Sintering of Silver Nanoparticles at Room Temperature," *ACS Nano,* vol. 4, no. 4, pp. 1943-1948, 2010.

[200] D. C. Corsino and M. Donnabelle, "Room temperature sintering of printer silver nanoparticle conductive ink," in *IOP Materials Science and Engineering*, 2017.

[201] P. Peng, L. Li, W. Guo and E. al, "Room-Temperature Joining of Silver Nanoparticles Using Potassium Chloride Solution for Flexible Electrode Application," *Journal of Physical Chemistry C,* vol. 122, no. 5, pp. 2704-2711, 2018.

[202] Phys. Status Solidi, "Karl Badeker (1877 - 1914) and the discovery of transparent conductive materials," *Phys. Status Solidi,* vol. 212, no. 7, pp. 1409-1426, 2015.

[203] K. Badeker, "Uber die elektrische Leitf fahigkeit und die thermoelektrische Kraft einiger Schwermetallverbindungen," *Physik,* pp. 749-766, 1907.

[204] K. Steinberg, "Uber den Halleffekt und die Widerstandsanderung im Magnetfelde bei jodhaltigem Kupferjodur, Dissertation, Universitat Jena, 1911.

[205] K. Badeker, "Vortrag und Diskussion auf der 84. Versammlung deutscher Naturforscher und Arzte in Munster,," *Phys. Z,* vol. 13, pp. 1080-1082, 1912.

[206] J. Coutts, “Transparent Conducting Oxides: Status and Opportunities in Basic Research,” National Renewable Energy Laboratory, Seattle, 1999.

[207] T. Minami, “Light Emission from Hot Electrons in Zinc Oxide MS Diodes,” *Physica Status Solidi,* vol. 73, no. 2, pp. 293-297, 1982.

[208] T. Coutts, “High Performance Transparent Conducting Oxides,” *Journal of Electronic Materials,* vol. 25, pp. 935-943, 1996.

[209] Y. Liu, Nanostructured Transparent Conducting Oxide Electrodes, Munich: Universitat Munchen, 2012.

[210] A. Stadler, “Transparent Conducting Oxides - An up to date overview,” *Materials,* vol. 5, pp. 661-683, 2012.

[211] M. Chen, “Intrinsic limit of electrical properties of transparent conducitng oxide filmes,” *J Phys D: Applied Physics,* vol. 33, pp. 2538-2548, 2000.

[212] READE, “Indium Tin Oxide Powder,” [Online]. Available: http://www.reade.com/products/indium-tin-oxide-powder-ito-in203-sn02. [Accessed 29 08 2017].

[213] M. Hofmann, Y. P. Hsieh, K. W. Chang and E. al, “Dopant morphology as the factor limiting graphene conductivity,” *Scientific Reports,* vol. 5, no. 1, p. 17393, 2015.

[214] PV Eduacation, “Doping,” [Online]. Available: http://www.pveducation.org/pvcdrom/doping. [Accessed 29 08 2017].

[215] J. Colinge, Physics of Semiconductor Devices, Springer, 2005.

[216] H. Hartnagel, A. Dawar, K. Jain and C. Jagadish, Semiconducting Transparent Thin Films, Bristol and Philadelphia: Institute of Physics, 1995.

[217] E. Hall, “On a new action of the magnet on electric currents,,” *American Journal of Mathematics,* vol. 2, no. 3, pp. 287-292, 1879.

[218] Univeristy of Saskatchewan, Hall Effect in Semiconductors, Canada: Univeristy of Saskatchewan, 2001.

[219] H. Unlu, “A thermodynamic model for determining pressure and temperature effects on the bandgap energies and other properties of some semiconductors,” *Solid State Electronics,* vol. 35, no. 5, pp. 1343-1352, 1992.

[220] A. Thellung, “Quasimomentum in the theory of elasticity and its conservation,” *Physical Review B,* vol. 12, no. 15, p. 7345, 1990.

[221] D. Ginley, H. Hosono and D. Paine, Handbook of Transparent Conductors, Springer, 2011.

[222] M. Nonnenmacher, “Kelvin probe force microscopy,” *Applied Physics Letters,* vol. 58, p. 2921, 1991.

[223] M. Hebert, Reflection and Transmission of light by a flat interface, Fresnels Formulae, Institut d'Optique, 2013.

[224] Y. Kashiwagi, “Direct transparent electrode patterning on layered GaN substrate by screen printing of indium tin oxide nanoparticle ink for Eu-doped GaN red light-emitting diode,” *Applied Physics A,* vol. 105, p. 223509, 2014.

[225] M. Mohammed, “Thickness dependence of the properties of indium tin oxide (ITO) FILMS prepared by activated reactive evaporation,” *Brazilian Journal of Physics,* vol. 39, no. 4, p. 629, 2009.

[226] N. Meshram, “Enhanced transmittance of ITO/Ag(Cr)/ITO (IAI) multi-layered thin films by high temperature annealing,” *Materials Letters,* vol. 145, pp. 120-124, 2015.

[227] J. Du, “Highly transparent and conductive indium tin oxide thin films for solar cells grown by reactive thermal evaporation at low temperature,” *Applied Physics A,* vol. 117, no. 2, pp. 815-822, 2014.

[228] T. Minami, “Transparent conducting oxide semiconductors for transparent electrodes,” *Semiconductor Science and Technology,* vol. 20, pp. 35-44, 2005.

[229] US GEOLOGICAL SURVEY, “Tin Resources,” USGS, Washington D.C., 1969.

[230] US GEOLOGICAL SURVEY, “Indium,” USGS, Washington D.C., 2007.

[231] IDTechEx, “Transparent Conductive Films (TCF) 2016 - 2026,” IDTechEx, 2016.

[232] I. Madhi, “Effect of temperature and NO2 surface adsorption on electrical properties of screen printed ITO thin film,” *Applied Surface Science,* vol. 355, pp. 242-249, 2015.

[233] H. Mbarek, M. Saadoun and B. Bessais, “Screen-Printed Tin-Doped Indium Oxide Films for Low Temperature and Fast Response Methanol Gas Sensing,” *Sensor Letters,* vol. 6, no. 4, pp. 507-510, 2008.

[234] H. Mbarek, “Porous screen printed indium tin oxide (ITO) for NOx gas sensing,” *Physica Status Solidi C,* vol. 4, no. 6, pp. 1903-1907, 2008.

[235] M. S. Hwang, B. Y. Jeong, J. Moon and E. al, “Inkjet-printing of indium tin oxide (ITO) films for transparent conducting electrodes,” *Materials Science and Engineering: B,* vol. 176, no. 14, pp. 1128-1131, 2011.

[236] K. Nagano, “Inhalation carcinogenicity and chronic toxicity of indium-tin oxide in rats and mice,” *Journal of Occupational Health,* vol. 53, no. 3, pp. 175-187, 2011.

[237] M. Kim, “Transparent Conductive Oxide Films for OLED devices,” INTECH, 2011.

[238] E. Klaus, Transparent Conductive Zinc Oxide, Springer, 2008.

[239] V. Khodvuk, “Optical and Luminescence Properties of Zinc Oxide,” *Optics and Spectroscopy,* vol. 111, no. 5, pp. 776-785, 2011.

[240] S. J. Pearton, Zinc Oxide Bulk, Amsterdam: Elsevier, 2006.

[241] D. Thomas, “The exciton spectrum of zinc oxide,” *Journal of Physics and Chemistry of Solids,* vol. 15, no. 1, pp. 86-96, 1960.

[242] M. Gilmore, “Transparent conducting aluminum-doped zinc oxide thin films for organic light-emitting devices,” *Applied Physics Letters,* vol. 76, p. 259, 1999.

[243] US GEOLOGICAL SURVEY, “ZINC,” US GOV, Washington D.C, 2016.

[244] Y. Kim, “Toxicity of 100 nm zinc oxide nanoparticles: a report of 90-day repeated oral administration in Sprague Dawley rats,” *International Journal of Nanomedicine,* vol. 9, pp. 109-126, 2014.

[245] E. Fortunato, L. Raniero, L. Silva, A. Goncalves, A. Pimentel, P. Barquinha, H. Aguas, L. Pereira, G. Goncalves, I. Ferreira, E. Elangovan and R. Martins, “Highly stable transparent and conducting gallium-doped zinc oxide thin films for photovoltaic applications,” *Solar Energy Materials and Solar Cells,* vol. 92, no. 12, pp. 1605 - 1610, 2008.

[246] E. Muchuweni, T. S. Sathiaraj and H. Nyakotyo, “Physical properties of gallium and aluminium co-doped zinc oxide thin films deposited at different radio frequency magnetron sputtering power,” *Ceramics International,* vol. 42, no. 15, pp. 17706-17710, 2016.

[247] T. Hitosugi, “Properties of TiO2 based transparent conducting oxides,” *Physica Status Solidi A,* vol. 7, pp. 1529-1537, 2010.

[248] W. Sinclair, “TEMPERATURE COEFFICIENT OF RESISTANCE OF TIN OXIDE FILMS DOPED WITH BOTH ANTIMONY OXIDE AND INDIUM OXIDE,” *Journal of the Electrochemical Society,* vol. 112, p. 182, 1965.

[249] R. R. Mehta and S. F. Vogel, “SPUTTERED CADMIUM OXIDE AND INDIUM OXIDE TIN OXIDE-FILMS AS TRANSPARENT ELECTRODES TO CADMIUM SULFIDE,” *Jorunal of the Electrochemical Society,* vol. 119, no. 6, p. 752, 1972.

[250] Kurt J Lesker Company, [Online]. Available: http://www.lesker.com/newweb/deposition_materials/depositionmaterials_sputtertargets_1.cfm?pgid=in3. [Accessed 22 08 2017].

[251] S. Rhia, “Cu2Se Nanoparticles with Tunable Electronic Properties Due to a Controlled Solid-State Phase Transition Driven by Copper Oxidation and Cationic Conduction,” *JACS,* vol. 133, no. 5, pp. 1383 - 1390, 2011.

[252] T. J. Coutts, “Transparent Conducting Oxides,” NREL, Washington D.C., 1999.

[253] A. Nath, J. Chongtham and K. Chandramani, “Titanate, Influence of ball milling parameters on the particle size of barium,” *Physica B,* vol. 405, pp. 430 - 434, 2010.

[254] H. Ghaffarian, M. Saiedi and A. M. Sayyadnejad, “Synthesis of ZnO Nanoparticles by Spray Pyrolysis Method,” *Iranian Journal of Chemical Engineering,* vol. 30, no. 1, pp. 1 - 5, 2011.

[255] Holmarc Products, “Flame Assisted Spray Pyrolysis Equipment,” Holmarc Products, http://www.holmarc.com/.

[256] M. Hasanpoora, “Microwave-assisted synthesis of zinc oxide nanoparticles,” *Procedia Materials Science,* vol. 11, pp. 320 - 325, 2015.

[257] Y. Liu, “ZnO-Based Transparent Conductive Thin Films: Doping, Performance, and Processing,” *Journal of Nanomaterials,* pp. 1 - 9, 2013.

[258] T. Lehnen, “Phase-selective microwave synthesis and inkjet printing applications of Zn2SnO4 (ZTO) quantum dots,” *Journal of Materials Chemistry,* vol. 22, p. 17732, 2012.

[259] S. Majeed and S. A. Shivashankar, “Rapid, microwave-assisted synthesis of Gd2O3 and Eu:Gd2O3 nanocrystals: characterization, magnetic, optical and biological studies,” *Journal of Materials Chemistry B,* no. 34, pp. 1 - 9, 2014.

[260] L. Znaidi, “Sol–gel-deposited ZnO thin films: A review,” *Materials Science and Engineering B,* vol. 174, pp. 18 - 30, 2010.

[261] Instituto di Fotonica e Nanotecnologie, “Sol-Gel Principles,” [Online]. Available: http://www.tn.ifn.cnr.it/facilities/sol-gel-room/sol-gel-principles. [Accessed 29 08 2017].

[262] A. Stadler, “Transparent Conducting Oxides - An up to date overview,” *Materials,* vol. 5, pp. 661 - 683, 2012.

[263] L. Gonzalez-Moragas, “Scale-up synthesis of iron oxide nanoparticles by microwave-assisted thermal decomposition,” *Chemical Engineering Journal,* vol. 281, pp. 87 - 95, 2015.

[264] S. Sundaresan, “Comparison of Solid-State Microwave Annealing with Conventional Furnace Annealing of Ion-Implanted SiC,” *Journal of Electronic Materials,* vol. 36, pp. 324 - 331, 2007.

[265] S. Kellici, K. Gong, T. Lin, S. Brown, R. J. H. Clark, M. Vickers, J. K. Cockcroft, V. Middelkoop, P. Barnes, J. M. Perkins, C. J. Tighe and J. A. Darr, “High-throughput continuous hydrothermal flow synthesis of Zn–Ce oxides: unprecedented solubility of Zn in the nanoparticle fluorite lattice,” *Philosophical Transactions of the Royal Society A,* vol. 368, no. 1927, pp. 4331-4349, 2010.

[266] M. Chen, C. Y. Ma, T. Mahmud, J. A. Darr and X. Z. Wang, “Modelling and simulation of continuous hydrothermal flow synthesis process for nano-materials manufacture,” *The Journal of Supercritical Fluids,* vol. 59, pp. 131-139, 2011.

[267] “Direct and continuous hydrothermal flow synthesis of thermochromic phase pure monoclinic VO2 nanoparticles,” *Journal of Materials Chemistry C,* vol. 6, pp. 11731-11739, 2018.

[268] C. Paine, “Applications and Processing of Transparent Conducting Oxides,” *MRS Bulletin,* pp. 22 - 27, 2000.

[269] M. Katayama, “TFT-LCD technology,” *Thin Solid Films,* vol. 341, pp. 140 - 147, 1999.

[270] Y. Ugai, T. Yukawa, Y. Hatta and S. Aoki, “Reduced process method for thin-film-transistor liquid-crystal display (TFT-LCD) with dry-etching tapered ITO data bus lines,” *JAPANESE JOURNAL OF APPLIED PHYSICS PART 2-LETTERS & EXPRESS LETTERS,* vol. 35, no. 8B, pp. 1027 - 1030, 1996.

[271] A. Van Slyke, “Organic electroluminescent diodes,” *Applied Physics Letters,* vol. 51, p. 913, 1987.

[272] J. Y. Ruan, “A Multi-Touch Interface Circuit for a Large-Sized Capacitive Touch Panel,” *Sensors,* pp. 309 - 314, 2010.

[273] M. B. Babu and S. Vadivel, “High performance humidity sensing properties of indium tin oxide (ITO) thin films by sol–gel spin coating method,” *Journal of Materials Science: Materials in Electronics,* vol. 28, no. 3, pp. 2442-2447, 2017.

[274] O. J. Gregory, “Piezoresistive Properties of ITO Strain Sensors Prepared with Controlled Nanoporosity,” *Journal of the Electrochemical Society ,* vol. 151, no. 8, p. 198, 2004.

[275] B. C. Yadav, K. Agrahari, S. Singh and T. P. Yadav, “Fabrication and characterization of nanostructured indium tin oxide film and its application as humidity and gas sensors,” *Journal of Materials Science: Materials in Electronics,* vol. 27, no. 5, pp. 4172-4179, 2016.

[276] J. Muller, “TCO and light trapping in silicon thin film solar cells,” *Solar Energy,* vol. 77, pp. 918 - 930, 2004.

[277] M. Kim, “Transparent Conductive Oxide Films for OLED devices,” INTECH, 2011.

[278] R. Moritz, “Flexographic printing of nanoparticulate tin-doped indium oxide inks on PET foils and glass substrates,” *Journal of Materials Science,* vol. 52, no. 9, p. 4588, 2016.

[279] A. Helden, S. Dupre and R. Gent, “The Origins of The Telescope,” *Amsterdamn University Press,* vol. 43, pp. 32-36, 2010.

[280] J. R. Michael, D. Joy, J. Henry, N. Ritchie, D. Newbury and J. Goldstein, Scanning Electron Microscopy and X-Ray Microanalysis, Springer, 2017.

[281] A. Einstein, “On A Heuristic Point of View Concering the Production and Transformation of Light,” *Annalen der Physik,* vol. 17, pp. 132-148, 1905.

[282] P. D. Ngo, “Energy Dispersive Spectroscopy,” in *Failure Analysis of Integrated Circuits. The Springer International Series in Engineering and Computer Science*, Boston, Springer, 1992.

[283] T. G. Mezger, The Rheology Handbook: For Users of Rotational and Oscillatory Rheometers, Vincentz Network GmbH, 2002.

[284] J. W. Gooch, Encylopedia Dictionary of Polymers, Berlin: Springer, 2010.

[285] V. G. Sears, S. M. Bleay, H. L. Bandey and V. J. Bowman, “A methodology for finger mark research,” *Science & Justice,* vol. 52, no. 3, pp. 145-160, 2012.

[286] N. Nadaud, N. Lequeux and M. Nanot, “Structural Studies of Tin-Doped Indium Oxide (ITO) and In4Sn3O12,” *Journal of Solid State Chemistry,* vol. 135, pp. 140-148, 1998.

[287] D. Choi, S. J. Hong and Y. Son, “Characteristics of Indium Tin Oxide (ITO) Nanoparticles Recovered by Lift-off Method from TFT-LCD Panel Scraps,” *MDPI Materials,* vol. 7, pp. 7662-7669, 2014.

[288] D. P. Howard, P. Marchand, L. McCafferty, C. J. Carmalt, I. P. Parkin and J. A. Darr, “High-Throughput Continuous Hydrothermal Synthesis of Transparent Conducting Aluminum and Gallium Co-doped Zinc Oxides,” *Combinatorial Science,* vol. 19, no. 4, pp. 239-245, 2017.

[289] Particle Technology Labs, “Problems in Particle Size: Laser Diffraction Observations,” GXP, 2011.

[290] D. S. Y. Jayathilake, “Microwave-assisted synthesis and processing of transparent conducting oxides and thin film fabrication by aerosol-assisted deposition,” Loughborough University, Thesis, 2018.

[291] Y. Li, A. Zhang, H. Lu, X. Zhang, W. Zheng and M. Li, “Effect of Polar Polymers of PEG and PVA on the Enhanced Microwave-Absorbing Properties of MWNTs,” *Journal of Physical Chemistry C,* vol. 122, no. 29, pp. 16956-16963, 2018.

[292] B. Onwona-Agyeman, M. Nakao, T. Kohno, D. Liyanage, K. Murakami and T. Kitaoka, “Preparation and characterization of sputtered aluminum and gallium co-doped ZnO films as conductive substrates in dye-sensitized solar cells,” *Chemical Engineering Journal,* vol. 219, pp. 273-277, 2013.

[293] M. J. Quinn Jr, Wildlife Toxicity Assessment for Nitrocellulose, Elsevier, 2015.

[294] P. Uprety, M. M. Junda, H. Salmon and N. J. Podraza, “Understanding near infrared absorption in tin doped indium oxide thin films,” *Journal of Physics D: Applied Physics,* vol. 51, pp. 295-302, 2018.

[295] A. Roch, L. Stepien, T. Roch, I. Dani, C. Leyens, O. Jost and A. Leson, “Optical absorption spectroscopy and properties of single walled carbon nanotubes at high temperature,” *Synthetic Metals,* vol. 197, pp. 182-187, 2014.

[296] H. Elbishari, J. Satterthwaite and N. Silikas, “Effect of Filler Size and Temperature on Packing Stress and Viscosity of Resin-composites,” *MDPI Molecular Sciences,* vol. 12, no. 8, pp. 5330-5338, 2011.

[297] H. Agura, A. Suzuki, T. Matsushita, T. Aoki and M. Okuda, “Low resistivity transparent conducting Al-doped ZnO films prepared by pulsed laser deposition,” *Thin Solid Films,* vol. 445, no. 2, pp. 263-267, 2003.

[298] A. V. Singh and R. M. Mehra, “Highly conductive and transparent aluminum-doped zinc oxide thin films prepared by pulsed laser deposition in oxygen,” *Journal of Applied Physics,* vol. 90, p. 5660, 2001.

[299] M. S. Dabney, M. F. van Hest, C. W. Teplin, P. S. Arenkiel, J. D. Perkins and D. S. Ginley, “Pulsed laser deposited Nb doped TiO2 as a transparent conducting oxide,” *Thin Solid Films,* vol. 516, no. 12, pp. 4133-4138, 2008.

[300] H. Ohta, M. Orita and M. Hirano, “Highly electrically conductive indium–tin–oxide thin films epitaxially grown on yttria-stabilized zirconia (100) by pulsed-laser deposition,” *Applied Physics Letters,* vol. 76, p. 2740, 2000.

[301] W. M. Tsang, F. L. Wong, M. K. Fung, J. C. Chang, C. S. Lee and S. T. Lee, “Transparent conducting aluminum-doped zinc oxide thin film prepared by sol–gel process followed by laser irradiation treatment,” *Thin Solid Films,* vol. 517, no. 2, pp. 891-895, 2008.

[302] H. J. Kim, M. J. Maeng, J. H. Park, M. G. Kang, C. Y. Kang, Y. Park and Y. J. Chang, “Chemical and structural analysis of low-temperature excimer-laser annealing in indium-tin oxide sol-gel films,” *Current Applied Physics,* vol. 19, no. 2, pp. 168-173, 2019.

[303] IVAM Microtechnology, “Häcker Automation GmbH,” [Online]. Available: https://www.ivam.com/members/haecker_automation_gmbh. [Accessed 14 08 2019].

[304] Polymedia SA, “Präzise elektrische Kontaktierung durch Mikro-Laserlöten,” [Online]. Available: https://www.polymedia.ch/OP/Articles/view/48. [Accessed 14 08 2019].

[305] S. Mihaiu, I. M. Szilágyi, I. Atkinson, O. C. Mocioiu, D. Hunyadi, J. Pandele-Cusu, A. Toader, C. Munteanu, S. Boyadjiev, J. Madarász, G. Pokol and M. Zaharescu, “Thermal study on the synthesis of the doped ZnO to be used in TCO films,” *Journal of Thermal Analysis and Calorimetry,* vol. 124, no. 1, pp. 71-80, 2016.

[306] C. H. Choi, S. Y. Han, Y. W. Su, Z. Fang, L. Y. Lin, C. C. Cheng and C. H. Chang, “Fabrication of high-performance, low-temperature solution processed amorphous indium oxide thin-film transistors using a volatile nitrate precursor,” *Journal of Materials Chemistry C,* vol. 3, no. 4, pp. 854-860, 2015.

[307] W. H. Qi, B. Y. Huang, M. P. Wang, Z. M. Yin and J. Li, “Shape factor for non-cylindrical nanowires,” *Physica B: Condensed Matter,* vol. 403, no. 13-16, pp. 2386-2389, 2008.

[308] D. Liu, G. Zhang, J. Li and O. Ostrovski, “Solid State Carbothermal Reduction of Alumina,” *Essential Readings in Light Metals,* pp. 1076-1081, 2009.

[309] R. S. Wagner and W. C. Ellis, “Vapor-liquid-solid mechanism of single crystal growth,” *Applied Physics Letters,* vol. 4, no. 5, pp. 89-90, 1964.

[310] Y. Zhang, N. Wang, S. Gao, R. He, S. Miao, J. Liu, J. Zhu and X. Zhang, “A simple method to synthesise nanowires,” *Chem Mater,* vol. 14, no. 8, pp. 3564-3568, 2002.

[311] M. O. Orlandi, P. H. Suman, R. A. Silva and E. P. Arlindo, “Carbothermal Reduction Synthesis: An Alternative Approach to Obtain Single-Crystalline Metal Oxide Nanostructures’,” in *Recent Advances in Complex Functional Materials*, Springer, 2017.

[312] B. Juergen, T. F. Baumann, D. Subho and H. Horst, “Nanoporous carbon tunable resistor/transistor and methods of production thereof”. United States Patent 8,703,523, 22 04 2014.

[313] J. S. Thorp, M. Akhtaruzzaman and D. Evans, “The dielectric properties of alumina substrates for microelectronic packaging,” *Journal of Materials Science,* vol. 25, no. 9, pp. 4143-4149, 1992.

[314] J. Cain, “PARASITIC INDUCTANCE OF MULTILAYER CERAMIC CAPACITORS,” AVX Corporation.

[315] Z. Ahmad, Dielectric Materials, InTech, 2012.

[316] DuPont Teijin Films, “Melinex O Polyester Film,” DuPont Teijin Films.

[317] T. Hiratsuka, H. Tanaka and M. T. Miyahara, “Critical energy barrier for capillary condensation in mesopores: Hysteresis and reversibility,” *The Journal of Chemical Physics,* vol. 144, p. 164705, 2016.

[318] T. Islam and M. Z. U. Rahman, “Investigation of the Electrical Characteristics on Measurement Frequency of a Thin-Film Ceramic Humidity Sensor,” *IEEE TRANSACTIONS ON INSTRUMENTATION AND MEASUREMENT,* vol. 65, no. 3, pp. 694 - 702, 2016.

[319] X. Li, X. Chen, X. Yu, X. Chen, X. Ding and X. Zhao, “A High-Sensitive Humidity Sensor Based on Water-Soluble Composite Material of Fullerene and Graphene Oxide,” *IEEE SENSORS,* vol. 18, no. 3, pp. 962 - 966, 2018.

[320] Z. Chen and C. Lu, “Humidity Sensors: A Review of Materials and Mechanisms,” *ASP: Sensors Letters,* vol. 3, pp. 274-295, 2005.

[321] A. K. Jonscher, “Dielectric relaxation in solids,” *Journal of Physics D: Applied Physics,* vol. 32, pp. 57 - 70, 1999.

[322] M.-S. Wang, J. Weifang and L. Ziyu, “Dependences of ionic conductivity and dielectric constant of amorphous nonpolar polymers on free volume,” in *3rd Internation Conference on Properties and Applications of Dielectric Materials*, Tokyo.

[323] L. Juhász and J. Mizsei, “Humidity sensor structures with thin film porous alumina for on-chip integration,” *Thin Solid Films,* vol. 517, no. 22, pp. 6198-6201, 2009.

[324] IDTechEx, “Transparent Conductive Films (TCF) 2016-2026: Forecasts, Markets, Technologies,” IDTechEx, 2016.